A scanning probe microscopy (SPM) study of Bi(110) nanostructures on highly oriented pyrolytic graphite (HOPG)

A thesis submitted in partial fulfillment
of the requirements for the Degree of

Doctor of Philosophy in Physics
in the
University of Canterbury

by

Ojas Mahapatra

Department of Physics and Astronomy
University of Canterbury
2013

To my family who supported me at every step of my life

Abstract

This research work is aimed at understanding the electronic properties of Bi(110) nanostructures. This study chiefly uses Scanning Tunneling Microscopy (STM), Scanning Tunneling Spectroscopy (STS) and Non Contact Atomic Force Microscope (NCAFM) to investigate the geometric and electronic structure of Bi(110) islands on highly oriented pyrolytic graphite (HOPG) substrate.

STM measurements are the primary focus of the thesis which involves imaging the bismuth islands and study of its atomic structure. STM images of the Bi(110) islands reveal a 'wedding cake' profile of the bismuth islands that show paired layers on top of a base. I(V) (Current vs voltage) data was acquired via STS techniques and its first derivative was compared to DFT calculations. The comparison implied the presence of a dead wetting layer which was present only underneath the bismuth islands. We observed bilayer damped oscillations in the surface energy that were responsible for the stability of paired layers in Bi(110) islands. Interesting Moiré pattern arising out of misorientation between the substrate and the overlayer are also observed in STM images on some bismuth islands.

Bright features pertaining to enhanced LDOS (local density of states) were observed on the perimeter of the bismuth islands and stripes in the STM images and STS dI/dV maps which appear at energies around the Fermi level. The bright features which we termed as 'bright beaches (BB)' are also observed on grain boundaries and defects that suggest that they are related to termination of the chain of bismuth atoms.

The Bi(110) islands and stripes were observed to form preferred widths with a well defined periodicity. This peculiar phenomenon was attributed to a lateral quantum size effect (QSE) that results from a Fermi wave vector with appropriate shifts in Fermi energy. The widths of the islands prefer to adjust themselves at the nodes of this in-plane Fermi wavelength.

NaCl deposited on a HOPG substrate forms cross shaped islands which were used as spacers to limit the interaction between the bismuth films and the underlying HOPG substrate. The NaCl islands are transparent to the flow of tunneling current and allow STS measurements. The LDOS of Bi/HOPG was very similar to the LDOS of Bi deposited on NaCl/HOPG which suggests that the wetting layer underneath the bismuth islands plays an important role in decoupling the film from the underlying substrate.

Table of Contents

1. Introduction

The electronic properties of ultra thin films of semi-metals have attracted considerable interest in past few years mostly because of the unconventional transport properties resulting from a unique electronic structure. Bismuth is a semi-metal with symbol Bi and atomic number 83. It is located in group-V of the periodic table, with an atomic electron configuration $6s_26p_3$. It was the first metal whose Fermi surface was experimentally identified [1, 2]. The mean free path exceeds 2 μm, that is almost two orders of magnitude greater than copper [3]. Bismuth is also known to have low carrier densities (10^{-5} electrons per atom), low effective masses (~10^{-2} m_e, where m_e being the mass of a free electron), high diamagnetic susceptibility and high dielectric constant [4]. The de Broglie wavelength of carriers in bismuth is very long (30-40 nm) which makes it an attractive case for quantum transport and finite size effects [5]. The peculiar electronic structure is thought to be responsible for the observation of desirable properties such as superconductivity [6] in particles with reduced dimensions and increased magneto resistance [7, 8] and enhanced thermoelectric efficiency [9] in thin films leading to extensive interest in their fabrication.

Bismuth thin film deposition has been investigated on a variety of substrates [10-16], with both island [13-16] and continuous film morphologies [17, 18] observed. When atoms are deposited from the vapor phase onto atomically smooth substrates, the prevailing growth mode (island or layer-by-layer) is dictated by the relative strength of the bonds formed between the adsorbate atoms, and the adsorbate/substrate interface [19]. In general, when bonding between an adsorbate and substrate is weak, island aggregation typifies the early stages of film growth, and can allow for the formation of well defined surface structures with abrupt adsorbate/substrate interfaces [20]. Since the de Broglie wavelength in bismuth is large, these well defined structures are suitable candidates for the observation of quantum confinement or quantum size effects [21, 22].

The first observations of quantum size effects in thin films of bismuth were reported in 1966 by Ogrin *et al* [23]. They studied thin Bi films and observed oscillations in the resistivity, the Hall constant, the magneto resistance, and the Hall mobility as a function of the film thickness. It was noticed that quantum confinement may also convert bismuth into a semiconductor by inducing a slight shift in energy of the electronic bands [24]. Numerous experiments have since been conducted to reveal the predicted semimetal to semiconductor transition in bismuth thin films [25-27]. These quantum confinement experiments have been performed mostly on Bi(111) oriented thin films (Note that we use rhombohedral indexing to specify the bismuth surfaces in this thesis) since it is the natural cleavage plane of bismuth and this is the direction along which the quantum confinement is

largest due the small effective mass of the electrons. Various growth strategies have been studied, and it has turned out that semimetal-semiconductor super lattices like Bi/CdTe(111), and Bi/PbTe(111), are interesting as indirect narrow-gap heterostructures with potentially attractive properties for optical and electro-optical devices [28, 29].

The relative importance of the surface increases as the size of the structures becomes smaller. One of the most fascinating aspects in the study of surfaces is that their properties can be radically different from the corresponding bulk material and bismuth is a striking example of possible differences between surface and bulk material properties [30]. The surfaces of bismuth are characterized by prominent surface states which dominate the density of states around the Fermi level [31]. The transport properties can, therefore, be considered to originate only from these states, forming a two-dimensional (2D) electron gas localized at the surface of the semi metal.

The presence of metallic surface states has been studied extensively on the Bi(111) surface [32-35]. The Bi(110) surface is very similar to the (111) surface and also supports metallic surface states [30, 31, 36-38]. The strong spin orbit coupling in Bi furthermore leads to a strong spin splitting of the surface states, which was experimentally observed on Bi(110) [30, 39, 40]. These surface states have much lower Fermi velocities than the bulk carriers and the Fermi surface elements are much bigger than the projected bulk Fermi surface. Both lead to a situation where the density of states at the Fermi level is considerably higher at the surface than in the bulk. Such a system is interesting for investigation of the properties of electronic interactions in 2D, e.g. correlation, screening, exchange, quasiparticle excitation and superconductivity. Interestingly, the Bi(110) surface and Bi(110) thin films have been vastly unexplored in contrast to Bi(111) systems. With the discovery of bismuth as an important parent material for exotic topologically protected states and prediction of topological edge states in thin Bi(111) films [41], the Bi(110) system is an important candidate for exploration of new and interesting properties.

Bi(110) thin films are the focus of the present research work. Before we describe our experiments, a background knowledge of the physical and electronic structure of Bi(110) thin films is deemed important to comprehend the results in this thesis. Hence we review the geometric structure and the electronic structure of bulk Bi(110) and Bi(110) thin films in the following sections. Spin orbit interaction (SOI) is an important component of the electronic structure of bismuth which would be briefly introduced in section 1.2.

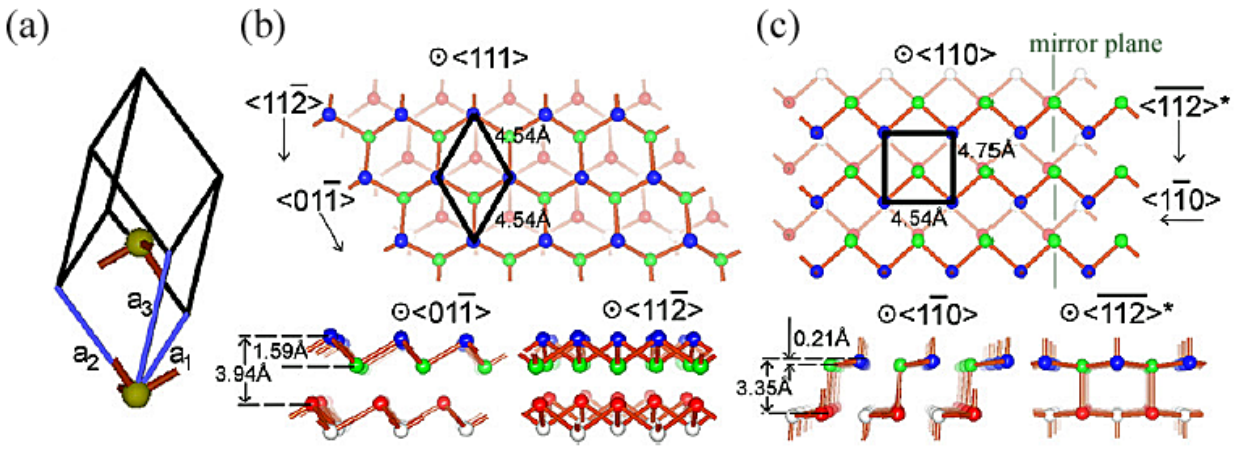

Figure 1.1: Crystallographic structure of bulk bismuth. (a) Rhombohedral unit cell, blue lines correspond to vectors spanning the lattice. (b) (111) and (c) (110) surface planes of ideal Bi crystal. The upper parts of (b) and (c) show top views and the bottom parts show two side views. Atoms in different layers are indicated using different colors–blue, green, red and white for 1st, 2nd, 3rd and 4th layer respectively.

1.1 Bi(110) surface geometric structure

The simplest way to describe bulk Bismuth is a rhombohedral Bravais lattice shown in Figure 1.1 (a) (A7, space group R3m) with two atoms per unit cell located at positions ±(u,u,u), where u = 0.234 at 4.2 K [42]. The primitive vectors a_1, a_2 and a_3 are of equal magnitude and measure 4.7236 Å [29]. They constitute a rhombohedral angle α = 57.3^0 between them. The surface of Bi (110) is shown in Figure 1.1 (c) and is characterized by the presence of two atoms and one dangling bond per unit cell. The surface unit cell is shown by the black pseudo square or more appropriately a rectangle with cell constants of 4.75 Å and 4.54 Å. The surface has low mirror symmetry with only one mirror line shown as the green dashed line in Figure 1.1 (c). The green atoms shown in the middle of the unit cell are slightly depressed by 0.2 Å. This can be seen in the $< 1\bar{1}0 >$ view in (c). This puckered layer of atoms is also referred to as a single 'bilayer' by other authors [31, 40]. However, as the vertical separation between the two atoms is really small (0.2 Å) we refer to these as a 'monolayer (ML)' in this thesis, where 1 ML is 3.35 Å thick (see $< \bar{1}10 >$ view in Figure 1.3 (c)). The dangling bond on every second blue atom is also visible in the $< 1\bar{1}0 >$ view. Atoms seen from the $< 110 >$ direction form zigzag chains with covalent bonds to the neighboring atoms and van der Waals forces between the chains. Upon careful inspection one can see that these chains are edges of Bi (111) monolayers (see Figure 1.1 (b), $< 01\bar{1} >$ view) which have been rotated by angle α. The '*' in the third direction labeled as $< \overline{112} >$* in Figure 1.1 (c) indicates that the vector is not quite aligned along $< 112 >$ direction [43].

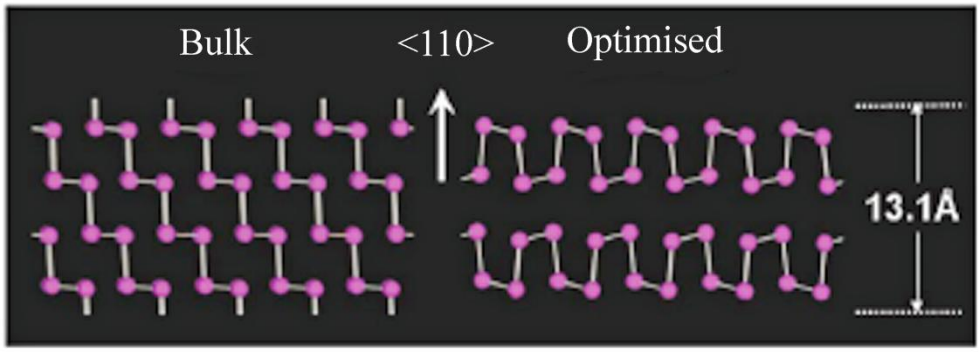

Figure 1.2: The left-hand side is a side view of a four layer Bi(110) phase with unrelaxed bulk structure. The right-hand side is the calculated atomic structure after structural optimization. The intrabilayer structure of this new nanofilm allotrope is analogous to the so called 'puckered-layer structure' of black phosphorus while their stacking sequence is different. Image reproduced from [44]

1.1.1 Layer pairing in thin Bi(110) films

The most common facet of a bismuth crystal is (111) due to its layered character, however the (110) facet has been often reported for thin films on Bi/HOPG [13-16] and Bi/Si [44-46]. It was found that in many cases the preferred structures in these films included paired (110) planes. The preferred selection of thickness was attributed to two reasons, (i) quantum size effects arising out of confinement of the electron within the film [47] and (ii) formation of a new allotrope [44]. We discuss the paired layers in Bi(110) thin films in section 3.2.1 and quantum size effects in Bi(110) thin films in section 5.2.

Nagao *et al* [44] discussed the formation of a new allotrope in Bi(110) thin films grown on silicon substrate as a function of thickness on the scale of several atomic layers. Using electron diffraction and STM they showed the presence of a wetting layer which is formed initially and bismuth grows with a new phase whose structure is significantly different from bulk bismuth. The *ab initio* calculations showed the presence of a new puckered-layer structure (also known as A17 structure [31]) which has been observed previously in black phosphorous only. This new structure is shown as the 'optimised structure' in Figure 1.2. The optimisation involves rotation of a bond which removes the dangling bonds from the (110) surface of the bulk structure which results in formation of a bilayer stacked configuration. This configuration shows 'paired layers' which are 2 ML thick and results in Bi(110) films with bilayer increment.

Sharma *et al* challenged the concept of layer pairing by exploring the growth of Bi(110) islands on quasicrystal surfaces [47]. They observed that bilayer islands were unstable on quasicrystal substrates in their experiments. The bismuth islands either reshaped into 4 ML islands or coalesced into a nearby 4 ML island. They also argued against the model described by Nagao *et al* that

predicted that 'the pairing of layers occurred independently from the nature of the substrate', as they found no evidence of layer pairing or 'magic heights' in an experiment where Bi was deposited on Pd(111) substrate.

The physical structure of Bi(110) thin films is an interesting issue with evidences for and against the new allotrope. We investigate the formation of the A17 allotrope in our experimental results and calculations in section 3.2.1 and 3.4 respectively. We now turn to the description of the Bi(110) electronic structure. We begin with a short description of the spin orbit interaction concept and also discuss its implications in bulk bismuth and bismuth thin films in the following section.

1.2 Spin orbit interaction (SOI)

Spin orbit interaction is a well known phenomenon that manifests itself in lifting the degeneracy of energy levels in atoms, molecules and solids [48]. It is a relativistic effect which is important for electronic structures of heavy atoms and their solids. An electron moving with velocity $\vec{v}$ in an electric field $\vec{E}$ experiences a magnetic field in its rest frame, which is given by:

$$\vec{B} = \frac{\gamma(\vec{v} X \vec{E})}{c^2} \qquad \text{Equation 1.1}$$

where $\gamma = (1 - \frac{v^2}{c^2})^{-\frac{1}{2}}$. The magnetic field $\vec{B}$ couples to the electron's spin, giving rise to the Hamiltonian:

$$H_{SOC} = \frac{\hbar}{4m^2c^2}(\vec{p}\, X\, \vec{E})\vec{\sigma} = \frac{\hbar}{4m^2c^2}(\nabla V\, X\, \vec{p})\vec{\sigma} \qquad \text{Equation 1.2}$$

where V is the potential, m is the mass of an electron, $\vec{p}$ is the momentum and $\vec{\sigma}$ is the Pauli spin operator. The Hamiltonian leads to the splitting of the states with different spins [30].

In a free atom, SOI can lift the degeneracy of states with the same orbital wavefunction but with opposite spins [49]. In solids, however such a splitting can be forbidden due to a combination of inversion symmetry [50] and time reversal symmetry [51]. For an electron with momentum $\vec{k}$ and spin ($\uparrow$ (up) or $\downarrow$ (down)), inversion symmetry is represented by:

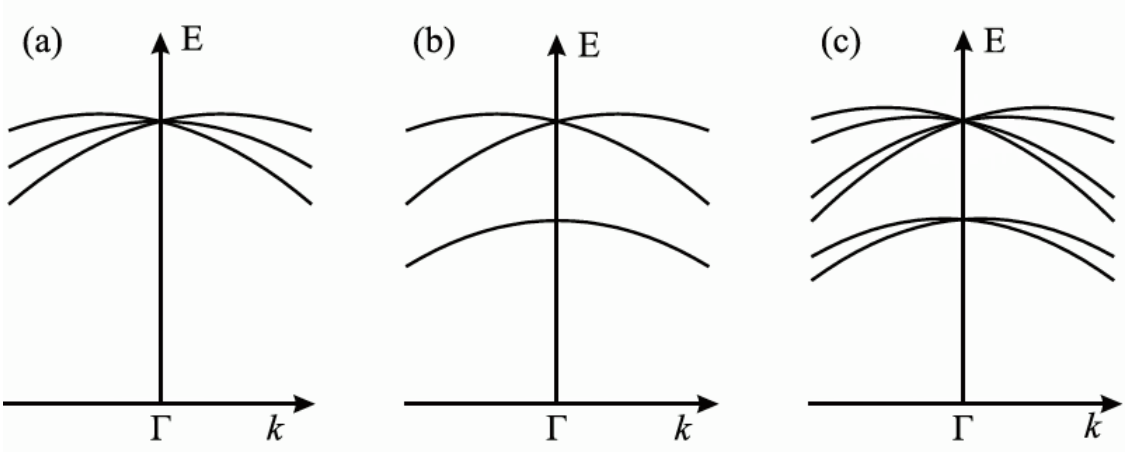

Figure 1.3: Schematic representation of the influence of SOI on the p levels at the centre of Brillouin zone (a) without SOC 6 degenerate p levels are observed at Γ point (b) Inclusion of SOC splits the band into $p_{3/2}$ and $p_{1/2}$ band but leaves the spin degeneracy in lattices with inversion symmetry. (c) The spin degeneracy is completely lifted in a lattice without inversion symmetry except for the Γ point.

$$E(\vec{k},\uparrow) = E(-\vec{k},\uparrow) \qquad \text{Equation 1.3}$$

Time reversal symmetry preserves the Kramer's degeneracy between a function ψ(k, s) and its complex conjugate ψ*(k, s) [52], where k is the wave vector and s is electron spin. Therefore at any point in the Brillouin zone, one can write the energy as:

$$E(\vec{k},\uparrow) = E(-\vec{k},\downarrow) \qquad \text{Equation 1.4}$$

A combination of time reversal symmetry and inversion symmetry results in a band structure with doubly degenerate bands:

$$E(\vec{k},\uparrow) = E(\vec{k},\downarrow) \qquad \text{Equation 1.5}$$

As an example, we consider the center of a BZ (Γ point) that has cubic symmetry. In a tight binding model, the p bands are made from atomic p wave functions. In a free atom without SOC, there are three degenerate p functions, so three p bands will appear in the model (see Figure 1.3 (a)). Each of these three p bands is doubly degenerate leading to six fold degeneracy at the Γ point. When spin orbit coupling is included the p bands split into two sub-bands with fourfold $p_{3/2}$ and twofold $p_{1/2}$ degeneracy [30, 53] (see Figure 1.3 (b)). The bands will now behave differently as we move away from the Γ point depending on whether or not there is inversion symmetry in the lattice. In crystals with center of inversion, the fourfold $p_{3/2}$ (with j = 3/2) band splits into two doubly degenerate bands with $m_j = \pm 3/2$ and $m_j = \pm 1/2$ (with projections taken in the direction of the vector k). If a center of inversion is absent then the $p_{3/2}$ and $p_{1/2}$ bands will additionally split due to spin

orbit interaction and the spin degeneracy is completely lifted giving rise to spin up or spin down bands (illustrated in Figure 1.3 (c)).

The degeneracy is broken for every material at the surface because of loss of inversion symmetry at the surface [30]. The electrons in the surface state can be viewed as two dimensional electron gas with a potential gradient perpendicular to the surface [54]. An electron moving on the surface thus experiences a magnetic field described by Equation 1.1. At k = 0, no splitting takes place because of the condition $E(0,\uparrow) = E(-0,\downarrow)$, as per symmetry requirements. Such vanishing of splitting usually happens at the symmetry points of a crystal. However as k becomes non zero, band splitting is observed where two eigenstates for each k are found which differ in energy and spin direction i.e.

$$\mathrm{E}(\mathrm{k},\uparrow) \neq \mathrm{E}(\mathrm{k},\downarrow) \qquad \text{Equation 1.6}$$

After the discovery of the analogy between the surface states and the two dimensional electron gas found in the semiconductor hetero structures, this spin orbit splitting on surface came to be commonly referred to as Rashba effect [55, 56]. Here the motion of an electron in the plane of the two dimensional electron gas (characterized by its Bloch vector $\mathrm{k}_{||}$) through a perpendicular electric field e_Z, results in a magnetic field in the rest frame of an electron, that couples to the spin, s, of the particle as:

$$\mathrm{H_R} = \alpha_\mathrm{R}(\mathrm{e_Z\ x\ k_{||}}).\ \mathrm{s} \qquad \text{Equation 1.7}$$

Petersons and Hedegard [57] showed that the Rashba parameter α_R can be simply written as a product of nuclear number Z and a parameter describing the asymmetry of the wavefunction. Hence the heavier an atom, the greater is the spin orbit splitting. The splitting of the surface states of course is an effect of spin orbit coupling. The term Rashba effect or Rashba splitting, however, is particularly used in cases where the spin orbit coupling completely lifts the spin degeneracy of the surface states [55] (analogous to the example shown in Figure 1.3 (c)).

SOI in bismuth thin films gives rise to many subtle and interesting effects in the surface electronic structure such as the emergence of topological insulators [41, 52, 58-60]. Ultra thin bismuth films are more interesting because of the loss of inversion symmetry at surface, the surface states show high electron density and large spin orbit coupling [31, 39, 40, 61, 62]. We describe the

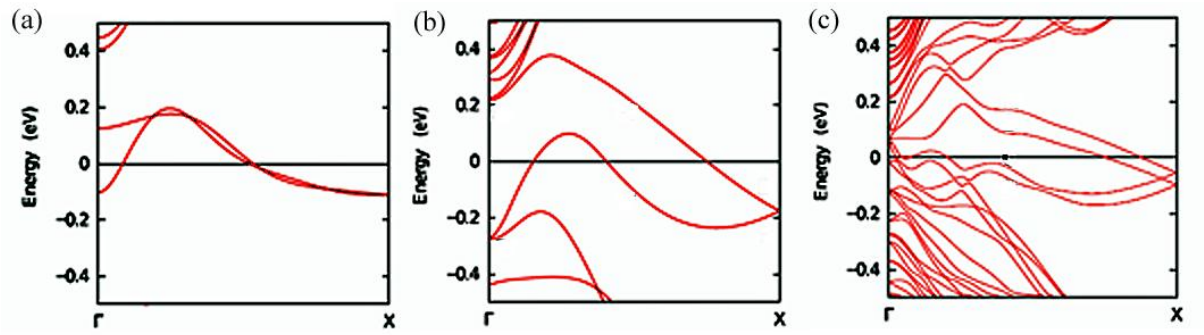

Figure 1.4: Band structure of zig zag nanoribbon of bismuth (a) excluding SOI and with inversion symmetry (b) including SOC and inversion symmetry (c) including SOC and excluding inversion symmetry. Image reproduced from [64]

SOI effects on bismuth films with a short sub-section on Bi(111) thin films since it is the most studied orientation of bismuth films. We describe the effects of SOI in the electronic structure of Bi(110) crystals in section 1.3 and then discuss band structure calculations on ultra thin Bi(110) films in section 1.4.

1.2.1 SOI in Bi(111) thin films

The loss of inversion symmetry is dependent on the interaction of the film with the substrate on which it is deposited [63, 64]. An effect of the substrate on the splitting of surface states of Bi (111) thin film is shown in Figure 1.4. The bands shown in Figure 1.4 (a) and (b) are calculated edge states on a free standing Bi(111) slab in which inversion symmetry is preserved. Edge states are modified surface states which are highly localized on the edges of the nanoribbon [64]. SOI was included in (b) and ignored in (a). It can be seen that inclusion of SOI enlarges the energy gap between the two edge states. The bands in Figure 1.4 (c) were calculated by placing the freestanding nanoribbon slab on top of a 1 bilayer Bi(111) film thereby simulating an interaction of the slab with a substrate. This kind of interaction is analogous to terminating the slab by H-bonds. In cases where the film interacts with the substrate, the inversion symmetry is broken in the system which leads to an additional splitting of bands and a complete lifting of spin degeneracy. A complete lifting of spin degeneracy is observed in Figure 1.4 (c) where the film interacts with the underlying substrate and splits into spin up and spin down bands.

The dependence of spin polarization of the surface states on the film thickness was studied by Takayama *et al* in Bi (111)/Si thin films [63]. Films of thicknesses ranging from 8 ML to 40 ML were studied by spin resolved ARPES (angle resolved photoemission spectroscopy). Figure 1.5 shows the result of the study in which the upper panel of the image shows the relative proportion of spin up and down spin in a particular thickness (red signifies spin up and blue is spin down). The lower panel quantifies the degree of polarization by subtracting the spin curves from one another in the upper

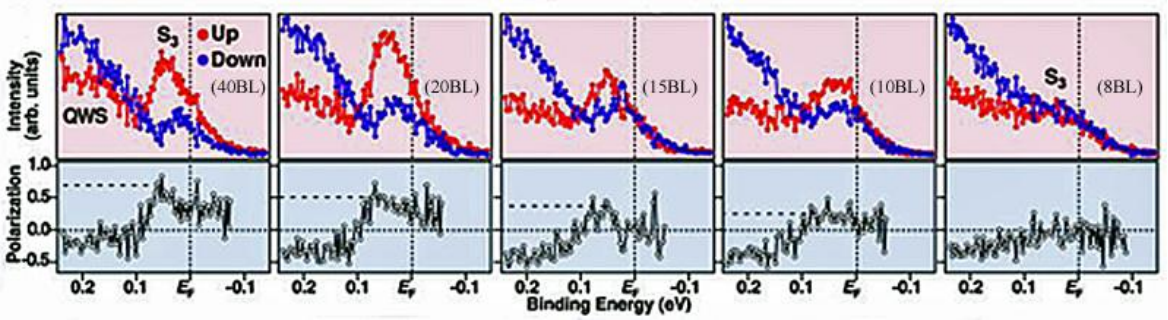

Figure 1.5: Dependence of spin polarization on the thickness of bismuth film. The upper panel shows spin resolved energy distribution curves and the lower panel shows the corresponding spin polarization. Image reproduced from [63]

panel. It can be seen that as the thickness of the film is increased from extreme right panel to the extreme left panel, the spin polarization decreases. In the present case the interaction between the Bi(111) films and the silicon substrate is very weak suggesting that the film is nearly free standing. In the case of free standing slabs, spin split states (also called Rashba states) emerge on both sides of the slab, however these two Rashba states should have opposite spin directions because of symmetry requirement as shown in Figure 1.6. When the film is really thin, these up and down spin states mix and hybridize leading to negligible spin polarization. However, if the film is thick enough (bulk like) then the Rashba states behave independent of each other which leads to a higher degree of spin polarization.

The spin split surface states are promising candidate in the field of spintronics [65]. Bismuth thin films are interesting because of their sizeable splitting and the contribution of these spin split states to the total density of states at the Fermi level which shows up in transport properties. Ultra thin films of Bi(111) especially have gained a lot of attention after they were predicted to house topologically protected edge states [41]. In fact Bi(111) films still remain the most studied

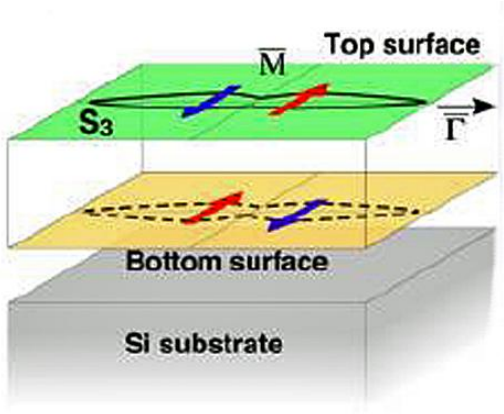

Figure 1.6: Schematic view of the spin vectors for the Fermi surface of the bismuth slab on top and bottom surfaces. Image reproduced from [63]

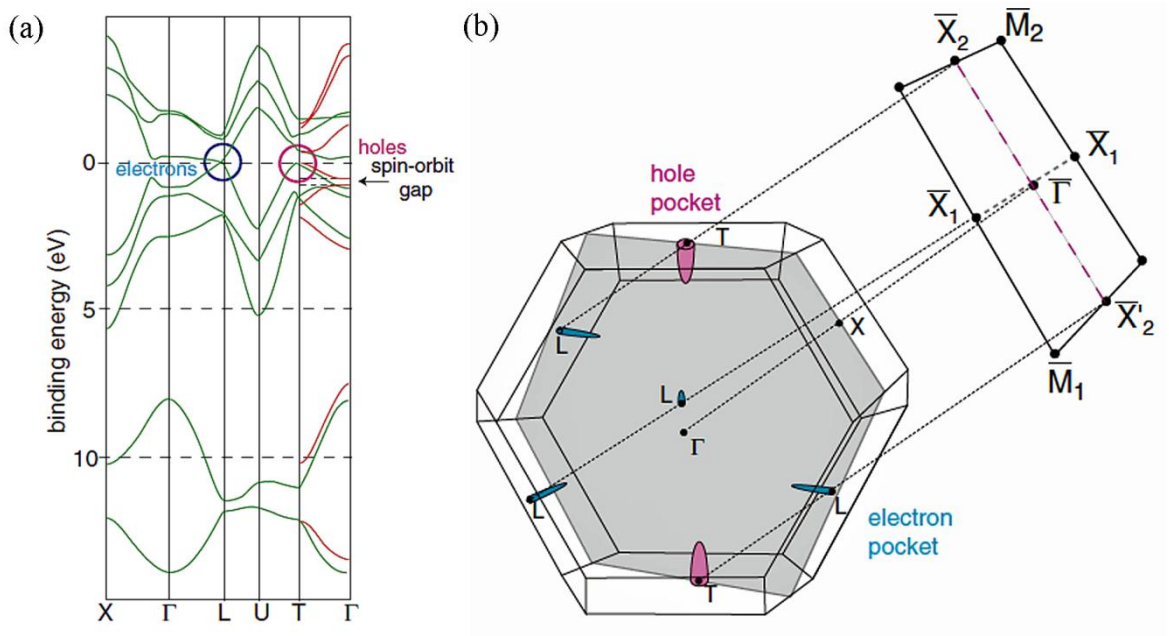

Figure 1.7: Bulk band structure of Bi from the tight-binding calculation of Liu and Allan (green lines); first principles calculation by Gonze *et al* (red lines), only in the $\Gamma - T$ direction. (b) Bulk Brillouin zone of Bi and a schematic sketch of the Fermi surface (not to scale). The $\Gamma - T$ line corresponds to the C_3 axis and the [111] direction in real space. Image reproduced from [30]

crystallographic orientation of bismuth thin films followed by Bi(110) films.

1.3 Bi(110) Surface Electronic structure

One of the earliest papers that studied the electronic band structure of Bismuth using pseudo-potentials was published by S. Golin [66] in 1968. After the discovery of de Haas-van Alphen effect in Bismuth [67] most of the efforts were directed to study the band structure close to the Fermi level. Gonze, Michenaud and Vigneron [68] employed the standard Hohenberg-Kohn-Sham density functional theory to study the electronic structure of As, Sb and Bi. However to decipher the electronic band structure near the Fermi level the *ab initio* methods are seldom accurate because of the small energy scale involved and they are also computationally expensive. Tight binding calculations are usually the method of choice in such scenarios and one such calculation was published by Liu and Allen whose parameters have been frequently used for the projection of bulk band structure on different Bi surfaces. The result of their calculation is shown in Figure 1.7 (a).

An inspection of Figure 1.7 (a) reveals the semi-metallic character of bismuth. The p bands cross the Fermi level close to the T and L points creating hole and electron pockets respectively. In a narrow energy window around the Fermi level the density of states drop dramatically. In the first principle calculations by Gonze *et al* [68], the inclusion of SOI did not have much effect on the lowest two bands (calculated only in Γ-T direction and shown by red lines in Figure 1.7 (a)) since they

predominantly have s character. The effect, however, is strongly felt on the bands near Fermi level and accounts for the hole Fermi surface at the T point. The inclusion of SOI however does not split the bands because the inversion symmetry is preserved in bulk [69] and each band is doubly degenerate.

The bulk Brillouin zone (BZ) of bismuth and the projected (110) surface Brillouin zone (SBZ) is shown in Figure 1.7 (b). The usual notation for symmetry points have been used for the BZ [70]. The shaded plane is the bulk mirror plane and its (110) projection is shown as a dashed pink line. The points at the side of the SBZ are called $\overline{\mathrm{X}}$ and the points at the corners are called $\overline{\mathrm{M}}$. The low symmetry of the SBZ with only a mirror plane is reflected in the electronic structure e.g. the $\overline{\mathrm{X}}_2$ and $\overline{\mathrm{X}}_2'$ points correspond to k points along the T-L-T line of the bulk BZ while the $\overline{\mathrm{X}}_1$ points correspond to k points along the L-L-L line. This means that the projection of the bulk electronic structure on the $\overline{\mathrm{X}}_2$ and $\overline{\mathrm{X}}_2'$ points is different from $\overline{\mathrm{X}}_1$. The two surface lattice vectors are equal to a rhombohedral unit vector a in the mirror plane and a hexagonal unit vector a_h perpendicular to the mirror plane (for details on rhombohedral and hexagonal vectors refer section 2.1.1.1). From the direct surface lattice the reciprocal surface lattice is generated by two perpendicular vectors $\overrightarrow{\mathrm{g}_1}$ and $\overrightarrow{\mathrm{g}_2}$ which are given by:

$$\overrightarrow{\mathrm{g}_1} = \frac{2\pi}{a_h} = 1.3855\ \text{Å}^{-1}$$
$$\overrightarrow{\mathrm{g}_2} = \frac{2\pi}{a} = 1.3239\ \text{Å}^{-1} \qquad \text{Equation 1.8}$$

1.3.1 Bi(110) Surface reciprocal lattice

The surface reciprocal lattice of Bi(110) and the SBZ is shown in Figure 1.8. Because of the presence of a mirror plane m (dashed line connecting $\overline{\mathrm{X}}_2$ and $\overline{\mathrm{X}}_2'$) one may think that the dispersion of electronic states would be different in the left and right sections of the SBZ. However, it is not so because of time reversal symmetry [30]. Time reversal symmetry dictates that if there is a surface state at $k_{||}$ with spin ↑, then there will also be an equivalent state at $-k_{||}$ with spin ↓. For example if one of the $\overline{\mathrm{M}}_1$ points is considered, then the opposite $\overline{\mathrm{M}}_2$ point would be equivalent. The mirror plane combined with the time reversal symmetry renders all the $\overline{\mathrm{M}}$ points equivalent and results in an effective mirror line m_2 perpendicular to m. Therefore in non-spin resolved measurements it is usually sufficient to measure one quarter of the SBZ [36, 40] and the rest can be constructed independently.

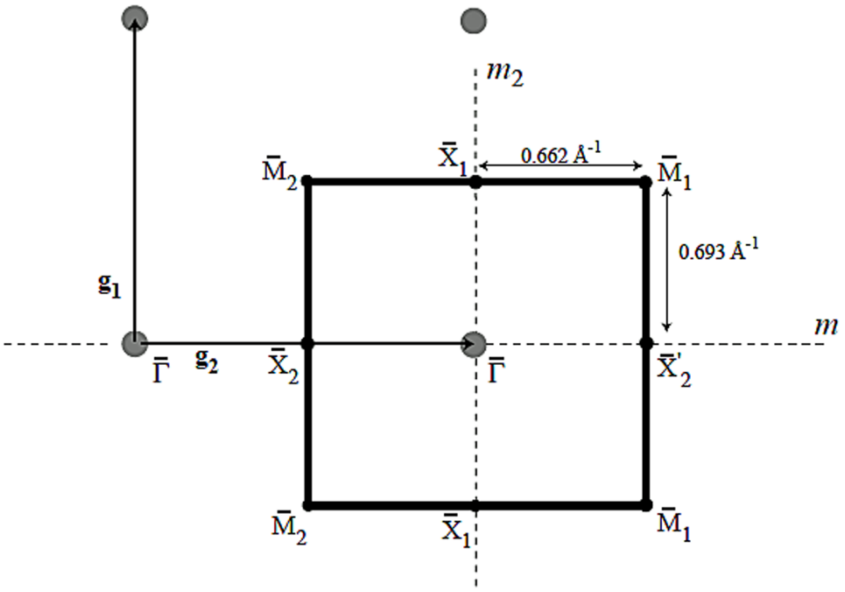

Figure 1.8: The (110) surface reciprocal lattice and the corresponding Brillouin zone. The dashed line m is the structural mirror plane, while the line m_2 is the effective mirror plane due to time-reversal symmetry.

The bulk Bi(110) surface has been studied extensively by ARPES [36, 40]. In Figure 1.9 (a) the surface electronic structure of bulk Bi(110) is shown [40]. The black bands shown in (a) are experimental results (bulk bands) and the red bands are a result of *ab initio* calculations (surface states). In a bulk crystal the inversion symmetry is broken at the surface and SOI lifts the Kramer's degeneracy and all the bands are non-degenerate i.e. they contain only one spin per band and k point [40]. It is only at certain special points in the SBZ, like $\bar{\Gamma}$ and $\bar{M}$, that the symmetry forces the spin split bands to be degenerate [39].

The large splitting results in a non-degenerate Fermi surface with four distinct elements (see

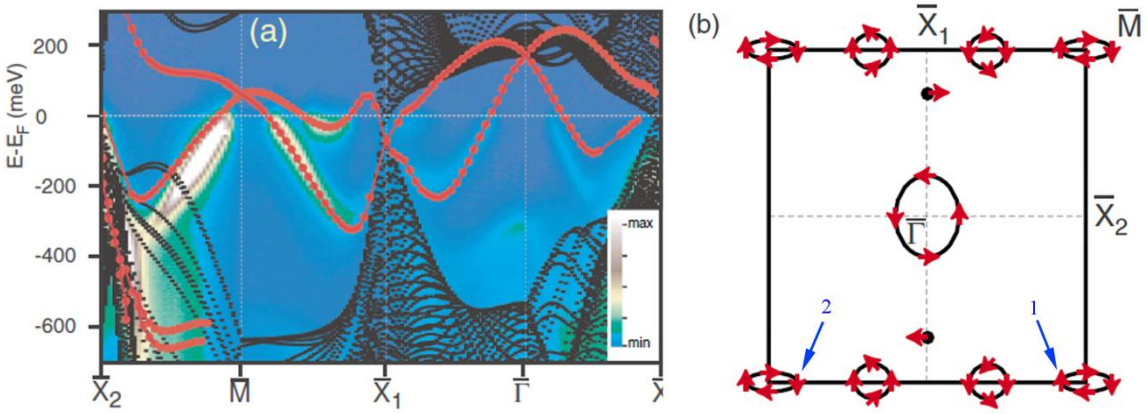

Figure 1.9: (a) Surface electronic structure of Bi(110). The color scale plot is the linear photoemission intensity measured by ARPES; the red markers are the result of *ab initio* calculation. (b) Sketch of the SBZ and the Fermi surface with an indication of the approximate spin direction. Image reproduced from [40]

Figure 1.9 (b)). There are two hole pockets around $\bar{\Gamma}$ and $\bar{M}$, a shallow electron pocket along $\bar{M}$-$\bar{X}_1$ and a small feature along $\bar{\Gamma}$-$\bar{X}_1$. The blue arrow 1 in Figure 1.9 (b) denotes a spin direction on the hole pocket at lower right $\bar{M}$ point, the corresponding spin direction is shown by blue arrow 2 in the lower left $\bar{M}$ point is flipped because of time reversal symmetry.

The backscattering of surface electronic states is prohibited in non degenerate spin systems (such as the one shown in Figure 1.9 (b)) because the incoming wave of E(k, ↑) is reflected back as E(-k, ↓) and the waves with opposite spins cannot interfere [40]. However, such spin texture can lead to other interesting electron scattering phenomena e.g. quasiparticle interference [40, 71] in which an electron can transit from a location to another location on the Fermi surface that has the same spin i.e. spin conserved transitions [40, 72, 73]. The spin conserved transitions can give rise to LDOS oscillations observable by STM (refer section 4.1.2 for more details).

1.4 Electronic structure of ultra thin Bi(110) films

Koroteev *et al* performed first principles calculations on 1-6 ML of Bi(110) thin films [31]. The results of their calculations are shown in Figure 1.10. In the case of 1 ML the p bands of Bi are seen separating into $p_{x\text{-}y}$ type bands with a strong bonding-antibonding splitting around E_F, while the p_z bands are located at the Fermi level. The lower occupied p_z band just touches the upper p_z band at $\bar{M}$ point and crosses the Fermi level in a small region around the $\bar{X}$ points. This results in a metallic nature in the 1 ML bismuth slab. In the case of 2 ML the p_z bonds again show the bonding-antibonding splitting widely around E_F in the vicinity of $\bar{M}$ point and open a tiny band gap leading to semiconducting behaviour. The 3 ML is metallic with p_z bands forming and crossing around the Fermi level around $\bar{M}$ point. These bands are regarded as the precursors to the surface states on bismuth bulk surface. 4 ML is once again semiconducting with a tiny band gap near $\bar{X}_1$ points. The even odd pairing continues till the film becomes thicker and reaches the limit of bulk (110) surface. The surface state seen in $\bar{X}_2$-$\bar{M}$-$\bar{X}_1$ direction in Figure 1.9 (a) looks quite similar to the ones observed in odd numbered bilayers in Figure 1.10. The hole pocket at $\bar{X}_1$- $\bar{\Gamma}$-$\bar{X}_2$ is also quite similar to the dispersion seen in even numbered bilayers.

All the Bi(110) electronic bands shown in Figure 1.10 are doubly degenerate. The calculations by Koroteev *et al* used free standing slabs in which inversion symmetry is preserved and the degeneracy is not completely lifted. The two surfaces of the film couple together to nullify the effect of spin orbit splitting in the case of free standing ultra thin films (see section 1.2.1). As the film grows thicker the interaction between the two surfaces decreases and after a critical thickness of the film

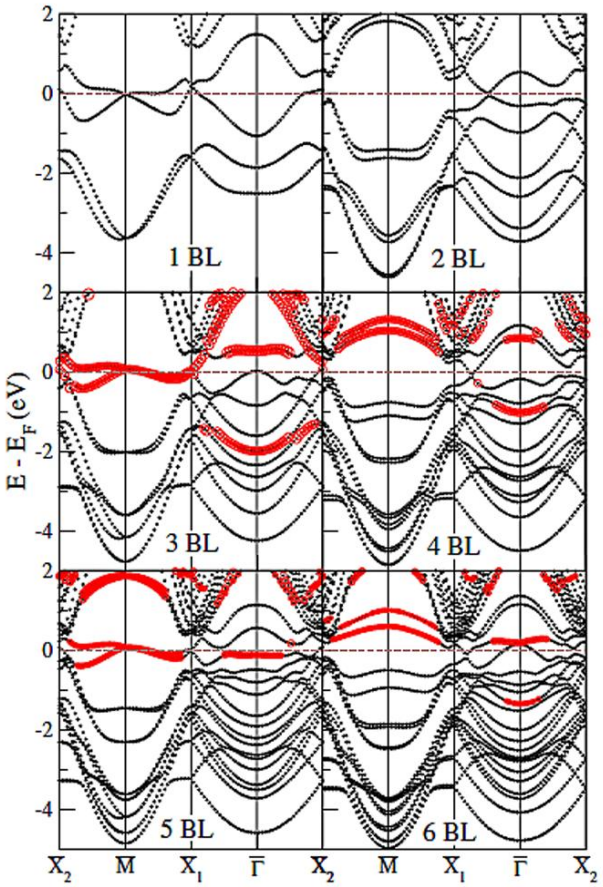

Figure 1.10: Band structures of Bi(110) films with one to six bilayer thickness. In the three to six BL band structures, states located predominantly more than 10% in the vacuum are marked by full red circles. All band structures were obtained for the relaxed geometries including spin-orbit coupling. Image reproduced from [31]

the two surfaces decouple leading to spin orbit splitting of bands. It is therefore important to incorporate appropriate film-substrate interaction conditions in the calculations for the observation of local spin dependent phenomenon in bismuth thin films [74].

1.5 Previous work at University of Canterbury

Thin films of bismuth have been the focus of research in Prof. Simon Brown's group at University of Canterbury. We are primarily interested in Bi(110) thin films because they are known to self assemble into interesting nanostructures e.g. star shaped islands [13, 16] and 1D wires [14, 75].

Bi/HOPG nanostructures were initially reported and studied in the doctoral thesis of Dr. Shelley Scott. In her research, she observed elongated star shaped islands (see Figure 1.12), with well defined stripe morphology on the graphite terraces [13]. With the flux constant an increase in coverage gave rise to larger lateral spread of the star shaped islands. The islands were determined to have their crystallographic (110) plane parallel to the graphite basal plane. In-plane orientations were aligned with the high symmetry directions of the substrate with the islands elongated along

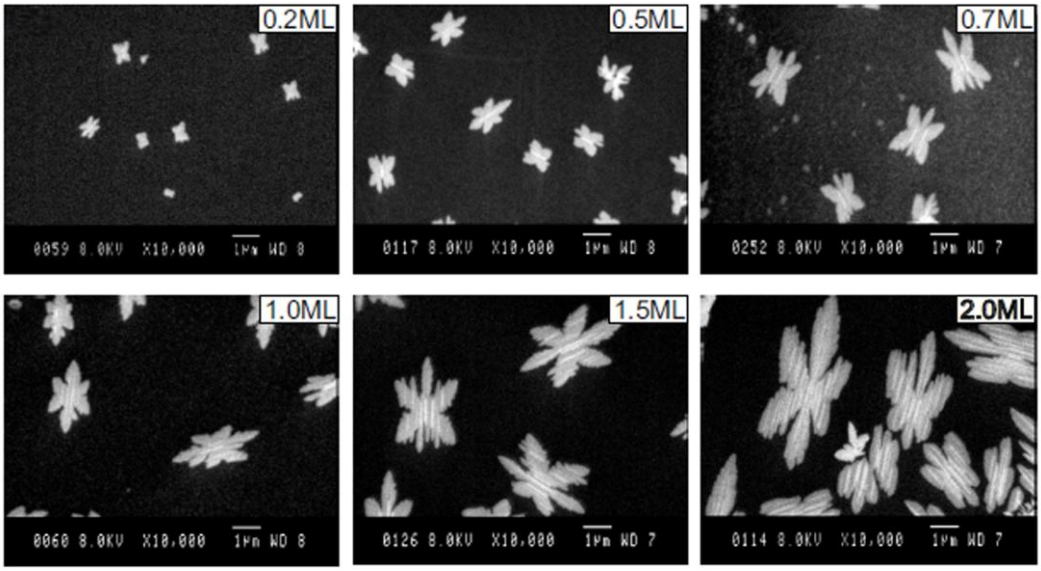

Figure 1.12: SEM micrographs of the evolution of island morphology with increasing coverage. The flux is kept constant at 0.005 Å/sec. Image reproduced from [76]

Bi$< \bar{1}10 >$ direction. It was observed that with increasing flux, there is an evolution to a higher density of smaller islands [16]. The growth mode of these islands was found to be approximately 2D, at a fixed base height of 1 nm. In the low flux limit, there was a cross over to a taller much more compact elongated hexagonal morphology. From a comparison with the mean field nucleation theory, the islands were determined to nucleate via adatom-adatom collisions, rather than on defect sites.

The sizes of the bismuth islands were found to have a predictable linear dependence on the coverage. The stripes featured on the island bases were determined to arise from the direct impingement of the particle flux onto the islands (see Figure 1.11 (a))[76]. With increasing coverage

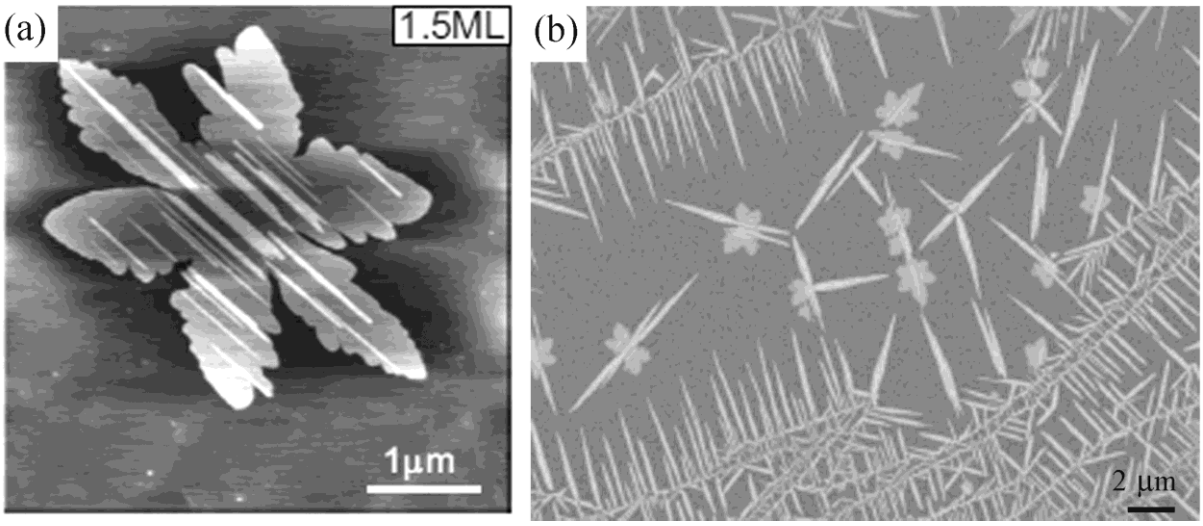

Figure 1.11: (a) AFM micrograph of a star shaped island with stripes on top (b) Rod like formation of bismuth island at T = 353 K. Image reproduced from [76]

the Bi(110) islands were observed to undergo a crystallographic orientation transition, to a Bi(111) oriented film with trigonal symmetry.

Dr. David McCarthy in his doctoral thesis studied bismuth films grown on mica, MoS_2 and HOPG substrates [77]. Bi films on MoS_2 and HOPG were reported to have the same crystallographic orientation i.e. Bi(110). Bi islands nucleating on HOPG terraces favor 1D morphology at low flux and high temperature (see Figure 1.11 (b)). A comparison of the 1D islands and morphologies of rods growing at the step edges of the HOPG found the two structures to be closely related. The high substrate temperature therefore has a similar effect on crystal morphology as the locally reduced flux at step edges. The 1D shape results from anisotropic bonding to the edges of the Bi(110) crystal plane, with unsatisfied intralayer bonds at rod tips and unsatisfied interlayer bonds at the rods sides [75]. Bi island densities on HOPG were measured as functions of flux and temperature. The flux dependence of the island density proved that island nucleation was homogeneous and strongly suggested cluster diffusion is activated.

1.6 Motivation for present work

The motivation of this research work was encouraged by the lack of any published literature on Scanning Tunneling Microscopy (STM) and Scanning Tunneling Spectroscopy (STS) studies on Bi(110) ultra thin films on HOPG. With the advent of literature on the use of bismuth as a parental material for topological insulators in recent years and the discovery of topologically protected edge states in Bi(111) ultra thin films [41, 78], the ultra thin films of Bi(110) were important candidates to explore new and interesting properties.

With the commissioning of a commercial variable temperature Ultra High Vacuum Scanning Probe Microscope (UHV SPM) at University of Canterbury in 2009 and the background knowledge of precise fabrication of Bi(110) islands and rods (on HOPG substrate) as a function of flux and temperature we decided to study the electronic structure of the Bi(110) films.

The interesting and well defined structures discovered by Scott *et al* [15, 16] were identified as the primary structures to investigate in this thesis as they exhibited a large base and very thin Bi(110) rods on top. The thin Bi(110) rods are very attractive candidates to study quantum confinement effects via an STM owing to the large de Broglie wavelength of bismuth.

The structure of Bi(110) films is also currently under debate after the report of a new allotrope [44] against the conventional bulk like structure [30]. We used STM manipulation, STS and oxidation of the thin films to study and resolve the physical structure of Bi(110) thin films (oxidation experiments not covered in this thesis, please refer [79]).

The access to the Australian Synchrotron via Dr B.Ingham (Industrial Research Limited, NZ), and the collaboration with strong theoretical research groups of Prof T.C.Chiang at University of Illinois, USA and Prof T.K.Woo at University of Ottawa was motivation to perform advanced experiments and calculations presented in this thesis.

1.7 Present work

The thesis is organized as follows: In chapter 2 we focus on the experimental procedures used in our research work. The design and operation of the commissioned commercial variable temperature UHV SPM is described. This includes system preparation, pumping, substrate preparation and deposition of thin films. The bulk structure of HOPG, bismuth and NaCl are described. The chapter also includes the principles of film characterization techniques namely STM, STS and Atomic Force Microscopy (AFM).

In Chapter 3 we discuss the preliminary investigations of Bi(110) films via X-ray photoelectron spectroscopy (XPS), STM and STS. We discuss the films orientation and island heights. We present atomic resolution images which allow us to measure the surface unit cell dimensions in our bismuth films. The focus of the chapter is STS measurements on Bi(110) islands. We establish a protocol for I(V) curve acquisition and filtering leading to analytical dI/dV(V) curves. The STS data are compared to Density Functional Theory (DFT) calculations.

Chapter 4 discusses the observation of a high local density of states (LDOS) at the edges of the Bi(110) islands and stripes. We refer to the high LDOS as ‘bright beach (BB)’ in the chapter. The BB is studied via STM and STS dI/dV maps. The occurrence of BB on island edges, defects and grain boundaries, the energy range in which the BB is formed, the width of the BB in dI/dV maps and the dI/dV(V) curves associated with the bright beach are carefully examined and compared to similar observations from literature. In absence of specific DFT calculations on edges, plausible explanations for the origin of the BB are discussed.

In chapter 5 we discuss the quantum size effect observed in Bi(110) film. We discuss the layer pairing observed in (110) planes of bismuth films from an energetics point of view. We also observe periodicity in widths in specific thicknesses of bismuth islands and stripe and report the discovery of lateral quantum size effects (QSE) in Bi(110) thin film. The origin of the lateral QSE that governs the widths of the bismuth islands and stripes is discussed via band structure calculations.

Chapter 6 describes the preliminary results obtained on moiré pattern formation on Bi(110) thin films. The moiré pattern is seen in STM, STS dI/dV maps and AFM images. We investigate the origin of the moiré pattern by studying the periodicity, angle to the main growth direction in Bi(110) islands, the energy range in which it appears in the STM images and dI/dV maps. We also show preliminary calculations for misorientation between Bi and HOPG slabs which could result in formation of moiré pattern.

In Chapter 7 we discuss the growth and formation of NaCl nanostructures on HOPG substrate. The NaCl island morphology is discussed in terms of growth and kinetic influences. The ultra thin films of NaCl were used to deposit bismuth on top and study the interaction of the underlying HOPG substrate with that of the bismuth overlayer. STM and STS measurements performed on the bismuth islands grown on top of NaCl/HOPG system are presented and discussed.

In chapter 8 the conclusions from the previous chapters are reviewed, including an outlook for future studies on Bi(110) thin films.

2. Materials and experimental techniques

We begin this chapter with an overview of the materials used in our experiments. Section 2.2 describes the important components of the newly commissioned Ultra High Vacuum Scanning Probe Microscope (UHV-SPM) which was used in the present research. In Section 2.4 we discuss sample preparation and film deposition parameters. The remainder of the chapter is devoted to the principles of the experimental techniques which were used for film characterization.

2.1 Materials

2.1.1 Bismuth

The indexing of the bismuth crystal is one of the most confusing things in literature as the indices in the bismuth crystal can be chosen to refer to either the rhombohedral unit cell, the hexagonal unit cell, or the pseudo cubic unit cell. In the following sections we introduce the three indexing systems used in literature for bismuth. However, we would like to mention that in this thesis we use only rhombohedral indexing.

2.1.1.1 Rhombohedral structure with 2 atom basis

The rhombohedral lattice is generated by three primitive vectors $\vec{a}_1, \vec{a}_2$ and $\vec{a}_3$ (see Figure 2.1 (a)) of equal magnitude *a*. The angle between any pair of the primitive vectors is α. The two basis vectors are $\pm u(\vec{a}_1 + \vec{a}_2 + \vec{a}_3)$ (not shown in the figure) and thus the crystal structure is completely described by a, α and u. The numerical values of the parameters are a = 4.7236 Å , $\alpha = 57.35^0$ and u = 0.23407 [30]. A fundamental property of a crystal is its symmetry and the symmetry elements in the bismuth crystal are (see Figure 2.1 (a)) -

(1) The trigonal axis (C_3) - the axis between the rhombohedral vectors has three fold symmetry and is the [111] direction.
(2) The binary axis (C_2) - the axis perpendicular to C_3
(3) The bisectrix axis (C1) - the axis perpendicular to both C_2 and C_3
(4) The mirror plane - the plane suspended by C_1 and C_3 axis

To calculate the bulk truncated structure, the Brillouin zone and the surface Brillouin zone, the lattice can be generated in a Cartesian coordinate system. The most natural way is to let the Cartesian coordinates coincide with the symmetry axes such that x = C_2, y = C_1 and z = C_3. This is the

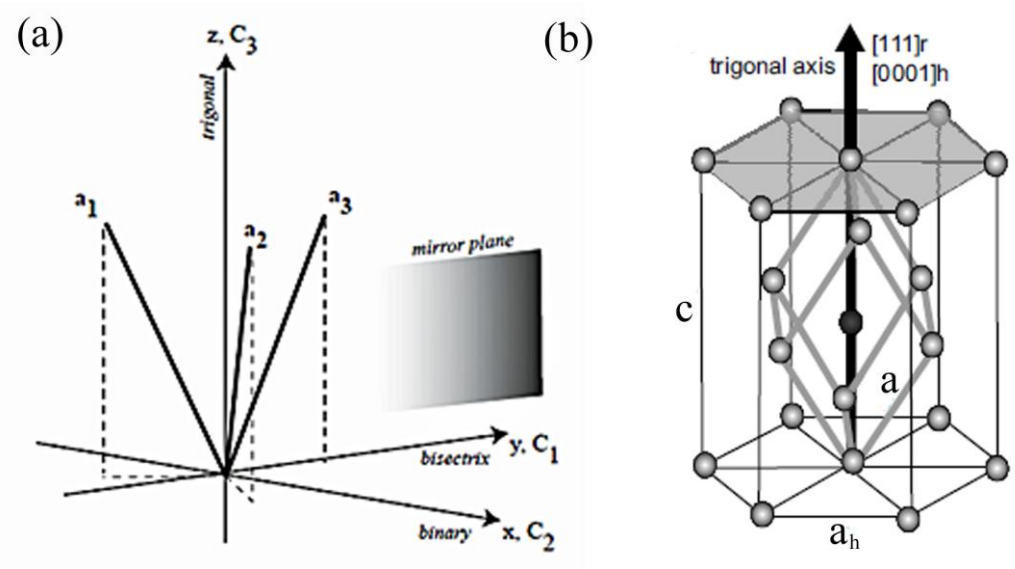

Figure 2.1: (a) The rhombohedral lattice vectors and symmetry elements with respect to a Cartesian coordinate system. (b) A single rhombohedral cell is inscribed inside a hexagonal cell.

case illustrated in Figure 2.1 (a). By introducing an angle θ between the primitive vectors and the z-axis the components are generated as:

$$\vec{a}_1 = (-\frac{\sqrt{3}}{2}a\sin\theta, -\frac{1}{2}a\sin\theta, a\cos\theta)$$
$$\vec{a}_2 = (\frac{\sqrt{3}}{2}a\sin\theta, -\frac{1}{2}a\sin\theta, a\cos\theta) \qquad \text{Equation 2.1}$$
$$\vec{a}_3 = (0, a\sin\theta, a\cos\theta)$$

The relationship between θ, the angle between the rhombohedral axes and the trigonal axis and the rhombohedral angle α is

$$\sin\theta = \sqrt{\frac{2}{3}(1-\cos\alpha)} \qquad \text{Equation 2.2}$$

2.1.1.2 Hexagonal structure with 6 atoms basis

The bismuth crystal structure can alternatively be described by a hexagonal lattice. A hexagonal lattice is generated by three primitive vectors $\vec{a}_{h1}$, $\vec{a}_{h2}$, $\vec{a}_{h3}$ and a 6 atom basis. The basic vectors are $\pm\overrightarrow{uc}$ and the 6 atoms are in position: $(0,0,u), (0,0,-u), \left(\frac{1}{3},\frac{2}{3},\frac{2}{3}+u\right), \left(\frac{1}{3},\frac{2}{3},\frac{2}{3}-u\right), \left(\frac{2}{3},\frac{1}{3},\frac{1}{3}+u\right), \left(\frac{2}{3},\frac{1}{3},\frac{1}{3}-u\right)$ [30, 80]. In this case the crystal is completely described by a_h, c and u whose numerical values are a_h = 4.5332 Å, c = 11.7967 Å and u = 0.23407 [30] (see Figure 2.1 (b)).

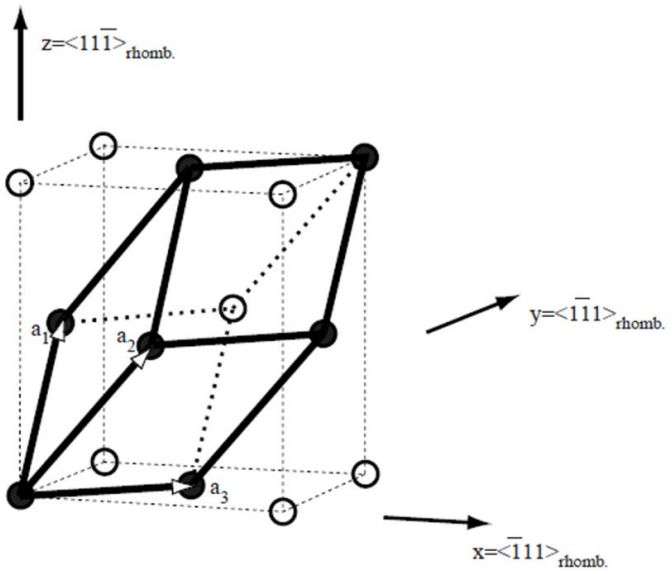

Figure 2.2: The pseudo-cubic lattice versus the rhombohedral lattice.

When describing a hexagonal structure a set of 4 indices (hkil) is normally used, though the structure is totally specified by the three indices that refer to the generating lattice vectors. The index i is related to h and k by:

$$\mathrm{i} = (-\mathrm{h} + \mathrm{k}) \qquad \text{Equation 2.3}$$

2.1.1.3 Pseudocubic structure

The relationship between the rhombohedral lattice and the pseudocubic lattice is shown in Figure 2.2. The lattice is not exactly cubic since the rhombohedral angle α is not 60^0. For this reason the lattice is termed pseudocubic. If the angle α was 60^0 then the lattice would be a face centered cubic lattice. With the rhombohedral vectors in $\vec{a}_1, \vec{a}_2$ and $\vec{a}_3$ in y - z, x - z and x - y planes respectively, the cubic vectors $\vec{x}, \vec{y}$ and $\vec{z}$ are written as:

$$\begin{aligned} \vec{x} &= -\vec{a_1} + \vec{a_2} + \vec{a_3} \\ \vec{y} &= \vec{a_1} - \vec{a_2} + \vec{a_3} \\ \vec{z} &= \vec{a_1} + \vec{a_2} - \vec{a_3} \end{aligned} \qquad \text{Equation 2.4}$$

The angle v between the cubic vectors is given by:

$$\cos \mathrm{v} = \frac{-1 + 2\cos\alpha}{3 - 2\cos\alpha} \qquad \text{Equation 2.5}$$

Likewise the pseudocubic lattice distance is found to be:

$$x = a\sqrt{3\sin^2\theta + 1} = a\sqrt{3 - 2\cos\alpha}$$ Equation 2.6

In case of bismuth at 4.2K, v=87.64^0 and x=6.54 Å^{-1} [30].

2.1.2 Highly oriented pyrolytic graphite (HOPG)

HOPG is a relatively new form of high purity carbon and provides experimentalists with an inert and smooth surface. Unlike mica, HOPG is completely non polar, and for samples where elemental analysis is also done, it provides a background with only carbon in the elemental signature.

The crystal structure of graphite has hexagonal symmetry. The unit cell of graphite can be reduced to a parallelogram that has two characteristic sides whose length is equal to the 'a' lattice parameter (a = 0.246 nm) (see Figure 2.3 (a)). The angle between these two sides measures 120^0 or 60^0 degrees. The repeat distance along its hexagonal axis is equal to the 'c' lattice parameter and is numerically equal to 0.67 nm (see Figure 2.3 (b)).

HOPG is available in three grades. SPI-1 or ZYA is the best quality or 'calibration quality' graphite exhibiting a mosaic angle of 0.4^0. Mosaic angle is a measure of how highly ordered is the HOPG. The lower the mosaic spread, the more highly ordered is the HOPG. The lateral grain size in SPI-1 HOPG is ~3 mm. SPI-2 or ZYB is an inferior grade to SPI-1 and exhibits a mosaic angle of 0.8^0. The lateral grain size in these HOPG crystals is 0.5 mm. SPI-3 or ZYH grade exhibits a mosaic angle of 3.5^0 and has a grain size not larger than 30-40 nm. In our experiments we use SPI-1 grade of HOPG. Refer section 2.4.1 for HOPG preparation.

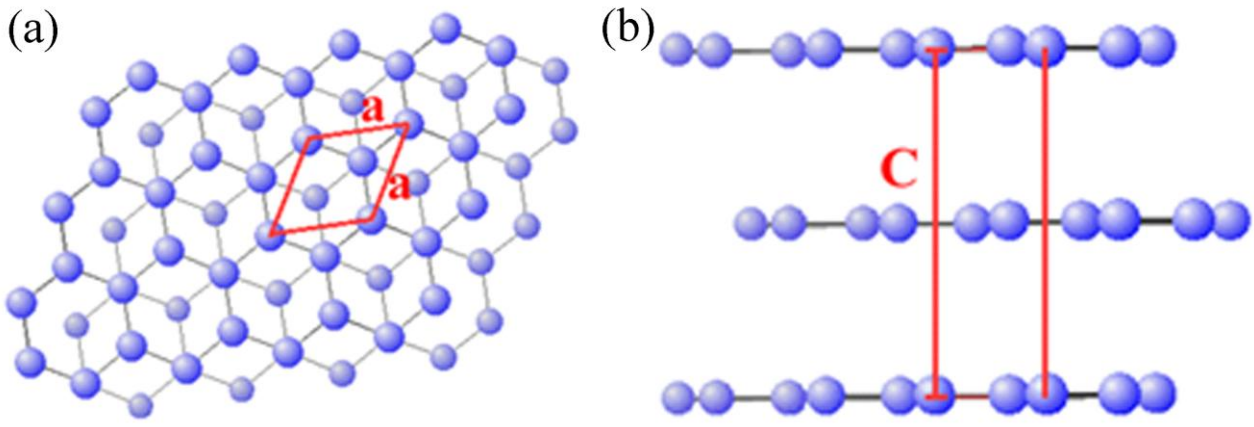

Figure 2.3: (a) The structure of graphite. Carbon atoms are shown in blue and the red parallelogram is the unit cell of graphite. (b) The hexagonal axis of graphite shown by red vertical lines.

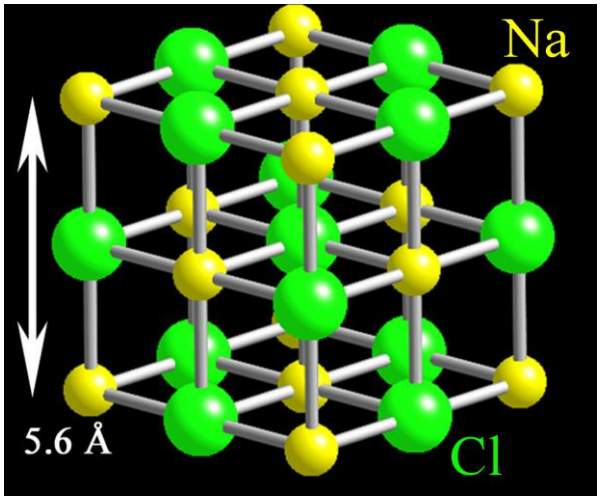

Figure 2.4: The NaCl lattice. The chlorine atoms are shown in green and the sodium atoms are shown in yellow.

2.1.3 NaCl

In solid sodium chloride, each ion is surrounded by six ions of the opposite charge. The NaCl crystal can be represented as a face-centered cubic (fcc) lattice with a two-atom basis or as two inter-penetrating face centered cubic lattices. The larger chloride ions (green color) are arranged in a cubic array whereas the smaller sodium ions (yellow color) fill all the cubic gaps between them (see Figure 2.4). The distance between like atoms is 5.6 Å. The same basic structure is found in many other compounds and is commonly known as the halite or rock-salt crystal structure. The NaCl used in our experiments was obtained from Ma TecK GmbH (http://www.mateck.com/).

2.2 The UHV SPM

We used the Omicron UHV VT AFM XA for all our experiments. The Omicron VT AFM XA is an ultra high vacuum scanning probe microscope for topographic and spectroscopic imaging of solid surfaces with sub nanometer resolution (see Figure 2.5). The important components of the UHV SPM are discussed below.

2.2.1 Chamber

The vacuum chamber in the Omicron VT AFM XA is made up of stainless steel that has all the essential features for sample and tip preparation. It is divided into two chambers: (i) main SPM chamber and (ii) fast entry lock (FEL) (refer Figure 2.9). The main vacuum chamber provides a manipulator with sample heating stage with the provision for direct current sample heating; a parking carousel for 6 samples/tips and a sample transfer wobble stick (see Figure 2.5). The vacuum

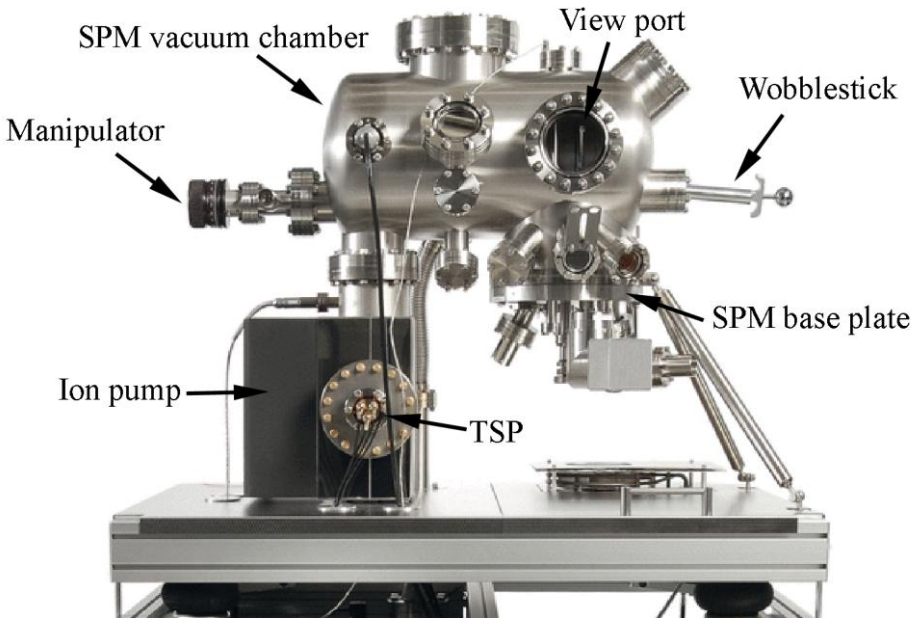

Figure 2.5: The UHV SPM used in our experiments. Important components of the system are labeled. Image reproduced from www.omicron.de.

chamber also houses the VT SPM. In addition to all the ports for SPM work, further ports on the chamber are allocated for LEED optics, evaporator, sputter ion gun, residual gas analyzer, sample viewing, pressure measurement and vacuum pumps. All removable seals that are exposed to the UHV environment are composed of knife edge flanges with copper gaskets.

The cleaning procedure for large components and the flanges involved wiping with analytical grade acetone and lint free tissues. Smaller components were treated in an ultrasonic bath in analytical grade acetone for 8-10 minutes. All the UHV components were always handled with lint free gloves. The cleaning procedure is particularly important to get rid of dust and oil/grease from surfaces.

2.2.2 Pumping

The SPM probe chamber is pumped by an ion getter pump and an additional titanium sublimation pump (TSP). A turbo molecular pump with a two stage rotary pump is used to pump the SPM chamber down via the FEL chamber from atmospheric pressure or when high dynamic gas loads are to be pumped (e.g. sputter gun). A manual gate valve is fitted between the SPM and FEL chamber so that the FEL chamber can be vented to atmosphere via its turbo pump's back-to-air valve while the SPM chamber is maintained at UHV.

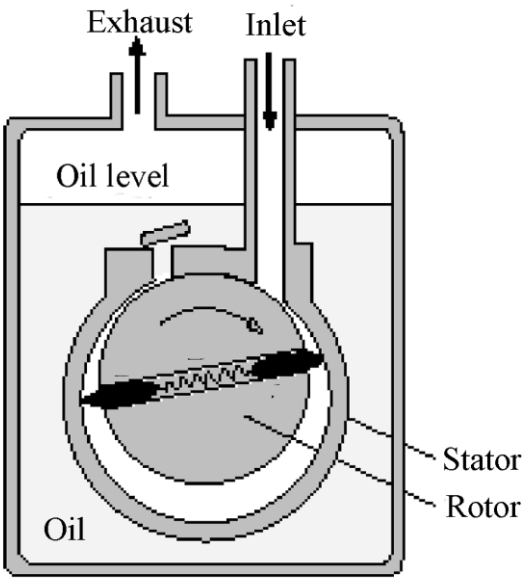

Figure 2.6: Schematic diagram of a rotary pump. Image reproduced from www4.nau.edu.

2.2.2.1 Rotary pump

A rotary vane pump is a positive-displacement pump that consists of vanes mounted to a rotor that rotates inside of a cavity (see Figure 2.6). In some cases these vanes can be variable length and/or tensioned to maintain contact with the walls as the pump rotates. The simplest vane pump is a circular rotor rotating inside of a larger circular cavity. The centers of these two circles are offset, causing eccentricity. Vanes are allowed to slide into and out of the rotor and seal on all edges, creating vane chambers that do the pumping work.

On the intake side of the pump, the vane chambers increases in volume. These increasing volume vane chambers are filled with gases, forced in by the inlet pressure. Often this inlet pressure is nothing more than pressure from the atmosphere. On the discharge side of the pump, the vane chambers decrease in volume, forcing gases out of the pump. The action of the vane drives out the same volume of fluid with each rotation. Multistage rotary vane vacuum pumps can attain pressures as low as 10^{-3} mbar (0.1 Pa).

2.2.2.2 Turbomolecular pump

The basic working principle of the turbo pump is similar to that of the turbine in an airplane. It consists of a stack of rotors with blades, or slots, depending on the specific pump. In between rotor disks are stators, fixed discs that contain the same blades, or slots, as the rotors, but oriented in the opposite direction. Figure 2.7 (a) shows a lateral view of the inside of a turbopump with rotor-stator

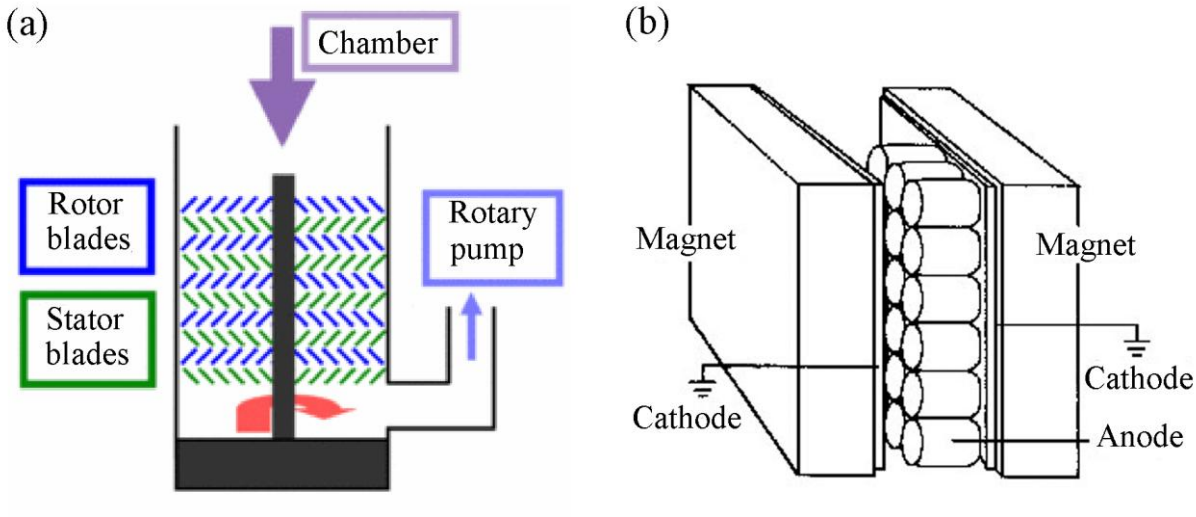

Figure 2.7: (a) Schematic diagram of a turbo pump. The diagram shows the assembly of rotor and stator blades and the exhaust which is connected to a rotary pump. Image reproduced from en.wikipedia.org (b) Schematic diagram of an ion pump. See text for details. Image reproduced from www.cae2k.com

pair. When the blades, spinning at 20,000-90,000 rpm, hit the molecules, they impart momentum to them. The succession of rotor-stator pairs drives the molecules towards the exhaust, where they are collected by a backing pump.

A rotary pump has to remove gases before the turbopump is turned on, down to about 10^{-3} mbar. At this pressure, the flow is called "molecular flow", meaning that molecules are relatively free and, to a good approximation, do not interact with each other. In this regime, the turbopump imparts momentum on each molecule independently, so they can go towards the other end of the pump. Once turned on, the turbopump can work for quite long time reducing the pressure, until at some point the pressure will not go down significantly any longer. This happens between 10^{-6} and 10^{-8} mbar, and it is mainly due to three effects:

a) Desorption of materials from the seals and bearings become greater at lower pressures. Desorption raises the pressure, counteracting the effect of the turbopump.
b) Leaks through the seals become more significant at lower pressures, due to the increased difference between the external and internal pressures.
c) The turbopump has reached its maximum compression ratio, defined to be the ratio of the outlet pressure to the inlet pressure.

2.2.2.3 Ion pump

In the ion pump the residual gas molecules in the vacuum chamber are adsorbed or “buried” into a titanium surface within the pump. The name of the ion pump comes from the fact that gas

molecules are ionized in order to give them a net charge [81]. The ion pump operates at pressures ranging from 10^{-6} mbar to 10^{-11} mbar. The interior of the pump consists of an array of positively charged, parallel axis, cylindrical anodes (see Figure 2.7 (b)). To the left and right of this array are two titanium plates (whose normal vectors point along the axes of the anodes) which are kept at a negative electric potential. Still outside of these plates lie permanent magnets which establish a magnetic field whose lines lie along the axes of the anodes.

Ionization of gas molecules in the chamber occurs when free electrons, which take on helical paths about the magnetic field lines, strike the free gas particles. When a gas particle is ionized in the collision, it takes on a net positive charge and is immediately accelerated toward one of the negatively charged titanium plates. Adsorption takes place when the ion carries sufficient kinetic energy to pierce the surface of the titanium. The process of adsorption between the gas ion and the titanium surface is chiefly chemisorption. Inert and lighter gases such as He and H_2 are physi-sorbed.

Operation of the ion pump is safe at a wide range of pressures. Above roughly 10^{-6} mbar, the pump will automatically shut itself off. This is not to say that operation in higher pressures is dangerous. However, at higher pressures, much more ionization of gas occurs, and hence there is more adsorption into the titanium. Consistent usage of the pump at pressures near 10^{-3} mbar will cause so much gas to be adsorbed that the titanium surface can become saturated, reducing the pump's effectiveness. The pump continues to reduce the pressure in the chamber till it reaches 10^{-9} to 10^{-10} mbar. At this point, mean free paths of the gas particles become large and collisions become very infrequent. The pump will cease to lower the chamber's pressure when the effect of out-gassing (emission of contaminants from surfaces in the chamber) balances that of ionization and adsorption in the ion pump.

2.2.2.4 Titanium sublimation pump (TSP)

Titanium sublimation pumps work by the chemisorption of gas molecules on titanium metal surfaces. Titanium is a common getter material with high sorption capacity. Titanium is evaporated to condense on the cool internal surface of the pump and to form a chemically active layer. Chemically active gas molecules in a vacuum system collide with the titanium surface and are captured. Though the overall process is dominated by the gettering process, the burial process also plays a vital role in pumping [82]. The adsorbed gas molecules may be covered (buried) by the oncoming evaporated titanium flux. The burial process contributes to the pumping of chemically inactive gases.

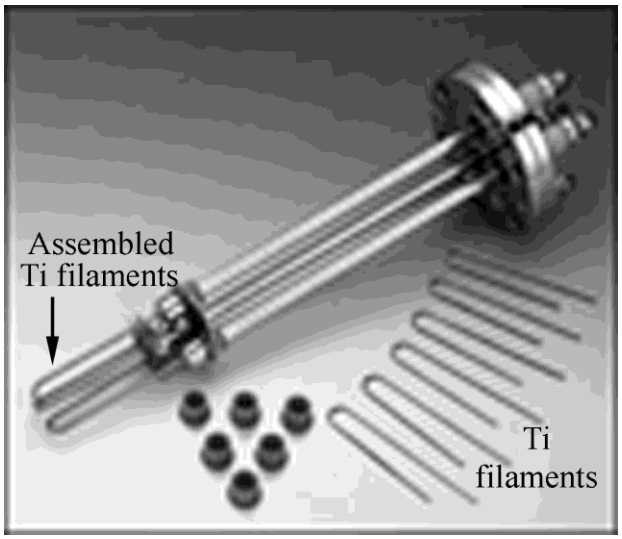

Figure 2.8: Titanium sublimation pump (TSP) assembled on a flange which is inserted inside the ion pump. Image reproduced from www.cat.gov.in

The pumping speed of sublimation pumps is proportional to the area of chemically active surface. These pumps can be constructed with high pumping speeds and can operate from 10^{-5} to 10^{-11} mbar. However the operation of sublimation pumps is not economical at low pressures because the active titanium layer saturates quickly at low pressures. Therefore, they are used in conjunction with an ion pump and are switched on in short bursts of a minute, such that titanium will be evaporated at regular intervals.

The TSP in our Omicron system is shown in Figure 2.8. The TSP consists of a flange which is inserted inside the ion pump chamber. Three Ti filaments are arranged in front of the flanges which are fitted using ceramic feedthroughs. The TSP is programmed to evaporate Ti for 1 minute every 8 hours.

2.2.3 Load lock/Fast Entry Lock (FEL)

The FEL is pumped by a rotary and turbo pump combination and is used to transfer samples/tip inside the main SPM chamber without breaking vacuum. The FEL consists of a magnetically coupled transporter arm (see Figure 2.9) which is designed to slide along two rods mounted on the side of the airlock chamber. The sample is introduced by opening the chamber and clamping it at the end of the transporter arm. The chamber is then pumped down to 10^{-8} mbar (in approximately 2 hours) and the gate valve between the FEL and main SPM chamber is opened to transfer the sample.

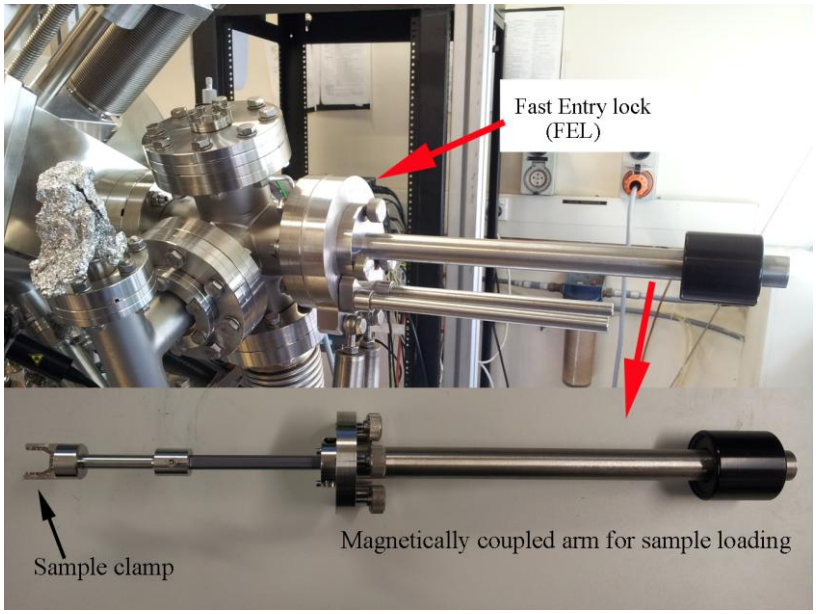

Figure 2.9: The fast entry lock (FEL) chamber with magnetically coupled arm for sample transfer.

The sample/tip transfer process is not very efficient because it contaminates the base pressure of the main chamber while the gate valve is open. This exposes any deposited sample films to lower pressures (~10^{-7} to 10^{-8} mbar) and could result in oxidation of the films. It is therefore advisable to conduct all necessary transfers before the deposition of a sample.

2.2.4 Cryostat

Experiments at very low temperature require cooling with liquid helium. For these applications a UHV compatible continuous flow cryostat is fitted to the sample stage. Thermal coupling between the cryostat and the sample is realized by a copper braid. Compared to a bath cryostat a continuous flow cryostat leads to a reduced consumption of the cryogenic liquid and allows cooling the sample to intermediate temperatures. This can be done very accurately by varying the flow through the cryostat.

An integral counter heating element provides a very precise way of temperature control of the cryostat. The heater element is fitted on the cryostat together with a silicon diode as a temperature sensor. The accuracy of the sensor is ±1 K below 305 K. Using a temperature controller any temperature below room temperature can be chosen by the helium flow regulation and counter heating the heat exchanger. The counter heating method can also be used for temperature stabilization, i.e. to compensate flow fluctuation and slow temperature drift.

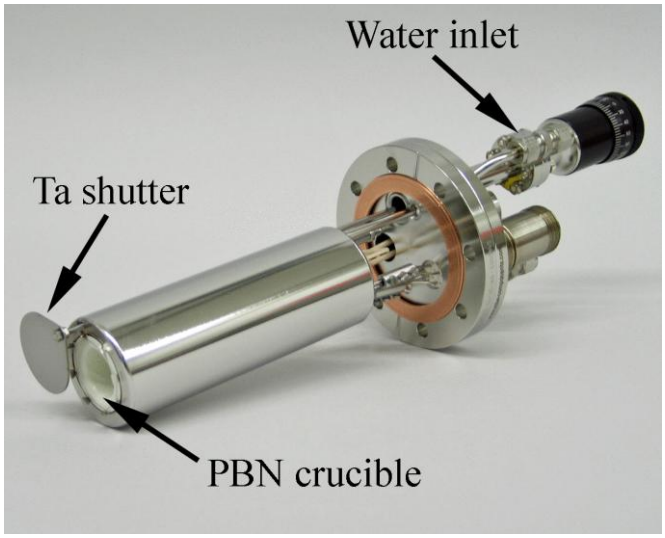

Figure 2.10: Effusion cell used to evaporate bismuth and NaCl in our experiments. PBN crucible was used to hold the evaporant materials. Image reproduced from www.omicron.de.

We use liquid Helium from a 100 liter dewar to cool our samples. A transfer tube provides the means of drawing liquid helium from the dewar via a rotary pump. The liquid helium is circulated in the cryostat and expelled to a custom built liquid helium recovery line. With appropriate flow conditions and counter heating, stable sample temperature down to 50 K can be attained.

2.2.5 Effusion Cell

The standard effusion cell with integrated water cooling shroud and rotary shutter is designed for evaporation of materials at operation temperatures up to 1400^0C. The effusion cell contains a crucible that is heated by thermal radiation from a tantalum (Ta) wire filament, which is supported by pyrolytic boron nitride (PBN) rings. The standard crucible materials suitable for most evaporants is PBN, but different crucible materials Al_2O_3, pyrolytic graphite or quartz are also available.

Temperature is measured by a Chromel/Alumel (Type K) thermocouple in direct contact with the crucible wall. The thermocouple wires are welded onto a tantalum sheet ring, which surrounds the crucible. Two pairs of thermocouple wires are used to achieve a reliable, stable temperature. A stable temperature is important it determines the flux of the evaporant beam. To assist in achieving a stable temperature the effusion cell is also cooled by an integrated water cooling shroud in which the entry and exit of water pipes is via Swagelok connectors. The cooling water flux should be >30L/hr.

The filling up of the crucible is performed in a clean environment, preferably under a laminar airflow chamber. Lint free gloves and grease free tweezers are essential in the filling process. In our

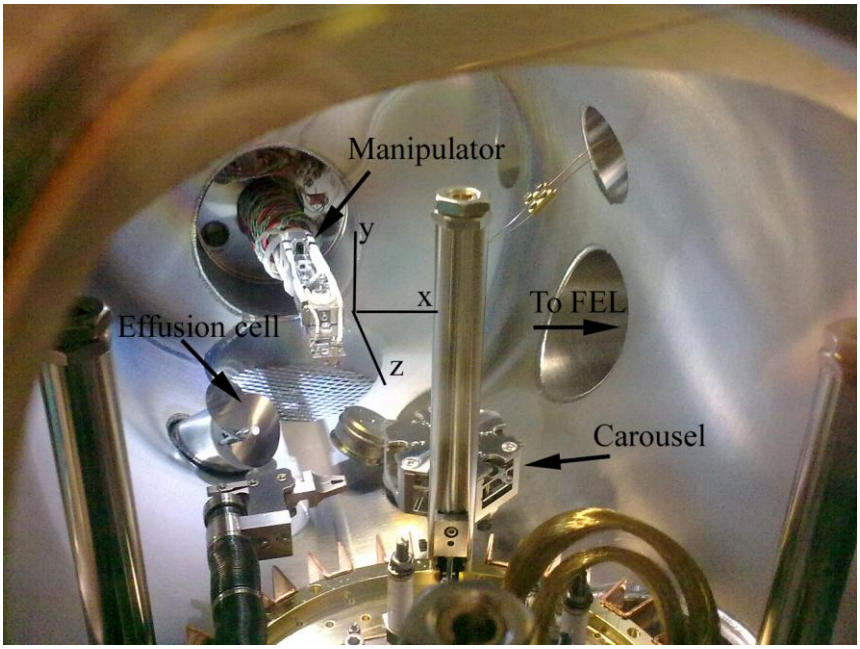

Figure 2.11: A view of the inside of the UHV SPM from a glass viewport. The manipulator with integrated heater is shown in the image. The manipulator can be moved in x, y and z directions to capture the evaporant beam from the effusion cell. The entrance to FEL and the sample storage carousel are also shown.

system we have installed two effusion cells for bismuth and NaCl deposition. The evaporant materials were filled in PBN crucibles (see Figure 2.10). The crucible materials are fragile, so it is necessary to avoid any mechanical shocks to the crucible by not dropping any hard lumps of material. It is recommended to hold the effusion cell at an inclination of about 45^0 and let the evaporant material gently slide into the crucible along its inner walls.

After the filling up of evaporant material, the effusion cells are installed in the designated ports in the UHV SPM. To outgas the cell and the material the vacuum system must be pumped below 5 x 10^{-8} mbar via turbo pump and rotary pump combination. The water flow is started before heating the crucible. Outgassing in our system is performed by an automatic temperature controller which is connected to a 60V power supply. The temperature controller reads the temperature from the thermocouple on the effusion cell and maintains a user defined temperature by varying the voltage in the power supply. We outgas the filled bismuth and NaCl effusion cells to ~200^0C for 15 minutes (standing temperature). The temperature is increased in a stepwise fashion at approximately 30^0C degrees every 20 minutes. During the outgassing procedure the chamber pressure must stay below 1x10^{-7} mbar at all times. If necessary the temperature increments can be slowed down.

2.2.6 Manipulator

The main SPM chamber houses a manipulator with an integrated sample heater for sample preparation. The integrated sample heater is connected to a 60V power supply which provides resistive sample heating up to ~1000^{0}C. The manipulator can be moved in x, y and z directions (see Figure 2.11) and it can also be rotated by ±180^0 (Θ). These movements facilitate the capture of the evaporant beam from the effusion cells in our system.

In a typical experiment the sample was inserted inside the main SPM chamber via the FEL and loaded on the manipulator by the wobblestick. The sample was cleaned via annealing (resistive heating) for 12 hours on the manipulator (see section 2.4 for sample preparation). For sample deposition the manipulator was moved in front of the effusion cell given by parameters: x = +13 cm, y = +14.4 cm, z = +45.8 cm and Θ = 150^0 (NaCl effusion cell) or 132^0 (bismuth effusion cell). The optimal manipulator position was determined by studying the system geometry in Omicron VT AFM user guide [83]. After the deposition was complete, the sample was moved to the microscope for further analysis.

2.3 Baking the system

The rate of desorption of molecules from the system's surface is a function of the molecular binding energy, the number of adsorbed monolayers and the temperature of the surface. Ultra high vacuum conditions in the range below 10^{-9} mbar can only be reached after a few days and when the system has been baked for a sufficient amount of time (typically 18-20 hours). After a new installation of the vacuum system or any installation of equipment that needs breaking the vacuum in the main SPM chamber the system needs to be baked to achieve UHV conditions.

2.3.1 Bakeout procedure

The recommended bakeout temperature for Omicron VT AFM XA is 150^{0}C with a maximum of 170^{0}C. The bakeout is performed while pumping from the turbo pump and rotary pump only. The Ion getter pump and the TSP are switched off during the bake. The gate valve between the main chamber and the FEL is kept open to pump the main SPM chamber. Before the bakeout procedure is performed the system is prepared by the following steps-

(i) Turn the rotary and turbo pump on after ensuring the closure of any open flanges. Wait till the pressure in the chamber reaches 10^{-5} mbar.

(ii) Remove all magnets from the system i.e. the sputter magnet and the magnet on the manipulator arm.

(iii) Remove all non-bakeable cables and adapters.

(iv) Remove all water lines to the effusion cells.

(v) Protect viewports with aluminum foils.

(vi) Cover STM preamp ports with blank connectors (provided with the system).

(vii) Assemble the bakeout tent.

After the preparation procedure is complete the system is typically baked via an inbuilt heater at 150^0C for 20 hours.

2.3.2 After the bake

(i) After the bakeout let the system cool down to approximately room temperature.

(ii) After the system has cooled down each TSP filament is degassed at least three times for 1 minute. As this causes a pressure rise in the chamber, deactivate the vacuum interlock (by pressing the 'override' button) during the outgassing process and reactivate when finished.

(iii) Switch on the ion getter pumps and degas at 3kV, 5kV and 7kV. In case of increasing pressure switch back off and restart after the pressure is below 10^{-6} mbar.

(iv) After the pumps are degassed the manipulator arm in the main chamber is degassed at 90 W for 1 hour (preferably overnight). During the degassing of the manipulator arm a Ta sample plate is used to cover the integrated heater.

(v) Close the gate valve between the main SPM chamber and FEL and shutdown turbo pump

2.4 Sample preparation

2.4.1 HOPG preparation

The weakness of the interlayer bonding of HOPG makes cleaving straightforward. However, the layers do not cleave uniformly, resulting in formation of step edges between the terraces on freshly cleaved graphite. Generally, lower grades produce more step edges and smaller terraces. The steps vary in height from 3.4 Å for a single step up to a thickness that is visible by eye. We used SPI-1 crystals for our experiments.

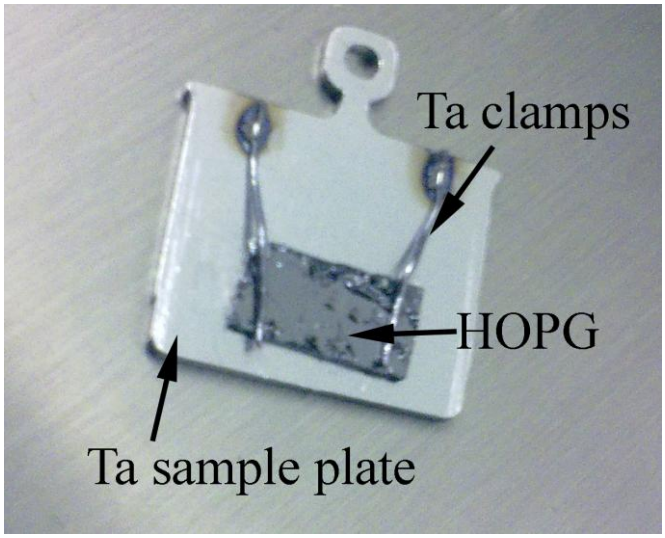

Figure 2.12: A Ta sample plate with Ta clams to hold cleaved HOPG in position

A comprehensive study of the optimum preparation of clean graphite surfaces is presented by Metois *et al* [84]. Most significantly, they find that cleaving in air, followed by immediate transfer to the UHV system for heating under vacuum at ~420^{0}C, yields surfaces of comparable cleanliness to UHV cleaving and heating. They do note however, that additional substrate contamination is observed if the chamber is baked after the samples have been loaded. We performed the following steps to prepare the sample for deposition-

(i) Adhesive tape is pressed on a 10 mm x 5 mm HOPG samples and then pulled off. The tape takes with it a thin flake of graphite.

(ii) The sample is visually inspected for a clean and uniform surface. The adhesive tape pull off procedure can be repeated in case of unsatisfactory surface.

(iii) The HOPG crystal is loaded onto a Ta or steel sample plate via Ta clamps (shown in Figure 2.12)

The sample plate is inserted in the system via the FEL chamber. It is then loaded onto the manipulator arm with the help of the wobblestick. The sample plate along with the HOPG crystal is heated up to 420^{0}C for 12 hours to yield a clean HOPG surface ready for deposition.

2.4.2 Flux determination

Before any deposition the flux of the evaporant beam is measured directly with a water cooled quartz crystal microbalance (Sycon STM-100) which is inserted in the main SPM chamber. The microbalance is connected to a retractable flange in our system which allows the user to keep it in the main SPM chamber even when not in use. The microbalance (deposition rate monitor (DRM))

uses the resonant frequency of the quartz crystal to sense the mass of deposited film attached to its surface [85].

Before the DRM can be used it has to be calibrated according to the evaporant material for deposition. Three factors affect the calibration material density, material Z factor and tooling. Density and Z factors are material factors which can be found in [85]. Tooling is a deposition system geometry correction (location of sensor relative to the substrate). Tooling determination is done by depositing 5000 Å of material on the sensor and the sample consecutively. After deposition the sample is removed to atmosphere and scratched by means of a tweezer and reinserted back in the chamber. The depth of the scratch is measured via AFM and the correct tooling factor is determined by:

$$\text{Tooling } \% = 100 \text{ x } \frac{\text{Substrate thickness}}{\text{Displayed thickness}} \qquad \text{Equation 2.7}$$

2.5 Scanning Probe Microscope

2.5.1 Scanner

The Omicron VT AFM XA uses a single tube scanner with a maximum scan range of about 10 μm x 10 μm with a Z-travel of about 1.5 μm. A schematic design of a tube scanner is shown in Figure 2.13. A thin-walled piezoelectric tube (PZT) is coated with metal on the inner and outer surfaces, with the outer surface divided into four equal quadrants by narrow metal-free regions. The inner surface is then used as the electrode for the vertical displacement (z), and the opposing pairs of outer electrodes are used for lateral motion (x and y). In this geometry a voltage applied between the inner and outer electrodes causes the tube to change length. Opposite voltages applied across opposing outer electrodes will induce one side of the tube to contract and the other to expand, causing a net lateral displacement (along with a small vertical displacement that can usually be ignored).

2.5.2 Vibration isolation

To achieve atomic-scale resolution, the mechanical and electrical components of a STM must enable the tip to be positioned within approximately 1 nm above the surface and then be controlled both vertically and laterally with a precision of <0.01 nm. This precision requires low-vibration mechanical systems combined with low-noise electrical circuitry. In our VT AFM XA system, the entire setup is mounted on vibration damping base stands. The SPM base plate is suspended by four

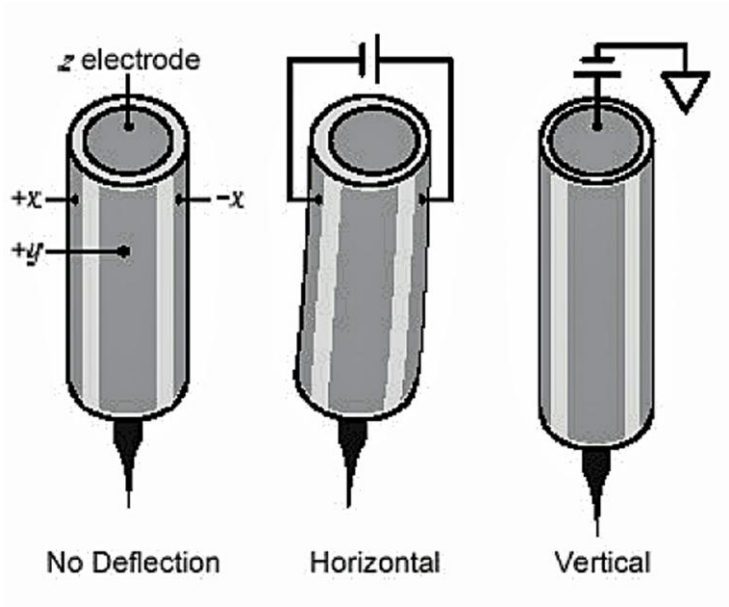

Figure 2.13: Schematic diagram of a tube scanner which is made of PZT material. See text for details

soft springs. The resonance frequency of the spring suspension is about 2 Hz. Vibrations of the suspension column is intercepted using an eddy current damping mechanism [86]. For this the VT AFM XA base plate is surrounded by a ring of copper plates which come between (permanent) magnets.

2.6 Film characterization

The deposition of bismuth and NaCl films is described in section 2.7. After the deposition of the films they were characterized via STM, STS and AFM techniques. In this section we present an overview of the principle of each technique and the probe used. The Omicron VT AFM XA utilizes inbuilt MATRIX software system for data acquisition [83] and SPIP software (www.imagemet.com) for data processing. In this section we also discuss the methods, parameters used in data acquisition. The methods of drift compensation in real time data acquisition and post data acquisition are also discussed.

2.6.1 Principle of STM

Binning and Rohrer invented Scanning Tunneling Microscopy (STM) in early 1980s [87] which used the tunneling effect to obtain a tunneling current between a sharp tip and a sample surface by applying a voltage between them. The tunneling effect, considered since the early days of quantum mechanics and observed in planar junctions [88, 89], allows the passage of a tunneling current without the tip and sample being in contact. The sample and tip are assumed as ideal metals in which the electrons are filled up to the Fermi energy E_F (see Figure 2.14). When the tip and sample

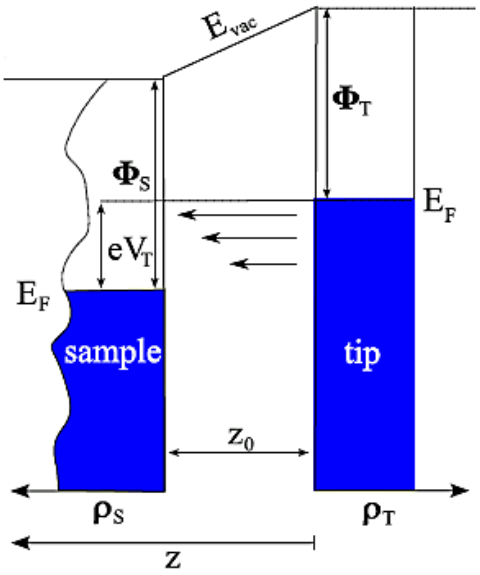

Figure 2.14: Schematic view of tunneling process between an ideal tip with a flat LDOS ρT and a sample with LDOS ρS. When a positive bias voltage is applied to the sample with respect to tip the Fermi energy of the tip rises facilitating tunneling of electrons from occupied states of the tip to the unoccupied states of the sample across a tunneling barrier.

are independent, their vacuum levels are considered to be equal and their Fermi energies lie below the vacuum level by their respective work functions Φ_t and Φ_s. When the tip and sample are separated by a distance z_0 and a bias voltage V_t is applied, the two Fermi energies are shifted with respect to each other by eV_t. By convention a positive bias voltage raises the Fermi energy of the tip [90]. The distance z, Φ_t and Φ_s (work function of tip and sample respectively) and eV_t lead to a trapezoidal tunnel barrier (see Figure 2.14) which electrons can tunnel through if the barrier is sufficiently narrow [91, 92].

At positive sample bias, the net tunneling current arises from electrons that tunnel from the occupied states of the tip into unoccupied states of the sample. At negative sample bias the picture is reversed and the electrons tunnel from occupied states of the sample into the unoccupied states of the tip. When the voltage V_t is applied only those states lying between E_F and E_F+eV_t contribute to the tunneling process.

2.6.1.1 The tunneling current

The following discussion of the tunneling current is based on the formalism by Hamers [93] and is directly applicable to all scanning tunneling spectroscopy (STS) techniques. Using the Wentzel-Kramers-Brillouin (WKB) approximation the probability of tunneling electrons through a one dimensional trapezoidal barrier is given by:

$$T(z, V_t, E) \cong \exp\{-2z\sqrt{\left(\frac{2m}{\hbar^2}\left[\frac{\Phi_s + \Phi_t}{2} + \frac{eV_t}{2} - (E_z)\right)\right\}} \qquad \text{Equation 2.8}$$

where $\frac{\Phi_s+\Phi_t}{2}$ is the average work function of the tip and the sample and E_z is the component of electron energy in the direction of the tunneling junction. A very distinct feature of the tunneling transmission probability is its exponential dependence on the tip-sample distance which is the reason for the vertical resolution of an STM. The resulting tunneling current in the tunneling junction depends on the density of states in the sample (ρ_s) and the tip (ρ_t) and is weighted by the tunneling transmission probability T(z, V_t, E):

$$I_t = \int_0^{eV_t} \rho_s(E).\rho_t(\pm eV_t \mp E).T(z, eV_t, E)dE \qquad \text{Equation 2.9}$$

From Equation 2.9 it can be noted that the tunneling current is a convolution of the DOS of the sample (ρ_s) and the tunneling transmission probability, if we assume that the tip DOS is constant. This situation brings up the difficulty for the interpretation of STM images as the z(x, y) data represents a combination of the real space topography and the variation in the local DOS. However, this circumstance can also be exploited to investigate the LDOS of the sample. In context, Ukraintsev [94] pointed out that the tunneling transmission probability depends exponentially on the bias voltage and thus the low bias voltage STM images correspond to true LDOS of the sample.

2.6.1.2 Measurement modes in STM

Topography: One of the most common modes of measurement in STM is constant current mode, also known as topography. STM topography is obtained by maintaining the tunneling current between the tip and the surface fixed. In this case, a constant voltage (V_t) is applied to the sample, and a constant current is demanded by user (I_t). As the tip scans over the surface, its piezoelectric tube extends and contracts to keep the flow of current fixed, and the height for which I_t was achieved is recorded.

dI/dV: Another STM mode of measurement is measuring the differential tunneling conductance dI/dV, which is directly proportional to the LDOS (see section 2.6.2). The measurement can be done at a single point is space or over an area of the sample. A general technique to obtain energy spectrum is to add an oscillatory voltage (dV) on top of the bias voltage and measure the

response (dI) by using a lock-in amplifier [95]. Thus, dI/dV for a particular value of energy can be measured and from Equation 2.11 it can be seen that it is proportional to LDOS of the sample. The measurement of the deferential conductance as a function of energy and space is the key measurement for obtaining energy-resolved information on the electronic structure.

Constant Height: In this mode the vertical position of the tip is not changed, equivalent to a slow or disabled feedback. The current as a function of lateral position represents the surface image. This mode is only appropriate for atomically flat surfaces as otherwise a tip crash would be inevitable.

2.6.1.3 STM tips

Electrochemical etching of a metal wire is a routinely used technique to generate good STM tips. The basic idea is to dip a small diameter metal wire into an electrolyte solution in which a counter electrode is sitting and to apply an AC or DC voltage between these two electrodes until enough dissolution of the wire has happened so that it displays a sharp tip shape [96]. We prepared our W tips in the Omicron tip etching kit using NaOH solution (5M) as etchant. The etching voltage was kept between 6-8 V and the time taken to etch a tip was usually 8-10 minutes. After the tip etching was completed the tip was washed with isopropyl alcohol and distilled water to remove any residual NaOH solution. For more details on tip etching procedure refer to [83].

Among the reasons why tungsten (W) is such a popular material for the production of STM tips is that an extremely sharp tip can be obtained in a single electrochemical step using fairly mild chemicals. The drawback is that due to its poor resistance to oxidation, the tungsten tip will most likely undergo surface contamination. Therefore it is essential that as soon as the tip is etched, it should be transferred immediately to the vacuum chamber.

Platinum Iridium (Pt-Ir) is also preferred for use in STM because platinum does not easily oxidize and the tiny fraction of Iridium in the alloy makes it much harder. We prepared the Pt-Ir tips by cutting Pt-Ir wire with a wire cutter. The wire is grabbed with the pliers and the cutters are held at an acute angle to the wire. As the wire is cut it is also pulled with the pliers which results in breaking of the wire at the end of the cut. The idea here is that because the wire broke apart the tip was never touched by the cutters, avoiding possible contamination of the tip.

The tip usually loses its sharpness during operation and becomes unusable. We re-sharpened the tip inside the vacuum chamber using a field emission procedure [97, 98]. In this procedure the STM tip is brought in close proximity to a metal surface (Au in our case) and a large bias voltage ~150V is applied. The distance between the tip and the metal surface is regulated such that there is ~20-30 μA current in the circuit which is maintained for 20 seconds.

2.6.1.4 Drift Compensation

One of the most common reasons for surface image distortion is the SPM tip drift with respect to the sample surface which is caused due to various factors e.g. temperature dependence of SPM components, creep etc [99]. These factors become important during atomic resolution scans and for determination of surface unit cell. There are two types of drift compensation methods that we used in our experiments:

Real time drift compensation

Thermal drift can be minimized by performing SPM scans at low sample temperatures (~50 K in our experiments) by using the cryostat provided with the system. SPM scans carried out at room temperature are almost always affected by thermal drift which are noticeable in atomic resolution scans. This is usually compensated real time during measurements by tracking some characteristic surface feature (image correlation technique). Based on a reference image the MATRIX software continuously calculates and automatically applies drift vectors for x and y after every image is acquired.

Post data acquisition drift compensation

In case of featureless regions (e.g. a regular field of atoms) compensation of drift is very difficult. To counter this problem a new method for drift compensation was developed by Dr. Pawel Kowalczyk based on comparison of two images recorded with different slow scan directions (for example up and down) [43]. Each pair of images has one common point which is the point at which the tip finishes the scan up and starts the scan down. This fact allows one to find the same feature on two recorded images and compensate the drift by skew transformation in one direction and compressing or extending it in other direction. The process was used on the STM images post data acquisition.

The post data acquisition drift compensation algorithm works well on atomically resolved STM images where the user has to measure fine distances e.g. the unit cell of any material. On the other

hand the real time drift correction method is indispensible in STS measurements. A typical STS data acquisition routine takes 30-40 minutes in which the sample can drift substantially. Therefore it is essential that real time drift compensation is performed thoroughly before recording any STS data.

2.6.2 Principle of STS

In STS the STM tip is used to record an I(V) curve from a point on the sample. The I(V) curve is numerically differentiated to yield a dI/dV(V) curve. Now by taking the first derivative of Equation 2.9 with respect to voltage we get:

$$\frac{\delta I_t(z,V)}{\delta V_t} \cong A\left[e.T(z,eV_t,E=eV).\rho_t(E-eV_t).\rho_s(E) + \int_0^{eV_t} T(z,eV_t,E).\rho_s(E).\left(\frac{d\rho_t(E-eV_t)}{dV_t}\right)dE + \int_0^{eV_t}\frac{dT(z,eV_t,E)}{dV_t}.\rho_s(E).\rho_t(E-eV_t)dE\right] \quad \text{Equation 2.10}$$

where A is a proportionality coefficient related to tip surface contact area. Equation 2.10 is quite complicated and to simplify the equation the local density of states (LDOS) in the tip is assumed to be constant [94]. Consequently the second term in the equation becomes zero and at very small bias voltages the third term is assumed to be negligible [100, 101]. Therefore in first approximation the differential conductance is proportional to the local density of states of the sample at energy eV_t:

$$\frac{\delta I_t}{\delta V_t} \propto \rho_s(x,y,E=eV_t).T(z,eV_t,E=eV_t) \quad \text{Equation 2.11}$$

Therefore, a measurement of dI/dV as a function of sample bias V allows in principle to measure the sample LDOS in a given energy range close to the Fermi energy. The situation is however complicated by the fact that the tunneling transmission probability is bias dependent. This non-constant contribution of the tunneling transmission probability to a dI/dV spectrum can be corrected to some extend by an appropriate normalization procedure. However, the drawback is that neither an analytical nor a universal experimental dI/dV normalization procedure exists [102].

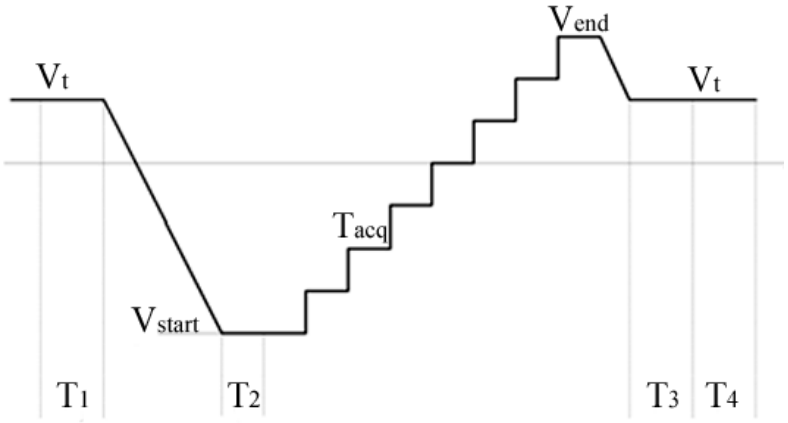

Figure 2.15: Schematic diagram to obtain an I(V) curve. Refer text for details. Image reproduced from [83]

The most prominent normalization procedure consists of computing (dI/dV) / (I/V) as proposed by Feenstra *et al* [103] and justified by Hamers [93]. This simple normalization procedure works well for weakly varying, metallic sample DOS but is not suitable for strongly varying sample DOS, e.g. when a pronounced pseudo-gap is present near the Fermi energy [94]. In our experimental results we observe a pronounced sharp decline in LDOS near the Fermi level (LDOS valley), similar to a pseudo gap. Therefore we prefer to show our experimental STS results as plain dI/dV(V) (see section 3.3 for details).

2.6.2.1 Current Imaging Tunneling Spectroscopy (CITS)

Having established in the previous section that the first derivative of the tunneling current is proportional to the LDOS of the sample we describe the method used to record an I(V) curve. Current imaging tunneling spectroscopy (CITS) is a STS technique in which an I(V) curve is recorded at every pixel (Grid CITS) of an STM topograph by ramping the bias voltage between preset values. The I(V) data thus obtained can be numerically differentiated to obtain the desired dI/dV(V) curve. The data acquisition procedure to obtain a single I(V) curve is described below and a schematic of the process is shown in Figure 2.15. The image in Figure 2.15 is explained for an I(V) curve recorded between ±1V. During the process-

- The tip sample distance is kept fixed during CITS by corresponding values of gap voltage V_t and tunneling current I_t, e.g. V_t = +1V and I_t = 1.5 nA.

- The tip moves to the first pixel of the scan window on the sample to record the first I(V) curve. It uses the parameters set for lateral scanning and has the feedback loop on during the process.

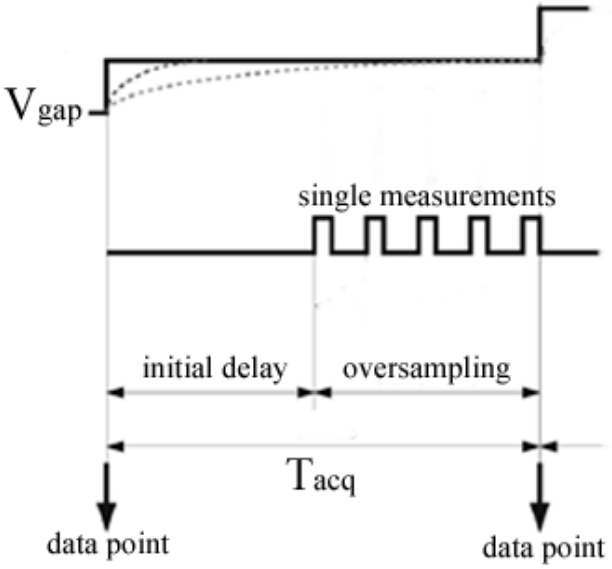

Figure 2.16: Spectroscopy data acquisition and oversampling. Image reproduced from [83]

- After reaching the first pixel the tip waits for a time T1 with the feedback loop on. After time T1 the feedback loop is switched off and the set parameters for spectroscopy measurement e.g. ±1V are applied to the tip with a pre-specified slew rate. Slew rate is the ramp speed for changing the gap voltage V_t from its default value to the first spectroscopy value.
- The tip waits for an additional time T2 to stabilize and the first data point on the I(V) curve is measured after an initial delay. Initial delay ensures that stable current values are being measured for a specific voltage step (see Figure 2.16).

- Each data point is measured during a set acquisition time (T_{acq}) and is an averaged value of number of measurements defined by the oversampling factor given by:

$$\text{data point} = \frac{\sum_1^{\text{oversampling factor}} \text{single measurement}}{\text{oversampling factor}} \qquad \text{Equation 2.12}$$

- After taking the last data point in the I(V) curve the gap voltage is returned back to specified value with the designated slew rate. After reaching the gap voltage the tip waits for time T3 with the feedback loop off.

- The feedback loop is switched on and the tip waits additional time T4 before moving to the next pixel.

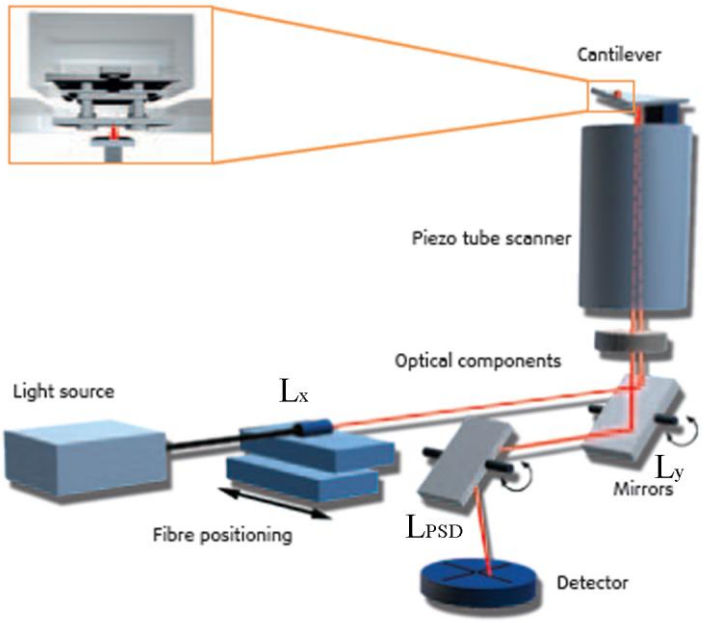

Figure 2.17: The AFM assembly in OMICRON VT AFM XA. The optics used in the AFM is also shown. Image reproduced from www.omicron.de

The procedure described above records a single I(V) curve. As it is a time consuming process, thermal drift can creep in during CITS data acquisition. Therefore CITS is usually performed with fewer pixels (128x128) and at low temperatures (~50 K) for optimum results.

2.6.3 Principle of AFM

In AFM a tip is scanned across a surface at close distance tracing the surface contour [104]. Interatomic, frictional, magnetic and electrostatic forces attract or repel the tip, which is mounted on a flexible cantilever [105, 106]. The resulting deflection of the cantilever can in turn be used to produce an image of the surface. Commercially, cantilevers tips made from silicon nitride and silicon single crystals with various spring constants, resonance frequencies and coatings.

The deflection of the cantilever is measured by detecting the deflection of a light beam reflected from the back of the cantilever onto a position sensitive detector (PSD) (see Figure 2.17). An infra red laser is used as a light source and a CCD camera is used for the alignment of the light beam. The laser beam is generated in the light unit and an optical fiber then passes the laser beam to the microscope stage. The primary beam can be positioned in x-direction by a little micro slide (L_x) and in y direction by a rotatable mirror (L_y). A third PSD mirror is used to project the reflected beam onto the photo sensitive detector.

2.6.3.1 Non Contact AFM (NCAFM)

In non contact AFM mode the feedback signal is derived from the force induced shift in resonance frequency of the vibrating AFM cantilever, the amplitude of which is set point regulated. The regulation works in a regenerative loop (positive feedback) in order to compensate energy loss via tip sample interaction.

To first order, the working of the NCAFM can be understood in terms of a force gradient model [107]. According to this model, in the limit of small amplitude (A), a cantilever approaching a sample undergoes a shift, 'df', in its natural frequency, f_n, towards a new value given by:

$$f_{eff} = f_n\left(1 - \frac{F'(z)}{k_0}\right)^{\frac{1}{2}} \qquad \text{Equation 2.13}$$

where f_{eff} is the new effective resonance frequency of the cantilever of nominal stiffness k_0 in the presence of a force gradient $F'(z)$ due to the sample. The quantity z represents an effective tip sample separation, while $df = f_{eff} - f_n$ is typically negative, for the case of attractive forces. The change in df is used as the input to the NCAFM feedback. The quantity df can be defined by the user and the NCAFM feedback loop moves the cantilever closer or far away from the sample accordingly. At this point the sample can be scanned in the x-y plane with the feedback keeping a constant df.

With the background of the experimental techniques in the previous sections we now outline the experiment in which films of bismuth and NaCl films were deposited on HOPG. We also discuss the parameters used for film characterization and data acquisition.

2.7 Experiments

2.7.1 Bismuth

Commercially available HOPG (SPI-1) was used as a substrate in all experiments. It was cleaved in air, then loaded into the UHV system and annealed at 420^0C for 12 hours to remove contaminants (see section 2.4.1). After the substrate cooled down to room temperature, high purity bismuth (99.999%) was evaporated from a PBN crucible at 200^0C. 2.5 ML thick bismuth films were deposited onto the substrates at flux ~0.01 Å/sec where 1 ML of bismuth corresponds to a thickness of 3.3 Å.

The morphology of the Bi films was stable for weeks in UHV. STM measurements were carried out at room temperature (RT) and 50 K sample temperature (LT) in the Omicron UHV VT AFM XA system at a pressure of 2 x 10^{-10} mbar. The STM measurements were performed at 256 x 256 pixels resolution. The STM tips used in these experiments were either etched tungsten (W) or Pt90%-Ir10% tips (for details on STM and tips see section 2.6.1). Typical scanning parameters used during STM measurements were V_t = +1V and I_t = 100 pA.

Grid CITS measurements were performed on the sample to acquire I(V) curves on bismuth islands. The data acquisition was performed both at room and at 50 K (using liquid Helium). An average scan size for CITS ranged between 30-50 nm^2. The number of pixels in the scan window was restricted to 128 x 128 points. STM topography images of the area of interest were recorded simultaneously with the I(V) curves. All CITS measurements were performed in 3.3 nA/800 Hz range (preamp settings [83]). I(V) curves were acquired in the bias voltage range of ±200mV, ±350mV, ±500mV, ±800mV and ±1V. The stabilization voltage was chosen as the first voltage set-point of the spectroscopy parameter to avoid sudden voltage jumps e.g. if the spectroscopy was performed in ±1V bias voltage range then the stabilization voltage was kept at V_t = +1V. The tunneling current was set between~1 - 1.5 nA. The raster time T_{raster} for the scan was kept at ~3 - 4 ms. The delay times T1, T2, T3, T4 and T_{acq} were 100 μs, 300 μs, 300 μs, 300 μs and 800 μs respectively. The initial delay time was kept at ~700-790 μs. With these time settings an oversampling factor of ~8 - 32 was achieved. Each I(V) curve was composed of 128 data points and with the settings above a single complete CITS measurement took 30-40 minutes to complete.

Non Contact Atomic Force Microscopy (NCAFM) measurements were performed at RT conditions with a frequency setpoint of ~-50 Hz to -100Hz and loop gain = 10%. We used silicon cantilevers with a spring constant of 24 N/m and a fundamental frequency of ~280 KHz. NCAFM images were recorded at 256 x 256 pixels.

2.7.2 NaCl

SPI-2 grade HOPG was chosen as the substrate and was cleaved in air to expose a fresh atomically flat surface and immediately loaded into the UHV chamber. Sample cleaning was performed by annealing at 400^{0}C. High purity NaCl (99.999%) was sublimated at 200^{0}C from the effusion cell (Flux = 0.058 Å/sec). The substrate was kept at room temperature during deposition. The coverage of NaCl is measured in units of monolayers where we define 1 ML of NaCl as 2.8 Å (which is the distance between adjacent chlorine and sodium atoms, Figure 2.4). 2 and 6 ML thick

NaCl films were deposited on HOPG which will be referred to as low and high coverage respectively in the text. Flux was kept constant in all depositions.

NCAFM measurements were performed at room temperature to characterize the NaCl films. Silicon cantilevers with a spring constant of 24 N/m and a fundamental frequency of ~280 KHz were used. Frequency setpoint values between -50 Hz to -300 Hz were used with a loop gain of 10%.

1.5 ML of bismuth was evaporated on pre-existing NaCl islands on HOPG. The Bi/NaCl/HOPG system was characterized by STM at 50 K sample temperature. Grid CITS was performed in the voltage range of ±1V. Electrochemically etched tungsten tip was used. I(V) curves in ±4V bias voltage range were recorded via single point spectroscopy.

3. Preliminary investigation of Bi/HOPG via XPS, STM and STS

In the previous investigations of bismuth structures on HOPG (described in chapter 1) the analysis was performed *ex situ*, hence the Bi structures were always covered by surface oxides. In this chapter we describe new series of *in situ* experiments using X-ray photoelectron spectroscopy (XPS), Scanning Tunneling Microscopy and Scanning Tunneling Spectroscopy. XPS measurements on clean samples show that the location of all core level features remain in good agreement with values recorded on bulk Bi. A shape analysis of the Bi $4f$ peaks, together with a well developed Fermi edge, reveals the highly metallic character of the film. This allows us to perform STM measurements. We have analyzed the heights of the flat islands which confirms their (110) orientation. We also present atomic resolution images for Bi on HOPG that allow us to estimate the surface unit cell. In this chapter we focus on STS measurements on the Bi(110) films. They are compared to DFT calculations to understand the electronic structure of the films.

3.1 XPS

In order to check the electronic properties of the films (whether they are metallic or semiconducting) as well as the quality of the film we performed XPS measurements on clean Bi samples which are dominated by the flat island morphology. The samples were grown *in situ* according to the procedure described in chapter 2 section 1. The XPS results are shown in Figure 3.1. The spectrum in Figure 3.1 (a) is characterized by the presence of lines from only Bi and HOPG. Each Bi line is accompanied by a broad feature shifted towards higher binding energy by 14.4 eV (as measured for Bi $4f$). This feature is related to a plasmon whose energy is in excellent agreement with earlier measurements for bulk amorphous bismuth [108]. The location and shape of the carbon C $1s$ peak (284.4 eV) corresponds well to clean graphite. The Bi $4f$ core level lines are depicted in Figure 3.1 (b). Both peaks (Bi $4f_{7/2}$ and Bi $4f_{5/2}$) have a slightly asymmetric shape with a small shoulder on the high binding energy side. Such shoulders are typical of materials with a high density of states at the Fermi level and result from interactions between conduction and photoionised electrons [109]. Apart from that asymmetry neither peak shows any additional features. Their full width at half maximum (FWHM) is equal to 0.73 eV which suggests the absence of bonding to the substrate (formation of bonds should result in formation of additional peaks and/or broadening of the main peaks). The lack of Bi–C bonds is consistent with DFT calculations that predict that Bi should be weakly physi-sorbed onto graphene [110].

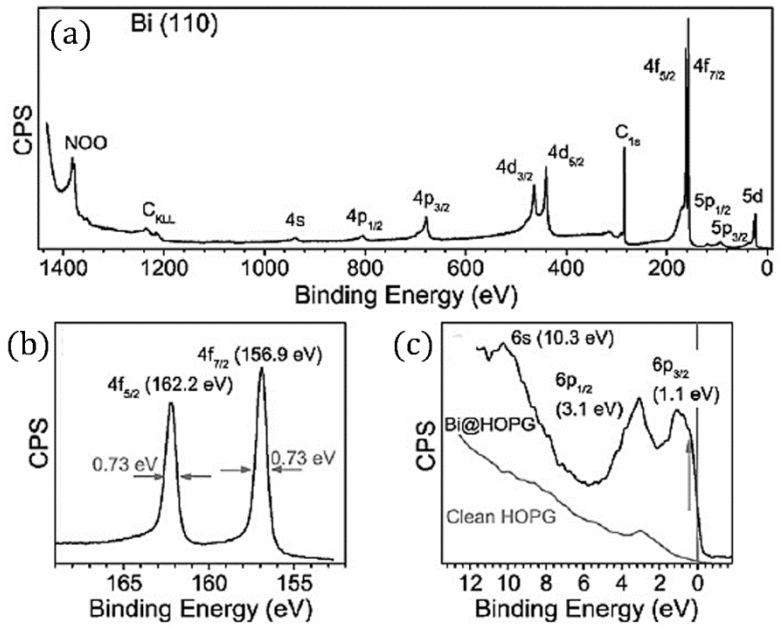

Figure 3.1: XPS results recorded on a clean Bi(110) film. (a) Survey spectrum (b) Bi 4$\boldsymbol{f}_{7/2}$ and Bi 4 $\boldsymbol{f}_{5/2}$ peaks. In (c) valence band spectra recorded for Bi on HOPG and for clean HOPG are shown. Spectra shown in (a) and (b) were recorded with photon energy equal to 1486 eV while (c) was recorded at 600 eV. Arrows in (b) indicate full width at half maximum of both 4$\boldsymbol{f}$ peaks. Vertical arrow in (c) shows location of sub-band, vertical line indicates location of the Fermi level.

In Figure 3.1 (b) the locations of the two main XPS maxima i.e. Bi $4f_{7/2}$ and Bi $4f_{5/2}$ are 156.9 eV and 162.2 eV. The separation between the peaks is Δ = 5.3 eV. These values are in excellent agreement with previous reports for bulk Bi [109, 111-114]. Based on the relative intensities of the C 1s and Bi4f lines it is possible to estimate the thickness of the film d_{Bi} [115]:

$$d_{Bi} = -\lambda_{Bi}\cos(\beta)\ln\left(1 - \frac{\frac{I_{Bi}I^{\infty}_{HOPG}}{I_{HOPG}I^{\infty}_{Bi}}}{\left(\frac{I_{Bi}I^{\infty}_{HOPG}}{I_{HOPG}I^{\infty}_{Bi}} + 1\right)\ominus_{Bi}}\right) \qquad \text{Equation 3.1}$$

where I^{∞}_{HOPG} = 0.01367 and I^{∞}_{Bi} = 0.3632 are photoionization cross sections for HOPG and Bi for the energy 1486.6 eV [116], I_{HOPG} and I_{Bi} are the areas under the C 1s and Bi 4f peaks, λ_{Bi} = 28.3 Å is the empirical mean free path of the inelastically scattered photoelectrons for kinetic energy equal to 1329.6 eV [115], β = 10^0 is the escape angle of the photoelectrons and $\ominus_{Bi}$ is the fractional coverage of HOPG by islands of typical height d_{Bi}. By analyzing SEM images (shown in section 1.5) recorded *ex situ* we estimate $\ominus_{Bi}$ = 71.5%. This estimate allows us to use Equation 3.1 to calculate d_{Bi} = 1.08 nm. Given that 1 ML corresponds to a thickness of 3.3 Å [14], this means that 71.5% of the surface is covered with islands which average thickness 3.27 ML. Assuming that the investigated islands are crystalline (which we show later using STM) this estimate allows us to conclude that the flat island bases are 3 ML thick. In Figure 3.1 (c) we show the valence band spectra for HOPG and flat bismuth

islands. For clean HOPG one can see a smooth nearly linear decrease of the intensity until it reaches a background level. This shape of the spectrum indicates the semi-metallic character of the substrate [115]. In the case of Bi films there is a rapid decrease of the intensity around zero binding energy indicating the presence of a well developed Fermi edge. Together with the asymmetry of the Bi $4f$ doublet discussed earlier, this proves that the islands have metallic character.

The XPS spectrum also exhibits two peaks with binding energies 1.1 eV and 3.1 eV. The peaks are associated with the Bismuth $6p$ doublet, with a spin-orbit (SO) splitting of 2.0 eV. This SO separation is slightly less than in the case of bulk Bi (2.3 eV) [108]. The broad peak with binding energy ~11 eV is most likely associated with the $6s$ band. Closer inspection of the data in Figure 3.1 (c) shows the presence of a shoulder ~ 0.4 eV below the Fermi level. This shoulder was present in all the energies with which the sample was studied and we believe that this shoulder can be related to the first quantum well subband (QWS) formed in the 3 ML base islands [31].

3.2 STM

In section 3.1 we established that the bismuth islands are metallic. This metallic character allows us to use STM as the main probe to study the growth and crystallographic orientation of the bismuth films. The experimental procedure to grow the films *in situ* and STM parameters are described in section 2.7.1.

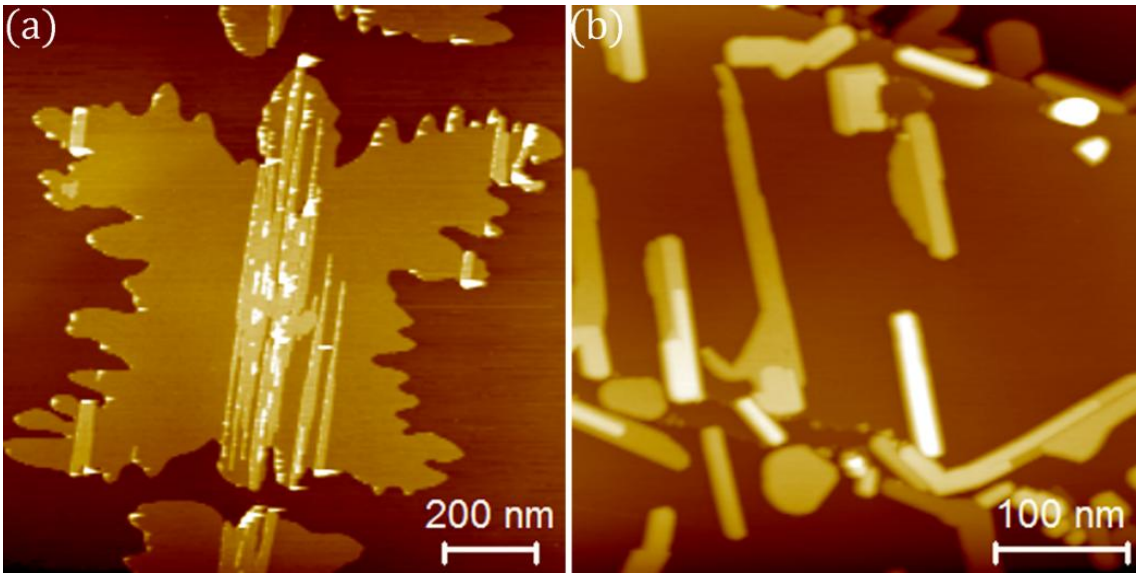

Figure 3.2: (a) STM image of a butterfly shaped island (V_t = -0.8V, I_t = 20pA) (b) STM image of bismuth islands and rods on a step edge (V_t = -0.8V, I_t = 20pA).

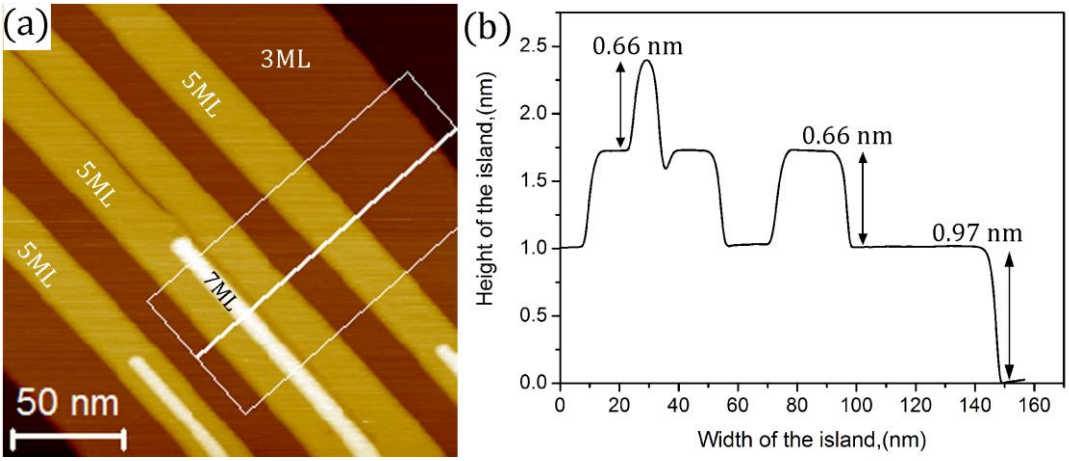

Figure 3.3: (a) STM image of a bismuth island showing 3 ML base, 5 ML and 7 ML stripe(V_t = +1V, I_t = 200 pA) . The white line drawn across the island is a line profile. The lateral extent of the white rectangle shows the number of lines averaged (b) line profile showing individual heights of 3, 5 and 7 ML thick islands and stripes.

In previous work described in section 1.5 most of the analysis was performed via SEM and NCAFM which does not yield an accurate height measurement. It is important to know the heights of individual islands or the number of monolayers contributing to each island or rod as this gives a strong indication of the crystallographic orientation of the island. In Figure 3.2 (a) we show an STM image of a butterfly shaped flat bismuth island. These flat bismuth islands with huge lateral spread are formed predominantly on the flat terraces of HOPG. In Figure 3.2 (b) we show the growth of the bismuth islands on step edges where they form rod like structures. The nucleation, early stage growth characteristics and orientation has been studied previously by Scott *et al.* [13-16] and McCarthy *et al.* [75]. In this section we are primarily interested in knowing more about the accurate height distribution in our bismuth films and the crystal orientation with respect to the underlying HOPG.

3.2.1 Island heights

In Figure 3.3 we show a line profile measurement on a typical bismuth island. The islands base is measured as 0.97 nm. It is possible to find base heights of 1.63 nm and 2.30 nm near the step edges but these islands are better classified as rods (see Figure 3.2 (b)). Most of the island bases in our experiments have stripes on the top like the one shown in Figure 3.3. The heights of these stripes are very uniform and measure 0.66 nm above the base. Some of the larger stripes have additional smaller stripes on top of them which also measure 0.66 nm above the larger stripes. The rods and stripes have similar morphology but we distinguish them via their height and location i.e. the rod is formed chiefly at step edges and is typically taller than the average base height (0.97 nm). The stripes are formed on top of the bismuth bases and other larger stripes. The heights of the bismuth islands were statistically verified by drawing and measuring similar line profiles on 200

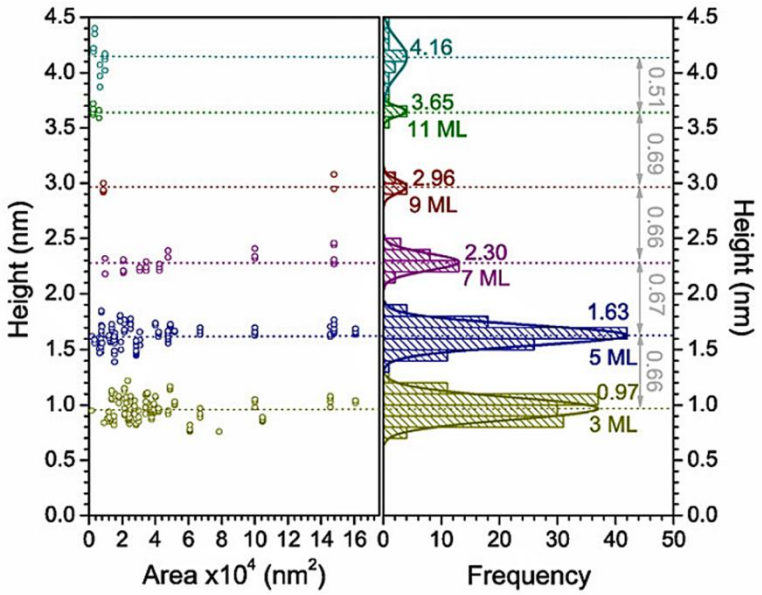

Figure 3.4: Height distribution of Bi islands deposited on HOPG and their dependence on area.

different islands. These islands were recorded across several hundred STM images. For each feature that was present on more than one scan, the measured heights were averaged resulting in one height per island, stripe or rod. The result of these measurements is shown in Figure 3.4. Almost all the island bases have uniform average height of 0.97 nm. The height of the stripes was also uniform and was 0.66 nm above the base followed by the smaller stripes which were 0.66 nm above the larger stripes. The sequence of heights (0.99, 0.66 …. 0.66 nm) corresponds precisely to Bi(110) layers with heights of 3, 5 and 7 ML. This indicates that the bismuth islands on HOPG grow as paired layers on top of a 3 ML base. Note that the area of the island has no effect on the observed heights of paired layers which means that the islands grow outwards but not upwards. It has previously been shown that the stripes aggregate from the material which directly impinges on the top of island bases [16].

Bi(110) paired layers have been reported previously on silicon [44] and quasicrystal surfaces (in quasicrystal surfaces the film resulted in metastable 2 ML and stable 4 and 8 ML thick films) [47]. Two explanations can be found in the literature for this phenomenon: one based on formation of BP like crystallographic structure [44] (see section 1.1.1) and the other on quantum size effects [47]. We report the formation of a dead wetting layer in the base of our Bi(110) island (see section 3.4) and thus in our case the bismuth islands have 2+1, 4+1 and 6+1 ML configuration where +1 stands for the dead wetting layer. This observation supports the 'layer pairing' theory proposed by Nagao *et al* [44]. We have also observed bilayer damped oscillations in the surface energy of the Bi(110) islands in the calculations performed by the team at UIUC (see section 5.2.1) which explains the stability of paired layers in our Bi(110) islands.

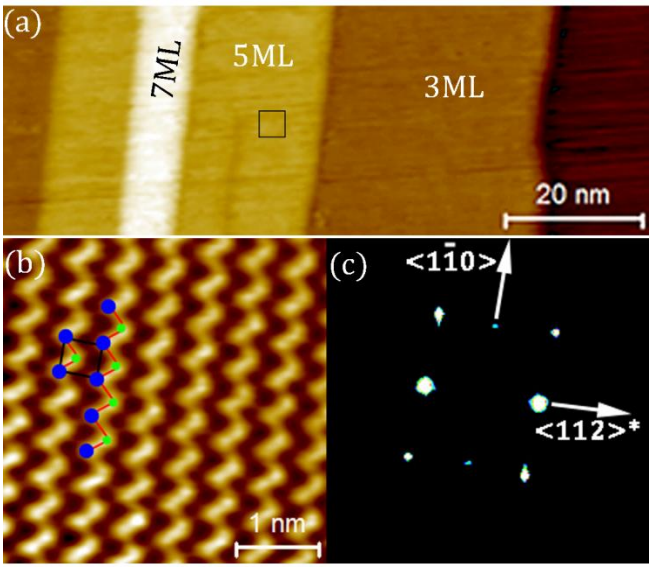

Figure 3.5: (a) STM image of an island showing 3,5 and 7 ML thicknesses (V_t = +1V, I_t = 200 pA). The black square shows the region from which atomically resolved images were obtained. (b) Atomic resolution obtained on region contained in the black square shown in (a) (V_t = +0.2V, I_t = 200 pA). (c) FFT showing the crystallographic directions in the bismuth island.

3.2.2 Atomic resolution images

In Figure 3.5 (a) a typical Bi(110) island with 3, 5 and 7 ML stripes is shown. Atomic resolution images on bismuth islands are difficult to obtain as compared to other metallic surfaces because bismuth is soft and the tip often interacts with the islands. Atomic resolution was obtained on the 5 ML stripe (recorded on the black square shown in Figure 3.5 (a)) at 50 K and is shown in Figure 3.5 (b). The zig-zag chains of bismuth atoms are clearly visible in the $< 1\bar{1}0 >$ direction of the stripe. A schematic diagram of the zig-zag chains (see Figure 3.5 (b)) is superimposed on the experimental data to visualize the structure. The unit cell is also shown as a small black square superimposed on the schematic zig-zag chains in Figure 3.5 (b). Figure 3.5 (c) shows the corresponding FFT from the atomically resolved image in (b). The dimensions of the unit cell extracted from the FFT are 0.47 nm x 0.45 nm. FFTs extracted from 30 different atomically resolved images of 3, 5 and 7 ML islands reveal the dimensions of the unit cell as 0.48 ± 0.03 nm x 0.46 ± 0.02 nm[1]. The measured unit cell is similar to the bulk surface unit cell of Bi(110) shown in chapter 1 Figure 11 [30]. The zig-zag chains are in the $< 1\bar{1}0 >$ direction and are perpendicular to the $< 110 >$ direction. The direction perpendicular to the zig-zag chains is labeled with $< 112 >$* direction (for details refer section 1.1).

[1]See the table of the dimensions of the unit cell shown in Appendix 1 which accounts for the error bars.

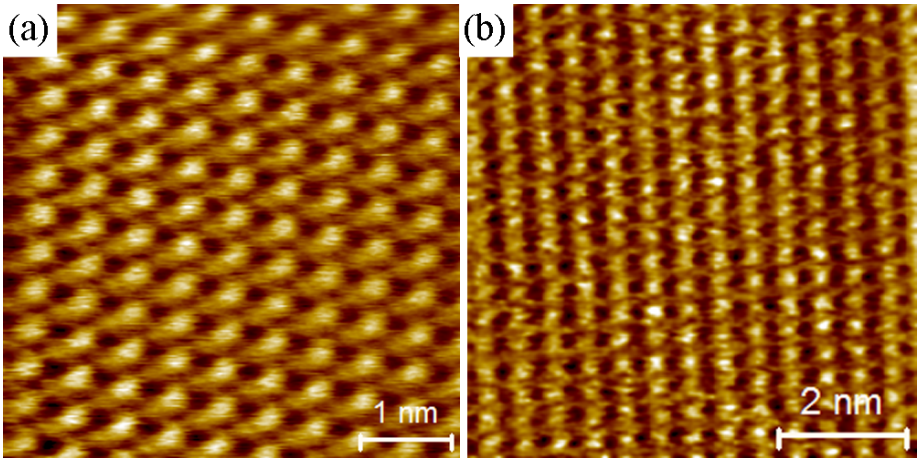

Figure 3.6: (a) Atomic resolution on a 5 ML thick island (V_t = +0.1V, I_t = 200 pA). (b) Atomic resolution on a 5 ML thick island (V_t = -0.850V, I_t = 900 pA) showing side atoms strongly.

Atomically resolved images showing the zig-zag chains on bismuth islands are rare and are formed under very stable conditions with a very sharp tip. In STM experiments even if the user starts with a very sharp tip, it seldom stays that way because of interaction with the bismuth islands and hence the best atomic resolution images are obtained only at low temperatures where the islands are stable. The most common atomically resolved images on Bi(110)/HOPG show the side atoms (blue atoms in the superimposed schematic structure in Figure 3.5 (b)) very strongly shown in Figure 3.6 (a). The middle atom (green atoms in the superimposed schematic structure in Figure 3.5 (b)) is usually weak because it is slightly depressed than the rest (refer section 1.1 for description of atomic structure). The atomically resolved images depend strongly on bias voltage and the sharpness of the tip. Atomic resolution is usually obtained at energies close to the Fermi level i.e. ~-0.1V to +0.1V; however in rare cases the tip picks up an atom while scanning and becomes unusually sharp and can show atomically resolved images at higher bias voltages e.g. V_t = -0.850V in Figure 3.6 (b). The atomic rows are nor very sharply defined in such high voltage images as the tip is further away from the sample.

The atomic resolution images are usually affected by thermal drift which hampers the accurate measurement of the unit cell. It is therefore important to perform real time drift compensation while scanning and also post experiment drift compensation. For more details on drift compensation refer to chapter 2 section 3 and [43]. Distortions from the ideal bulk value of the surface unit cell of Bi(110) has been reported in Bi/Si(111)[44] where the unit cell was measured as 0.46 nm x 0.49 nm and also on Bi/Au(111) [117] where the unit cell was 0.46 nm x 0.50 nm. In contrast Bi islands on Ag(111) seem to grow in perfect agreement with the bulk structure [118]. The measured unit cell in our case is very close to the bulk surface unit cell. We speculate that the slight deviation observed in the experimental measurements of our Bi(110) unit cell from the bulk surface unit cell values could

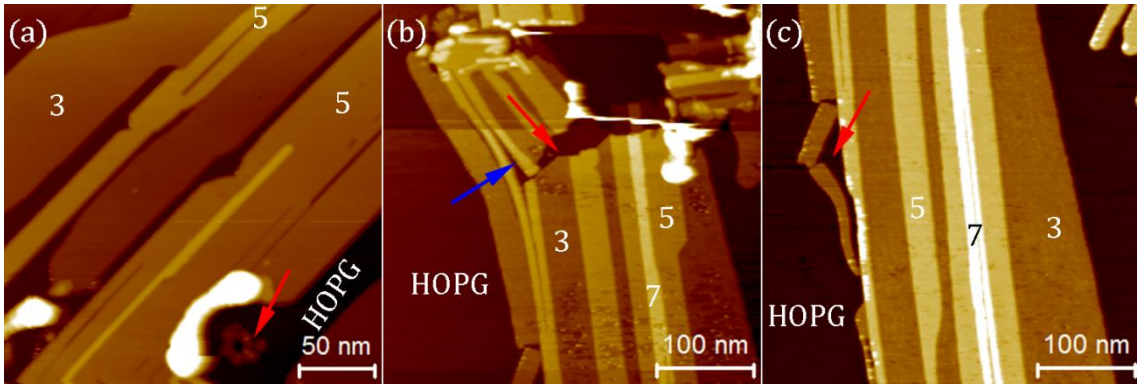

Figure 3.7: Island modifications as a result of pulsing the STM tip. The red arrows represent the approximate site of impact of the STM tip. The blue arrow in (b) shows the splitting of the 5 ML stripe into roughly equal halves.

originate from stress at the substrate-film interface [13]. The visualization of zig-zag chains in conjunction with the measured surface unit cell is consistent with the (110) orientation of our bismuth islands reported in [13, 14, 16].

3.2.3 Island modification by STM tip

In order to check if we were dealing with the BP structure in our islands [44] we attempted to use the STM tip to disrupt the bismuth islands, chiefly by applying a voltage pulse. We expected that if the BP structure exists then we would be able to peel off some layers off the islands as there are strong covalent bonds within the paired layers and weak van der Waals bonds between them (see section 1.1). This experiment did not meet with success as we were not able to remove any paired layers, rather all the layers from the island were removed). In Figure 3.7 (a) the voltage pulse (pulse position shown by red arrows) resulted in removal of the entire portion of the island and a hole can be seen in the HOPG surface as well. In Figure 3.7 (b) the entire island was torn off by the voltage pulse. It is very interesting to see the 5 ML stripe (shown by blue arrow) which breaks into two roughly equal 5 ML stripes. In Figure 3.7 (c) the 3 ML base breaks independently of the 5 ML stripe as if there are no bonds between the base and the 5 ML stripe [30].

The removal of all the layers instead of the topmost paired layer suggests that in our islands strong forces exist within the bases and between the base and the stripes. This observation is rather in contradiction with the paired layer BP model proposed by Nagao *et al*. Yaginuma *et al*. demonstrated that the interaction with the substrate is an important governing factor in formation of the BP-like phase. In their experiments strong interaction with the substrate prevented the formation of BP-like structure and retained the bulk like structure [46]. The present result might indicate that the interaction between the bismuth films and the HOPG substrate is stronger and

would not result in a BP structure. However, we know that this is not the case because we observe paired layers in our system and we also have evidence that there is a weak interaction between the film and the underlying HOPG via XPS results. However, it is still not clear why we are unable to remove paired layers via STM tip manipulation. Hence, there is evidence both for and against the BP-like structure in our experiments.

3.3 Scanning tunneling spectroscopy (STS)

3.3.1 I(V) and dI/dV(V)curves

In Figure 3.8 we show several I(V) curves and their corresponding differentiated dI/dV(V) curves. All the curves were recorded on a 5 ML thick island at 50 K. In Figure 3.8 (a) a spike can be seen in the I(V) curve near Fermi level. This spike is not present exactly at 0V but nearby in the negative bias voltage region. The stabilization bias (V_t) was +1V in this particular example and during the course of the voltage sweep the bias voltage changes from positive to negative and consequently the direction of the tunneling current also changes. We speculate that this sudden change of direction of tunneling current sometimes results in picking up or dropping off of a bismuth atom at the tip which results in formation of a spike. This speculation is supported by the fact that the spike is always formed only at the first negative data point on the I(V) curve (first positive data point when the stabilization bias voltage is V_t = -1V) (see Figure 3.8 (b)) and the shape of the spike is randomly upright or inverted. We categorize such curves as 'defective curves' and in our case these defective curves are quite common because bismuth is a very soft material. These spikes are also retained in the differentiated curves shown in Figure 3. (b) and (d). Defective I(V) curves such as the one shown in Figure 3.8 (e) are also common. These defective I(V) curves account for 5-10% of a STS dataset which are unusable. In MAS software [119] we remove those defected curves by using an algorithm which compares each I(V) curve to a user defined polynomial. If a satisfactory match is not achieved e.g. a curve with a spike, then the software rejects it. An extensive manual inspection of the rejected curves concluded that a polynomial of degree 11 works suitably to remove all defective curves. After performing a pre-screening of the curves and removal of defective curves any further analysis is commenced. An example of a good I(V) curve and its corresponding dI/dV curve is shown in Figure 3.8 (g) and (h) respectively. One of the striking differences between the dI/dV(V) curves of the defective and good I(V) curves is that the intensity of the dI/dV curve for a good I(V) curve is always positive.

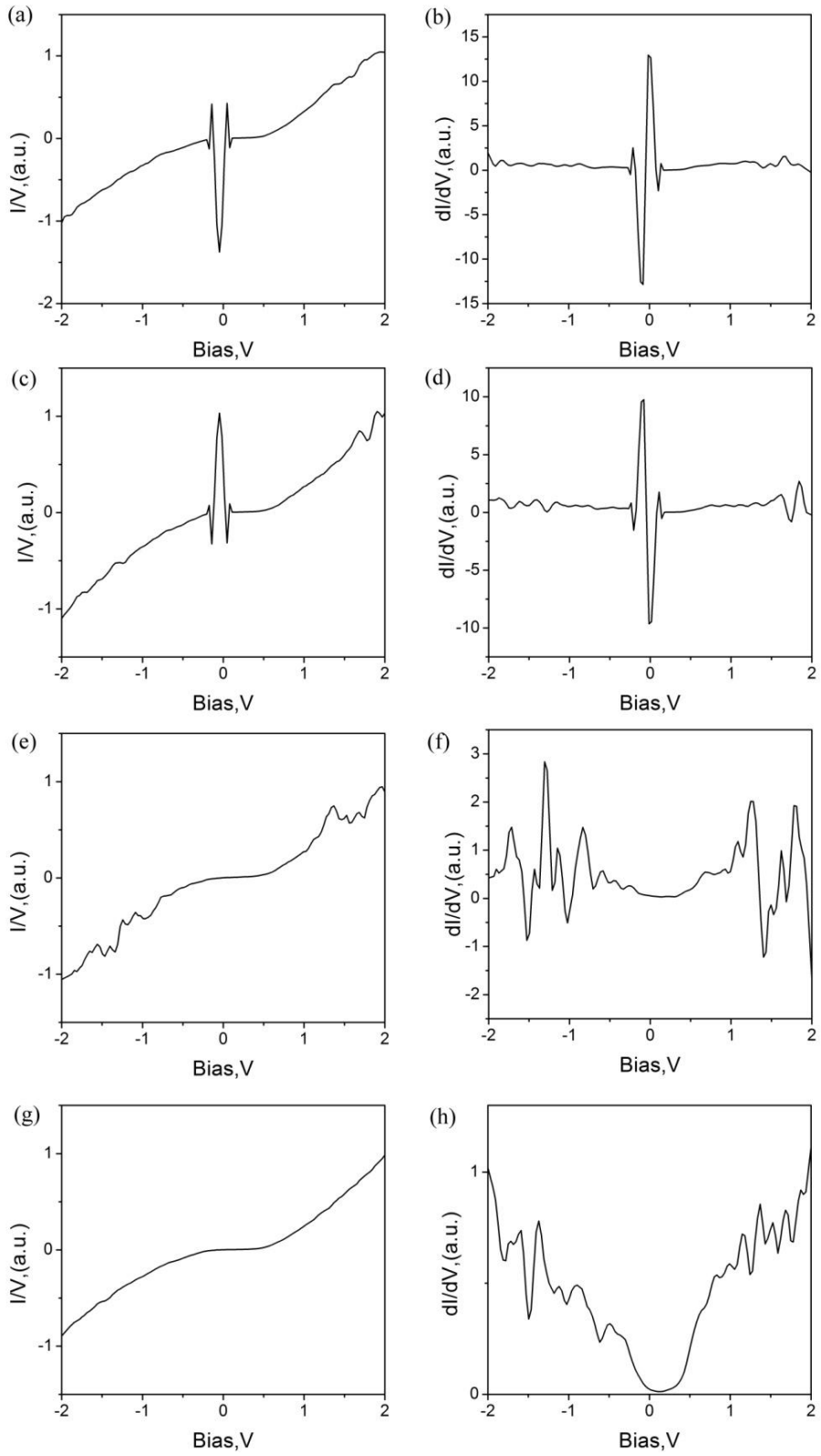

Figure 3.8: (a), (c) and (e) defective I(V) curves originating out of tip and system instability. (b), (d), (f) are corresponding dI/dV(V) curves which retain the defect and are not useful for analytical purpose. (g) is good raw I(V) curve and (h) is its corresponding dI/dV(V) curve.

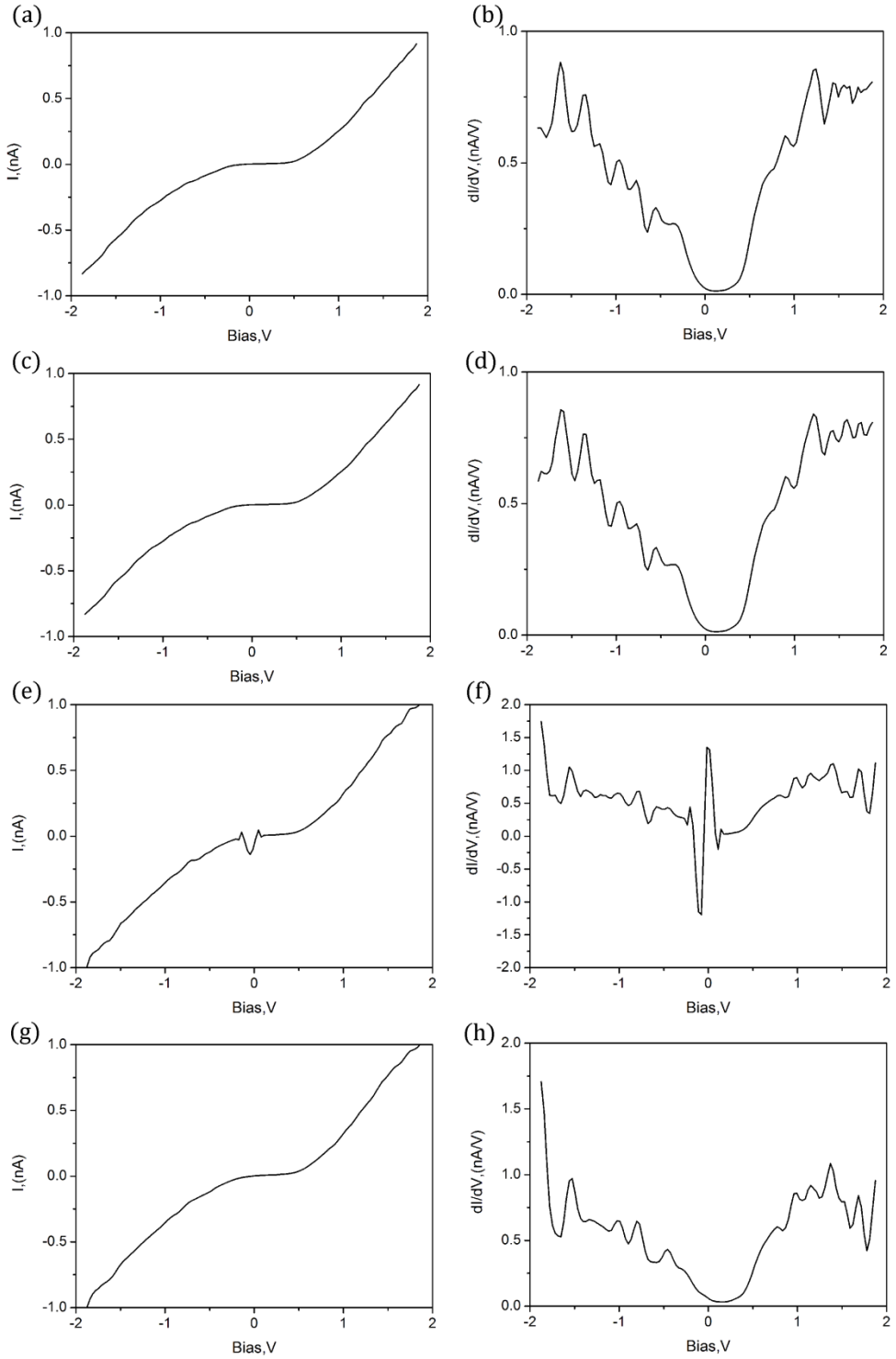

Figure 3.9: (a) and (b) are raw good I(V) and corresponding dI/dV(V) curves respectively. I(V) curve in (a) was processed by a 5 point median filter and its result is shown in the I(V) curve in (c) and its corresponding dI/dV(V) curve in (d). (e) and (f) are a defective I(V) curve and dI/dV(V) curves respectively. I(V) curve in (e) was processed by a 5 point median filter and its result is shown in the I(V) curve in (g) and its corresponding dI/dV(V) curve in (h). See text for details.

3.3.2 The median filter

After the removal of defective I(V) curves we turn to the good I(V) curves. The good curves are also somewhat affected by the equipment noise and/or tip sample interaction and therefore need to be pre-processed. The good I(V) curves are smoothened by a 5 point median filter. The median filter runs through each current value and replaces each entry with the median of the neighboring entries. This 'window', which slides, entry by entry, over the entire signal, in our case is 5 data points. In Figure 3.9 (a) and (b) we show a good I(V) curve and its corresponding dI/dV(V) curve. A 5 point median filter was applied on the I(V) curve and then the curve was differentiated. The result is shown in Figure 3.9 (c) and (d). The effect of the median filter is quite negligible to the eye on the I(V) curve shown in Figure 3.9 (c) but the corresponding dI/dV(V) curve is smoothened. The characteristic feature of the median filter is that it gets rid of high amplitude noises. The application of the median filter does not change the absolute position of the peaks.

Figure 3.9 (e) & (f) shows a noisy defective curve and its corresponding differentiated curve respectively. Such kind of defective curves are usually filtered out during the initial screening process. However, we choose this curve to demonstrate the effectiveness of the median filter. A 5 point median filter was applied to the I(V) curve shown in Figure 3.9 (e) and the resulting I(V) curve is shown in Figure 3.9 (g). It can be seen that the spike in the defective curve has been completely removed by the filter and it has smoothened down as well. The corresponding dI/dV(V) curve in Figure 3.9 (h) is also defect free and less noisy. The LDOS minimum is also pretty similar to the dI/dV(V) curve in (d).

The noise in a defective curve is pushed towards the end of the curve by the median filter. Therefore it is desirable to remove 5 points from the end of the curve (corresponding to 5 point window in median filter) before using it for analytical purposes. The CITS data is affected by noise from the tip-sample interactions and equipment noise which results in defective curves [120]. Most of the defective curves are taken care of by the initial screening process and in this section we demonstrated that any other curves which manage to escape the screening process can be processed by a 5-point median filter to yield good quality data. This robust data analysis procedure comprising of initial screening for defective curves and application of a 5-point median filter has been used in all the CITS data shown in this thesis. Median filter has been traditionally used to process STM images [121, 122] but the use of median filter in CITS data processing has never been reported in literature and is a new technique developed by Dr Pawel Kowalczyk and is used in this work.

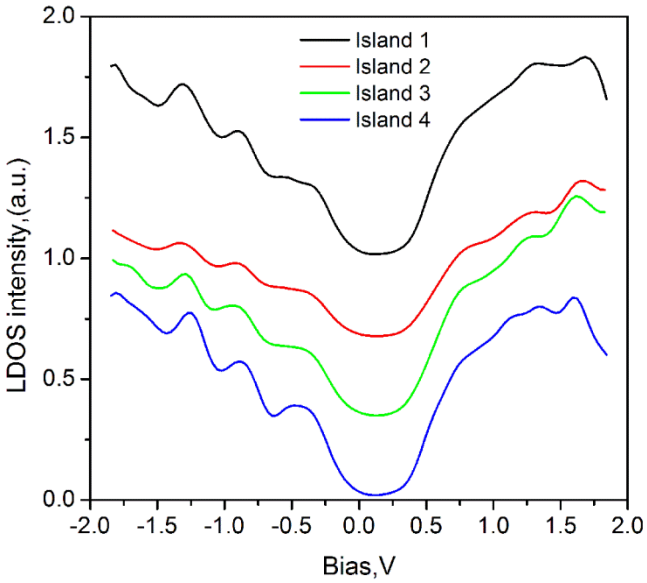

Figure 3.10: Comparison of averaged dI/dV(V) curves obtained from four different 5 ML thick islands at different times.

If we compare the dI/dV(V) curves shown in Figure 3.9 (d) and (h) we will see that the two curves are fairly similar but with some differences. The origin of these differences is unknown because they could be caused due to real variations in LDOS. The best way to resolve these differences is to average multiple curves from the same thickness of the island which would increase the signal to noise ratio [123-125]. It is also important to compare these averaged curves recorded over different islands with different tips which would allow a comparison between the LDOS peaks in the dI/dV(V) curves and their reproducibility.

To verify the data analysis procedure above we extracted dI/dV(V) curves from four different 5 ML thick islands (which were recorded at 50K at different times with different tips). These four dI/dV(V) curves are shown in Figure 3.10. Each dI/dV(V) curve shown in Figure 3.10 is produced by averaging 16 (black), 20 (red), 18 (green) and 20 (blue) individual dI/dV(V) curves from their respective islands. There is good agreement between the curves. The negative energies in the spectrum contain three distinct peaks at ~-0.46V, -0.9V and -1.3 V. The positive energies in the spectrum also shows peaks at ~+0.75V, +1.25V and +1.5V. This result shows that the CITS spectra recorded on 5 ML thick island is reproducible in different experiments.

Now we turn to the finer details in the CITS spectra on the 5 ML thick island. In the black curve shown in Figure 3.10 we see that the LDOS peak at ~-0.5V is made up of two shoulders. It is important for us to verify whether this effect is caused by changes in the LDOS across the island or is just noise. The obvious way is to check all dI/dV(V) curves for a particular 'shoulder' and study its

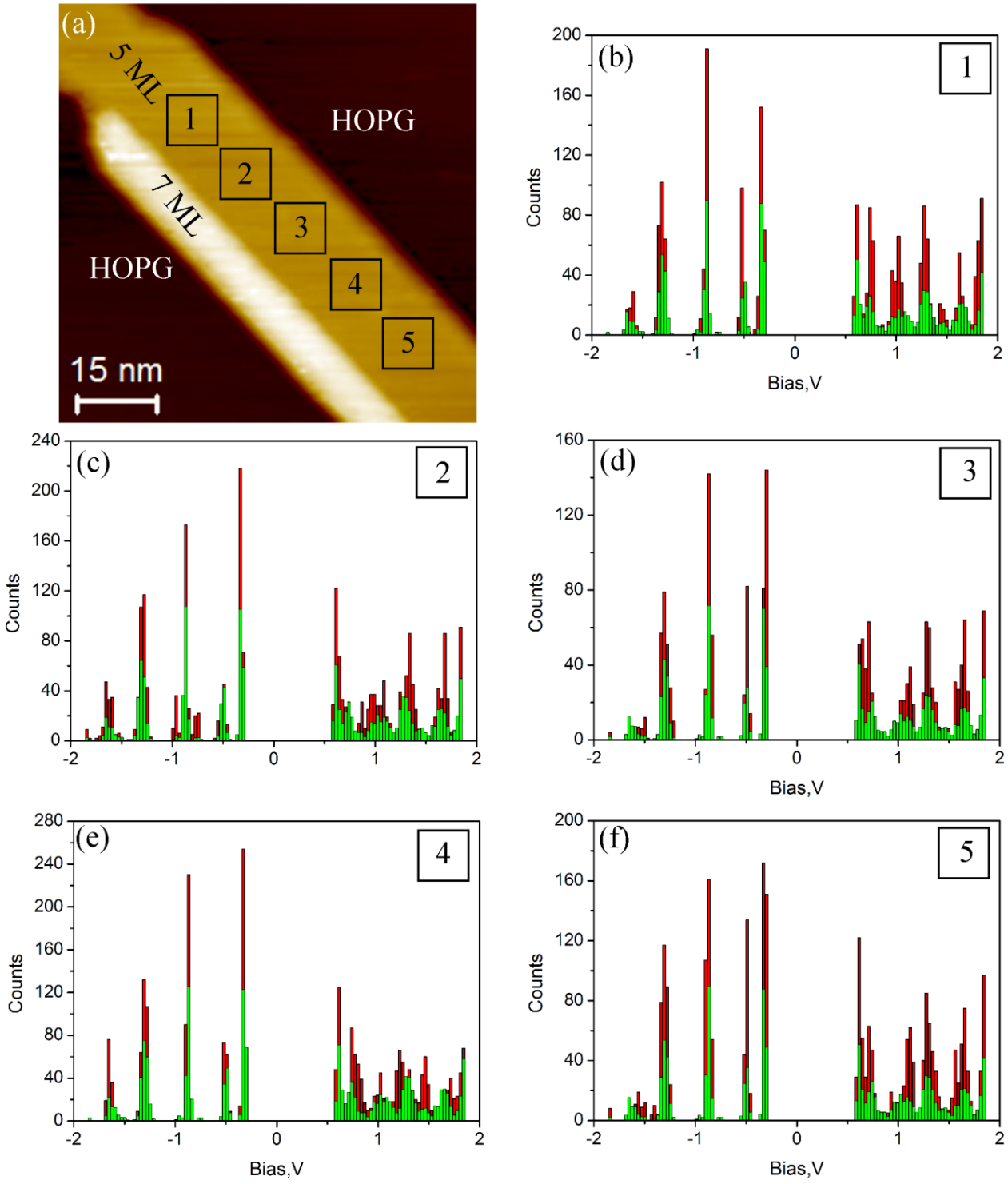

Figure 3.11: (a) STM topograph of the sample containing 5 and 7ML thick islands on HOPG. The black squares marked 1-5 are areas where spectral histograms were recorded. (b)-(f) Corresponding spectral histograms(red) recorded on black squared region shown in (a). The superimposed green colored histogram is the result of addition of all 5 ML histograms in (b)-(f). The counts for green histogram are not shown.

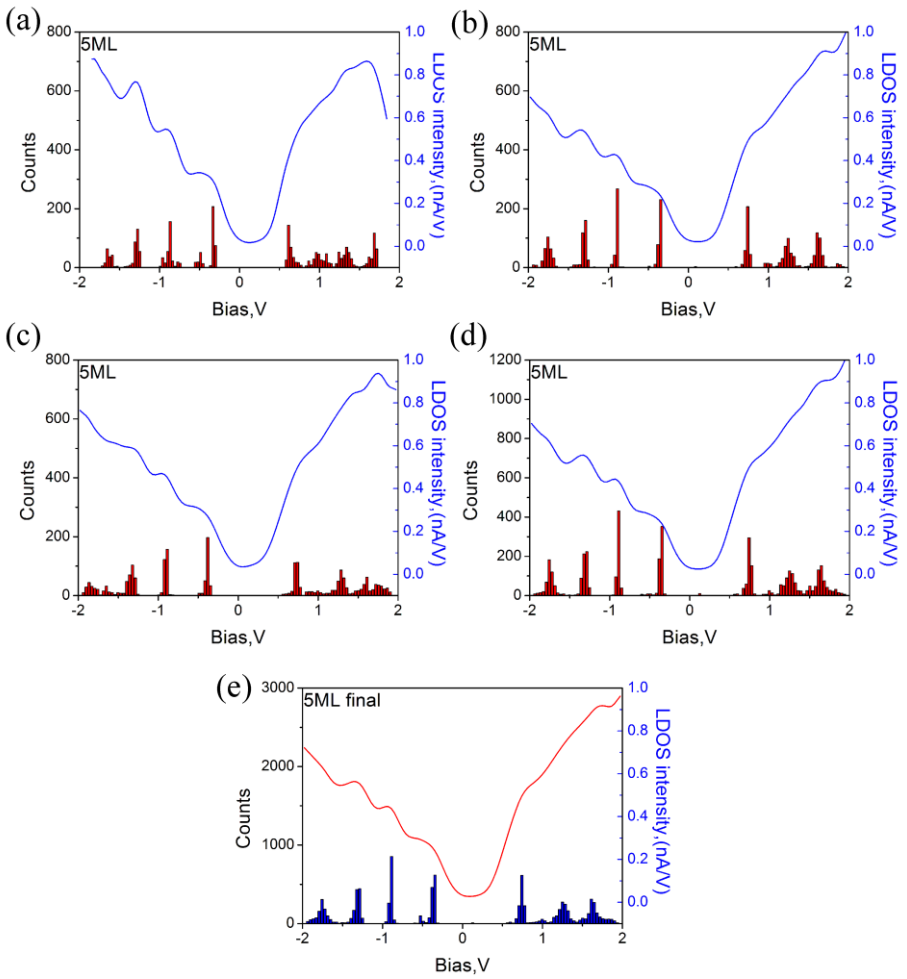

Figure 3.12: Spectral histogram on a 5ML thick island. The black curve is a dI/dV(V) curve which has produced by averaging 30 different dI/dV(V) curves on 5 ML thick island.

occurrence and energy position across the island. This approach is however impractical because a typical CITS data set contains 128 x 128 = 16,384 curves and going through each of them is time consuming. Hence we use histograms of the peak positions as described in the next section.

3.3.3 Spectral histograms

A 'spectral histogram' is a useful tool in cases where a huge amount of dI/dV(V) curves have to be analyzed. This tool in the MAS software [119] allows the user to select a defined region in an STM image and the algorithm counts the occurrence of peaks and shoulders in all the dI/dV(V) curves associated with the area of interest. Histograms are acquired from various positions on the same thickness of the island and added together to yield a final histogram. In Figure 3.11 (a) we show a STM topograph of a 5 ML island with a 7 ML stripe formed on top. CITS was performed on the 5 ML region and spectral histograms were prepared for different regions of the 5 ML stripe. The black squares show the regions in the 5 ML thickness from where the histograms were recorded. The

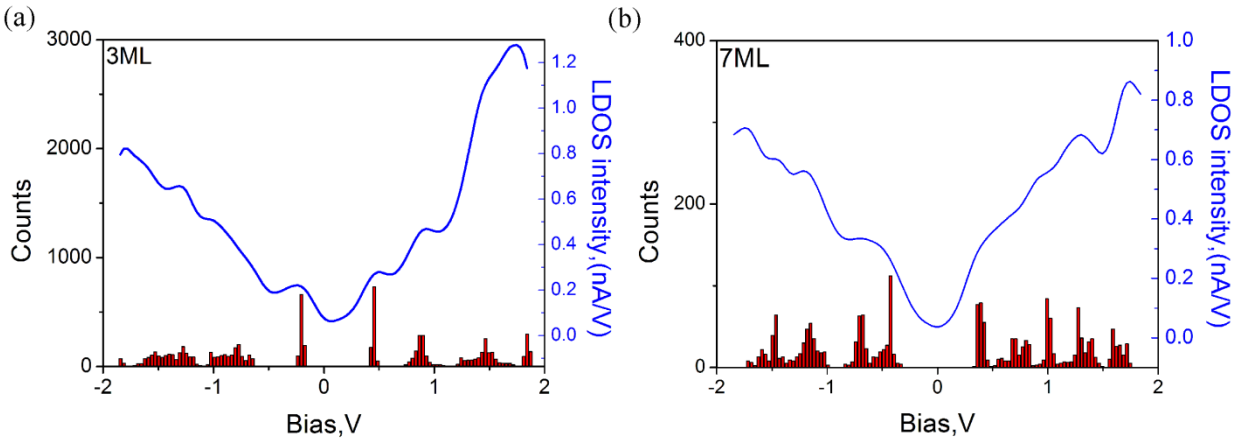

Figure 3.13: (a) Spectral histogram on 3 ML thick island compared with a 3ML dI/dV(V) curve (b) Spectral histogram on 7 ML thick island compared with a 7ML dI/dV(V) curve.

corresponding histograms are shown in Figure 3.11 (b)-(f). The green colored superimposed histogram is the result of adding all the histograms. Care was taken to avoid the edges of the island in those histograms as the edges show additional peaks in the LDOS which is discussed in section 4.2. On comparing the histograms it can be seen that all the peaks are faithfully reproduced from different regions of the island. The green histogram along with a representative dI/dV(V) curve is shown in Figure 3.12 (a). The dI/dV(V) curve shown in Figure 3.12 (a) is an average of 30 individual dI/dV(V) curves. The peak at -0.5 V in the dI/dV(V) curve in Figure 3.12 (a) appears to be broad and is actually made up of two sub peaks/shoulders which have been clearly resolved in the spectral histogram. It is also to be noted that the features in the dI/dV(V) curves line up very nicely with the peaks in the histogram. This is because of the fact that the dI/dV(V) curve shown in Figure 3.12 (a) has been obtained by averaging 30 curves which increase the signal to noise ratio. To verify the reproducibility of the STS data spectral histograms were recorded on three additional 5 ML islands and are shown in Figure 3.12 (b)-(d). The dI/dV(V) curves in these histograms in made by averaging 20, 25 and 30 curves respectively. The histogram peaks in Figure 3.12 (b)-(d) also line up well with their corresponding dI/dV(V) curves. However the histogram peak observed at -0.5V in Figure 3.12 (a) is not observed in (b) and (c). It is faintly observed in Figure 3.12 (d). The positions of the LDOS peaks in the histograms correlate quite well with each other. The sum of all four histograms has been shown in Figure 3.12 (e) and it serves as the final histogram for 5 ML thickness. A good correlation is seen between the final histogram and the histograms obtained from different 5 ML islands shown in Figure 3.12 (a)-(d).

After demonstrating the robustness of the analysis routine in Figure 3.12 the same procedure was applied to 3 ML and 7 ML thicknesses. The spectral histograms with the corresponding dI/dV(V) curves are shown in Figure 3.13. The dI/dV(V) spectra for 3 ML shown in Figure 3.13 (a) is dominated

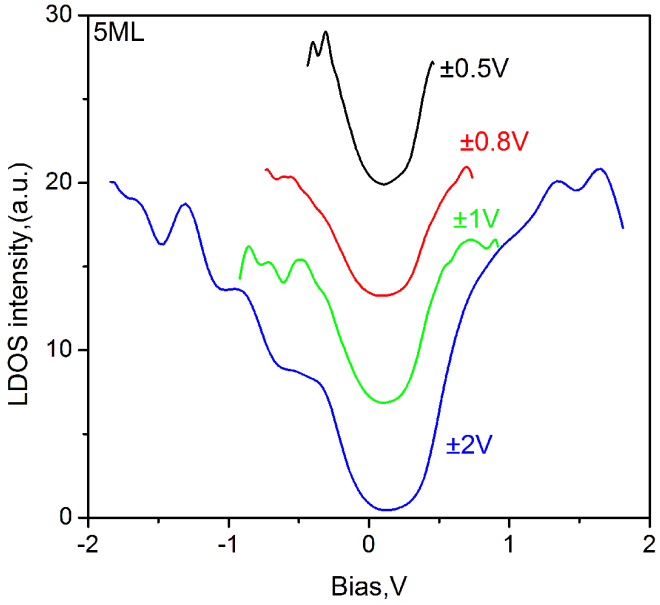

Figure 3.14: CITS spectra recorded on 5ML thick island in different bias voltage ranges. The spectra were collected from four different islands.

by three clear peaks at ~-0.25V, +0.5V and +0.8V. The negative side of the 3 ML spectra is characterized by two broader peaks in the range of ~-0.5V to -1V and ~-1.2V to -1.75V. The spectral histogram suggests that these broader peaks are formed due to shifts in energy of the LDOS peak. These energy shifts of peaks are discussed in section 3.5. The peaks at positive energies in 3 ML are much more distinct compared to the 5 ML spectrum with prominent peaks at ~+0.5V, +0.85V, +1.5V and +1.8V.

The dI/dV(V) curve for 7 ML shows higher LDOS as compared to the 3 ML and 5 ML thick islands which is expected as the film grows thicker [63]. Multiple LDOS peaks are observed in the histogram at energies ~-1.5V, -1.2V, -0.75, -0.4V, +0.45V, +0.75V, +1V, +1.25V and +1.6V. The distribution of the LDOS peaks in the case of 7 ML is very interesting because the LDOS peaks in the negative energies are almost mirrored in the positive energies. A broad peak in the dI/dV(V) curve is seen at ~ -0.55V in Figure 3.13 (b) that is actually composed of two sub peaks/shoulders as seen via histogram. The broad peaks in the dI/dV(V) curves are sometimes composed of a single peak (e.g. -0.25V in 3 ML) or two sub peaks (e.g. -0.4V and -0.75V in 7 ML) which are deciphered clearly only by spectral histograms. Spectral histogram is a powerful tool in CITS data analysis and we stress on the fact that the dI/dV(V) curve and the spectral histogram are complimentary tools in characterizing spectroscopic information.

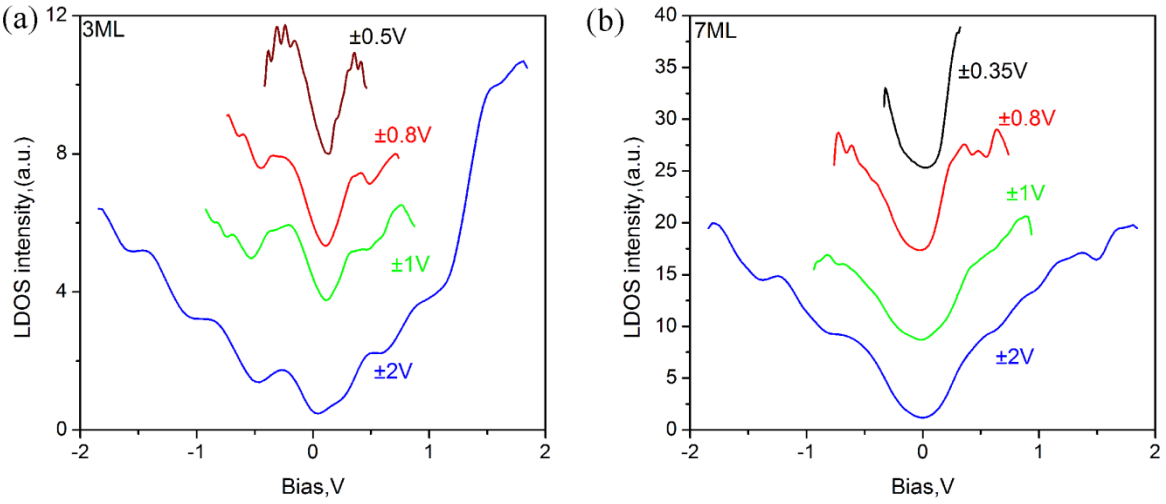

Figure 3.15: (a) CITS spectra recorded on 3ML thick island in different bias voltage range (b) CITS spectra on 7ML thick island with various bias voltage range (I_t = 1.5nA). All the curves have been recorded on different islands.

3.3.4 Influence of tip sample distance on LDOS

The tip- sample distance is influenced by the setpoint bias voltage and set point tunneling current. The tip-sample distance in varying bias voltage is not a linear relation because it is governed by the LDOS of the sample at different bias voltages [94] i.e. the current does not increase linearly with the bias voltage but depends on the DOS at a particular energy. Keeping the bias voltage constant and changing the set point tunneling current is a better way of controlling the tip sample distance in a linear fashion. Nevertheless we have investigated both the options below.

3.3.4.1 Varying set point bias voltage

All the STS data shown so far were obtained in the range of ±2V with a stabilization voltage of V_t= +2V. To record CITS spectra in say ±1V region, the stabilization voltage has to be changed to V_t=+1V to avoid any rapid voltage jumps and instability. In consequence, the tip-sample distance also changes. For example, if a dI/dV(V) curve is recorded with a stabilization voltage of V_t = +1V and another with V_t=+2V (with the same set-point current) then the tip-sample distance will be smaller in former. Experiments were performed to record CITS spectra in ±2V range with a reduced tip sample distance i.e. by setting V_t= +1V, +0.5V etc. All such experiments failed because application of such high voltages with a reduced tip-sample distance often resulted in destruction of the soft bismuth island. Therefore CITS experiments were always performed with the V_t value set as the first parameter in CITS current ramp e.g. V_t = +0.5V for a bias voltage ramp between ±0.5V.

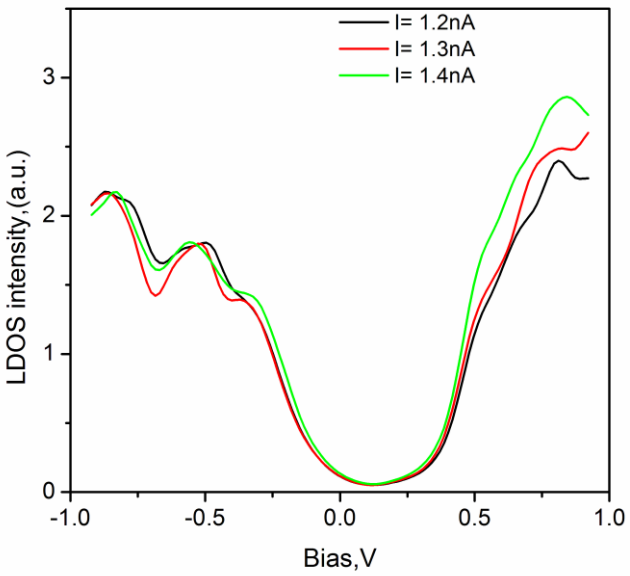

Figure 3.16: CITS spectra recorded on a 5 ML thick island with a constant set point V_t=+1V with varying set point tunneling current.

In Figure 3.14 we show CITS data which was recorded on a 5 ML island with different voltage set points. Each dI/dV(V) curve represents CITS spectra with a different tip-sample distance. Each curve is an average of 10 individual dI/dV curves. The curves have been offset to aid visualization. It can be seen that the LDOS valley in all the cases have similar shape. Though one to one matching of the spectral features is not possible between all the datasets, it is possible to compare the red (±0.8V) curve, green (±1V) curve and the blue (±2V) curve. The LDOS valley near the Fermi level is well reproduced and there is a clear onset of a state near ~-0.5 in all three of them. The onset of the shoulder at ~+0.5V on the positive side of the spectrum is also quite well reproduced. Similar plots are shown in Figure 3.15 for 3 ML and 7 ML thicknesses. In Figure 3.15 (a) all the dI/dV(V) curves for 3 ML taken at different bias voltage ranges show the appearance of two states at ~-0.25V and +0.5V rather sharply. In Figure 3.15 (b) the shape of the LDOS valley for 7 ML is maintained in all the CITS datasets and the states at ~-0.5V and the shoulder at ~+0.5V are faithfully reproduced. Such an analysis shows that the gross features in CITS curves recorded on different thicknesses are reproducible and reliable.

3.3.4.2 Varying set point tunneling current

In Figure 3.16 we show dI/dV(V) curves recorded on different 5 ML thick islands with a constant set point bias voltage (V_t = +1V). The tunneling current was changed from in the three experimental datasets to vary the tip sample distance. The tunneling current has been changed between 1.2 nA to 1.4 nA only which is a small range. It is because higher tunneling current values resulted in destruction of the bismuth islands and lower current values suppresses LDOS features (which could

be seen only with high currents) because of increased tip sample distance [91]. It can be seen that the dI/dV curves shown in Figure 3.16 are very similar. Each dI/dV curve shown in the figure is an average of 10 individual curves. The LDOS peaks in all the three curves are reproduced well and we do not see any prominent effect of the change in tip-sample distance on the sample LDOS.

3.4 DFT calculations

In Figure 3.17 we compare an experimental dI/dV(V) spectra obtained on a 5 ML thick island with the calculated DOS for a 4 ML and 5 ML thick free standing infinite slab. The calculations were performed by Guang Bian and X.Wang in the group of Prof. T.C.Chiang at University of Illinois, Urbana Champagne (UIUC), USA. Spin orbit coupling was included in the calculations using relativistic LDA approximation. The calculated DOS in Figure 3.17 was obtained by integrating over the entire Brillouin zone. Surprisingly, it can be seen that the experimental 5 ML LDOS curve matches quite well to the 4 ML calculated DOS curve e.g. the states on the negative side of the spectrum are reproduced quite well. The spectral positions of the peaks are not perfect but the position of LDOS peaks is quite similar. The positive side of the spectrum is not very distinct in the 5 ML experimental curve but the shoulder at ~ +0.5 to +0.75V is reproduced very well in the 4 ML calculated curve. On the other hand the 5 ML calculated curve bears no resemblance to the 5 ML experimental curve. Encouraged by this result we extended the analysis to the experimental dI/dV(V) spectra of 3 and 7 ML thick islands.

The comparison between the 3 ML experimental dI/dV(V) data, 2 ML calculated DOS and 3 ML curve is shown in Figure 3.18 (a). Once again the 3 ML experimental spectrum showed a good resemblance to the 2 ML calculated DOS curve. The states on both sides of the spectrum are very well reproduced in the 2 ML calculated curve. The alignment between peak positions is not perfect but the number and position of LDOS peaks is very similar. In Figure 3.18 (b) we compare the 7 ML experimental dI/dV(V) data with 6 ML calculated DOS and 7 ML calculated DOS. The 7 ML experimental spectrum is again similar to that of the 6 ML calculated DOS curve. There is a very good correlation between the states on the negative and positive side.

We also performed comparisons of the experimental data with calculations performed on slabs with different surface relaxations, free standing slabs, H-termination on one side of the slab (to imitate substrate effect) and thicknesses from 1-10 ML (shown in Appendix 2). However, the best match of the experimental spectra of an n ML thick bismuth island was achieved with bulk DOS of an

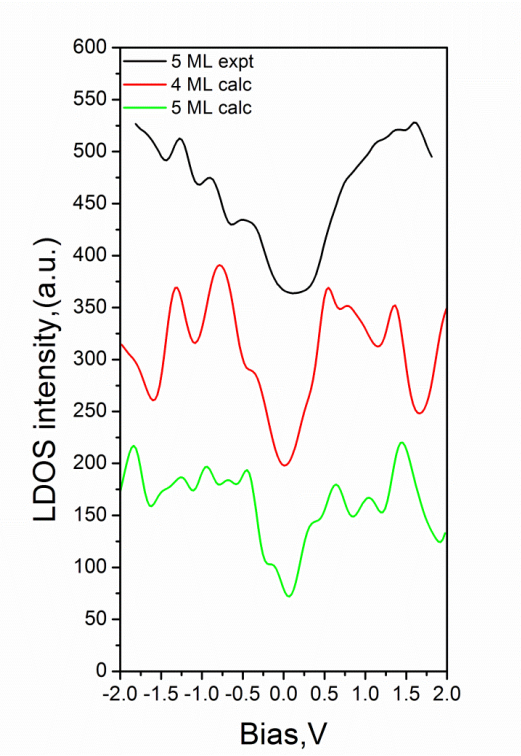

Figure 3.17: Experimental dI/dV(V) spectra obtained from a 5 ML thick island(black) is compared to calculated DOS from a 4 ML thick slab (red) and a 5 ML thick slab (green).

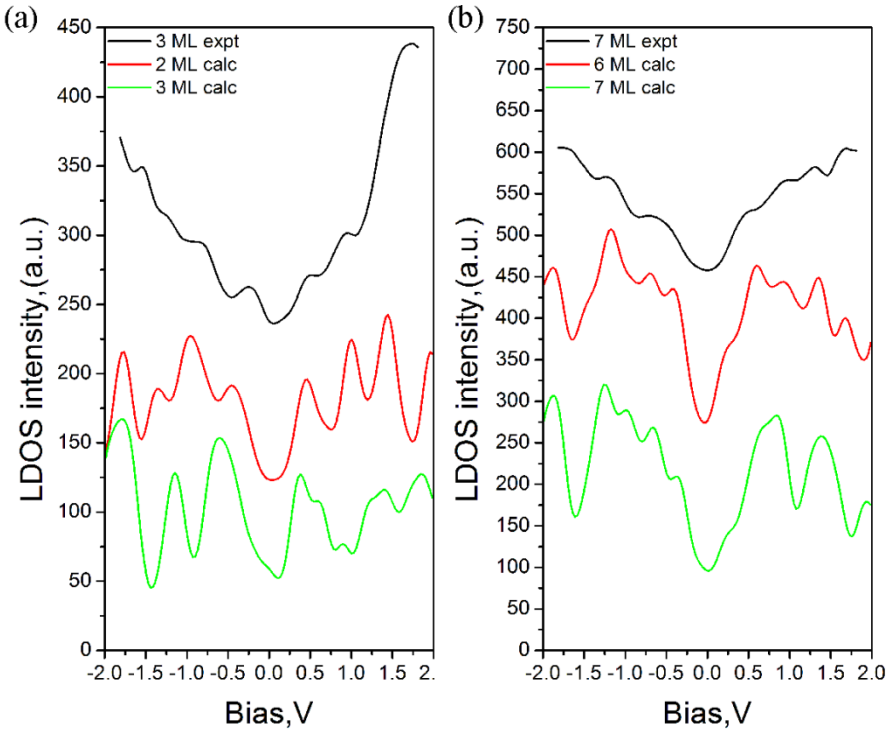

Figure 3.18: (a) Experimental dI/dV spectrum obtained on 3 ML thick island is compared to calculated DOS from 2 ML and 3 ML free standing bismuth slab. (b) Experimental dI/dV spectrum obtained on 7 ML thick island is compared to calculated DOS from 6 ML and 7 ML free standing bismuth slab.

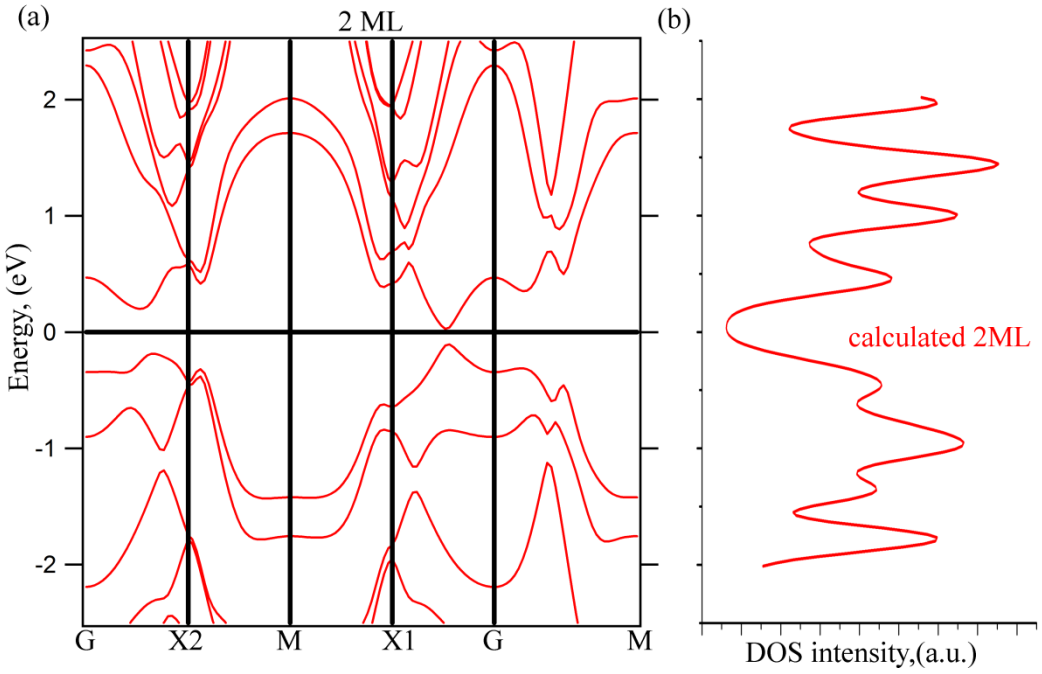

Figure 3.19: (a) Calculated band structure of a 2 ML thick free standing bismuth slab (b) Calculated 2 ML DOS curve.

(n-1) ML thick free standing slab of bismuth. These results indicate the presence of a 1 ML thick 'wetting layer' under the bismuth island which does not contribute to the LDOS spectra. Formation of wetting layer in bismuth films is not unusual and has been reported previously in [44, 47, 53]. We have, however, never observed the 'wetting layer' in our STM experiments because it is formed only under the bismuth base islands.

3.4.1 Band structure

We now look at the band structures for different thicknesses of bismuth islands. In Figure 3.19 (a) we show the band structure of a 2 ML thick bismuth film from which the calculated 2ML DOS spectrum (red) in (b) is obtained. Symmetry points in the Brillouin zone are indicated on the x-axis of Figure 3.19 (a) and energy on the y-axis. Because of the free standing nature of the bismuth films in the calculations, two surfaces are created (top and bottom surfaces of the film) which in ultra thin films couple together to nullify the effect of SOC (see chapter 1 for details). Therefore each band shown in the band structure in Figure 3.19 is doubly degenerate. This effect however decreases with increasing thickness of the film where the two surfaces of the film cannot interact anymore and the splitting of the bands into non degenerate bands should be observed in calculations [63]. Few bands are seen perpetuating at energies around the Fermi level with a Fermi level crossing at G-X1 line that result in an electron pocket. A band gap is also observed between G and X1. In these band structures the position of the Fermi level determines the nature of the film i.e. if it behaves as a weak metal or

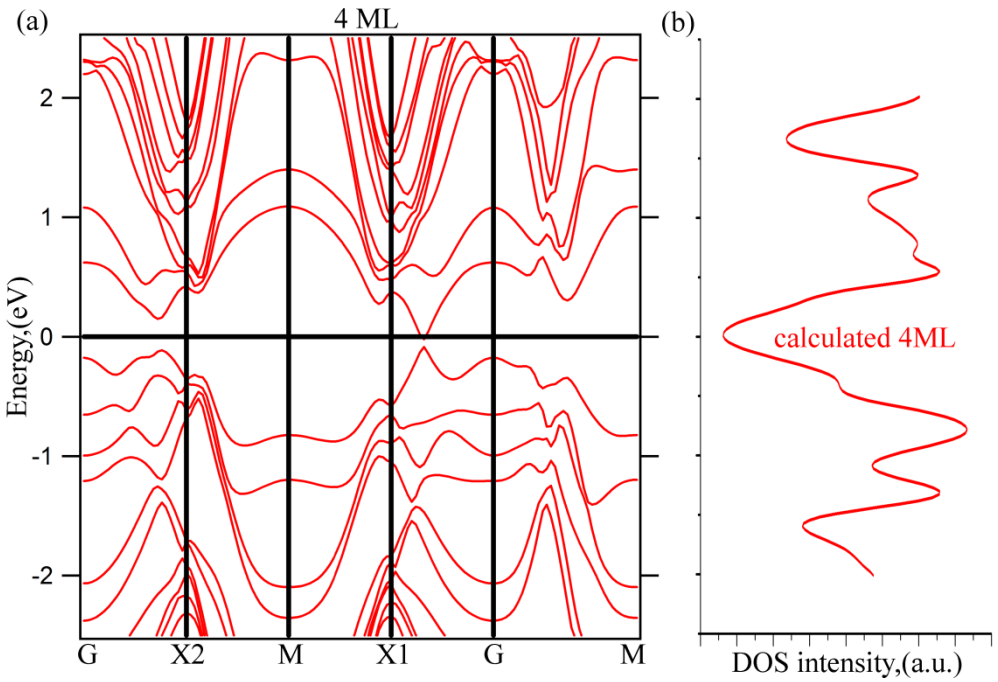

Figure 3.20: (a) Calculated band structure of a 4 ML thick free standing bismuth slab (b) Calculated 4 ML DOS curve.

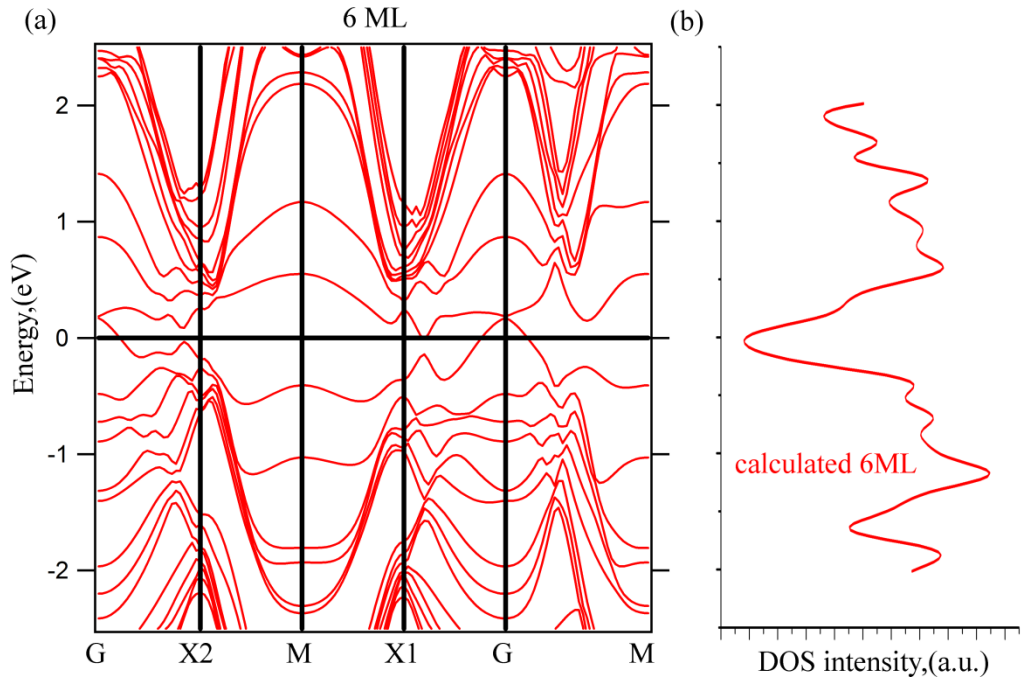

Figure 3.21: : (a) Calculated band structure of a 4 ML thick free standing bismuth slab (b) Calculated 4 ML DOS curve.

semiconductor. For example if the Fermi level is shifted towards more positive energies an electron pocket is created which increases the electron density at Fermi level leading to metallic behavior [30]. If the Fermi level is shifted downwards then the band gap would result in a semi-conducting behavior. The position of the Fermi level in turn depends on the charge transfer or doping from the substrate which will be discussed in detail in section 5.2.4. There is also a very prominent density of bands which start ~+0.4eV and -0.3 eV and continues to higher positive and higher negative energies respectively. These bands are the 'bulk bands' that are usually situated away from the Fermi level and whose presence is largely felt throughout the bulk of the film.

In Figure 3.20 (a) and (b) we show the band structure of a 4 ML thick free standing bismuth slab and the comparison between the calculated 4 ML DOS curve and the 5 ML experimental dI/dV(V) curve respectively. The most striking feature in the calculated band structure is that the number of bands has increased dramatically with a thicker bismuth slab. The bulk band continuum starts at ~ +0.4eV on the positive side of the spectrum and ~-0.3eV on the negative side. Once again, the region around the Fermi level is not congested and it can be seen that one of the bands crosses the Fermi level in G-X1 direction. The same band was seen touching the Fermi level in the 2 ML band diagram in Figure 3.19 (a). In Figure 3.21 (a) we show the band structure of a 6 ML thick free standing bismuth slab with its calculated DOS in (b). The band structure begins to become more complicated with increasing thickness. Only one band is seen crossing the Fermi level near gamma (G) point.

The layer pairing effect in Bi(110) islands gives rise to electron confinement [63, 61] in the vertical direction i.e. $< 110 >$ direction. This quantization is difficult to visualize in CITS data because the data shows density of states (DOS) associated with certain energy. Such vertical quantization has been previously reported in bismuth films [61] in which quantum well states (QWS) were observed via ARPES. ARPES has a substantial advantage over STM in viewing QWS because visualization along a particular crystallographic direction is possible (but only in negative energies or occupied states). ARPES on our samples are not possible because of the ultra thin nature of the film. However, since we have the calculated band structures, we can clearly see the quantization of bands in the $< 110 >$ direction. For example the number of quantized bands increases at G and M point as a function of thickness [63]. If we look at the M point, only the negative energies (hypothetical ARPES), then we see that there are 2 quantized bands in 3 ML (2 ML + 1 ML wetting layer) thick bismuth island, followed by 4 bands in 5 ML (4 ML + 1 ML wetting layer) thick film and 6 in 7 ML (6 ML+1 ML wetting layer) thick film.

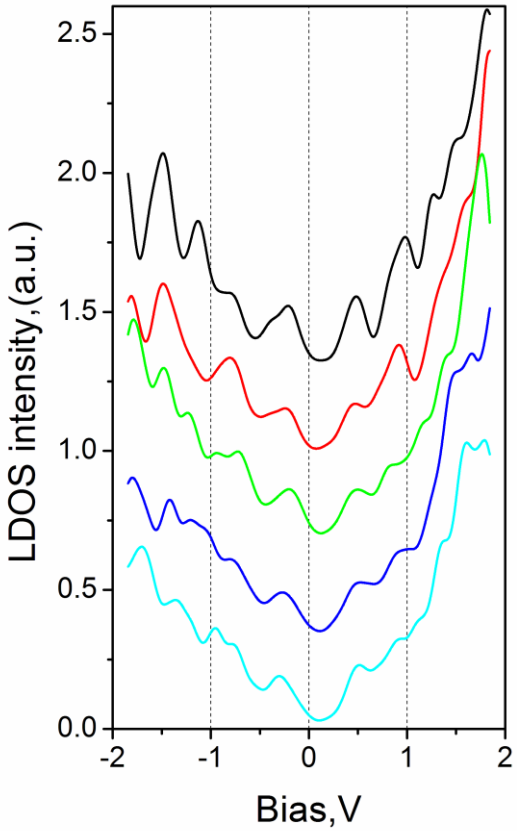

Figure 3.22: Five individual dI/dV(V) curves extracted from various positions in a single 3 ML thick island.

3.5 Effect of stress/strain on bismuth islands

While preparing spectral histograms we observed that some of the LDOS peaks show a distribution rather than a sharp peak (see Figure 3.13 (a)). This would mean that the maximum of the LDOS peaks shifts in energy as a function of location on the sample. To investigate this phenomenon further we extracted 5 individual dI/dV(V) curves from various positions on a 2+1 ML island in Figure 3.22. It can be seen that there are two very sharp peaks at ~-0.3V and +0.5 V which do not shift in energy much. However the peaks e.g. at ~-0.8 V, +1V, +1.2V seems to shift its position across different positions on the 2+1 ML island. If we look at the spectral histogram for 2+1 ML in Figure 3.13 (a) then we see that there is a distribution of peaks around ~-1V, -1.5V and +1.4V which is consistent with the 5 curves shown in Figure 3.22. To understand this further the team at UIUC performed calculations in which the unit cell was distorted slightly. The dimensions of the surface unit cell of bulk Bi(110) are A = 4.5332 Å and B = 4.7236 Å [29]. A slice of a 2 ML thick bismuth slab is shown in Figure 3.23 (wetting layer not shown). Letters A, B and C show inter atomic distances in the x, y and z directions. The distortion of the unit cell was performed in 4 ways-

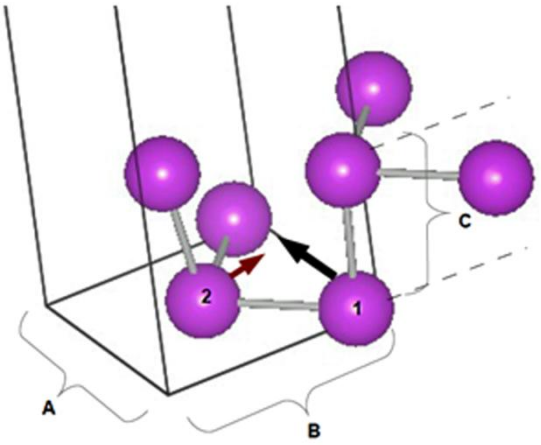

Figure 3.23: A slice of 2 ML thick bismuth slab (wetting layer not shown) showing various unit cell distortion processes (refer text for details).

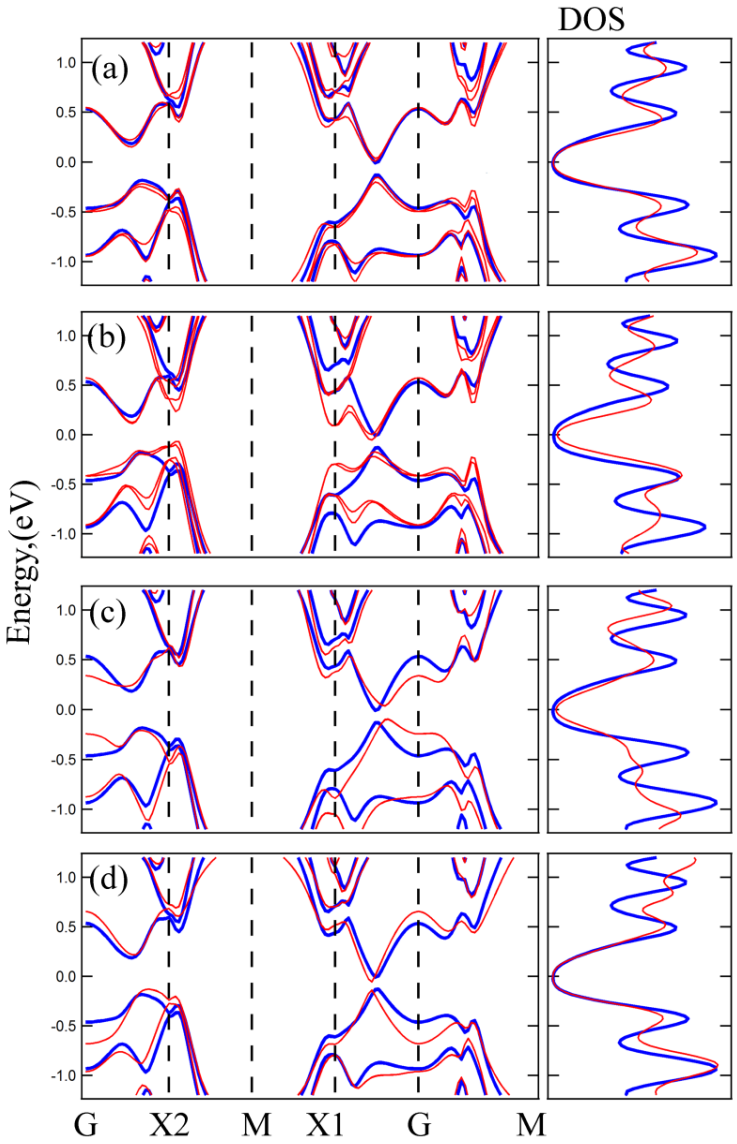

Figure 3.24: Band structure and its corresponding DOS resulting out of various distortions of the unit cell. The original band structure and DOS is shown in blue. Red color corresponds to altered band structure and DOS due to distorted unit cell (refer text for details).

(1) By shifting atom 1 along the vector A by 0.05Å. Vector B and C remained unchanged (black arrow in Figure 3.23).
(2) By shifting atom 2 along the vector B by 0.05Å. Vector A and C remained unchanged (maroon arrow in Figure 3.23).
(3) By expanding vector C by 15%.
(4) By contracting vector C by 15%.

The band structure and DOS resulting from these distortions in the unit cell is shown in Figure 3.24 (a)-(d) respectively. In Figure 3.24 (a) it can be seen that by shifting atom 1 along vector A the LDOS peak at ~ -0.2V shifts slightly towards higher energies. By shifting atom 2 along the vector B shifts in LDOS peaks were noticed in Figure 3.24 (b) i.e. the peak at ~ -0.2V shifted to higher energies and the peak at ~ +1V shifted to lower energies. A small magnitude of band splitting leading to non degenerate bands is also seen in Figure 3.24 (a) and (b) as a consequence of distortions (1) and (2). The LDOS peaks also exhibit energy shifts in the case of expansion and contraction of vector C via distortions (3) and (4). This indicates that the presence of slight distortions in the unit cell can give rise to the shifts in energy positions of the LDOS peaks. Such kinds of distortions might be expected at the substrate-film interface in ultra thin bismuth films. The 3 ML base experiences the maximum stress/distortions in its unit cell owing to its position next to the substrate and as the film grows thicker the distortions slowly fade away. Again, it is emphasized that the nature of the wetting layer is not well understood [126].

3.6 Summary

We have investigated ultra thin films of bismuth deposited on HOPG substrates via XPS, STM and STS. XPS measurements reveal the good quality and metallic nature of the films. An intensity analysis of the C 1s and Bi $4f$ peak allowed us to estimate the height of the islands bases to be 3ML. The main peaks in XPS spectra at 156.9 eV and 162.2 eV are attributed to the Bi $4f$ doublet. A weak shoulder located at 0.4 eV below the Fermi level was detected in all spectra and interpreted as a quantum well sub-band characteristic for ultra thin bismuth films. The XPS results also suggest the absence of bonds between HOPG and the bismuth film or a weakly physi-sorbed film.

The height measurements via STM show that the islands grow in paired layers on top of a 3 ML base. These results indicate that the films grow with the (110) plane parallel to the substrate's surface. Atomic resolution images were obtained via STM on the islands and the surface unit cell has been estimated to be 0.48 ± 0.03 nm x 0.46 ± 0.02 nm which is reasonably similar to the bulk Bi(110)

surface unit cell. We were not able to remove individual paired layers by pulsing the STM tip or by tip-sample interactions which indicate some kind of bond formation between the paired layers [79].

We demonstrated that a pre-screening procedure with an application of a 5-point median filter is a robust routine to remove noise from the STS data. The spectral histograms in conjunction with multiple averaged STS curves are a reproducible characteristic of Bi(110) islands. The LDOS peaks observed in the STS curves are not affected by changing the tip-sample distance i.e. no energy shifts are observed as a function of tip-sample distance. Comparison of the experimental STS data with DFT calculations shows that the LDOS of an 'n' ML thick bismuth island is similar to an 'n-1' ML thick bismuth slab. This implies the presence of a 'dead' wetting layer. This wetting layer is not present anywhere else on the HOPG substrate except underneath the bismuth islands. XPS, STS and DFT calculations reveal the free standing nature of the Bi(110) films on HOPG that results in formation of two symmetrical surfaces (top and bottom). The two surfaces interact and couple to each other rendering all the electronic bands doubly degenerate in the 3, 5 and 7 ML islands.

In our spectral histograms we observe that the maximum of some LDOS peaks shift in energy as a function of location in the sample. Calculations show that introduction of slight stress/strain in the film can result in such energy shifts.

4. Bright Beaches

In chapter 3 we discussed CITS measurements on Bi(110) islands and extraction of dI/dV(V) from Bi(110) islands. In this chapter we concentrate on spectroscopic measurements on the edges of the bismuth islands and stripes. Differential conductivity maps acquired via CITS reveal a localized high density of states at the edges of Bi(110) islands and stripes at energies near the Fermi level. This high LDOS is also visible in STM constant current topographs at low bias voltages where it appears as raised edges on the islands. The high LDOS at the edges is observed both at room temperature and at 50 K. We refer to these high LDOS features at the edges of Bi(110) islands as 'bright beaches (BB)' as they appear as a bright feature in the dI/dV maps and resemble 'a beach on a coastline'. The term 'bright beach' was first used in [127] where it was used to show high LDOS at the edges of Potassium islands on HOPG.

With this background a plausible explanation for the origin of the bright beach on the edges of Bi(110) islands and stripes is sought. Similar phenomena have been observed by STM and STS on thin films/bulk crystals of bismuth and other metallic/alloy films in the literature. Pertinent effects are reviewed below.

4.1 Literature review

4.1.1 Edge reconstructions

Termination of a bulk structure results in formation of a surface which possesses dangling bonds. The presence of dangling bonds raises the energy of the structure therefore the system tries to minimize it by introducing surface reconstructions e.g. the formation of the well known 7 x 7 reconstructed surface of Si(111) [128]. Edge reconstructions are similar to surface reconstructions but they occur when a 2D sheet of atoms terminates resulting in formation of stripes or ribbon like structures. Edge reconstructions significantly affect the electronic and magnetic properties of a 1D stripe or nanoribbon. The reconstruction is usually associated with charge redistribution leading to formation of localized edge states. These states have been observed for example in nanoribbons of TiO_2 [129], BN [130], SiC [131] and graphene with a zigzag edge [132]. The localized state observed on the zig zag edge of highly oriented pyrolytic graphite (HOPG) is shown in Figure 4.1 (the edge states appear as bright spots in the image indicating areas of high LDOS). The energy bands corresponding to such localized states are usually flat and thereby give a sharp peak in the DOS. These localized edge states are usually found at energies close to the Fermi level and they play an important role in determining the DOS at the Fermi level [133]. These edge states can be influenced

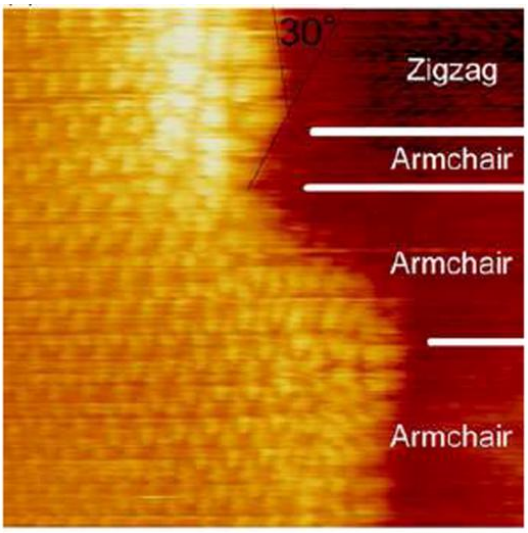

Figure 4.1: An atomically resolved UHV-STM image (9 x 9 nm^2) of hydrogenated step edge of HOPG. Bright spots are observed on the top part of the image which are localized edge states formed on the zig-zag edge of HOPG. Image reproduced from [132].

by transverse electric fields [134] or edge modifications to give rise to semiconductor-half metal transitions in some materials e.g. graphene [135].

Edge reconstructions significantly affect the properties of armchair and zigzag nanoribbons of 1 ML thick Bi(111). The armchair bismuth nanoribbon is an indirect semiconductor and the zigzag nanoribbon exhibits a metal-semiconductor transition as a function of width of the nanoribbon [136]. The charge densities of the valance band maxima (VBM) and conduction band minima (CBM) in those nanoribbons are mostly distributed around the edge and sub edge atoms and decay exponentially on approaching the interior. Thus in an STM scan at bias voltages corresponding to the energy of the localized edge state, the edges of the nanoribbon appear taller because of enhanced tunneling as compared to the interior of the nanoribbon.

In an STM study by Yin *et al* enhanced tunneling at the edges of Potassium (K) islands on HOPG was observed [127]. This high LDOS at the edge was termed 'bright beaches'. The edge reconstruction of Potassium islands on HOPG shrinks the K-K bond lengths and drags them towards the graphite surface [127]. Bader charge analysis reveals that as a consequence of the edge reconstruction the interior of the island is positively charged by 0.2 eV/atom and the edges are positively charged as much as 0.6 eV/atom (a K_{19} cluster and a K_{24} stripe is shown in Figure 4.2 (c) and (d) respectively). As the STM scans these islands, a bright feature or 'bright beach' is observed on the edges [127] only at high negative bias voltages. The strong negative bias voltage (or a positive tip) attracts electrons back to a K island located beneath the tip. Since the edges of the islands are net positively charged a field induced preferential accumulation of the restored electrons occurs at

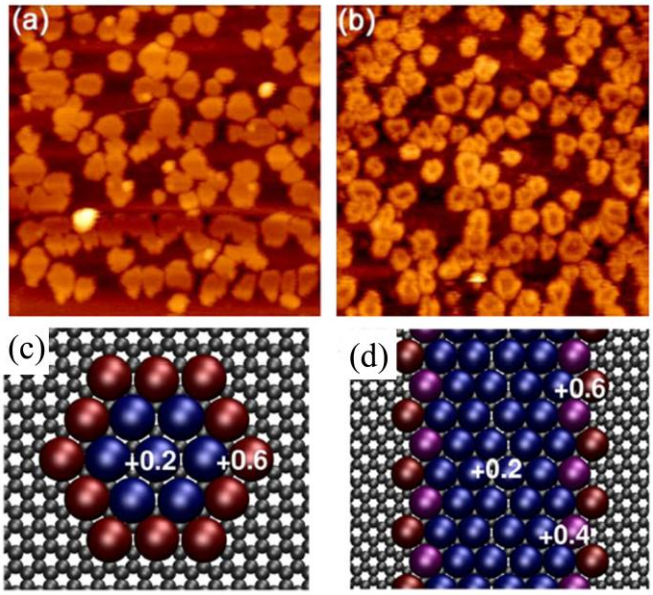

Figure 4.2: (a) Constant current STM image of K islands on graphite (U = -2.0V, I = 40pA, Coverage = 0.86ML) (b) Everything same as (a), only the bias voltage was changed to -4V. (c) and (d) K_{19} cluster and K_{24} stripe respectively with corresponding Bader charges in the interior and the edge. Image reproduced from [127].

the edges. It should also be noted that in the presence of the field the total electronic charge on the K islands is distributed approximately evenly, but the wavefunctions of the 'beach' electrons decay more slowly into vacuum because of a lower coordination number at the island's edges; this gives rise to an increased tunneling rate and thus the larger apparent height at the edges of the island (see Figure 4.2 (a) and (b)).

4.1.2 Quantum interference

Crystal imperfections such as a step edge and defects are always present on a surface and act as scattering centers for electron waves [137]. When an electron wave hits a step edge (defect) it is reflected back where it interferes constructively with the incoming wave and forms a 'standing wave'. One of the remarkable feats achieved by an STM is the possibility to image the standing waves associated with the interference of quasi-free electronic wavefunctions. This was achieved for the first time on a copper surface, for electrons confined in a circular resonator created with iron ad atoms, a structure well known as the 'quantum corral' [138-141]. The standing waves arising in the presence of surface inhomogeneities are also called as 'Friedel oscillations' [142], where the term Friedel oscillations was first used to describe the asymptotic dependence of the perturbed density of states of a free electron gas in the presence of a disorder. The Friedel oscillations are characterized by $\Delta n \sim (\cos 2k_F x)$ [142], where Δn is the charge density deviation, k_F is the Fermi wave vector and x is the distance from the perturbing impurity, and is governed by the k_F of the surface state that has been perturbed. Such a periodic modulation decays away as a function of distance from the step

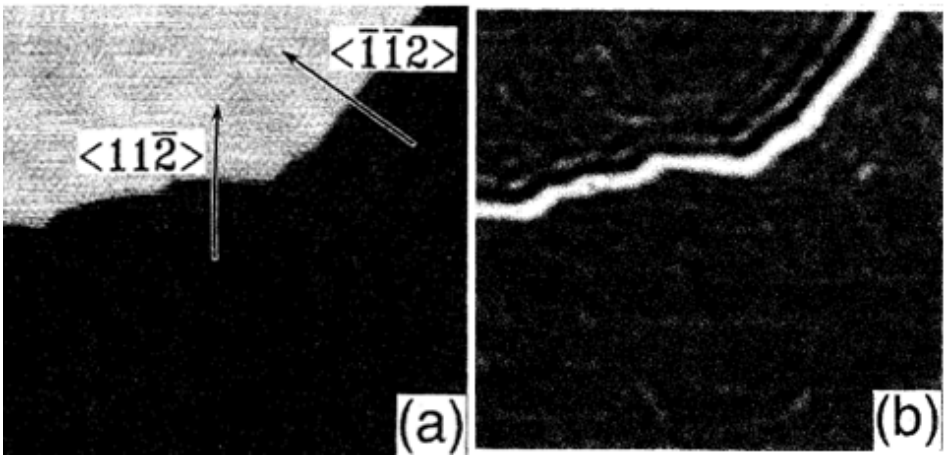

Figure 4.3: (a) STM image of Au(111) surface with a step (b) LDOS image from tunneling spectra calculated at +0.15V obtained over the same area as (a). Image reproduced from [137]

edge [137, 143]. STM offers the possibility to study the standing waves in the LDOS which are in fact energy resolved Friedel oscillations for 2D and 1D electron gases. The local density of surface states was first observed via an STM by Hasegawa and Avouris [137] on confined Shockley states of Au(111) (see Figure 4.3) surfaces at room temperature and by Crommie *et al* on Cu(111) at 4 K.

The standing waves have been imaged not only at the Fermi level but also at different energies. This requires spatial mapping of dI/dV at different applied voltages V, which allows one to focus on individual values of the energy specified at V, and avoids integration over all the wavelengths corresponding to the energies between the considered energy level and Fermi level

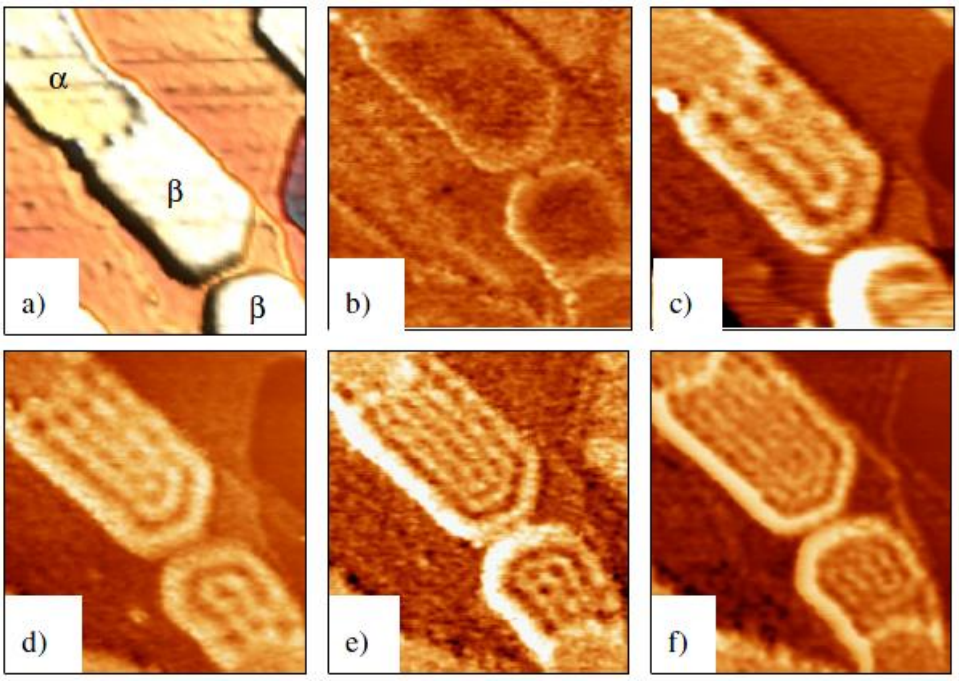

Figure 4.4: (a) STM topograph image of submonolayer deposit of Ni on Cu (111). (b-f) closed conductance images of (a) taken at increasing bias voltage: -200mV (b), +200mV (c), +300mV (d), +450mV (e) and +620mV (f). Image reproduced from [54].

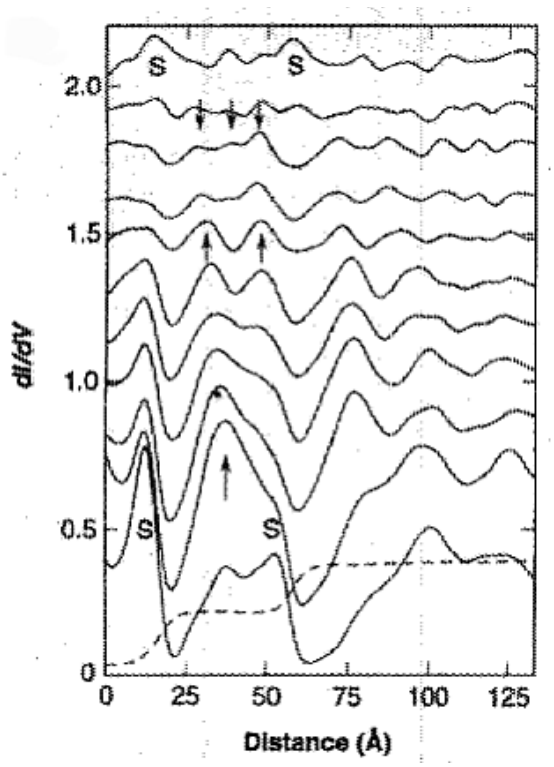

Figure 4.5: dI/dV line scans for individual bias voltages obtained on Au (111). The voltage varies from -0.47 V (bottom) to +0.39V (top). The dotted line is a constant current STM line scan and the step edge peals are marked by S. Image reproduced from [151]

[144]. This technique has been used to study standing waves in artificial quantum mechanically confined nanostructures. Quantum confinement is realized when the dimensions of the nanostructures are of the same magnitude as the wavelength of the trapped wavefunction [54, 145]. dI/dV maps on such nanostructures exhibit standing wave like patterns corresponding to eigenstates of an electron trapped in a two dimensional box. These waves can be confined within 'resonators' or well defined portions of the sample delimited with step edges or artificially created boundaries [146]. Quantum confinement of surface state electrons have been observed in surfaces of naturally occurring stepped terraces of Cu, Au, Ag [147] and artificially made nanostructures [145, 146, 148, 149]. An example of quantum confinement effect in Ni islands on Cu (111) [54] is shown in Figure 4.4. The α island shown in the figure is composed of two Ni(111) layers while the β island is composed of a Ni rich plane inserted in a Cu (111) crystal in a sub surface position [150]. The frequency of the standing wave inside the resonator increases with increasing energy (as seen in Figure 4.4 (b-f)).

4.1.3 Smoluchowski smoothening

In 1994 Avouris *et al* [151] observed a 1D state along the step edges of Au(111) via STS maps at room temperature (see Figure 4.5). They observed that the surface state spectrum of Au(111) was

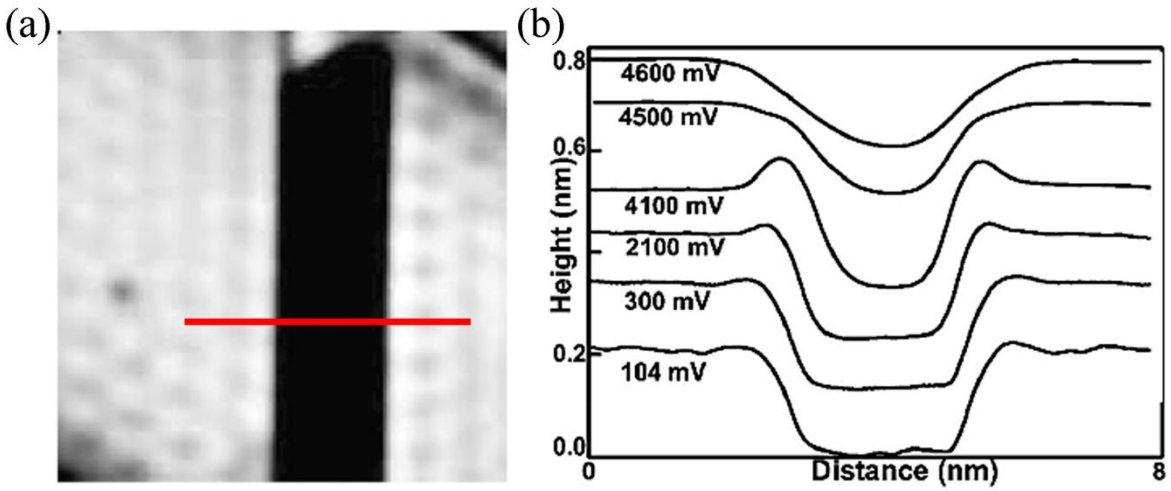

Figure 4.6: (a) STM image of a Cu(111) surface (b) Line profile corresponding to red line in (a) at six different bias voltages showing tip height vs. distance perpendicular to the step on Cu(111) surface. Image reproduced from [154].

not observed when the tip was over a step and that the step edge peaks (labeled S in Figure 4.5) were observed at energies below the onset of the surface state. While these peaks were observed in the vicinity of the step, they were observed to change their position as the sign of the applied bias changed, i.e. as the energy is swept through the Fermi level. Specifically the peaks are centered near the bottom of the step when the sample bias is negative, so that occupied states are probed. The peaks moved 3-4 Å towards the top of the step when the bias is positive and unoccupied states are probed. These changes in the step edge peaks led to clues about the origin of the step edge peaks and were attributed to 'Smoluchowski smoothening'. Smoluchowski [152] pointed out that for electron kinetic energy to be minimized at the step edges, there would be a 'smoothening effect', where the electron density will not follow the abrupt change in geometry but will flow from the upper part of the step edge to the lower part. As a result of this electron density smoothening there is a local increase in electron density at the bottom of the step and a corresponding decrease at the top. The observed movement of the step edge peak reflects these changes in the electron density. The charge rearrangement generates a step edge dipole with an orientation opposite to that of the surface electronic dipole. This effect is responsible for the lowering of workfunction at the step edges, leading to a reduced effective barrier and enhanced tunneling near the step edges, thus giving rise to step edge peaks.

4.1.4 Image states

Image states arise on metal surfaces due to a charge redistribution in response to an electron near the surface [153], in this case due to the STM tip. Bartels *et al* observed similar sharp linear protrusion in STM LDOS images on Cu(111) step edge (see Figure 4.6) at high positive bias voltages.

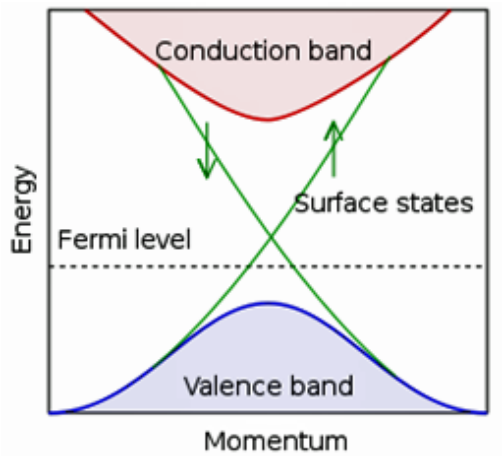

Figure 4.7: Schematic diagram of the band structure of a topological insulator. The green lines represent surface states with opposite spins shown by arrows. Image reproduced from [59]

The sharp protrusion at the edge was observed over a large range of positive bias voltages (~+1.5V to +4V). This elongated feature on the step edge was explained as an image state whose energy was modified by the dipolar potential at the step [154]. This dipolar potential arises out of Smoluchowski smoothening at the step edge. These protrusions are significantly different from the well known surface state oscillations (section 4.1.2) as these protrusions associated with the image states are much larger and show up at high positive bias voltages indicating an alternative origin at higher energies.

4.1.5 Topological edge states/ quantum spin hall (QSH) state

In recent times a new class of material called 'topological insulators' have emerged in which the role of the magnetic field is assumed by spin orbit coupling (SOC) and the topological states (also referred to as quantum spin hall states, QSHs) are protected by time reversal symmetry [52, 59, 155-162]. 'Topology' is a branch of mathematics which studies objects which are invariant under smooth deformations and as the name suggests topologically protected states or QSH states are robust under smooth deformation. The band structure near the Fermi level in these materials exhibits spin filtered surface bands (see Figure 4.7). Back scattering between these states is strictly prohibited because a state with E (k, ↑) cannot interfere with another state at E (-k, ↓), where the arrows represent spin up and spin down directions respectively (see section 1.2).

QSH states are similar to quantum hall states [163], however the major difference is that quantum spin hall states do not require a magnetic field for their existence nor they break any symmetries e.g. time reversal or parity [164]. For details on spin orbit coupling and time reversal symmetry please refer to section 1.2. Figure 4.8 shows a comparison of a quantum hall (QH) state with a quantum spin hall state. In the QH state (Figure 4.8 (a)) the electrons move along the edge

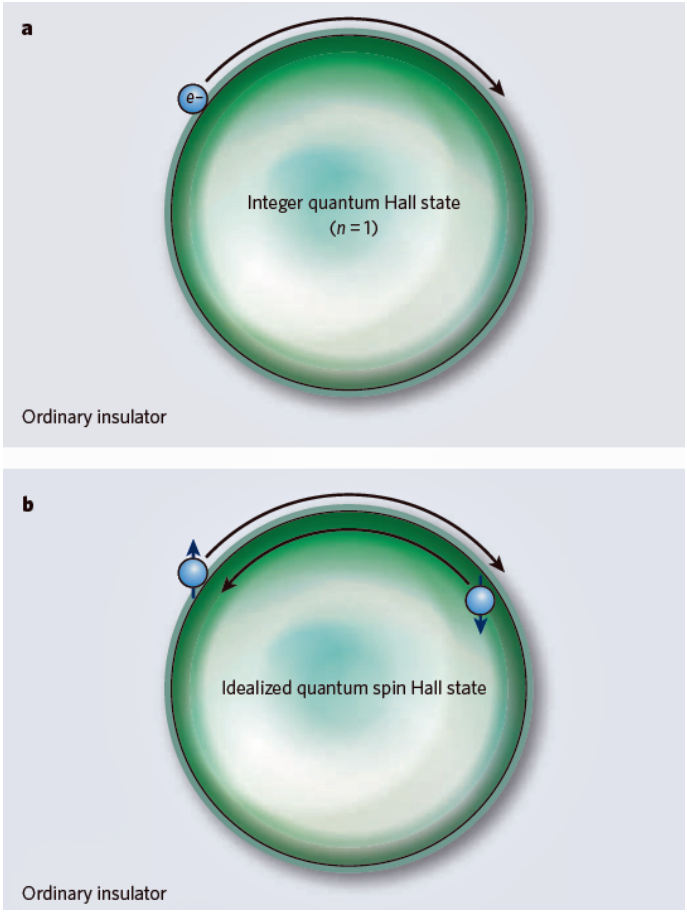

Figure 4.8: (a) Edge of an integer quantum hall state where the electrons are confined to a 2D droplet with a metallic edge. (b) Edge of a quantum spin hall state (topological insulator). Image reproduced from [60].

only in one direction, which is determined by the sign of the magnetic field applied perpendicular to the droplet. The integer n describes the number of propagating edge modes. In the case of a QSH state the spin up electron moves clockwise and spin down electron moves anti-clockwise giving rise to spin filtered transport in two directions (see Figure 4.8 (b)). With such spin filtered pathways these materials find an important role in spintronics and other fields.

4.1.6 Edge state in bismuth and bismuth based materials

As discussed in section 1.4, bismuth is a heavy metal which exhibits strong SOC and is a parent material for topological insulators [73, 58]. Very recently Bismuth (111) ultra thin films have been proposed to exhibit spin quantum Hall states (QSH) [41]. In spite of the predicted reduction of scattering on Bi(111) [159, 41], electron scattering was demonstrated at a local defect and the step edge on a thin Bi(111) film [72] (see Figure 4.9). The scattering around the defect results from superposition of three monochromatic waves which arise from spin conserving transitions between different spin-orbit split states in the highly anisotropic Fermi surface of Bi(111). The origin of the

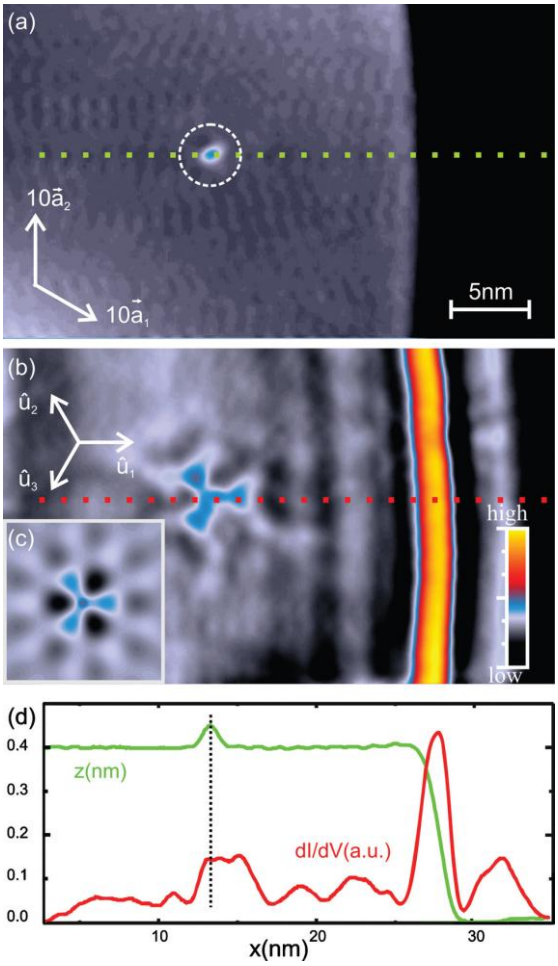

Figure 4.9: (a) STM topography of an area with a defect marked with dashed circle (V_t = -1mV, I = 110pA). (b) and (c) are the measured dI/dV map and numerical simulation performed for the same defect respectively. (d) Line profiles of the topography and the dI/dV signal across the defect and the step edge taken along the dotted line in (b). Image reproduced from [72].

periodic modulation or 'standing wave' at the step edge which results in an intense maximum at the step edge has not been discussed by the authors.

STM studies of the local LDOS of a surface state near a step edge of the strong topological insulator Bi_2Te_3 were performed by Alpichsev *et al* [73, 165]. The crystal structure of Bi_2Te_3 is shown in Figure 4.10 (a). They performed STS measurements at 9K on undoped crystals (see Figure 4.10 (d)) and to understand the various regimes in the LDOS curve they compared it to ARPES results. In Figure 4.10 (b) six constant energy ARPES contours are shown. A Dirac point is seen at -335mV and the contour changes from a circle to a hexagon, and become warped at energies above ~-100mV. The inset in Figure 4.10 (c) shows the full dispersion of the surface state band in the two principle direction of the Brillouin zone, together with portions of bulk conduction band (BCB) and bulk valence band (BVB) in vicinity. The integrated DOS from ARPES is shown in Figure 4.10 (c) which matches quite well with the dI/dV(V) curve obtained via STS in Figure 4.10 (d). In both figures zero marks the Fermi level. E_A corresponds to the bottom of the bulk conduction band and E_B

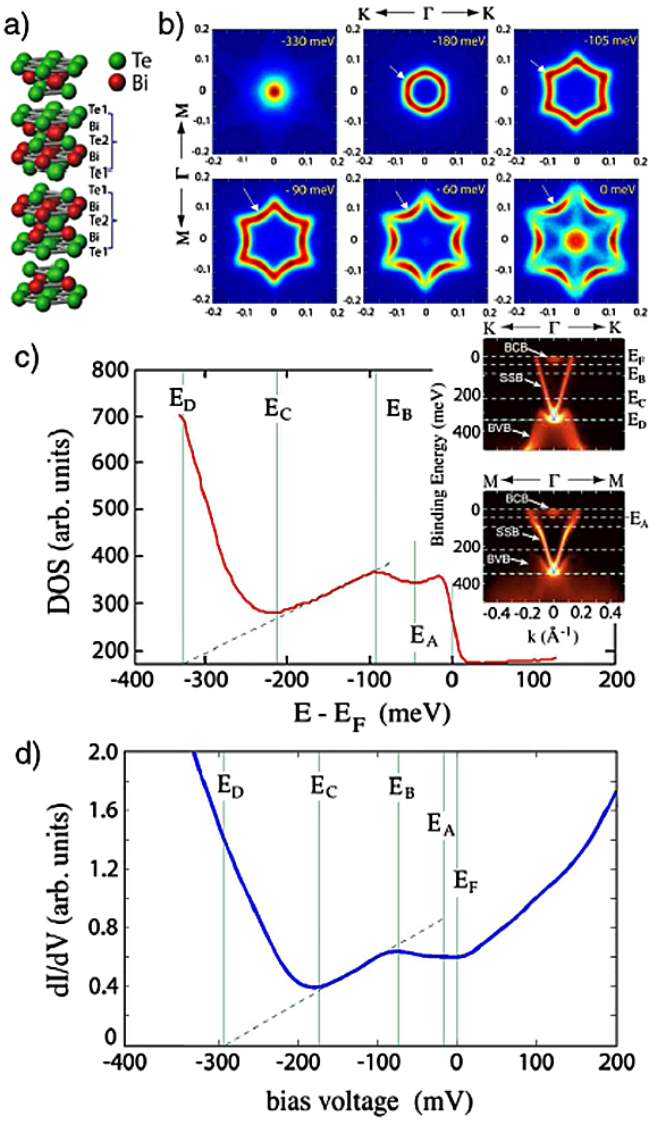

Figure 4.10: (a) Crystal structure showing three quintuple units of Bi_2Te_3. (b) ARPES measured constant energy contours of the surface state band. Strength of DOS grows from blue to dark red. (c) Integrated DOS from ARPES (refer text for details) (d) Typical STS spectrum of a 0.27 % Sn doped Bi_2Te_3. Image reproduced from [73].

corresponds to the point where the surface state band becomes warped. The linearly dispersing Dirac band extends from its tip at E_D to ~E_B, while E_C denotes the top of the bulk valence band.

In Figure 4.11 Alpichsev *et al* show a LDOS modulation across the step at various bias voltages. The blue dotted line represents raw data and the red curve shows a fit to a 1D oscillation [73]. Examination of the figure yields the following observations: (i) Friedel like oscillations that originate from the step are observed for all energies above E_b (~-100mV), the energy above which the surface state band warps; (ii) the period in this energy range increases with increasing bias voltage and (iii) the normal oscillations become strongly attenuated below E_b. The oscillations observed at higher energies are related to a spin conserving nesting vector in the hexagram band (see Figure 4.10 (b)).

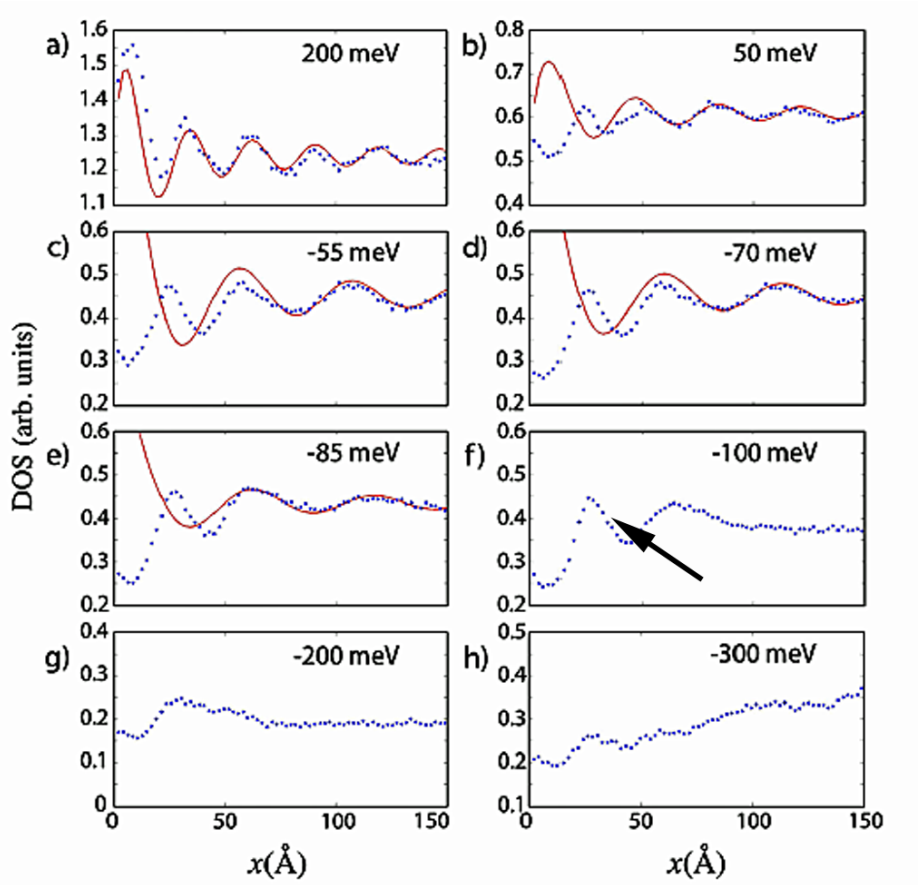

Figure 4.11: Averaged LDOS as a function of distance from the step for 8 energies. Red lines are fits to data (see text). (a)- (e) correspond to energies above E_B showing pronounced oscillations. (f)- (h) correspond to energies within the surface state band. Image reproduced from [73].

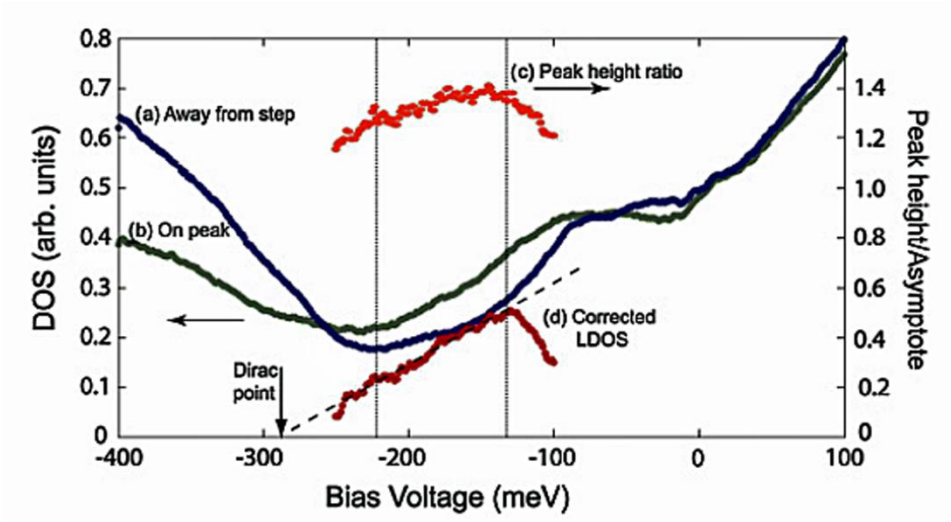

Figure 4.12: (a) LDOS spectra as a function of energy away from the step. (b) at the position of the maximum of the peak. (c) the ratio between the peak height and the asymptotic LDOS. (d) the extracted coherent part of LDOS. Image reproduced from [165].

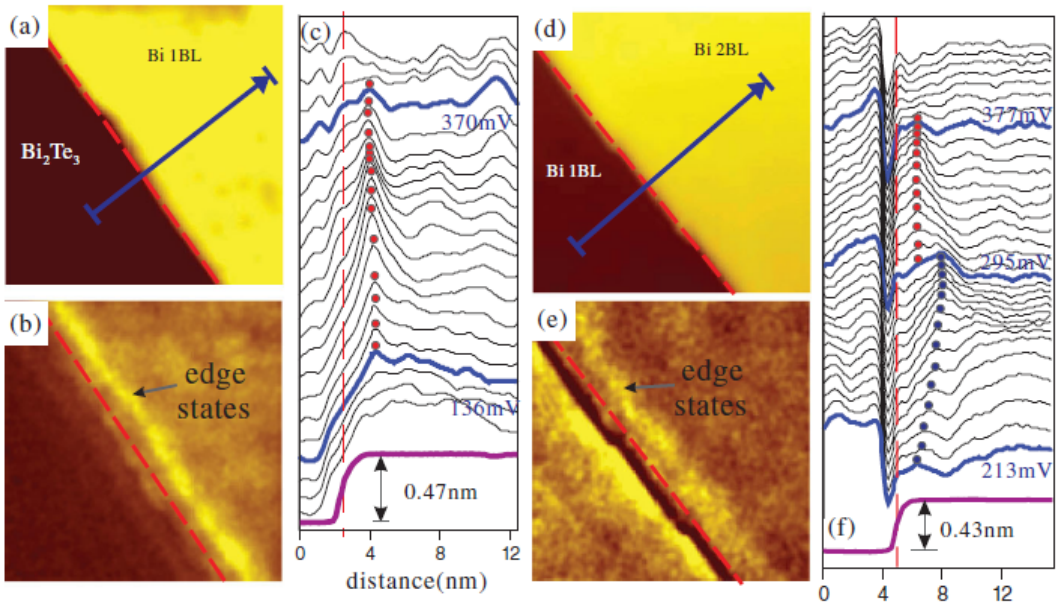

Figure 4.13: (a) STM image of a step edge of Bi(111) 1 BL on Bi_2Te_3 substrate (V_t = 0.75V, I_t = 245pA). (b) STS map at +283mV corresponding to (a). (c) Line profiles of STS dI/dV maps along with STM line profile along the blue arrowed line shown in (a). (d) STM image of a step edge between Bi(111) 2 bilayer and Bi(111) 1 bilayer (V_t = 1V, I_t = 300pA). (e) STS map at +338mV corresponding to (d). (f) Profiles of STS maps together with a STM line scan taken along the arrowed blue line in (d). Image reproduced from [78]

Their data also revealed the presence of a one dimensional bound state that runs parallel to the step edge and is bound to it at some characteristic distance. This bound state was observed in the bulk band gap region where the Friedel oscillations are suppressed (see black arrow in Figure 4.11 (f)) and also at higher energies where it becomes entangled with the oscillations of the warped surface band [165].

In Figure 4.12 Alpichsev *et al* show two dI/dV(V) curves (a) extracted away from the edge and (b) on the bound peak near step edge. It can be clearly seen that between ~-220mV to -100 mV the bound peak curve shows higher intensity of LDOS than the curve recorded away from the edge that shows up as the bound peak at the edge in the line profiles shown in Figure 4.11. The theory behind the formation of the bound state has not been published by the authors yet.

The presence of a topologically protected edge state on Bi(111) was shown experimentally by Yang *et al* [78] via STM, STS and ARPES. Figure 4.13 (a) shows an STM image of a Bi(111) bilayer on top of a Bi_2Te_3 substrate and in Figure 4.13 (b) the corresponding CITS dI/dV map is shown which shows the presence of the edge state on Bi(111) bilayer step edge. The edge state is seen as a bright one dimensional stripe across the edge. Line profiles at different energies corresponding to the blue line in Figure 4.13 (a) are shown in Figure 4.13 (c) where the position of the edge state is marked by a red dot. They were also able to directly observe and resolve the one dimensional edge states of single bilayer Bi(111) islands on Bi(111) covered-Bi_2Te_3 substrates (see Figure 4.13 (d) and (e)). The

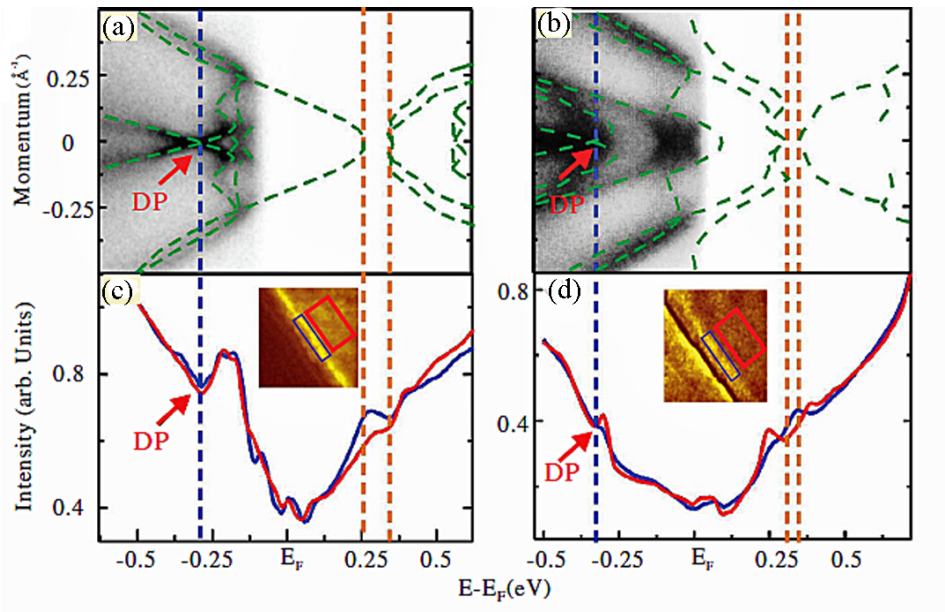

Figure 4.14: (a) and (b) ARPES spectrum for 1 BL and 2 BL Bi(111) on 40 quintuple Bi_2Te_3 together with calculated DFT bands (green). (c) and (d) STS of the step edge (blue) and the inner terrace (red) of 1 BL/Bi_2Te_3 and 1BL/ Bi-Bi_2Te_3. The ARPES and STS data are aligned by the 'Dirac point' as indicated by the vertical blue dashed line. The orange dashed lines mark the band gap of topmost Bi BL. Image reproduced from [78].

edge states were localized in the vicinity of step edges having a ~2 nm wide spatial distribution in real space (as seen in the line profiles in Figure 4.13 (f)). The blue dots in Figure 4.13 (f) indicate the surface state oscillations which change their position as a function of bias voltage.

Figure 4.14 (a) and (b) show ARPES results on 1 BL and 2 BL of Bi(111) on Bi_2Te_3. The superimposed green lines are calculated DFT bands. Figure 4.14 (c) and (d) show the dI/dV curves of the inner area (marked by red rectangle in inset) and the edge area (marked by blue rectangle in inset) in the islands of 1 BL/Bi_2Te_3 and 1BL on Bi/Bi_2Te_3. The Dirac points in the ARPES results are lined up against their corresponding dI/dV curves by the vertical blue dotted line. The Dirac points are marked by red arrows and they correspond to the dips in the dI/dV curves due to its zero density of states. The energy positions of the edge states relative to the band gap are shown by the window between the two vertical orange dashed lines. In the window the intensity of blue dI/dV curve is noticeably higher than the red curve. It is reasonable to expect that the STS attains higher contrast when the tip scans over the edge states within the energy window of the band gap, where the surface electronic states are absent and the edge electronic states are highly localized within. Based on the ARPES data, the line profiles in Figure 4.13 can be explained, e.g. in Figure 4.13 (f) the edge states (red dots) are seen in the energies corresponding to the band gap and the blue dots correspond to quantum interference of scattered electrons. The interference peak changes its position as a function of bias voltage.

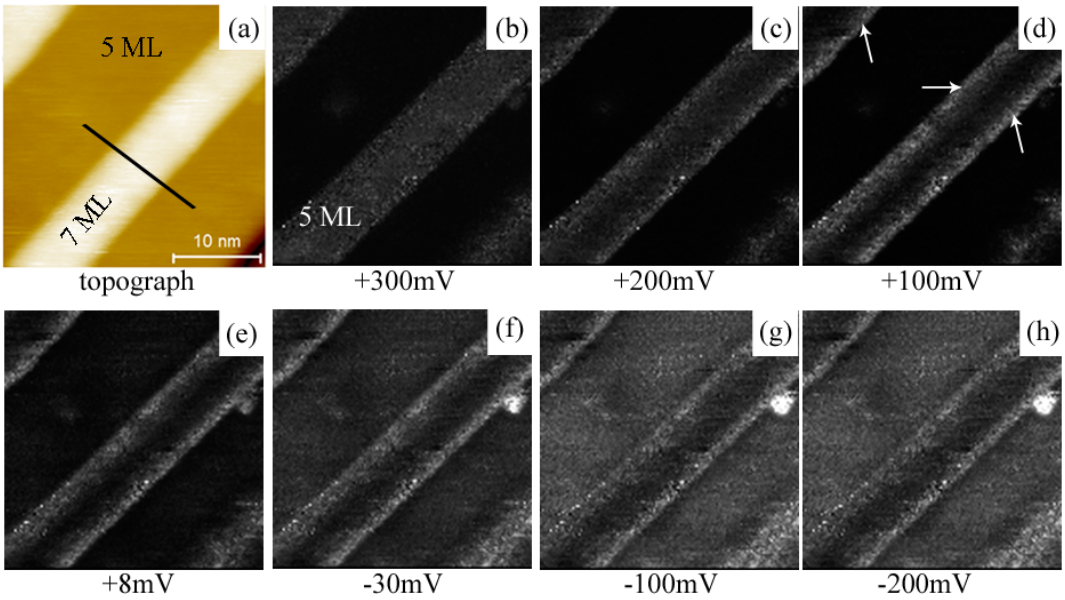

Figure 4.15: (a) STM image of a 5 ML thick island with two 7 ML stripes (V_t = +1V, I_t = 300pA). The black line on 7 ML stripe is a line profile. (b)- (h) dI/dV maps acquired via CITS on (a). White arrows in (d) show a prominent bright feature on the edges of 7 ML stripe. The CITS dI/dV maps are color coded e.g. brighter areas correspond to high LDOS and vice versa.

It is intriguing to see that a variety of underlying mechanisms can result in a 'bright beach' at a step edge. The bright beaches observed on our Bi(110) islands are very similar to many of the cases described in the literature review. In the following sections we will focus on STS measurements and various characteristics of the BB at the edges of our islands and stripes which would allow us to understand the origin of the bright beaches in Bi(110) islands.

4.2 Results

4.2.1 CITS on the 7 ML edge

In Figure 4.15 (a) we show an STM topograph of a 7 ML stripe which is formed on top of a 5 ML island with its corresponding dI/dV maps in Figure 4.15 (b)-(h). The dI/dV maps have been shown in greyscale in which the brighter regions correspond to higher LDOS at that bias voltage/energy. CITS was performed at 50 K and in the ±1V voltage range. Only selected dI/dV maps have been shown to highlight important features. The first noticeable thing in Figure 4.15 is that the contrast in the dI/dV maps changes as the bias voltage is changed. This is an indication of the evolution of the LDOS as a function of bias voltage. A prominent bright feature is seen on the edge of the 7 ML stripes (shown by white arrows in Figure 4.15 (d)). This bright feature starts forming on the edges of the 7 ML at ~+200mV, is seen very sharply at ~+100mV and disappears at ~-200mV. The bright feature is highly localized at the edge i.e. it does not change its position as a function of bias voltage and appears to have a finite width of ~2 nm around the whole perimeter of the island. The LDOS in the interior of

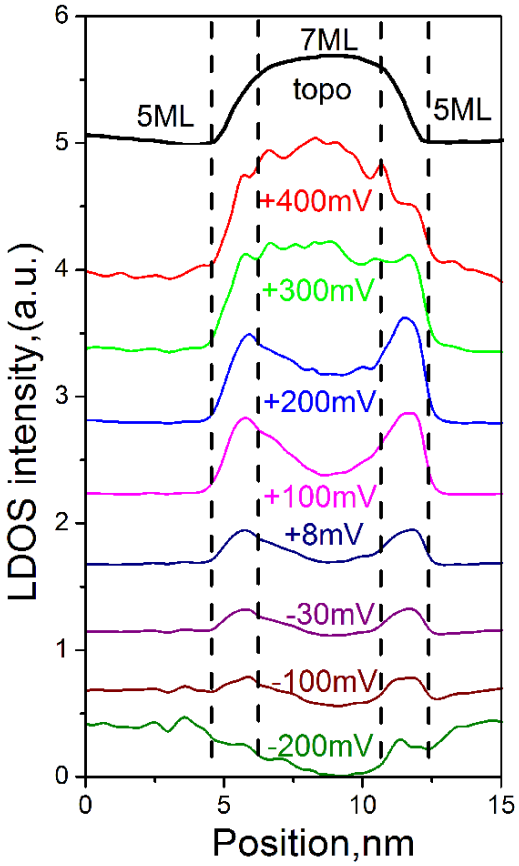

Figure 4.16: Profiles of STS maps (colored) along with a line profile on STM topograph (black) taken from the line profile shown in Figure 4.15 (a). The dotted vertical lines indicate the region of curvature at the edge.

the 7 ML stripe shows an evolution from bright (high at ~+300mV) to dark (low at ~-30mV) as a function of bias voltage. This simply reflects the electronic band structure of the thin film (see calculations in section 3.4). The LDOS in the interior of the 5 ML island also can be seen evolving as a function of bias voltage i.e. it is dark at ~+300mV and then gradually becomes brighter at higher negative bias voltages.

To examine the bright feature on the edge of the 7 ML stripe a line profile was drawn on the STM image (see black line in Figure 4.15 (a)) and compared with corresponding line profiles drawn on dI/dV maps at various bias voltages in Figure 4.16. The black line profile in Figure 4.16 is the topograph and the coloured lines are dI/dV data. Each line profile is an average of 20 adjacent line profiles. The vertical dotted line shows the region of curvature on the 7 ML edge. This curved region appears prominent in 7 ML stripes as they are very narrow. We will refer to this region of curvature as the '7 ML edge' and the rest of the region in the 7 ML stripe as '7 ML interior'. In the line profiles the 7 ML interior shows slightly higher LDOS compared to the 7 ML edge at +400mV and a considerably high LDOS intensity compared to 5 ML at the same bias voltage. The LDOS intensity in

the 7 ML interior gradually decreases as the bias voltage approaches the Fermi level. It is comparable to 5 ML LDOS at ~+100mV and then decreases more to dip below the 5 ML LDOS at ~-200mV.

The 7 ML edge appears to evolve into two LDOS peaks (one at each 7 ML edge) which appears at ~+200mV and disappears at ~-200mV. This peak is very clearly observed in the region of curvature which we refer to as the '7 ML edge' and is responsible for the observation of the bright feature in the dI/dV maps at the edges of the 7 ML stripe. The LDOS peak at the 7 ML edge does not seem to exhibit additional modulations like a Friedel oscillation (section 4.1.2) or quantum confined state (section 4.1.2). It is therefore important to examine the dI/dV(V) curves from different regions to understand the origin of the LDOS peak on the 7 ML edge. Since a single CITS dataset contains thousands of curves, studying individual features can be time consuming. A LDOS intensity plot is a much simpler way of visualizing multiple curves in a single plot. The LDOS intensity plot is color coded with red and blue as high and low intensity extremes of the dI/dV(V) curves respectively. The y-axis in the LDOS plot shows the bias voltage and the x-axis corresponds to the position along the line profile in the STM topograph.

In Figure 4.17 we compare the line profile taken on the STM topograph of the 7 ML stripe (a) to its corresponding LDOS intensity plot in (b). The LDOS intensity plot shown in Figure 4.17 (b) is made by averaging 20 adjacent dI/dV(V) curves. The central blue color in the LDOS intensity plot in Figure 4.17 (b) shows the LDOS valley of the dI/dV(V) curves and it can be seen that the horizontal position of the blue region is different in 5 ML and 7 ML interior regions. A bright spot (high LDOS) is clearly visible in the LDOS intensity plot at ~V_t = +150mV at ~x = 4nm and x = 10.5nm (black circles in Figure 4.17(b)). When compared to the line profile in Figure 4.17 (a) it can be seen that the states at +150mV are localized on the 7 ML edge. Some faint additional states at ~V_t= -150mV at the 7 ML edge are seen as well. These states are responsible for the 'bright beach' on the 7 ML edge in the dI/dV maps and we will refer to them as bright beach states (BBS) in the following text.

To further investigate the 7ML bright beach three dI/dV(V) curves were extracted from the LDOS intensity plot for the 5 ML interior, 7 ML edge and 7 ML interior regions (see Figure 4.18). Each dI/dV(V) curve is an average of 20 individual dI/dV curves. In Figure 4.18 (a) the dI/dV(V) curve from the 5 ML interior (±1V) is compared to the 5 ML curve (±2V) from section 3.3.3 and it shows remarkable similarities. The LDOS valley in both the curves have the same shape and the LDOS peak at -0.5V is reproduced well in the 5 ML interior curve with two sub peaks. We established in section

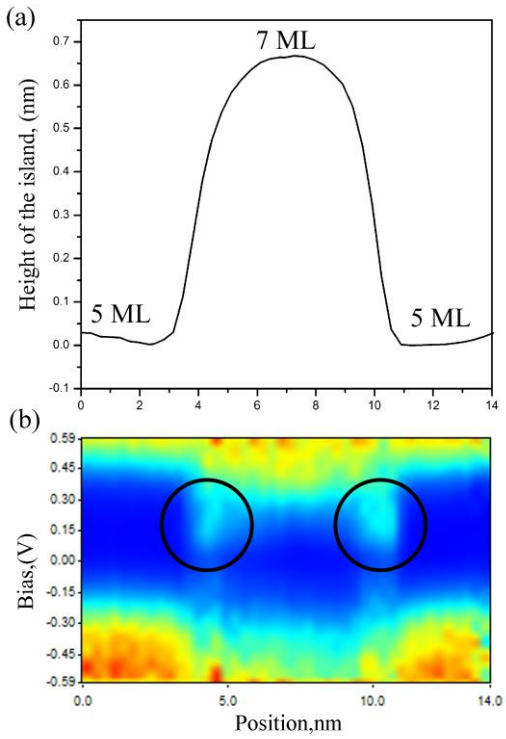

Figure 4.17: (a) A line profile on an STM topograph showing 7 ML stripe on a 5 ML island (b) an LDOS intensity plot showing corresponding states on the line profile. Two bright states are visible at ~ +150mV at x = 4nm and x = 10.5nm. These positions correspond to the 7 ML edge in the line profile shown in (a).

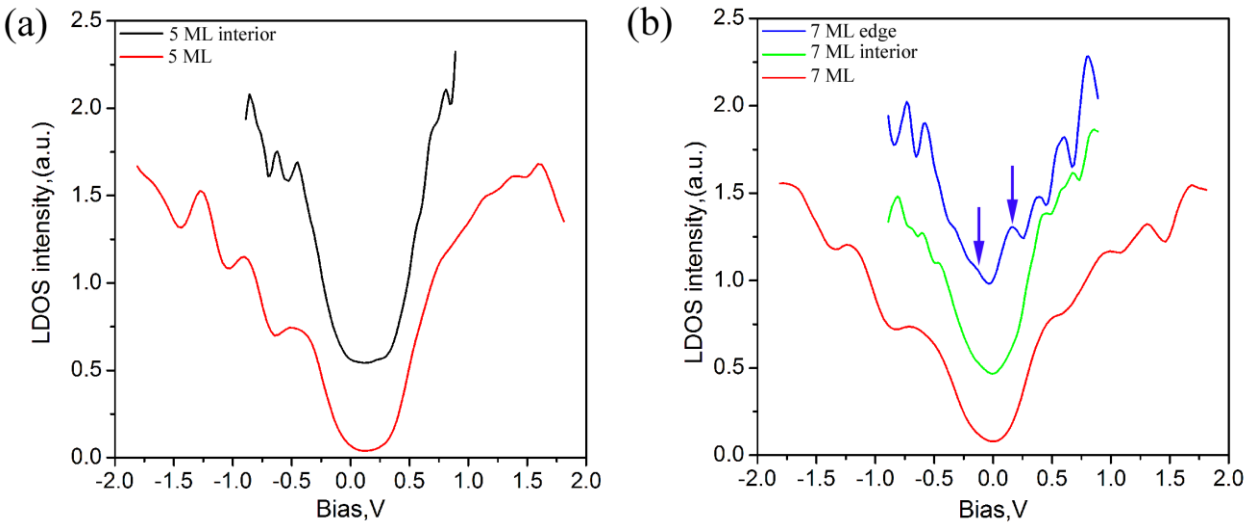

Figure 4.18: (a) dI/dV curves extracted from 5 ML interior (black) compared to data for the 5 ML interior from section 3.3.3 (b) dI/dV(V) curves from 7 ML edge (blue) and 7 ML interior (green) compared to 7 ML interior curve from section 3.3.3. The blue arrows show the BBS on 7 ML edge.

3.3.3 that the 5ML -0.5V LDOS peak is actually composed of two sub peaks and these sub peaks are resolved quite well in the 5 ML interior curve recorded at ±1V. The tip sample distance is reduced in the 5 ML interior curve as compared to the ±2V voltage range because the stabilization voltage is set at V_t = +1V. This reduced tip sample distance facilitates better resolution on the dI/dV(V) curves [94]. Similarly in Figure 4.18 (b) the 7 ML interior curve (±1V) is compared to a 7 ML curve (±2V) from

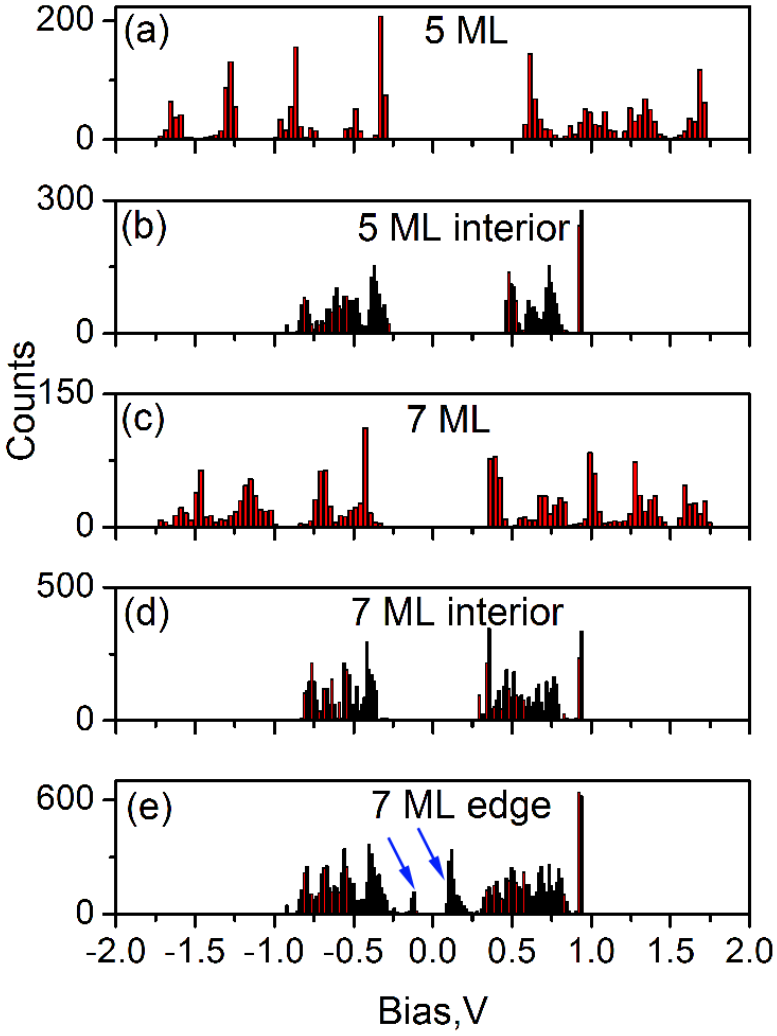

Figure 4.19: Spectral histograms on (a) 5 ML (from section 3.3.3.). (b) 5 ML interior (c) 7 ML (from section 3.3.3.) (d) 7 ML interior and (e) 7 ML edge. The blue arrows in (e) show the BBS on 7 ML edge.

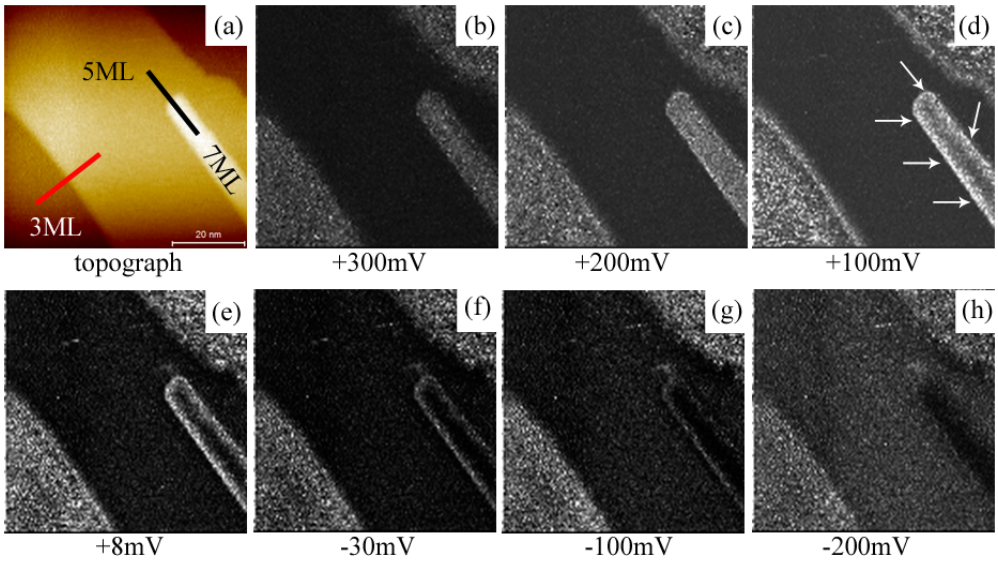

Figure 4.20: (a) STM image of a 5 ML thick island with a 7 ML stripe's top edge (V_t = +1V, I_t = 200pA). (b)- (h) dI/dV maps acquired via CITS on (a). White arrows in (d) show prominent bright feature on the perimeter of the 7 ML stripe. The CITS dI/dV maps are color coded e.g. brighter areas correspond to high LDOS and vice versa.

section 3.3.3. The LDOS valley once again shows very good resemblance and the broad peaks at -0.5V and +0.5V in the 7 ML (±2V) curve are resolved into sub peaks in the 7 ML interior curve (see Figure 3.13 (b)). The 7 ML edge dI/dV curve (blue) also resembles the LDOS valley of the 7 ML interior curve except it shows a very distinct LDOS peak at ~+150mV and a faint shoulder at ~-150mV (see blue arrows). This LDOS peak is seen as the bright spot in the LDOS intensity map at ~+150mV in Figure 4.17 (b) and corresponds to the BBS. The bright beach on the 7 ML edge is seen very clearly in the dI/dV maps in a bias range of ~+200mV to -100mV because the 7 ML and 5 ML interior dI/dV curves are featureless in this bias voltage range and the only striking feature are the 7 ML BBS. Notice that it is the interplay between the intensities of the dI/dV(V) curves of 5 and 7 ML islands that leads to the evolution in contrast in the dI/dV maps shown in Figure 4.15.

The presence of the 7 ML BBS was also verified statistically by preparing spectral histograms on 5 ML interior, 7 ML interior and 7 ML edge regions (see Figure 4.19). Since the data on 7 ML BBS was recorded in the ±1V range the histograms show LDOS peaks only in the ±1V bias voltage range. In Figure 4.19 the 5 ML interior (a) and 7 ML interior (d) histograms are compared to the ±2V range 5 ML (a) and 7 ML (c) histograms from section 3.3.3 respectively. Like the dI/dV(V) curves the LDOS peaks in the ±2V histograms are reproduced well in the 5 ML and 7 ML interior histograms with better resolution. For example In Figure 4.19 (a) the peak at ~+0.6V is seen to resolve into additional sub peaks in (b). One of the key observations from the histograms shown in Figure 4.19 is that the region around Fermi level is featureless in the 7 ML interior and the 5 ML interior. The 7 ML edge histogram appears very similar to the 7 ML interior histogram. Two peaks corresponding to 7 ML BBS appear at V_t ~ +150mV and V_t ~ -150mV in the 7 ML edge histogram. These histograms support the fact that the BBS are located only on the 7 ML edge along the stripe's length.

Having established that these BBS are associated with the 7 ML edge across its entire length (see Figure 4.15), it is important to know if these states are formed on the whole perimeter of the 7 ML stripe e.g. the top end of the stripe (the $(\bar{1}10)$ plane).

4.2.2 The $(\bar{1}10)$ edge of the 7 ML stripe

In Figure 4.20 (a) we show an STM topograph of a sample area in which the end of a 7 ML stripe is visible. In Figure 4.20(b)-(h) CITS dI/dV maps of the same region are shown in which the arrows in Figure 4.20 (d) show the presence of the bright feature on the whole 7 ML stripe. The bright feature is seen clearly at the end of the 7 ML stripe as well, in the bias voltage range of ~+200mV to -100mV. Apart from the bright feature on 7 ML it is also noticeable in Figure 4.20 (d) that bright features are

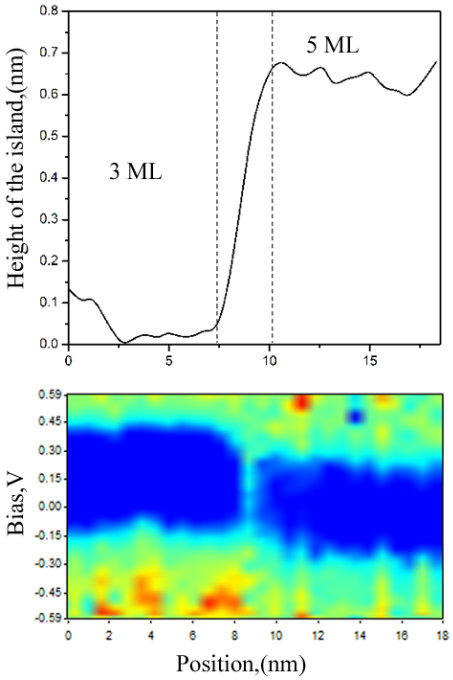

Figure 4.21: (a) A line profile corresponding to the black arrowed line in Figure 4.20. The profile is in the $< \bar{1}10 >$ direction of the 7 ML top edge (b) corresponding LDOS intensity plot.

formed on the 5 ML edge as well which will be discussed in the next section. Since the area on the top end of the stripe is very small, preparing a spectral histogram is not possible. However, a LDOS intensity plot can be made. A line profile corresponding to the black line in the STM topograph in Figure 4.20 (a) is shown in Figure 4.21 (a). Its corresponding LDOS intensity plot is shown in Figure 4.21 (b). The LDOS intensity plot is formed by averaging 3 lines on the top end of the 7 ML stripe. It can be seen that BBS are also present at the top end of the stripe (at x = 8.2nm) at ~+150mV. The BB states extend over the whole width of the rounded edge i.e. between the vertical dotted lines.

It should be noted that the width of the BB states in the LDOS intensity plots are affected by the choice of threshold of the color palette. The color palette in the current example is adjusted in a way such that the maximum of the BB states can be seen sharply i.e. at ~+150mV. The central bluish region that corresponds to the LDOS valley from the dI/dV curves of 5 and 7 ML interior is in perfect agreement with Figure 4.17 (b) i.e. the horizontal position of bluish region of the 5 ML interior extends between ~±0.3V. The presence of these BBS across the whole perimeter of the 7 ML stripe is important as it suggests that the formation of these BBS are independent of the crystallographic plane that forms the edge or the end of the stripe.

4.2.3 Edge reconstruction on the 7 ML edge

In Figure 4.22 we show an STM topograph of the edge of a 7 ML stripe. The image was taken at V_t = -0.85V at room temperature and has been filtered by Fourier transformation (see Appendix 3) to show individual atoms more clearly. A typical bulk Bi(110) surface unit cell is shown in the inset with dimensions of 4.75 Å x 4.54 Å [30] where the blue atoms are present on the sides of the unit cell and the red atom is in the middle. Both blue and red coloured atoms are bismuth atoms but the red coloured atoms are slightly depressed than the blue atoms (refer section 1.3 for unit cell description). The zig zag chains that form in the $< \bar{1}10 >$ direction can be seen clearly. A schematic diagram of the unit cell has been superimposed on the chain of atoms in the STM image of the 7 ML edge to visualize the structure. A careful inspection of the STM image reveals that the red atoms on the edge are slightly brighter than the red atoms in the interior of the island. This phenomenon can be observed more clearly in line profiles which were drawn on rows of atoms (rows 1 to 6 in Figure 4.22).

In Figure 4.23 we show latitudinal line profiles on rows 1, 3 and 5 (blue atoms) and row 2, 4 and 6 (red atoms). In the line profiles drawn on row 1, 3 and 5 the first 'blue atom' at the edge is seen slightly lower than rest of the atoms (see blue arrow in Figure 4.23 (a)). In contrast, the first 'red atom' in row 2, 4 and 6 is much taller than other red atoms in the interior (see Figure 4.23 (b)). These observations suggest a distorted unit cell at the edge in which-

(i) the position of the first 'red atom' at the edge is slightly higher than that of other red atoms in the interior of the stripe and

(ii) the position of the first 'blue atom' on the edge is slightly lower than that of other blue atoms in the interior of the 7ML stripe.

This indicates that the edge of the 7 ML bismuth stripe has undergone some form of reconstruction. Edge reconstruction in thin bismuth films, chiefly in stripes or narrow nano-ribbons is common and more details can be found in section 4.1.1 and 4.1.6.

We were able to obtain atomic resolution on bismuth island edges extremely rarely because the islands are soft and the STM tip interacts strongly. The result shown in Figure 4.22 is special because while scanning the tip picked an atom and became very sharp and we happened to be able to obtain atomic resolution at V_t = -0.850V.

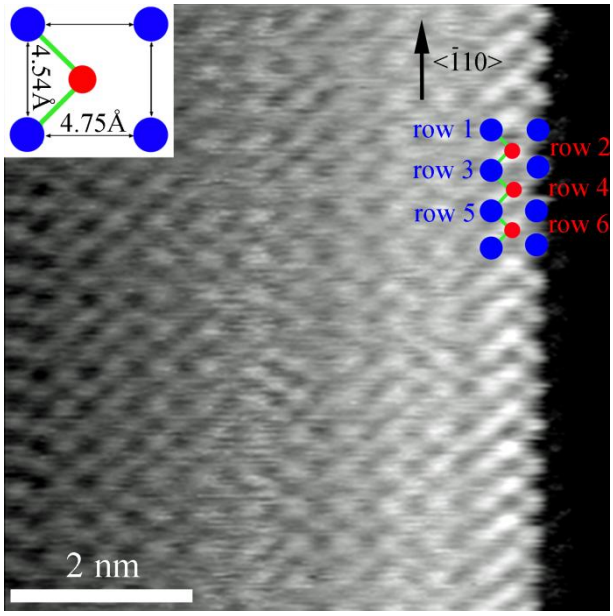

Figure 4.22: Atomically resolved image of a step edge on 7 ML stripe (V_t = -0.85V, I_t = 900pA). The inset shows the bulk Bi(110) surface unit cell. The unit cell is superimposed on the STM image to correlate atomic positions.

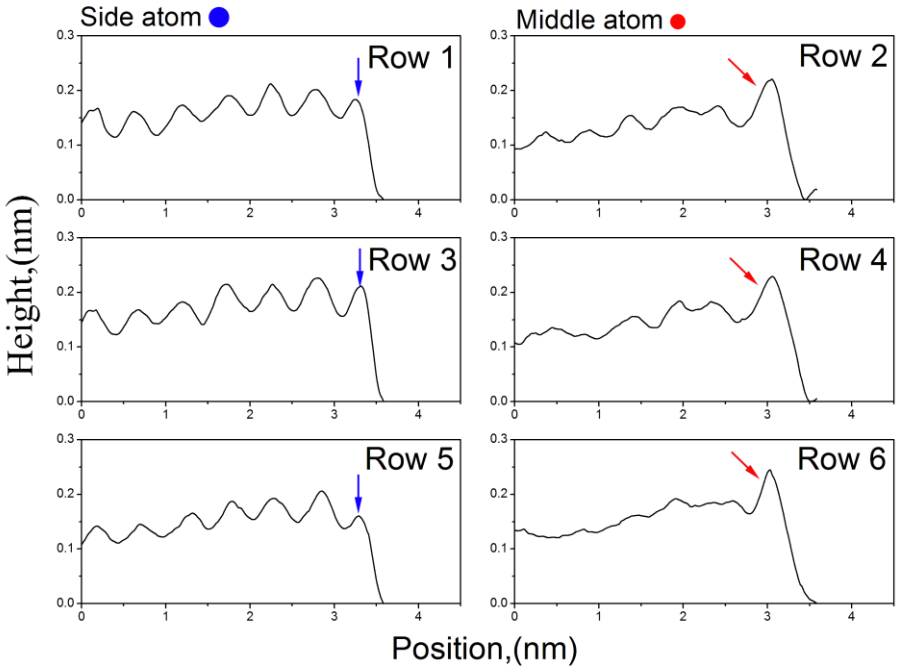

Figure 4.23: STM line profiles of rows of atoms on 7 ML edge. Rows 1, 3 and 5 are line profiles drawn on the side atoms of the unit cell. The first atom at the edge in these rows appears to be slightly lower than the rest (shown by blue arrows). Rows 2, 4 and 6 are line profiles drawn on the middle atom in the unit cell. The first atom at x = 3nm in those line profiles appears to be taller than the other middle atoms (shown by red arrows).

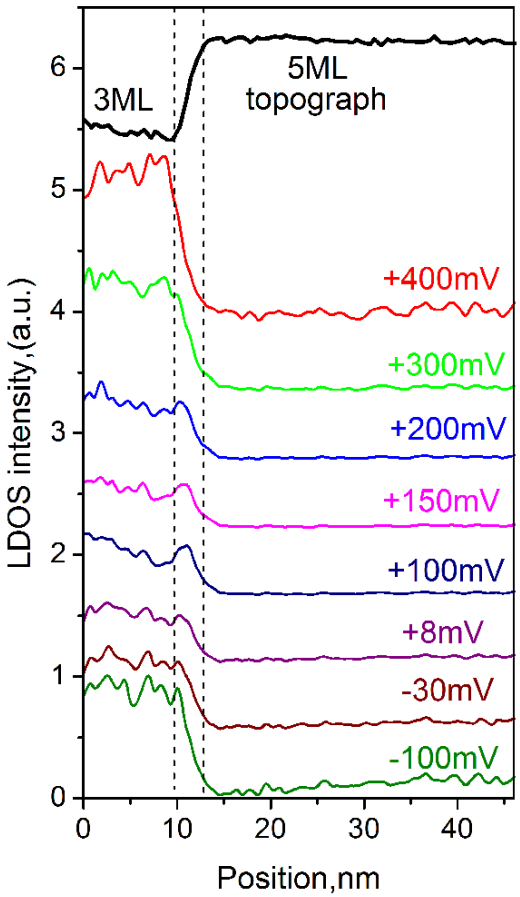

Figure 4.24: Line profiles corresponding to the red line in Figure 4.20 (a). The black line is drawn on the STM topograph and the colored lines are corresponding dI/dV line profiles.

4.2.4 CITS on the 5 ML edge

4.2.4.1 5 ML-3 ML boundary

In the previous section in Figure 4.20 (a) we showed an STM topograph of a 5 ML island which is formed on top of a 3 ML base. In Figure 4.20 (d) a bright beach is also visible on the 5 ML edge. This bright feature appears around ~+200mV and disappears at ~+8mV (at positive bias voltage as compared to negative in the 7 ML stripe). Line profiles were drawn on the 5 ML stripe as shown by the red line in Figure 4.20 (a) and are shown in Figure 4.24. The topmost black line is the STM topograph and the colored lines are corresponding dI/dV line profiles. CITS was performed at ±1V range but only selected bias voltages are shown in dI/dV maps and line profiles to highlight important features. There is a significant difference in LDOS intensity between the 5 ML and 3 ML interiors at +400mV (reflecting the band structure in section 3.4). This difference is smaller in the voltage range +200mV and -30mV and increases again at higher negative bias voltages. A BBS peak is seen at the edge in the voltage range ~+200mV to +8mV which accounts for the bright feature on the 5 ML edge in the dI/dV maps. Similar to the BBS peak in the 7 ML edges shown in section 4.2.1, the BBS peak in 5 ML island is also located on the region of curvature.

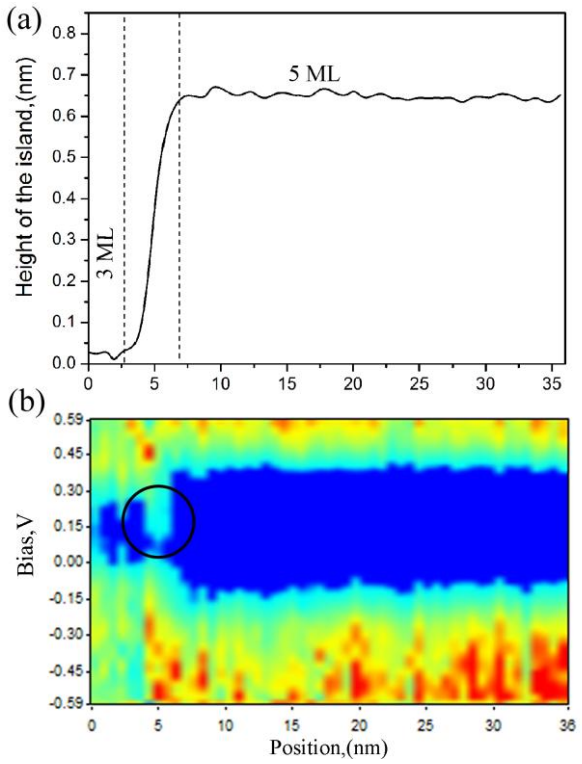

Figure 4.25: (a) A line profile corresponding to the red line in Figure 4.20. (b) Corresponding LDOS intensity plot.

An LDOS intensity plot corresponding to the line profiles on 5 ML edge in Figure 4.25 (a) is shown in Figure 4.25 (b). In a very similar fashion to the 7 ML edge the 5 ML edge also reveals additional BBS around ~+150mV. The LDOS intensity plot is compared to the line profile drawn on STM topograph of the 5 ML edge and it is clearly evident that the BBS are formed exactly on the 5

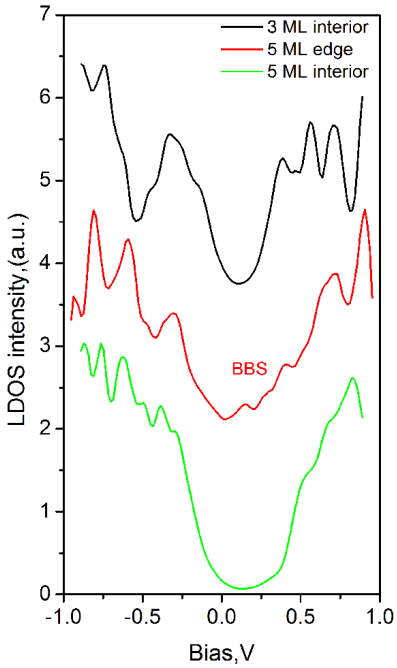

Figure 4.26: dI/dV curves extracted from 3 ML interior (black), 5 ML edge (red) and 5 ML interior (green).

ML edge. dI/dV(V) curves were extracted for comparison from the LDOS intensity plot and are shown in Figure 4.26.

The comparison between the dI/dV(V) curves is not as neat as for the 7 ML stripe because the LDOS minimum of the 3 ML base is very narrow. The BBS in the 5 ML are seen very prominently around ~+150mV. At ~+150mV the valley in the LDOS minimum of the 5 and 3 ML interior show no features and consequently the bright beaches are the brightest feature in the dI/dV maps. The 5 ML edge curve is similar to the 5 ML interior curve, but the similarities between the 5 ML edge curve and 3 ML interior curve cannot be ignored i.e. the LDOS peaks in the 5 ML edge curve at -290mV, +385mV, +720mV match rather perfectly with the LDOS peaks in 3 ML interior curve. This indicates that the 5 ML edge curve could have contributions from both the 3 and 5 ML regions. We speculate that since the STM tip is large compared to the size of the bismuth islands, the sampling area (under the STM tip) at the edge could have contributions from states from neighboring thicknesses.

4.2.4.2 5 ML-HOPG boundary

5 ML islands are sometime formed on HOPG directly as shown in the STM topograph of Figure 4.27 (a). The image area also shows a 3 ML base adjacent to the 5 ML island. This region is quite interesting as the 5 ML island has a tapered portion (top right hand corner of Figure 4.27 (a)) and also a 7 ML stripe on top of it. Figure 4.27 (b)-(h) show dI/dV maps which were acquired via CITS (±0.8V range, 50K). The bright beach is seen very clearly on the edge of the 5 ML base at energies close to the Fermi level. A bright beach is also formed on the tapering portion of the 5 ML island (see arrows in Figure 4.27 (d)). The width of the bright feature is fairly uniform for the whole perimeter of the 5 ML island. The 7 ML stripe also shows a very prominent bright feature as expected from section 4.2.1. Interestingly, a bright feature is also present on the adjoining 3 ML base (see red arrow in Figure 4.27 (d)) and this will be dealt with in section 4.2.6. The 5 ML bright beach appears in the voltage range ~+300mV to -100mV. Defects are also shown by white arrow in the dI/dV maps in Figure 4.27 (e). The defects are not very clearly visible in the STM topograph but they are clearly seen in dI/dV maps with a bright beach around them and more interestingly their appearance and disappearance in the dI/dV maps coincides with the bright features on the 5 ML edge (see section 4.2.5).

LDOS intensity plots were drawn on the edge and the tapering portion of the 5 ML island and are shown in Figure 4.28 (a) and (b) respectively. The left hand side of the figure is a dI/dV map (V_t = +100mV) and the right hand side shows the corresponding LDOS intensity plot. The red line profiles

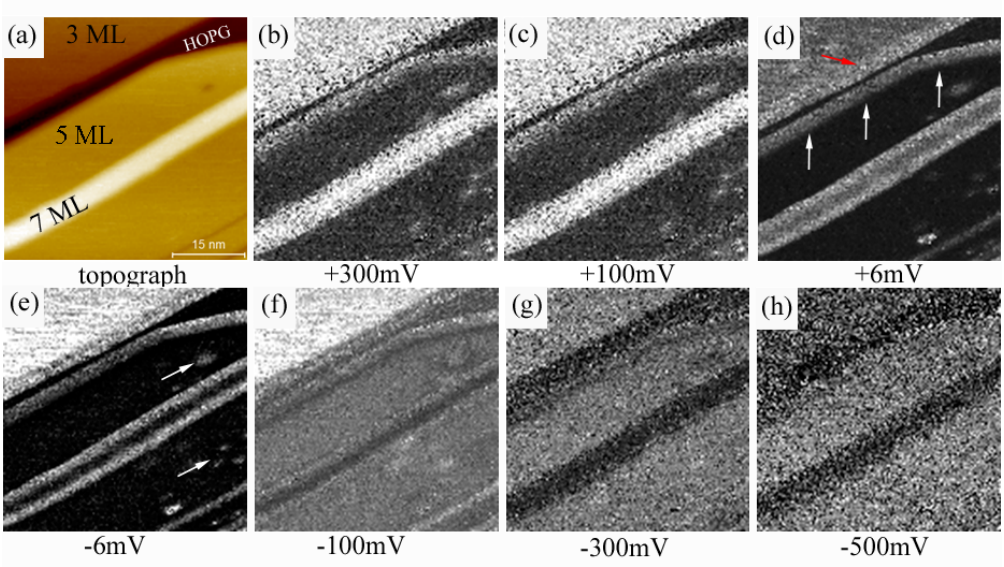

Figure 4.27: (a) STM image of a 5 ML thick island formed on HOPG with a 7 ML stripe on top (V_t = -0.8V, I_t = 100pA). A 3 ML base is also present next to the 5 ML island (b)-(h) dI/dV maps acquired via CITS on (a). (d) White arrows show prominent bright feature on the perimeter of the 5 ML stripe. A red arrow shows bright feature on the 3 ML edge. The CITS dI/dV maps are color coded e.g. brighter areas correspond to high LDOS and vice versa.

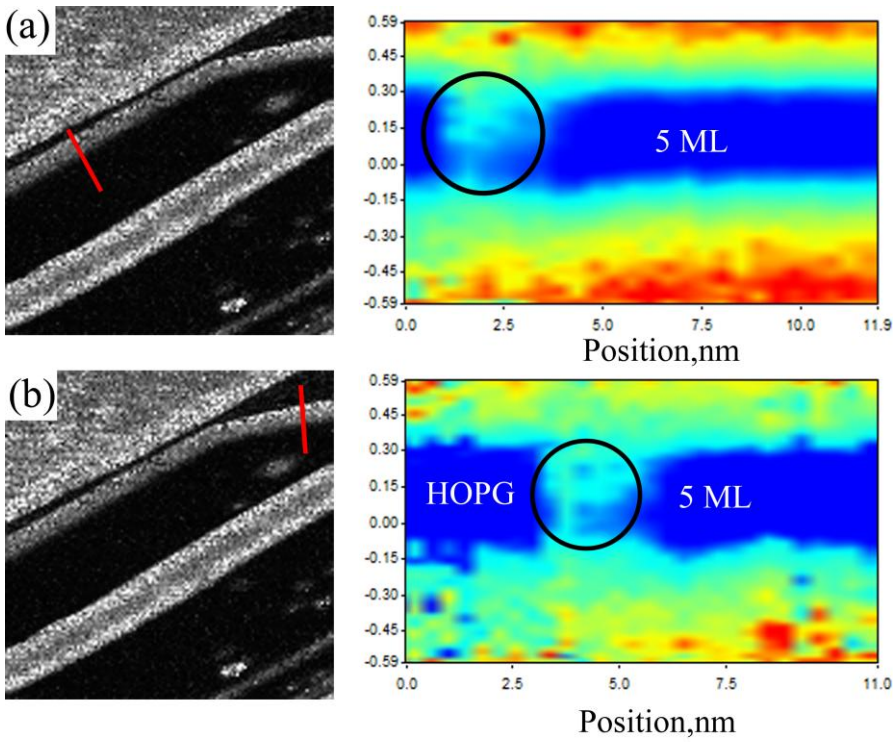

Figure 4.28: (a) and (b) are dI/dV maps taken at +150mV showing a region containing 3, 5 and 7 ML islands. The red lines show the position at which the corresponding LDOS plots were acquired.

in the dI/dV map show the position at which the LDOS intensity map was acquired. The LDOS intensity plots were prepared by averaging 20 and 9 adjacent lines for the edge and tapering portion respectively. It can be seen from the LDOS intensity maps in Figure 4.28 that the BBS on the 5 ML edge and the tapering portion of the 5 ML island are formed around ~+150mV. The presence of bright beaches on the tapered portion is important as it indicates that the formation of the bright beach is independent of the crystallographic plane at the edge and it could be related with the termination of chain of bismuth atoms at the edges. The width of the BB is also uniform for the whole perimeter of the island and it does not change over the tapered portion. Another interesting feature in the image is the presence of a narrow bright beach on the lower right hand corner of the image. This narrow BB is formed on a thin 5 ML stripe. The presence of two different widths of BB on a 5 ML island indicates that there could be an effect of the boundary at which the BB is formed or the width of the stripe on which it is formed. We discuss the widths of the BB in detail in section 4.2.9.

4.2.5 Defects on 5 ML island

One of the striking features of the 5 ML island shown in Figure 4.27 is the presence of defects on the surface. These defects are visible very clearly in the dI/dV maps and their appearance and disappearance follow roughly the same pattern as that of the 5 ML bright beach. An STM topograph showing the defect in more detail is shown in Figure 4.29. The black square in Figure 4.29 (a) shows the area which was zoomed in to see the defect clearly in Figure 4.29 (b). Such defects are not unusual in STM images on the surface of bismuth islands and appear to be holes. We extracted an individual dI/dV(V) curve associated with the defect and it is shown in Figure 4.29 (c) along with a 5 ML interior curve (red). The black curve is the dI/dV curve associated with the defect and it shows a tiny LDOS peak with a maxima around ~+115mV. The defect curve exhibits higher LDOS than that of the interior curve (that gives the bright appearance to the defects in dI/dV maps) in the bias voltage range of ~+300mV to -80mV (which is very similar to the 5 ML bright beach occurrence). Such defects and their associated states are often seen on 5 ML islands and 3 ML bases. Defects are very rarely observed on 7 ML stripes. The BBS observed on the defects differ slightly in energy from the BBS observed on the edges of the islands and stripes i.e. they form a dI/dV(V) maximum ~+115 mV and the BBS on the edges are formed at ~+150mV. The presence of BB on defects supports the suggestion that the BBS are formed on all edges where atoms have a reduced coordination number.

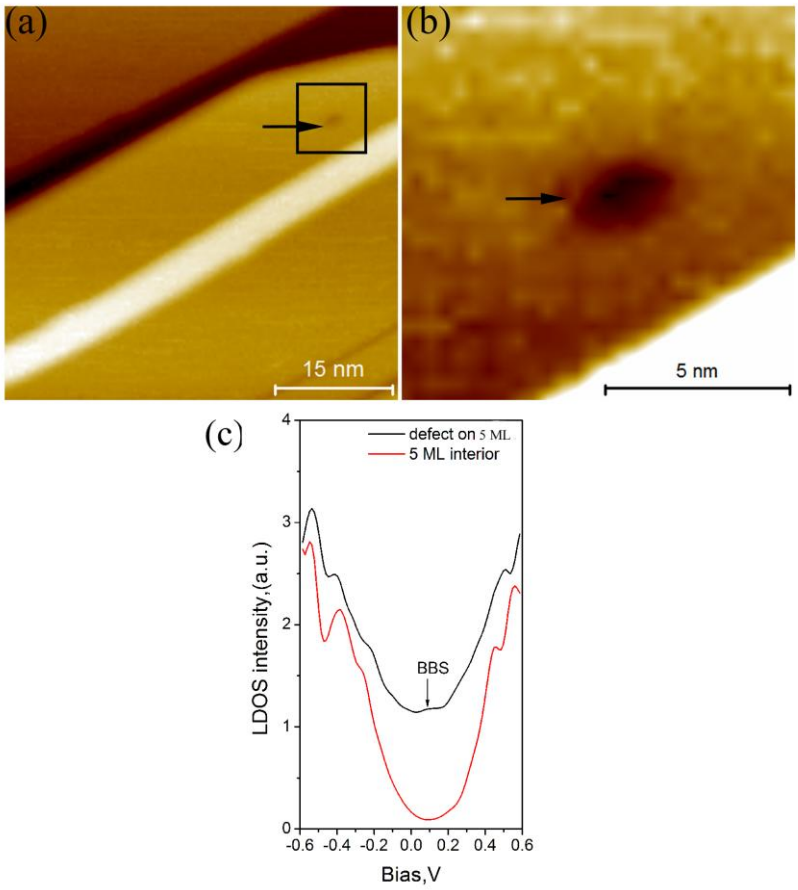

Figure 4.29: (a) STM topograph of a region containing 3, 5 and 7 ML islands (V_t = -0.8V, I_t = 100pA). The area in black square in (a) was magnified to shows a defect in (b). (c) dI/dV curves extracted from the defect in 5 ML (black) and 5 ML interior (red) are shown

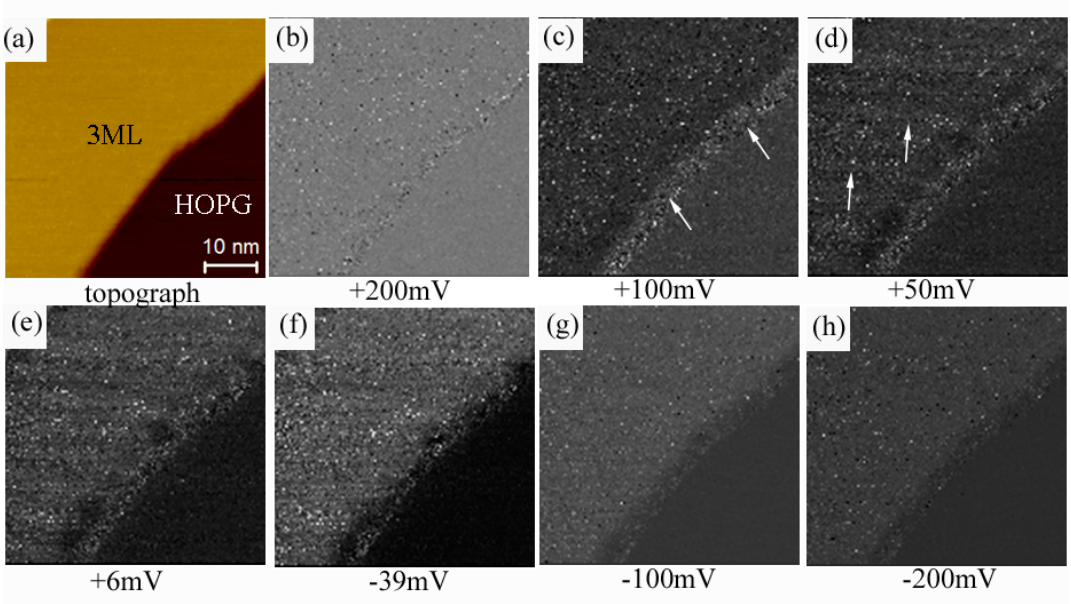

Figure 4.30: (a) STM image of a 3 ML thick island formed on HOPG (V_t = +0.5V, I_t = 300pA). The black line indicates a line profile. (b)- (h) dI/dV maps acquired via CITS on (a). (c) White arrows show prominent bright feature on the edge of the 3 ML island. (d) Arrows indicate Moiré pattern which is formed on the 3 ML island.

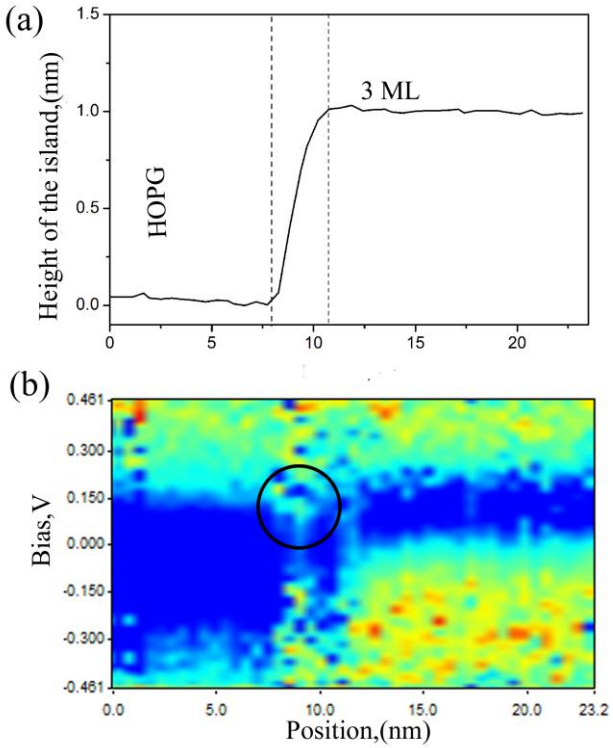

Figure 4.31: (a) A line profile corresponding to the black line in Figure 4.30 (a).The line profile shows an edge of a 3 ML base. (b) LDOS intensity plot showing the BBS associated with the 3 ML edge (black circle).

4.2.6 CITS on 3 ML edge

In Figure 4.27 we showed that bright beaches are also formed at the edges of a 3 ML base. It is usually difficult to perform CITS or to find a bright feature on the 3 ML islands. Defects are also found more frequently on the 3 ML surface. However in a few experiments we were successful in obtaining CITS data on a 3 ML base and we show the STM topograph of that region in Figure 4.30 (a). Corresponding dI/dV maps are shown in Figure 4.30 (b)-(h). The bright feature is very weak but is formed on the 3 ML in the range of ~+150 mV to +6 mV. The BB are very clearly observed at ~+100 mV (see arrows in Figure 4.30 (c)). A Moiré pattern (see section 5.7) on the 3 ML island is shown by white arrows in Figure 4.30 (d). The bright features turn into slightly darker edge at higher negative bias voltages. In Figure 4.31 (a) a line profile is drawn on the 3 ML base and we show its corresponding LDOS intensity plot in Figure 4.31 (b). Faint BBS states are seen at the 3 ML edge at x = 9nm at V_t = +150mV.

The BBS is seen most prominently on 7 ML followed by 5 ML. The BBS on 3 ML edge appears slightly faint. This is because of the fact that the LDOS valley of 3 ML is narrow as compared to 5 and

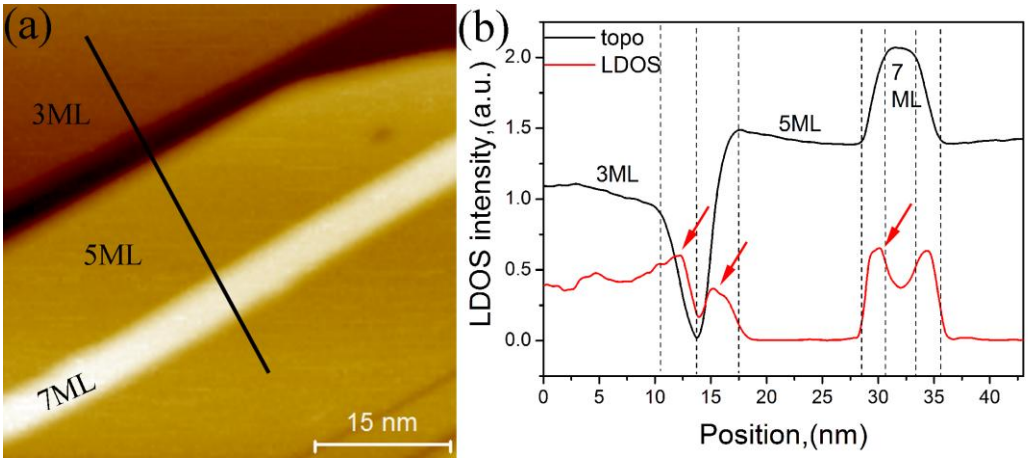

Figure 4.32: (a) STM topograph of a region showing 3, 5 and 7 ML thick islands (V_t = -0.8V, I_t = 100pA). (b) Line profiles corresponding to the black line in (a) drawn on STM topograph and dI/dV map (LDOS). The vertical dotted lines show the region of curvature of individual islands

7 ML and the LDOS valley of HOPG is not very featureless at energies around ~+150mV. Thus the BBS are not seen as clearly as they are in 5 and 7 ML islands and stripes.

4.2.7 Relative LDOS intensity of the BBS

So far we have examined the bright feature associated with the 3, 5 and 7 ML edges and have identified a LDOS peak (BBS) in the dI/dV(V) curve with it. Now we compare the individual LDOS intensities of the BBS found on 3, 5 and 7 ML thick islands. This kind of analysis is tricky because the LDOS intensity is influenced by tip conditions, set point voltage and tunneling current [94] hence straightforward one to one comparison between different CITS datasets in not possible. However if 3, 5 and 7 ML thick islands are present in a single CITS dataset then a one to one comparison of the LDOS intensity at the edge is possible. In Figure 4.32 (a) we show an STM topograph of a region which contains 3, 5 and 7 ML thick islands on which CITS was performed in ±0.8V range at 50 K. The line profile corresponding to the line profile in Figure 4.32 (a) is shown in (b) as the black line. The same line profile was also drawn on its CITS dI/dV map acquired at +150 mV and is shown as the red line. The red line shows the LDOS intensity across the line profile and individual bright features are visible as peaks on the edges of the islands. It can be clearly seen that the LDOS intensity of the 7 ML bright beach is highest followed by 3 ML and 5 ML at +150 mV.

4.2.8 BB in STM topographs

In Figure 4.33 we show a montage of low bias voltage STM topographs on a region containing 3 and 5 ML islands. The images are arranged in the sequence in which they were scanned i.e. (a) was scanned first followed by (b) and so on. Each image has a white arrow on the top right hand corner

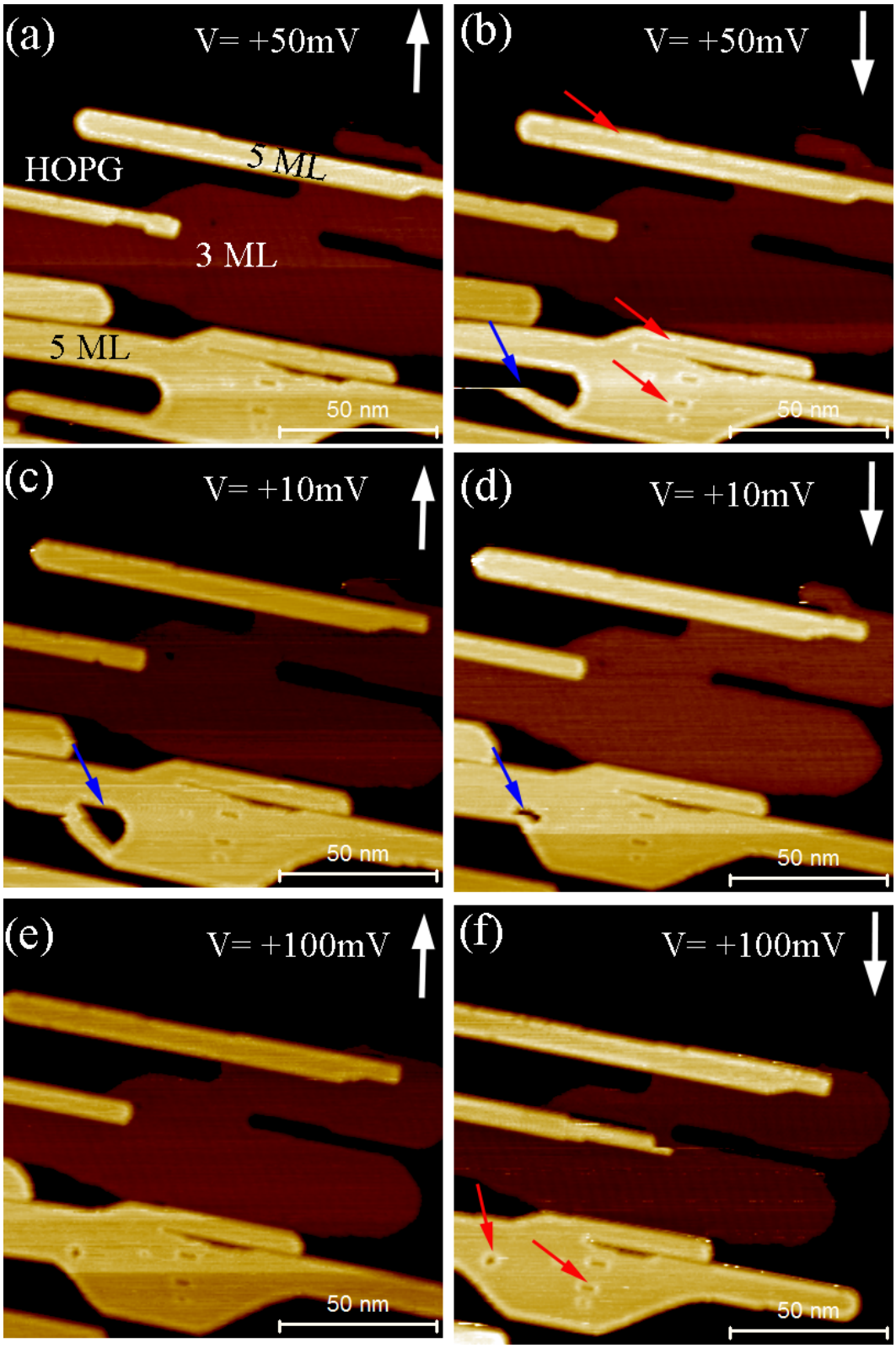

Figure 4.33: (a)-(f) STM topographs showing 3 and 5 ML islands acquired at various bias voltages near Fermi level. Bright beach are seen in 5 ML island and stripes. The white arrow in top right hand corner of the image indicates the scan direction. The red arrows in the images show edge states on 5 ML edges and defects. The blue arrows show tip induced modification of a 5 ML stripe. (I_t = 200pA)

which shows the scan direction e.g. if the image shows an up (down) arrow it means that the image was acquired in 'scan up' ('scan down') mode. In Figure 4.33 (a) and (b) we show scan up and scan down STM topographs acquired at V_t = +50mV. The bright features are visible quite clearly on the 5 ML edges and on defects on the surface as well (see red arrows in Figure 4.33 (b)). The blue arrow in Figure 4.33 (b) shows a 5 ML stripe which interacts with the STM tip during scan down. In Figure 4.33 (c) we see that the 5 ML stripe that interacted with the STM tip previously has merged into the main 5 ML island. While acquiring this image the V_t was changed to +10mV. During scan down in Figure 4.33 (d) it can be seen that the 5 ML stripe has merged almost completely with the main 5 ML island. It is, however, very interesting to note that in this island modification process the bright feature is still seen on the edge of the 5 ML stripe (show by blue arrow) and also formed around the hole/defect that it forms after it merges with the main island. The merging process is complete in Figure 4.33 (e) and (f). At V_t = +50mV the bright features are observed more clearly on the edges and the defects on the 5 ML stripe. No bright feature is seen on the 3 ML edge in this montage. A Moiré pattern however is observed in the 3 ML island's interior in those low bias voltages (seen faintly in Figure 4.33 (d)).

4.2.9 Width of the Bright beach

It was noticed in all the BB images shown in the previous sections that the width of the BB on the perimeter of the islands and stripes is ~2-4 nm. This gives rise to the question whether the widths of individual thicknesses i.e. 3, 5 and 7 ML are similar? The estimation of the widths of the BB could give us vital clues about the origin of the BBS. For the same we measured the HWHM (half width at half maximum) of the BB peak and doubled it to yield the FWHM (full width at half maximum).

The HWHM was measured from the line profiles at +150mV because the BB is seen very sharply and attains maximum height in the LDOS profiles at this energy. In Figure 4.34 (a) we show an example of HWHM measurement on the BB of a 5 ML island. The vertical dotted lines show the rounded edge in topography and the vertical red lines show the HWHM of the BB peak. The FWHM thus obtained gives us an approximation of the width of the BB peak.

To see the effect of different types of edges and the effect of the widths of the islands on the widths of these BB we plotted the FWHM values as a function of island and stripe width in Figure 4.34 (c). The BB is formed on 4 kinds of boundaries e.g. 3 ML-HOPG, 5 ML-3 ML, 5 ML-HOPG and 7 ML-5 ML where 3 ML-HOPG indicates a 3 ML island formed on HOPG, 5ML-3ML indicates a 5 ML

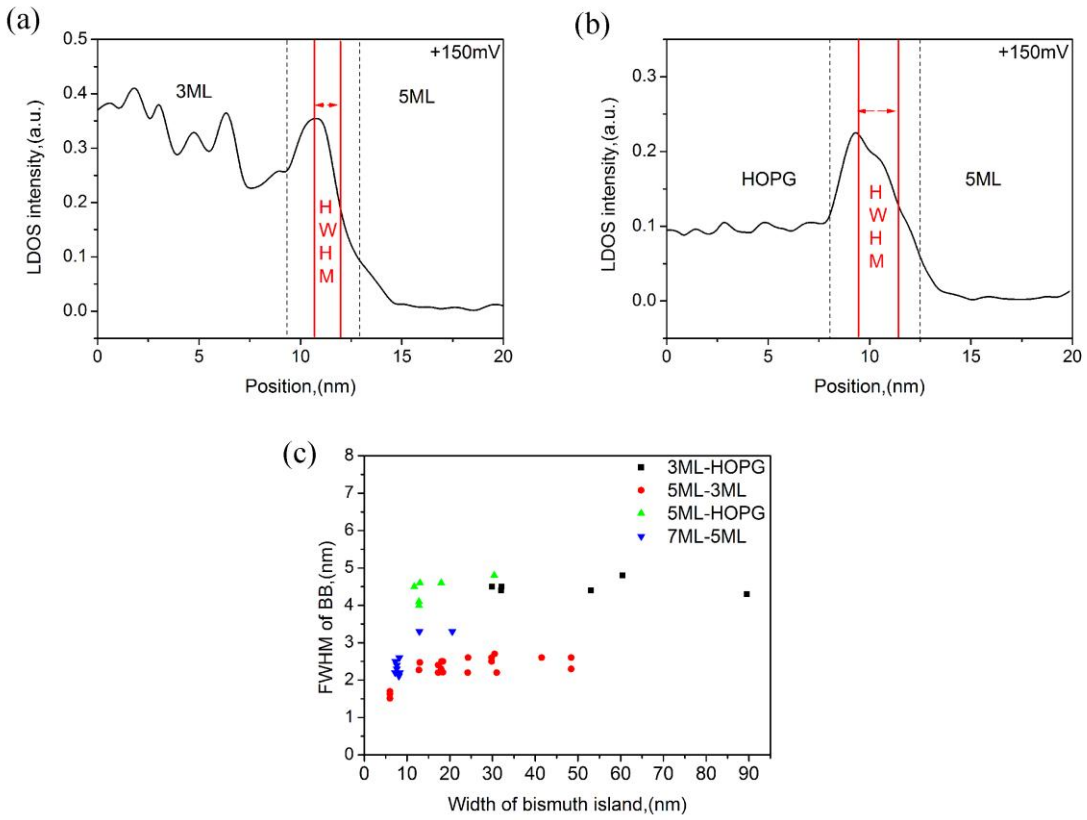

Figure 4.34: (a) dI/dV line profile at V_t = +150mV on a 5 ML-3 ML boundary (b) dI/dV line profile at V_t = +150mV on a 5 ML-HOPG boundary. The vertical dotted line indicates the region of curvature of the 5 ML edge. The vertical red lines show the HWHM of the BB peak. (c) Plot of FWHM of the BB vs. the width of the island. The FWHM values obtained at various boundaries are given distinguishing symbols.

island on top of 3 ML island and so on. The plot shows that the width of the BB in 5 ML-3 ML and 7 ML-3ML are mostly ~2.5 nm wide with few exceptions. The BB in <10 nm wide 5 ML islands is slightly narrower (~1.5 nm). The BB peak in 3 ML-HOPG and 5 ML-HOPG boundary are ~4-5 nm wide. A comparison of BB on 5 ML-3 ML edge and 5 ML-HOPG edge is shown in Figure 4.34 (a) and (b). It can be seen clearly that the HWHM of the 5 ML-HOPG peak is slightly wider than that of the 5 ML-3 ML edge. Such an observation could indicate that the BB is affected by the boundary at which it is formed.

In Figure 4.27 (d) the width of the BB formed on a thin 5 ML stripe on the lower right hand corner of the image is significantly different than the BB formed on the 5ML-HOPG boundary which is an argument in favour of boundary condition affecting the width of the BB. However the precise dependence of the BB width on the boundary conditions is still inconclusive and further calculations are necessary to understand its effect.

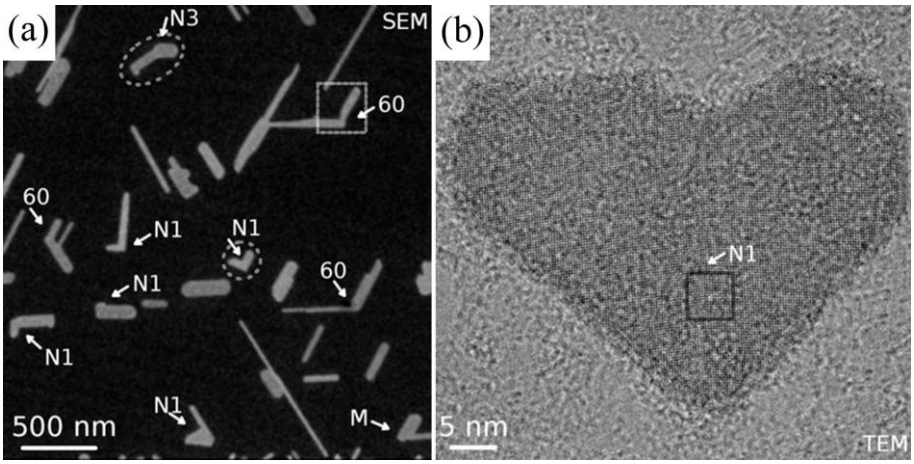

Figure 4.35: (a) SEM image showing different types of Bi junctions. The islands indicated using circle, oval and M show grain boundaries. N1, N3 correspond to 90^0 and 150^0 grain boundaries respectively. (b) TEM image showing a 90^0 grain boundary. Image reproduced from [166].

4.2.10 BB on Grain Boundaries (GB)

The GBs in Bi(110)/HOPG thin films were studied via STM (Dr Pawel Kowalczyk, Ojas Mahapatra) and high resolution TEM (HRTEM)(Dr Domagoj Belic) [166]. Dr Pawel Kowalczyk developed a model of tilt [110] grain boundary in bismuth (for details see [166]). In Figure 4.35 (a) we show an SEM image of 3 ML thick elongated rods grown near HOPG step edges [14]. A large number of such bent structures composed of at least two different grains can be seen in Figure 4.35 (a). The most common angle between the grains is ~90^0 (labelled N1). Another frequently observed angle is ~150^0 (labelled N3). The presence of such angles cannot be explained by the interaction of the grains with the substrate – if that was the case then one would expect angles which are multiples of 60^0, due to substrate symmetry [16] (such angles can be sometimes found - see the structure denoted 60 in (a)). In SEM the GBs cannot be studied because of limited resolution therefore we decided to use HR-TEM. One example of an HRTEM investigated island is shown in Figure 4.35 (b). It is characterized by a dihedral angle of ~93^0 and has a heart shape (another very similar island is indicated by a circle in Figure 4.35 (a)). The GB is located between the notch and the tip of the heart. For more details on dihedral angle and HR-TEM results refer [166]. We performed preliminary STS experiments on the GB which are discussed in the following section.

4.2.10.1 GB on 5 ML

In Figure 4.36 (a) we show an STM topograph of an island with two 5ML grains aligned at ~150^0 to each other. In Figure 4.36 (b)-(h) we show CITS dI/dV maps acquired at 50 K in ±1V bias voltage range. Only selected voltages are shown to highlight important features. The BBs are seen near 3 and 5 ML island edges. A BB is also formed on the grain boundary (see arrow in Figure 4.36 (d)). The

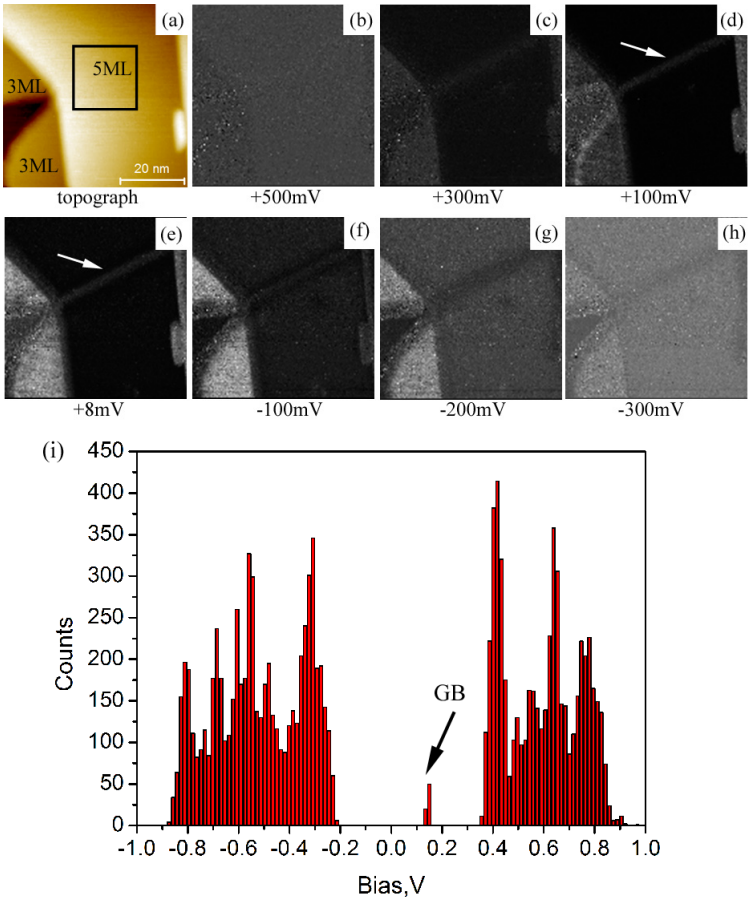

Figure 4.36: (a) STM topograph of a region showing a N3 GB on 5 ML island (V_t = +1V, I_t = 300pA). (b)- (h) dI/dV maps obtained via CITS on (a). The white arrow in (d) and (e) show the BB on the GB on 5 ML island. (c) Spectral histogram recorded on the black square shown on 5 ML island in (a). Black arrow shows the LDOS peak associated with GB at ~ V_t = +150mV.

BB on the GB is first observed at ~+300mV and disappears at ~-200mV. The energy range at which a BB on GB is observed is slightly larger than the BB on the edges. A spectral histogram was recorded at the sample region shown by the black square in Figure 4.36 (a) and the result is shown in Figure 4.36 (i). An LDOS maximum is seen at ~+130mV which is responsible for formation of the BB on the GB on 5 ML island (similar to BB on 5 ML edge). It is also interesting to note that in Figure 4.36 (g) and (h), the BB becomes dark. This is because the LDOS intensity of the BB curve is lower than the interior of the 5 ML island at higher negative bias voltages.

4.2.10.2 GB on 7 ML

In Figure 4.37 (a) we show a ~90^0 junction formed on a 7 ML island. CITS was performed on the region at 50 K in ±1V bias voltage range. CITS dI/dV maps are shown in Figure 4.37 (b)-(h) in which we show BB forming on the edges of the 7 ML island. Note that the STM tip was double during this experiment and the effect of the double tip is seen on the right edge of the vertical 7 ML stripe forming the 90^0 junction. This results in asymmetrical widths of BB on the edges of vertical 7 ML

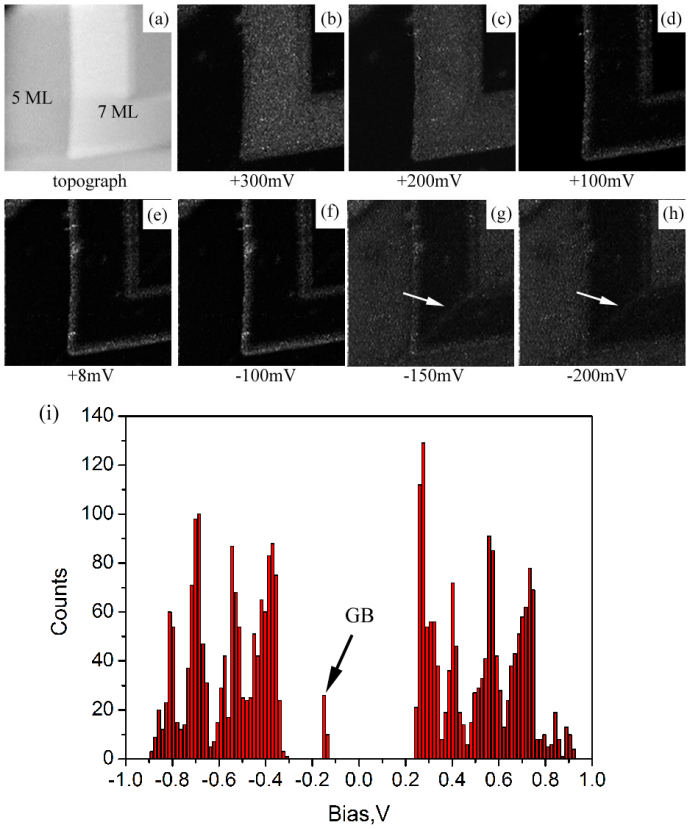

Figure 4.37: (a) STM topograph of a region showing a N1 GB on 7 ML island (V_t = +0.5V, I_t = 200pA). (b)- (h) dI/dV maps obtained via CITS on (a). The white arrow in (g) and (h) show the BB on the GB on the 7 ML island. (c) Spectral histogram recorded on the black square shown on 7 ML island in (a). Black arrow shows the LDOS peak associated with GB at ~ V_t = -140mV.

stripe. A BB is seen on the GB formed at the 90^0 junction but it is formed at negative bias voltages (~-150mV to -300mV). A spectral histogram recorded on the black square in Figure 4.37 (a) is shown in Figure 4.37 (i). An LDOS maximum associated with the BB on 7 ML GB is seen at ~-140mV which is similar to the energy position of one of the BBS peak in Figure 4.19 (There are two histogram peaks which are seen for the 7 ML BB in Figure 4.19 that are positioned at ~+120mV and -130mV).

4.2.10.3 GB on 3 ML

In Figure 4.38 (a) we show an STM image of an island formed near a step edge. The sample region is quite messy with several grain boundaries in the 3 and 5 ML regions. The black square in (a) shows the area in which CITS was performed at 50 K in ±1 V bias voltage range. CITS dI/dV maps are shown in Figure 4.38 (b)-(h) which shows the formation of BB on the edges of 3 and 5 ML islands and a GB forming on the 3 ML island. The 5 ML stripe points towards the fast growth direction of the bismuth island and by studying its orientation with respect to the GB it can be deduced that the angle between the two grains is 150^0. The GB appears between ~+200mV to +30mV (similar to the 150^0 GB in 5 ML stripe in section 4.2.10.1).

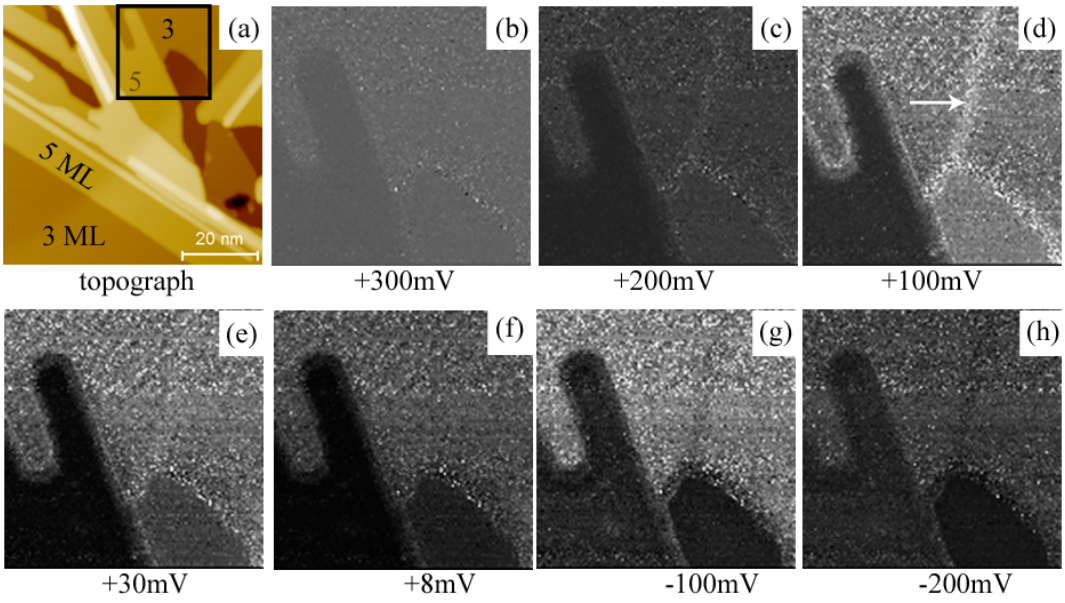

Figure 4.38: STM topograph of a region showing a N3 GB on 3 ML island (V_t = +1V, I_t = 200pA). (b)- (h) dI/dV maps obtained via CITS on the black square in (a). The white arrow in (d) shows the GB on the 3 ML island.

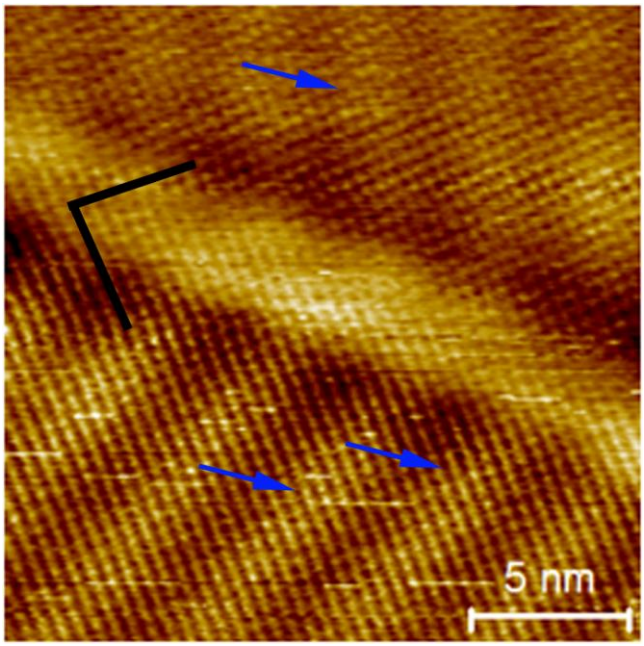

Figure 4.39: STM topograph of a 3 ML island showing a N1 GB (V_t = +0.150V, I_t = 200pA). The GB is seen as a bright stripe running diagonally from top left to lower right corner of the image. The angle between the grains is shown by two black lines, Moiré pattern is shown by blue arrows.

The GB is also visible in low bias voltage STM images of 3 ML islands. In Figure 4.39 we show an atomically resolved STM image of a 3 ML island which is formed near a step edge. The image was recorded at room temperature and V_t = +150mV and the directions of the chain of atoms are shown by the black lines in Figure 4.39 and the angle formed between them is ~90^0. A Moiré pattern is seen on both of the grains indicated by blue arrows (see section 6.2.1 for details on Moiré patterns). The GB is seen as a central bright diagonal stripe formed at the intersection of the chains of atoms aligned at ~90^0 to each other.

The BBs observed on GBs are very similar to the ones observed on the edges of the bismuth islands. They are observed both in CITS dI/dV maps and STM images. The BBs on GBs are also formed at energies around the Fermi level and are observed in the LDOS minimum of the dI/dV(V) curves associated with 3, 5 and 7 ML islands. They are observed at 50 K and room temperature. The formation of BBs on GBs supports our hypothesis that the BB are formed on abnormally terminated chain of atoms since a GB is also a kind of termination of atoms.

4.3 Summary

We observe a bright feature on the perimeter of 3, 5 and 7 ML islands and stripes in the dI/dV maps and STM images at energies close to the Fermi level. We refer to these bright feature as 'bright beaches (BB)' [127] as they resemble a 'beach on the coastline'. In dI/dV maps the BB are formed in the voltage range ~+200mV to -200mV in 7 ML stripes, ~+200mV to +8mV in 5 ML islands and ~+150mV to +6mV in 3 ML islands. These bright beaches are seen in dI/dV maps and STM topographs both at room temperature and 50K. Spectral histograms recorded on the edge of 7 ML stripe shows two clear LDOS peaks in a featureless LDOS valley. These LDOS peaks responsible for the bright beach in dI/dV images are termed 'bright beach states (BBS)'. The BBS are also present in the dI/dV(V) curves extracted from 5 ML and 3 ML edges. The bright beaches are formed on the entire perimeter of the islands and stripes, including tapered regions which indicate that the formation of BB is independent of the crystallographic plane and is related to the edges only i.e. they are formed on terminated atomic chains of bismuth. Bright beaches are visible in 5 and 7 ML STM topographs at energies close to Fermi level and they are robust against deformation via STM tip manipulation. They are faintly seen on 3 ML STM topographs at energies close to Fermi level.

The bright beaches appear as peaks in line profiles drawn on dI/dV maps and evolve in intensity as a function of bias voltage. The maximum height of the BB in the line profiles is achieved at $\sim V_t$ = +150mV. The peaks in line profiles are seen to be localized on the rounded edge. LDOS intensity maps show states associated with the bright beach which appears localized on the rounded edge. The BB does not show any dispersion as a function of bias voltage or additional modulations which suggest that they are not Friedel oscillations (section 4.1.2) or a quantum confined states (section 4.1.2). The bright feature does not shift as a function of polarity of the bias voltage which indicates that Smoluchowski smoothing is not the origin of these bright beaches.

Bright beaches are also present near defects and at grain boundaries (GB) at energies close to the Fermi level in dI/dV maps and STM topographs. The BBS on a 90^0 GB on 7 ML island are formed

at ~-140mV and on 150^0 GB in 3 and 5 ML islands they are formed at ~+150mV. The BBS near the defects are present at ~+115mV in the dI/dV(V) curves.

The LDOS peak observed in our dI/dV line profiles are very similar to the dI/dV line profile on the edges of a Bi(111) thin film [72] shown in Figure 4.9. In Figure 4.9 the LDOS peak is also observed on the rounded step edge in the Bi(111) film. The origin of the intense maximum at the step edge has not been discussed by the authors. Edge states are also observed in Bi(111) 1 BL and 2 BL films on Bi_2Te_3 substrates [78] but the edge state observed in these films was localized ~1 nm away from the step edge (see Figure 4.13). It is interesting to note that on the same Bi(111) thin film system, the LDOS maximum was formed at the rounded edge in one case [72] and ~1 nm away from the step edge in another [78]. The width of the edge state observed on Bi(111) thin films in references [72, 78] is ~2-3 nm. The line profiles on the topologically protected edge state in Bi_2Te_3 [165] (see Figure 4.11) show that it is also localized ~1-2 nm away from the actual edge and is ~2-4 nm wide. Interestingly the widths observed in our Bi(110) islands are also ~2-4 nm.

Topologically protected edge states are seen in the band gap of Bi(111) and Bi_2Te_3 systems. The dI/dV(V) curves associated with these edge states show an increase in the LDOS intensity in a narrow energy window in the band gap (see Figure 4.14). The dI/dV(V) curves recorded on the edges of our Bi(110) islands also show similar dI/dV(V) curves with prominent LDOS peaks near Fermi level. In the band structure calculations shown in section 3.4.1 we saw that around the Fermi level there are few bands which results in a large dip in LDOS around the Fermi level (LDOS valley in the dI/dV(V) curves for 3, 5 and 7 ML). However, the presence of additional LDOS peaks in the dI/dV(V) curves on the edges of our islands and stripes indicate that there are additional bands which are present only at the edges. These additional bands are not seen in the band structure calculations in section 3.4.1 as the calculations are performed on a semi infinite Bi(110) slab.

In the absence of calculations it is difficult to conclusively say anything about the origin of the bright beaches on Bi(110) islands. Our experimental observations suggest that they are related to highly localized electronic bands on the edges of Bi(110) islands and stripes that propagate at energies near the Fermi level. The similarity of the widths of the BB on Bi(110) islands with that of the widths of edge states in Bi(111) and Bi_2Te_3 could indicate a similar nature or origin. We have shown that the widths of the BB are affected by the boundary at which they are formed e.g. BB on 5ML-HOPG is wider than the BB on 5 ML-3 ML. This could indicate an edge reconstruction which is affected by the different boundary conditions.

Wada *et al* in their calculations on Bi(110) nanoribbons predicted that the edge states in a Bi(110) nanoribbon are topologically trivial [41]. However they do not divulge the dimensions of the Bi(110) nanoribbon on which their calculations were performed. In section 5.2.2 we show that the lateral widths of the Bi(110) islands are quantized and we speculate that the incorporation of these quantized widths in the band structure calculations of nanoribbons would have profound effect on the band structure. It would be very interesting to re-determine the topological order of the bright beaches and the Bi(110) thin films.

We emphasize that calculations on a Bi(110) nanoribbon of finite thickness and finite width are vital in understanding the true origin of these bright beaches. Such calculations are difficult because of the unknown structure of Bi(110) edges – a detailed model is necessary.

5. Quantum size effects (QSE)

Electronic effects have been well established as determining the sizes of free clusters [167] and thickness of flat islands [168-171] but so far there has been no demonstration of control of the lateral dimensions of nanostructures. Bismuth is an ideal material for demonstration of such effects as it exhibits strong quantum effects because of its small Fermi surface features in reciprocal space [68].

In section 3.2.1 and 3.4 we showed that our Bi(110) islands have a 'wedding cake' profile comprising 2, 4, 6 ML thick layers on a 1 ML wetting layer. In this chapter we show that the widths of the bases and the stripes (measured along $< 112 >$* direction) are restricted to certain well-defined values. The widths of the islands and stripes were measured by STM and we investigate the underlying mechanism of the 'quantized widths' via band structure calculations. We begin with an introduction to quantum size effects that have been observed previously in literature.

5.1 Literature review

The electronic structure of a solid/crystal is changed when its dimensions approach inter-atomic distances or the electron's wavelength [171, 172]. Such reduction in size results in confinement of electrons that gives rise to quantum size effects (QSE) in ultra thin films [173, 174], two dimensional islands [169, 175, 176], clusters [167] and one dimensional nano-wires [177, 178]. These QSEs are manifested in physically observable and measurable quantities e.g. conductivity [179], surface energy [173], Hall effect [180, 181] etc.

Tringides *et al* [171] describe quantum size effects in metallic nanostructures in which they establish a relationship between the quantized energy levels and the stability of nanostructures. In bulk, nearly free electron metals, the Fermi surface can be represented by the surface of a sphere whose radius k_F is determined by its electron density ρ. The k_F is related to electron density ρ as:

$$k_F = (3\pi^2\rho)^{\frac{1}{3}} \qquad \text{Equation 5.1}$$

and the Fermi wavelength is defined by:

$$\lambda_F = \frac{2\pi}{k_F} \qquad \text{Equation 5.2}$$

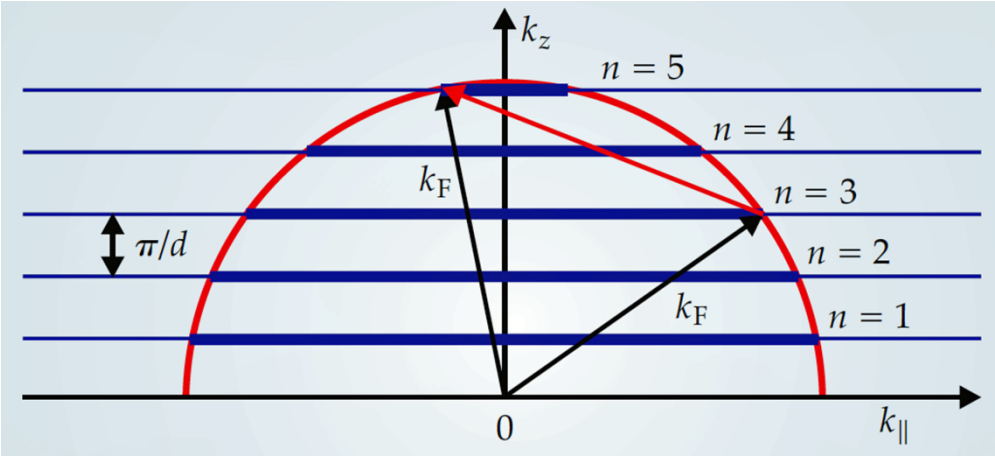

Figure 5.1: In a metal electrons occupy nearly continuous distributed states inside the Fermi surface, often represented as the surface of a sphere of radius k_F. In an ultra thin film of thickness d, quantization of the wave vector normal to the Fermi surface, k_z, divides the Fermi surface into a discrete collection of two dimensional subbands each separated by π/d for the ideal case of a indefinitely deep well. Image reproduced from [171]

In an ultra thin film of thickness d, the quantization of the wave vector normal to the film's surface k_z divides the Fermi sphere into discrete collection of two dimensional sub bands separated by:

$$\Delta k_z = \frac{\pi}{d} \qquad \text{Equation 5.3}$$

(see Figure 5.1). These sub bands are called quantum well states (QWS). If the depth of the confining well is infinite then the allowed values of k_z are nπ/d. Therefore as the film thickness d increases, additional sub bands fall below Fermi level. As more quantum states become available, a periodic modulation of physical properties e.g. conductivity, surface energy and scattering rate is observed. QSEs are most clearly observed when the values of n and d are small i.e. when the separation between the energy levels is large enough to avoid broadening due to inelastic scattering (see red arrow in Figure 5.1). These Fermi level crossings have also been referred to as one dimensional shell effects akin to the shell effects associated with the periodic table [182].

Remarkably the reverse is also possible i.e. by altering the energy levels in a nano scale system the size and geometry of the structures can be controlled. This phenomenon was observed during the epitaxial growth of metal thin films on semiconductors and was first reported on Ag/GaAs [183] and later in a few other systems such as Pb/Si(111) [174-176, 184, 185] and Ag/Si(111) [186]. In these examples the quantum size effects induced the metal atoms to self assemble themselves into islands of selective height with flat tops and steep edges. The total energy of these islands contains a term given by the electronic energy [176]. The electronic energy is maximized when a

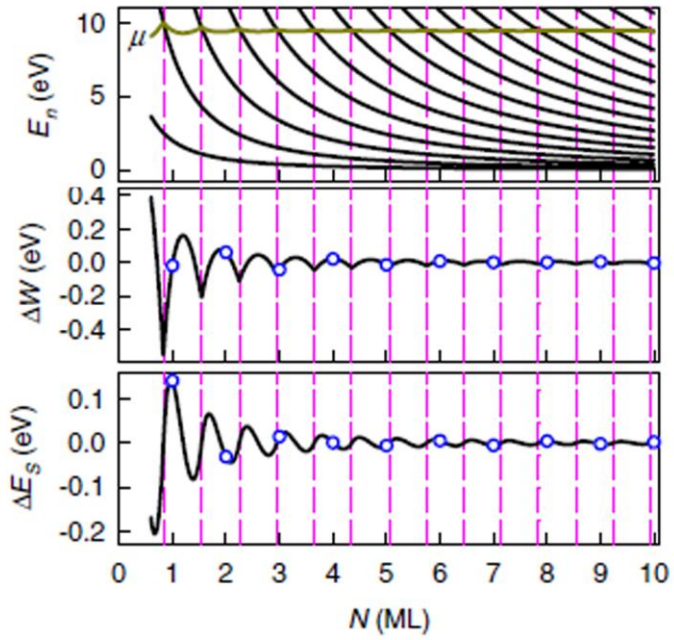

Figure 5.2: From top to bottom: the quantized electronic structure and the chemical potential μ, the work function relative to the bulk limit, and the surface energy per surface atom relative to the bulk limit. Subband crossings are marked by vertical dashed lines. The values of E_S and W at integer N's are indicated by circles. Image reproduced from [169]

QWS has the same energy as the Fermi energy and it will decrease when the QWS passes above the Fermi level. The local topographic and spectroscopic data suggested that the films rearrange their heights to avoid the energetically unfavorable situation of having a QWS, and thus, a high DOS, at the Fermi level [184, 185, 187].

5.1.1 QSE in Pb films

Pb films have been one of the first systems in which quantum size effects have been studied extensively. The growth of Pb films on various substrates was characterized by the presence of 'magic heights' that were stabilized via QSE [173, 184, 188-191]. Miller *et al* in their first principles calculation showed even-odd oscillations in the surface energy (E_S) and work function (W) on free standing Pb(111) films. Their calculations were based on a standard quantum well model with the quantization condition:

$$2k_n h + 2\Phi = 2(n-1)\pi \qquad \text{Equation 5.4}$$

where k is the wave vector, h is the width of the quantum well, Φ is the electron phase shift at each boundary (assuming a symmetric well), and n = 1,2,3… is a quantum number. From Equation 5.4, successive subband crossings of the Fermi level occur at the film thickness increment of:

$$\Delta h = \pi / k_F \qquad \text{Equation 5.5}$$

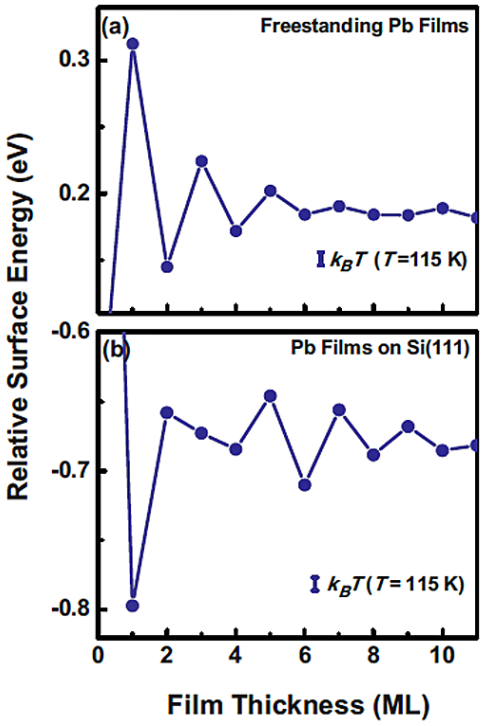

Figure 5.3: Relative surface energies as a function of film thickness, based on a first principles calculation for (a) free standing Pb films and (b) Pb films on Si(111). Image reproduced from [173]

where k_F is the Fermi wave vector and the thickness of the film varies with a period of Δh which equals one half of the Fermi wavelength. The results of their calculation are shown in Figure 5.2 where the top panel shows the evolution of the quantized electron structure E_n. The sub-bands cross the chemical potential (or Fermi level) μ with a period of ΔN = 0.7 ML; the crossing are marked by vertical dashed lines. The middle panel displays the work function and the bottom panel shows ΔE_S (surface energy) relative to the bulk limit. The damped oscillations in the surface energy (see blue circles in Figure 5.2) explains the observation of stable even monolayer height in Pb(111) films. However, the work function exhibits downward cusps at each subband crossing, while the E_S has maximum positive slope; thus the oscillation maxima in E_S lead the maxima in W by 1/4 of a period. Miller *et al* observed the same phase relation between E_S and W in Ag(100) films grown on Fe(100) which led them to derive a rule that the oscillations in surface energy lead the oscillations in work function by 1/4 of a period in metallic films [169]. They also showed that the phases of the oscillations associated with one dimensional shell effects in films depend on the properties of interest.

5.1.2 Influence of the substrate

The choice of substrate has an impact on the interface formed between the film and the substrate. The nature of the interface governs the the total energy of the films leading to different

preferred thicknesses. Pb films grown on HOPG [173] showed prevalence of even thicknesses of 2, 4, 6 and 8 over the odd thicknesses suggesting that there is a significant difference in the surface energy between the even and odd film thicknesses (similar to Miller *et al* [169]). The experimental observation of preferred heights were consistent with the first principle calculations of the surface energies of free standing films which suggested that the interaction between the Pb film and HOPG substrate is weak. A plot showing the surface energy of Pb/HOPG films is shown in Figure 5.3 (a) which clearly shows bilayer damped oscillations. On the other hand the surface energy obtained for Pb/Si(111) is in stark contrast with the Pb/HOPG film; an effect attributed to the strong interfacial interaction between the QWSs and the substrate's electronic structure. The Si(111) surface is highly reconstructed with remnant dangling bonds that have the capacity to bind with the deposited film. Additionally Si(111) has a band gap which is only 1 eV below the Fermi level and thus the overlayer's states which reside below the gap easily couple into the Si electronic states. In contrast the HOPG surface is structurally and chemically stable and has a large band gap which doesn't allow coupling between the overlayer and substrate.

We have discussed QSE and the theory behind formation of 'magic heights' in various nanoscale systems. We should point out that in section 3.2.1 and 3.4 we established that the bismuth islands on HOPG substrate also form bilayers on a 1 ML dead wetting layer and behave as a free standing film. We will begin the results section with a short prelude on the formation of bilayers in the $< 110 >$ direction (direction perpendicular to the substrate) and continue to the observation of preferred widths in the $< 112 >$* direction. It is worthwhile mentioning that QSE have never been observed previously in the lateral direction.

5.2 Results

5.2.1 QSE in the $< 110 >$ direction

The presence of magic heights in Pb islands on various substrates is attributed to oscillations in the total energy of the film. As mentioned before the Bi(110) islands also exhibit a bilayer periodicity in the $< 110 >$ direction. However, in contrast to the k_F wave vector observed in Pb islands, there is no evidence of a similar Fermi wavelength in Bi(110) islands in the $< 110 >$ direction.

The bilayer periodicity in Bi(110) films can be explained in terms of surface energy of the film (see Figure 5.4). The surface energy calculation was performed by the team at UIUC. In Figure 5.4 we see bilayer damped oscillations in surface energy of the Bi(110) thin films which are responsible for

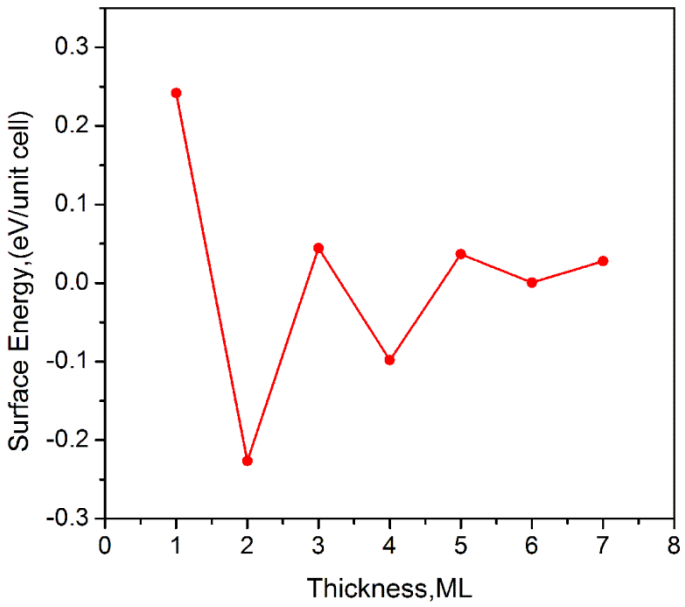

Figure 5.4: Surface energy of Bi(110) films on HOPG as a function of thickness

the observation of paired layers on a 1 ML thick wetting layer (see section 5.1.2). The calculated surface energies for odd numbered thicknesses of Bi(110) are generally higher than those for even numbered thicknesses which accounts for the preference of even numbered thicknesses.

Similar bilayer damped oscillations of adsorption energy have also been reported for the BP allotrope of bismuth on Si(111) substrate [44]. The observation of paired layers in Bi(110)/Si(111) system has been attributed to formation of a unique puckered layered structure. We have discussed evidence for and against this BP structure in our Bi(110)/HOPG system in section 3.2.3. In the band structure calculations performed at UIUC, we were not able to determine any Fermi wavelength in the $< 110 >$ direction (perpendicular to the substrate) which could give rise to preferred thicknesses in the Bi(110) thin films analogous to the 'magic heights' in Pb films. We believe that the observation of paired layers in Bi(110) thin films in not a true quantum size effect, rather the layer pairing is caused due to a simple allotropic modification which involves the rotation of a bond. In this case the energetics of the Bi(110) film is sufficient enough to explain the observed bilayer periodicity in the thickness.

5.2.2 Periodic widths

In the course of our experiments we noticed that in the STM images of Bi(110) islands the widths of the 7 ML stripes look strikingly similar (see black arrows in Figure 5.5). This observation encouraged us to measure the widths of the islands and stripes and look for any periodicity in widths. A typical example of the measurement of widths of a 7 ML stripe via line profiles is shown in

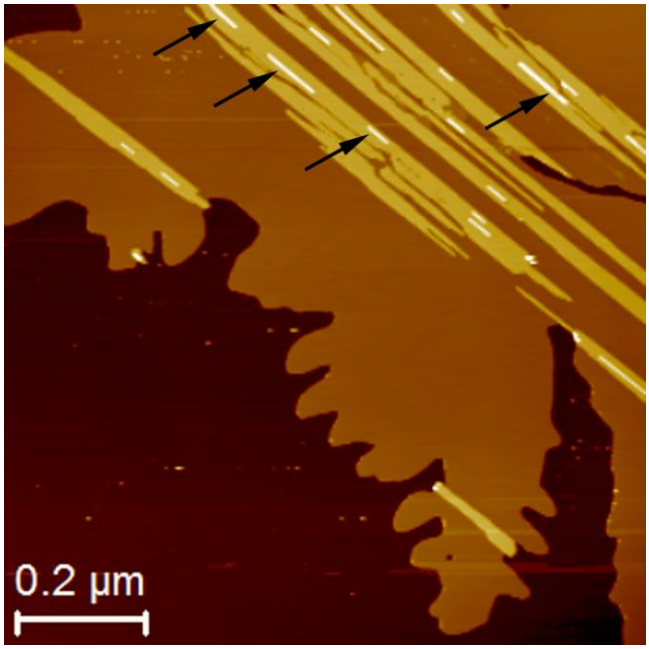

Figure 5.5: STM image of a Bi(110) island (Vt = -0.8V, It = 10pA). The black arrows show 7 ML stripes which appear to have similar widths.

Figure 5.6. The line profile shown in Figure 5.6 (b) is shown as the black line in (a) and is an average of 30 adjacent lines. The number of adjacently averaged line varied from image to image depending on the size of the scan window and was usually between 15-40 lines. The width of the stripe was measured by measuring the distance between the points of inflexion on the region of curvature (as seen by vertical dotted lines in Figure 5.6 (b). The width of the 7 ML stripe shown in Figure 5.6 (a) was measured as ~8.45 nm. The measurement on 7 ML stripes is relatively straightforward but the measurement of 3 and 5 ML islands is tricky because of the huge lateral spread of the former and the tendency to form tapering regions in the latter.

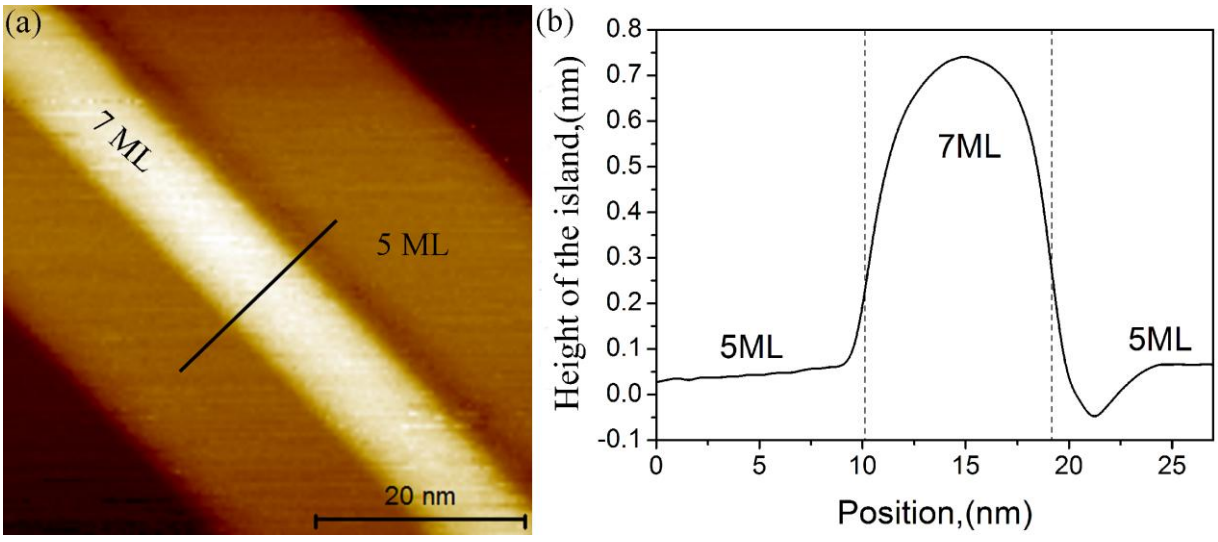

Figure 5.6: (a) STM topograph of an island showing a prominent and uniform 7 ML stripe (V_t = +1V, I_t = 100pA). (b) Line profile corresponding to the black line in (a). 30 individual line profiles were averaged together to yield the line profile in (b).

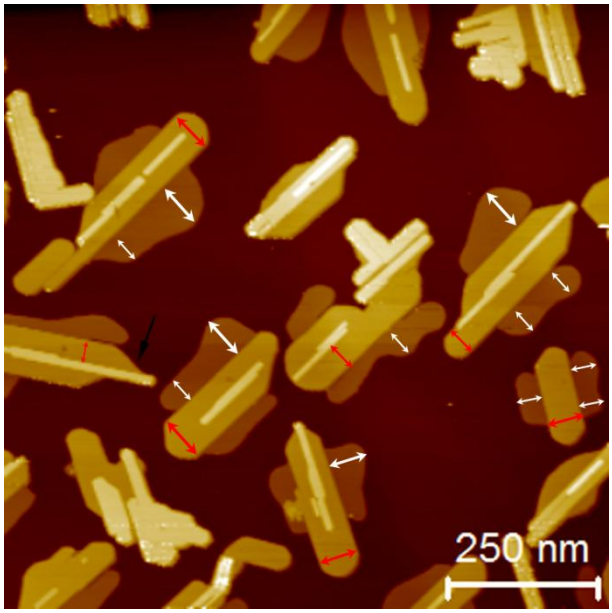

Figure 5.7: STM topograph of bismuth islands grown on a low grade substrate (V_t= -0.8V, I_t= 100pA). The white and red arrows depict the width measurements on 3 ML and 5 ML thick islands respectively.

We dealt with these issues by preparing samples grown on specially selected substrates where a high density of defects results in a higher density of islands and smaller lateral dimensions [13, 15, 16]. An STM image from such a sample is shown in Figure 5.7. It can be seen that the lateral spread of the 3 ML bases is reduced and the density of islands have increased. The widths on 3 ML islands were measured from the 5 ML-3 ML edge to the furthest point in the 3 ML base i.e. the maximum extent of the bulge (treating it as the major axis of a hypothetical ellipse). The white arrows in Figure 5.7 show examples of the widths of the 3 ML bases. The measurement of widths on 5 ML stripe is shown by red arrows in Figure 5.7. The tapering regions on 5 ML thick islands such as the one shown by the black arrow in Figure 5.7 were avoided (see section 5.2.3).

The widths of over 1000 bases and stripes were measured and are recorded in histograms shown in Figure 5.8. The grey bars are histograms of raw data. Each measured width has an uncertainty that depends on the resolution (scan size), for example a 50 nm x 50 nm scan with 256 points has higher resolution than a 200 nm x 200 nm scan with 256 points. We accounted for the different uncertainties by substituting each single count by a normalized Gaussian distribution with variance:

$$\sigma^2 = s/r \qquad \text{Equation 5.6}$$

where s is the scan width measured in nm and r is the number of raster points per scan line. The black lines superimposed over the grey bars in Figure 5.8 are the sum of Gaussian distributions obtained this way.

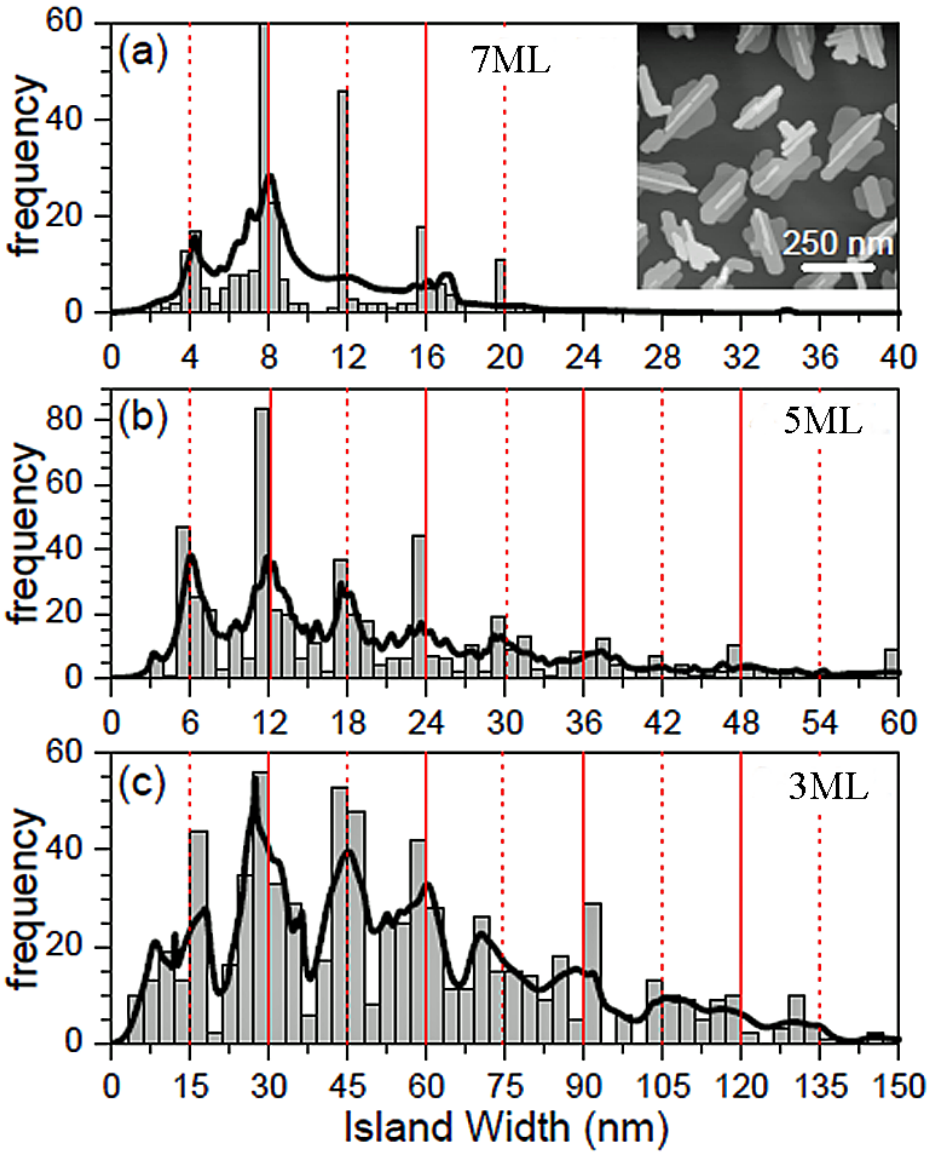

Figure 5.8: Histograms of widths of (a) 7 ML, (b) 5 ML and (c) 3 ML thick islands obtained from ~ 1500 measurements of ~ 400 islands. Gray bars are histograms of raw data while the broadening in the black curves accounts for the uncertainty inherent in the experimental measurements (see text for description). For all island thicknesses a regular sequence of peaks is visible in the histograms i.e. there are preferred island widths due to a quantum size effect. Vertical solid and dotted lines indicate multiples of the Fermi wavelength λ_F and $\lambda_F/2$ respectively. Measured λ_F are 8 nm, 12 nm and 30 nm for 7, 5 and 3 ML thick islands respectively. Inset in (a) shows typical island morphologies: flat, broad 3ML bases with thicker rods and stripes near their centers. The widths recorded in the histograms are the widths of the individual bases, rods and stripes.

It is readily apparent that the 7 ML stripes have very similar widths as demonstrated by the histogram in Figure 5.8 (a). Two distinct maxima can be seen, centered roughly at 4 nm and 8 nm, as well a series of weak shoulders at 12, 16 and 20 nm. These features are regularly spaced, i.e. occurring every ~4 nm. The vertical red solid and dotted line indicate the periodicity in the width of these 7 ML stripes. This is the first indication that the growth of these islands is governed by QSEs, in which case the island width (w) follows the rule: $w = n\lambda_F^{6ML}/2$, where n is a natural number, and

the Fermi wavelength can be estimated to be λ_F^{6ML} = 8nm. We write 'λ_F for 6 ML' because the wetting layer is a 'dead' layer which does not contribute to DOS of the film (see section 3.4).

In Figure 5.8 (b) we show the widths of 5 ML islands which also show peaks at 6, 12, 18, 24…, that correspond to a periodicity of 6 nm. The Fermi wavelength associated with 5 ML islands is therefore λ_F^{4ML}= 12nm. The widths of the 3 ML islands show distinct peaks at 15, 30, 45, 60 nm… that corresponds to a periodicity of 15 nm and hence the Fermi wavelength associated with 3 ML is λ_F^{2ML} = 30 nm. We ignore the first peak at ~8.3 nm since in data for wider bases the observed period is ~15 nm.

5.2.3 QSE in decay of islands

In order to confirm that there are preferred widths governing growth (or decay) of bismuth islands we performed mechanically mediated coarsening of the islands [192]. In this process a scanning probe interacts gently with the islands, providing energy in a way that is analogous to thermal annealing and results in morphological changes. In this case it is possible to perform STM imaging and at the same time slowly modify the island's morphology; results of a typical experiment are shown in Figure 5.9. In Figure 5.9 (a) there is a large 3 ML base surrounding a 5 ML stripe (seen in the top part of the image). During scanning the size of the 3 ML base decreases in area and the 5 ML region grows because of migration of atoms to that region. Remarkably, the width of the 3 ML region remains constant (see white arrows in Figure 5.9 (a-c)), while its length decreases.

We analyzed 7 different bases recorded (for over 6 hours) in a set of 34 images (~150 separate width readings) and created a histogram of widths (see Figure 5.9 (b)). The grey bars are raw data and the black line is the sum of Gaussian distributions. In the histogram two very distinct maxima are observed at ~15 nm and 30 nm. The location these peaks correspond perfectly with the first two peaks in 3 ML histogram shown in Figure 5.8. This is a clear evidence of the influence of QSE on the observed decay of bismuth islands.

5.2.4 The Fermi surfaces

Having observed well defined periodicity in the widths of Bi(110) islands and stripes we now investigate the electronic structures of the film that could give rise to long range periodicities and affect the dimensions of the nanostructures. In section 3.4 we established that in our Bi(110) films the effect of spin orbit coupling is nullified because of a weak interaction with the substrate.

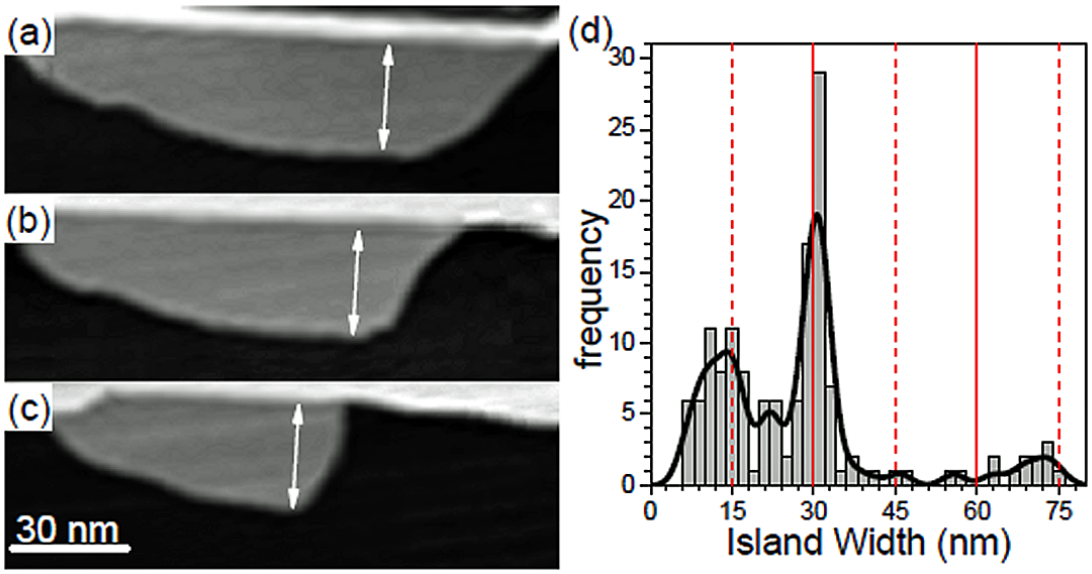

Figure 5.9: (a)-(c) A series of STM images recorded during mechanical coarsening of a typical 3 ML thick island at room temperature. The images are recorded approximately 60 minutes apart (the scanning process took 11 min per image). The white arrows indicate a constant width of 30 nm in (a)-(c), while the overall island size changes significantly. (d) Width histogram for all 3 bases measured during the evolution of a complex structure that included eight 3 ML thick island segments (the black line includes broadening and the gray bars are raw data). The main maxima occurs for widths ~14 and ~30nm. Solid and dotted vertical lines correspond to multiples of λ_F and $\lambda_F/2$.

The fast growth direction in Bi(110) islands is $< \bar{1}10 >$ and it corresponds to $\bar{\Gamma}$-$\bar{X}_1$ in reciprocal space. We observe the periodicity in widths in the $< 112 >$* or $\bar{\Gamma}$-$\bar{X}_2$ direction. In Figure 5.10 (a) and (b) we show the calculated 2ML band structure (section 3.4.1) and the corresponding Fermi surface respectively. In the calculated band structure we see that a band crosses the Fermi level in the $\bar{\Gamma}$-$\bar{X}_1$ direction. The corresponding Fermi surface of the 2 ML slab is an ellipse shaped electron pocket situated in the $\bar{\Gamma}$-$\bar{X}_1$ direction. This electron pocket has:

$$\lambda_F = \frac{2\pi}{k_F} \qquad \text{Equation 5.2}$$

The Fermi wave vector we are interested in lies in $\bar{\Gamma}$-$\bar{X}_2$ direction and is indicated by the grey arrows as shown in Figure 5.10 (b). The Fermi wavelength associated with the electron pocket is calculated by Equation 5.2 and we observe that the Fermi wavelength of the electron pocket located at $\bar{\Gamma}$-$\bar{X}_1$ matches the experimental widths if a small shift of the Fermi level is allowed. To get the agreement with the experimentally estimated for λ_F^{2ML} = 30 nm, an upward energy shift of 35 meV is required. This upward energy shift lifts the Fermi level to the new position as shown by the green horizontal line in Figure 5.10 (a) and makes the electron pocket slightly bigger as shown by red arrows in Figure

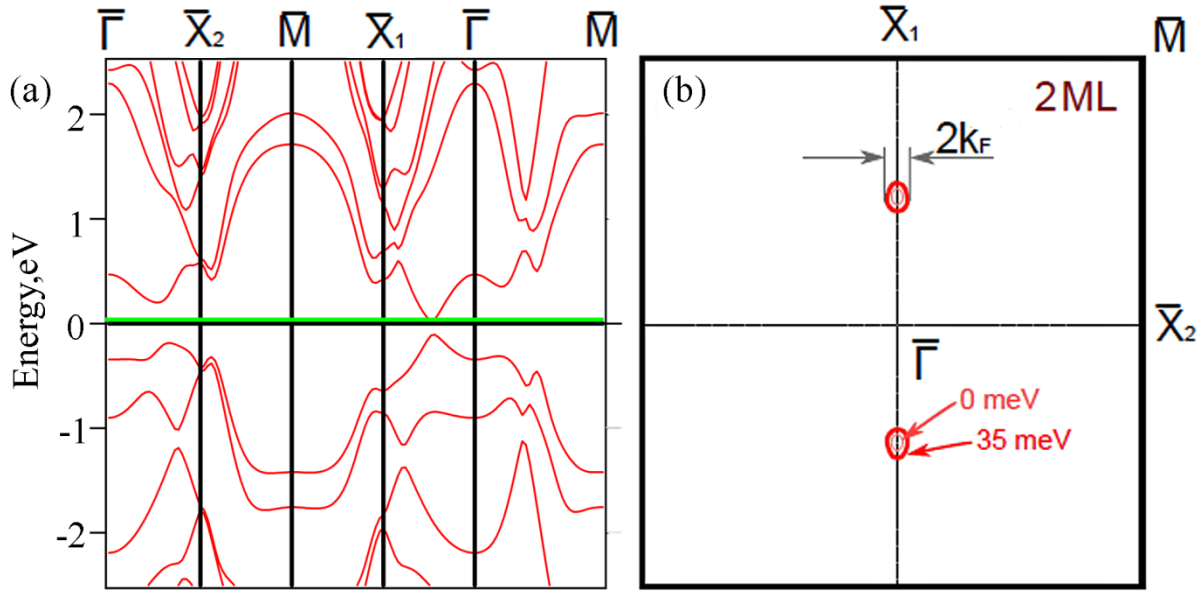

Figure 5.10: (a) Calculated dispersion relation for 2 ML film. Horizontal gray line indicates the as calculated location of the Fermi level while the green line indicates the Fermi level after optimized charge transfer from the substrate to the film. (b) Calculated Fermi surface for the 2 ML film with electron pockets indicated in red color. Different color tones show Fermi surfaces after different shifts of the Fermi energy (due to charge transfer from the substrate).

5.10 (b). The shift allows us to measure k_F = 0.021 Å^{-1} which yields λ_F = 30 nm. Such energy shifts correspond to charge transfer from HOPG to the bismuth islands (n-type doping) [193]. Angle resolved photoelectron spectra for >6ML films of Bi on HOPG [194]and Bi on Si [195] are also consistent with n-type doping.

In Figure 5.11 (a) and (b) we show the calculated band structure of a 4 ML bismuth slab and the corresponding Fermi surface respectively. The band structure of the 4 ML also contains a band that crosses the Fermi level in the $\bar{\Gamma}$-$\bar{X}_1$ direction. The corresponding Fermi surface shown in Figure 5.11 (b) is also an ellipse. The experimentally observed Fermi wavelength in 5 ML islands and stripes is λ_F^{4ML} = 12nm. To find an agreement between the calculated Fermi wavelength and the experimental wavelength, an energy shift equivalent to 120 meV is introduced that lifts the Fermi level up as shown by the horizontal green line in Figure 5.11 (a).The resulting electron pocket yields a k_F = 0.0523 Å^{-1} (shown by grey arrows in Figure 5.11 (b)) which corresponds to a λ_F = 12nm.

The extraction of a calculated Fermi wavelength is straightforward for 2 ML and 4 ML bismuth slabs. The 2 and 4 ML band structures show only a single band that crosses the Fermi level and with appropriate charge transfer we are able to match the experimental and calculated Fermi wavelengths. In the case of the 6 ML band structure (shown in Figure 5.12 (a)) additional bands are

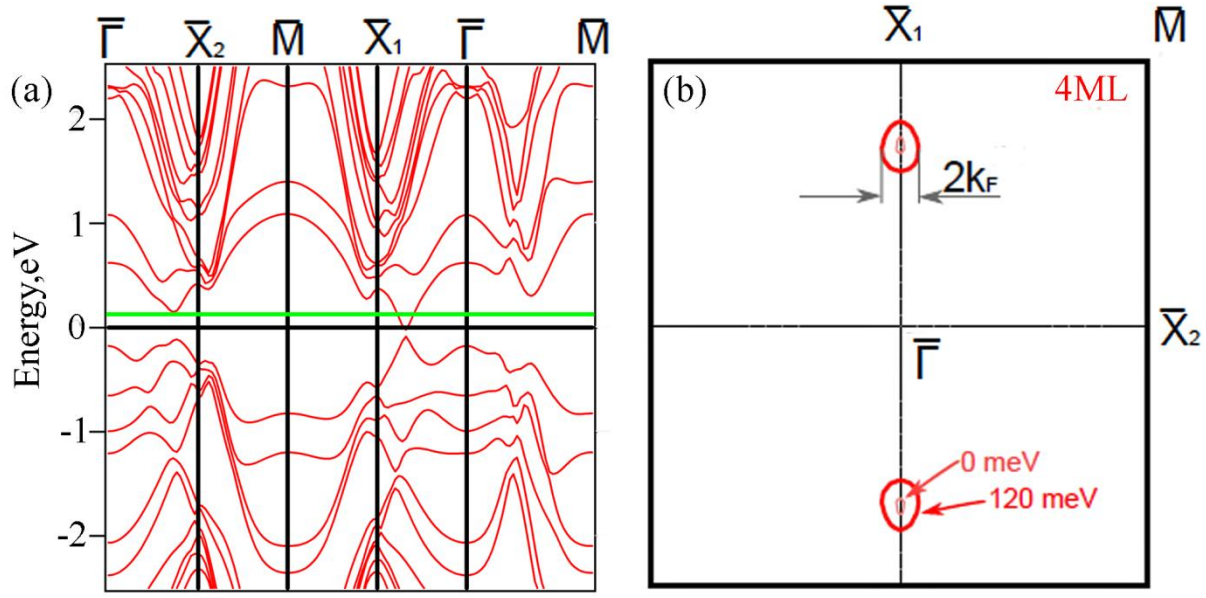

Figure 5.11: (a) Calculated dispersion relation for 4 ML film. Horizontal gray line indicates the as calculated location of the Fermi level while the green line indicates the Fermi level after optimized charge transfer from the substrate to the film. (b) Calculated Fermi surface for the 4 ML film with electron pockets indicated in red color. Different color tones show Fermi surfaces after different shifts of the Fermi energy (due to charge transfer from the substrate).

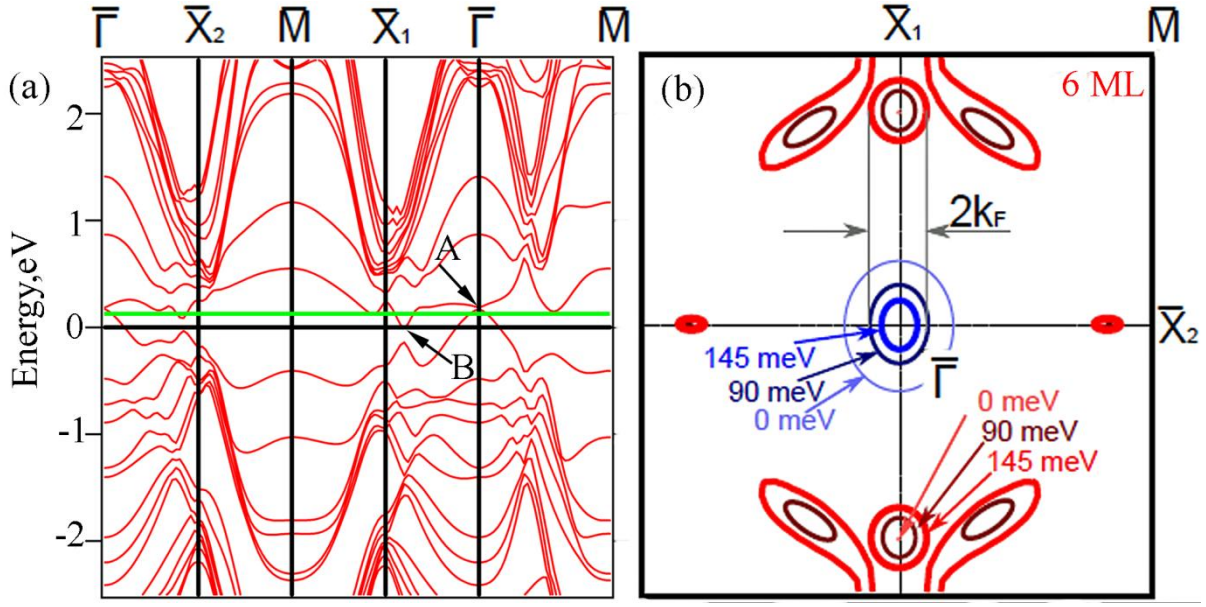

Figure 5.12: (a) Calculated dispersion relation for 6 ML film. Horizontal gray line indicates the as calculated location of the Fermi level while the green line indicates the Fermi level after optimized charge transfer from the substrate to the film. (b) Calculated Fermi surface for the 6 ML film with electron and hole pockets indicated in red and blue color respectively. Different color tones show Fermi surfaces after different shifts of the Fermi energy (due to charge transfer from the substrate).

seen at energies around Fermi level. They cross the Fermi level around the $\bar{\Gamma}$ point and also in $\bar{\Gamma}$-$\bar{X}_1$ and $\bar{\Gamma}$-$\bar{X}_2$ directions. In the corresponding Fermi surface (shown in Figure 5.12 (b)) the Fermi level crossing around $\bar{\Gamma}$ point leads to formation of a hole pocket and the crossing in $\bar{\Gamma}$-$\bar{X}_1$ and $\bar{\Gamma}$-$\bar{X}_2$ directions leads to formation of electron pockets. The experimental Fermi wavelength obtained on 7 ML islands and stripes is λ_F^{6ML} = 8nm. To find agreement between the calculated Fermi wavelength and the experimental wavelength, energy shifts were introduced in the Fermi level again (shown as shades of red and blue in Figure 5.12 (b)). But in this case we have a complicated Fermi surface that consists of an electron pocket located in $\bar{\Gamma}$-$\bar{X}_1$ direction accompanied by a hole pocket at the $\bar{\Gamma}$ point. The calculated k_F that corresponds to the experimental Fermi wavelength of 8 nm is 0.0785Å^{-1} and can be obtained from the electron pocket in the $\bar{\Gamma}$-$\bar{X}_1$ direction by introducing an upward energy shift of 145 meV. Surprisingly, the required k_F can also be found from the hole pocket at the $\bar{\Gamma}$ point by introducing an upward shift of 90 meV. It is interesting to see that the charge transfer to achieve the required calculated Fermi wavelength from the electron pocket or the hole pocket is not significantly different. It is, therefore, very difficult to conclusively state whether the electron or the hole pocket is responsible for the observation of quantized widths in the 6 ML film. However, we have already observed in the case of 2 and 4 ML bismuth slabs that the electron pocket in the $\bar{\Gamma}$-$\bar{X}_1$ direction is responsible for the observed periodicities in widths, hence it is not improbable that the same electron pocket in the $\bar{\Gamma}$-$\bar{X}_1$ direction in the 6 ML Fermi surface is also responsible for the observation of quantized widths in 6 ML bismuth films.

5.2.5 Nature of the electronic wavefunctions

In the previous section we showed that electron wave associated with an electronic feature in the band structure is responsible for the observation of periodic widths Bi(110) thin films. We now investigate the nature of the wavefunction associated with the electron pocket to understand the propagation of the electron wave in the islands.

In Figure 5.13 (a) we look at the plane averaged charge densities of the bands marked A and B in Figure 5.12 (a) (Band B forms the electron pocket in $\bar{\Gamma}$-$\bar{X}_1$ direction). The charge densities are shown as a function of thickness of the film. It can be seen that charge density associated with band A (maroon color) is localized at the surface of the film and the charge density associated with band B is spread evenly across the bulk of the island. The 'bulk character' of the electronic wavefunctions of the band B indicates that they penetrate the whole of the slab. Consequently, these wavefunctions are confined by the boundaries between parts of the structure with different thicknesses. For example, in Figure 5.13 (b) we show a schematic side view of a 2 ML high stripe on top of a 4 ML

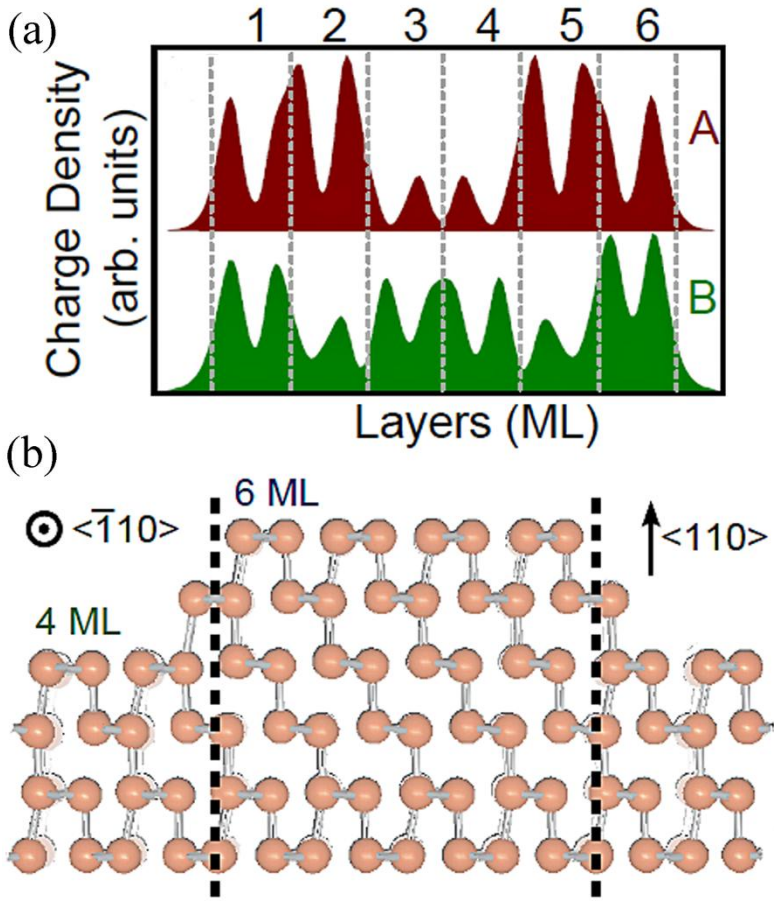

Figure 5.13: (a) Calculated plane-averaged electronic charge densities within the 6 ML film (the vertical dashed lines separate the atomic layers) for the states labeled A and B in Figure 5.12 (a). (b) Schematic side view along $< \bar{1}10 >$ of a 2 ML high stripe on top of a 4 ML thick layer. Dashed lines delimit boundaries between regions of different thickness.

thick layer (wetting layer not shown). The vertical dashed lines delimit the boundaries between regions of different thicknesses and serve as barriers for the confined electronic wavefunctions.

5.3 Summary

As we mentioned in section 3.2.1 the Bi(110) thin films are characterized by 2 ML thick bismuth layers on top of a 1 ML wetting layer. In the calculations performed by the team at UIUC we observed clear minima in the surface energy for even layer thicknesses which are consistent with the sequence of experimentally observed thicknesses when this wetting layer is accounted for. Similar damped bilayer oscillation in adsorption energy and formation of paired layers have been reported previously in Bi(110) films on Si(111) [44]. The observation of paired layers in Bi(110)/Si(111) system has been attributed to formation of a unique puckered layered structure (see section 3.2.1). It is clear that electronic effects (oscillations in surface energy) rather than any vertical QSE are involved in stabilizing the Bi(110) film structure in the vertical direction.

We have observed well defined periodicities in the widths of 3 ML, 5 ML and 7 ML Bi(110) islands and stripes. The widths were measured in the $< 112 >$* direction from the STM images. The periodicity was analyzed via histograms made from widths obtained via STM images. We accounted for the different uncertainties in the measurement by substituting each single count by a normalized Gaussian distribution with variance $\sigma^2 = s/r$. The resulting histogram shows widths with a periodicity of ~15 nm in 3 ML, ~6 nm in 5 ML and ~4 nm in 7 ML islands and stripes. The quantized widths are the first indication that the growth of Bi(110) islands is governed by QSEs, in which case the island width (w) follows the rule: $w = n\lambda_F/2$, where n is a natural number, and λ_F is the Fermi wavelength. We therefore estimated the experimental Fermi wavelength of 3, 5 and 7 ML islands to be λ_F^{2ML} = 15 nm, λ_F^{4ML} = 6 nm and λ_F^{6ML} = 8 nm.

The phenomenon of quantized widths is also observed in decay of islands where the islands are deformed via STM tip manipulation, a process analogous to thermal annealing. It was seen that the islands maintained a constant width throughout the decay process, while their length decreases. We prepared a histogram of widths observed during the decay process for seven 3 ML islands and it showed peaks at ~14 nm and ~30 nm.

To understand the mechanism behind the formation of quantized widths we investigated the band structure of 2, 4 and 6 ML bismuth slabs. The Fermi surface of 2 and 4 ML slabs show an electron pocket in the $\overline{\Gamma}$-$\overline{X}_1$ direction. This pocket has a k_F in the $\overline{\Gamma}$-$\overline{X}_2$ ($< 112 >$*) direction which matches the observed experimental Fermi wavelength in 2 and 4 ML Bi(110) islands respectively. For 6 ML the required Fermi wavelength could be generated from both hole and electron pockets with charge transfers of 90 meV and 145 meV respectively. However, we speculate that since the electron pocket is responsible for observation of quantized widths in 2 and 4 ML islands, it is highly likely that the electron pocket in the 6 ML islands is also associated with quantized widths in 7 ML islands.

The association of the quantized widths observed in 3, 5 and 7 ML islands with an electron wave propagating in plane to the bismuth film is a clear evidence of a 'lateral quantum size effect'. Bi(110) thin films are a complex system in which electronic effects are involved in stabilizing the film structure in the vertical as well as lateral direction. The complex interplay between structural and electronic effects merits further investigation, but we believe the present observation that electronic effects control structure in two orthogonal directions is unique.

6. Moiré pattern in Bi(110) films

In section 1.5 we discussed that the elongation direction of the bismuth islands (stripes and rods) is Bi$< \bar{1}10 >$ || HOPG$< 100 >$. This results in majority of the islands rotated by 60^0 with respect to one another due to the symmetry of the substrate [13, 16]. We observed a distinct and periodic Moiré pattern on some of the 3 ML islands via STM images and STS dI/dV maps. The Moiré pattern mostly appears at energies around the Fermi level and the periodicity of the pattern does not change as a function of bias voltage or sample temperature. The Moiré pattern on the islands was further investigated by non-contact AFM to understand its nature and origin. In the current chapter we discuss preliminary results obtained on Moiré pattern on 3 ML islands. Further experimental investigations and calculations are proposed to completely comprehend the origin of Moiré pattern in Bi(110) thin films on HOPG. We begin the chapter with a brief literature review of the occurrence and origin of Moiré pattern on HOPG and thin bismuth films.

6.1 Literature review

Superposition of two grids at an angle or different mesh sizes results in formation of a Moiré pattern [196, 197]. In thin films the two grids are formed by the periodic lattice of the substrate and the overlayer. Incommensurate structures leading to formation of Moiré patterns have been investigated by Transmission Electron Microscopy (TEM) [198, 199], Low Energy Electron Diffraction (LEED)[200, 201] and STM [202, 203].

In TEM images Moiré patterns are observed when electrons are transmitted through two layers with slightly different lattice constants. However, it is questionable that this picture is also applicable to the Moiré pattern observed in STM, because in STM, electrons tunnel directly from inner as well as from outermost layers [204, 205]. Most of the early STM results also interpreted presence of Moiré pattern as a result of multiple tip [203] and tip contamination [206]. In another theory of Moiré pattern in STM images, the formation was attributed to the modulation of the electronic structure of the overlayer by the influence of lattice mismatched substrates [202, 207, 208]. However, this reason is not sufficient as the Moiré pattern is also observed in layered materials e.g. graphene on metal surfaces [209, 210] and in transition metal dichalcogenides [211-213]. In those materials the interlayer attraction is very weak which should result in less effect of the substrate on the overlayer [204]. Kobayashi [204] pointed out that the sub-surface structures are generally visible in an STM if they have nanoscale dimensions. In his model he described the observation of Moiré patterns in STM images via 3-dimensional tunneling phenomena.

6.1.1 The Kobayashi model

In the case of TEM imaging, the kinetic energy of the electrons determines the behavior of the electrons transmitted through matter. The behavior of electrons transmitted through matter depends on the kinetic energy of incident electrons. When the kinetic energy is much larger than strength of the scattering potential in the matter, a perturbative treatment is valid. In this case the wavefunctions of the transmitted electrons are expressed in terms of superposition of waves singly scattered by each atomic potential. Therefore high energy electrons transmitted through two layers with slightly different lattice constants show Moiré pattern.

Another factor in determining the scattering behavior of the electrons is channeling. Because of the conservation of kinetic energy, the numbers of propagating channels are restricted. When the kinetic energy is E, then the channels with momenta larger than $\sqrt{2E}$ do not propagate in direction perpendicular to the substrate. Therefore no image if obtained on a screen far from a sample surface when $E < (2\pi/a^2)/2$, where 'a' is the lattice constant of the sample. However when the electrons transmit through two layers with lattice constants 'a' and 'b', they can gain a small lateral momentum of $2\pi/l = [2\pi/a - 2\pi/b]$ by the multiple scattering. Therefore a structure with period 'l' is observed if $E < (2\pi/l^2)/2$.

In the case of TEM the number of propagating channels of scattered electrons is limited by the choice of electron kinetic energy but in the case of STM, there are no propagating channels and all the waves decay in the vacuum region. Multiple scattering processes become important in this scenario because the kinetic energy of the electrons is comparable to the potential strength. Since electronic states in the vacuum region are very sensitive to only outermost layers, STM images reflect usually atomic structures of the outermost layers. Therefore, it seems that even when the lattice constants of the outermost and second layers are slightly different, Moiré patterns such as those in high-energy TEM cannot be observed in STM.

Several STM experiments reporting information on the inner layers or sub surface structures e.g. bulk defects [214-216] and Moiré pattern in lattice mismatched systems [202, 217-219] are quite curious from a theoretical point of view. The most important conclusion from this observation is that subsurface structures are generally visible in STM if they have nanoscale dimensions.

It was described that the main component of the wave functions in the vacuum near the outermost layer is the wave with a lateral momentum of $2\pi/a$. The component with the lateral

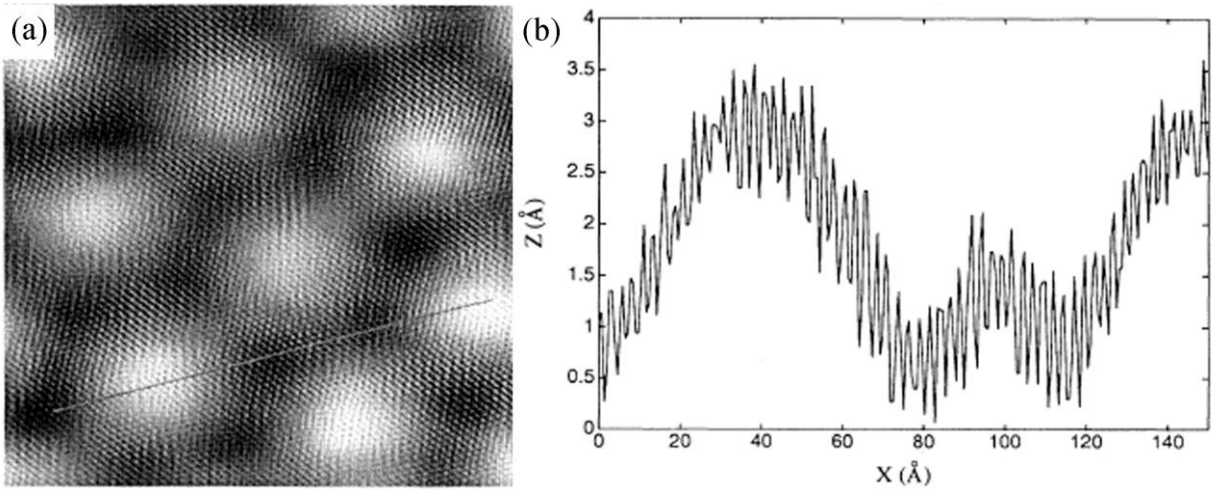

Figure 6.1: A close up view of the superlattice on which the graphite atoms are resolved. The image is taken with a set current 5.6nA, tip bias 72mV and scan size of 20 nm x 20 nm.(b) A cross section along the direction indicated by the line in (a). Image reproduced from [202]

momentum of $2\pi/l$ produced by multiple scattering is a higher order term and its amplitude is generally very small. However, waves with larger lateral momenta decay faster, as a wave with a lateral momentum q decays in the vacuum region as:

$$e^{-\lambda z}, \lambda = \sqrt{2|E| + q^2} \qquad \text{Equation 6.1}$$

where E is the energy of the wavefunction measured from the vacuum level and the z axis is perpendicular to the surface. The large lateral structure of l is observed in STM images when the tip is scanned far from the sample surface. Therefore if the tip-sample distance is properly chosen the large lateral structure and the atomic structure can be observed simultaneously.

The nature of Moiré patterns investigated by most STM and STS results suggests an electronic nature of the patterns [220, 187, 221-223]. However, it is extremely difficult to generalize the origin of a Moiré pattern as 'purely electronic' or 'purely structural' as the Moiré pattern could arise out of structural deformation because of lattice mismatch or out of a redistribution of electronic states or a combination of both. Nevertheless, the occurrences of Moiré pattern on thin films have been a subject of interest as it gives rise to interesting properties. For example, it was shown that the presence of a Moiré pattern could result in opening of a band gap in a 2D electron gas [224]. It is also worth noting here that the Moiré pattern finds application in nanotechnology as substrates for patterned growth of clusters e.g. metallic clusters on graphene Moiré [225-228].

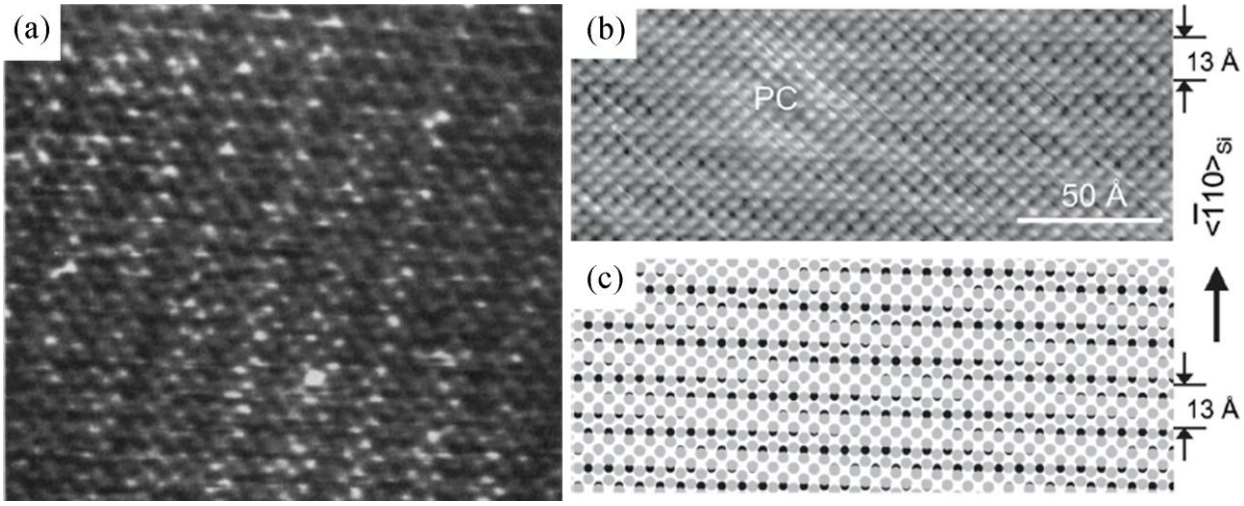

Figure 6.2: (a) 10 nm x 10 nm STM image of a Bi monolayer on Au(111). Image reproduced from [229] (b) STM image of (8 nm x 20 nm) showing faint Moiré feature on 4 ML Bi(110) film (also called as pseudocubic film (PC)) on a Si(111) substrate taken at V_t = +0.6V. (c) Model of orientation relationship between the Bi(110) over layer (grey dots) and the $\sqrt{3}$ x $\sqrt{3}$ substrate (black dots). Image reproduced from [46]

6.1.2 Moiré pattern on Graphite

Moiré pattern on HOPG was first reported and explained by Kuwabara *et al* [217] as resulting from the overlap between a mis-oriented top graphene layer and the underlying single graphite crystal. Xhie *et al* also observed giant lattices via STM that exhibited hexagonal symmetry on HOPG [218]. Cobalt particles deposited on the surface were found on the top sites of the Moiré pattern that suggested that the high LDOS at the Fermi level may determine adsorption sites for atoms and clusters.

Rong *et al* [202] observed a hexagonal superlattice with a periodicity of 66 Å on part of a graphite sample scanned by STM. They observed that a boundary, resembling a string of beads, of more than one micrometer long separated the HOPG(0001) cleavage plane into a normal graphite region and a superlattice region. A close up view of the superlattice is shown in Figure 6.1 (a) where the corrugation of both the atomic lattice and super lattice can be seen (see Figure 6.1 (b)). The hexagonal superlattice is a Moiré pattern caused by a 2.1^0 rotation of the top layer with respect to bulk and the STM contrast of the Moiré pattern comes from the strong influence of sub surface layers on the surface electronic structures near the Fermi level.

6.1.3 Moiré pattern in bismuth films

Chen *et al* [229] in their STM scans of the Bi-covered Au surface showed an apparent 0.02 ± 0.01 nm modulation in height which was interpreted as a Moiré pattern. The Moiré pattern formation on bismuth film on Au(111) substrate is shown in Figure 6.2 (a) that arises out of

mismatch between the bismuth overlayer and the underlying Au substrate (periodicity ~1 nm). The height modulation was seen only in one direction and indicated that the bismuth layer was incommensurate in only one lattice direction, in agreement with their surface X ray scattering (SXS) measurements.

Yaginuma *et al* [46] observed Moiré pattern on Bi(110) islands grown on $\sqrt{3}$ x $\sqrt{3}$ Si(111) substrate (shown in Figure 6.2 (b)). The Moiré pattern consists of stripes having a periodicity of ~13 Å. They prepared a schematic model of the of the rectangular lattice (shown in Figure 6.2 (c)) of the Bi(110) (grey dots) surface superimposed on the $\sqrt{3}$ x $\sqrt{3}$ lattice (black dots) which reproduces the Moiré pattern seen in the experiments. A comparison of the experimental result with the calculated Moiré pattern indicated that the Bi(110) lattice plane (d_{110}= 3.28 Å) is slightly expanded by 1.2% to match the $\sqrt{3}$ periodicity of (6.65 Å) in the $[11\bar{2}]_{Si}$ direction. Because of this commensurate relationship where $2d_{110} = \sqrt{3}\, a_{Si}$ (a_{Si} = 3.84 Å is a unit cell of the Si(111) plane), anisotropic island alignment takes place.

As far as we know Moiré pattern on bismuth films on HOPG substrate has never been reported previously. In the next section we present our experimental results on Moiré pattern recorded via STM, STS and AFM.

6.2 Results

6.2.1 Moiré pattern in STM images

In Figure 6.3 (a) we show an STM image of an island formed near the step edge of a HOPG substrate. The image was acquired at V_t = +1V and I_t = 500pA. As mentioned before in section 1.5 and [13, 16], most of the bismuth islands on HOPG prefer to align themselves to the symmetry axes of graphite. The bismuth island in the present case does not follow the symmetry of the underlying substrate indicated by the 44.5^0 angle it makes with the HOPG step edge. The misorientation is also seen in the variety of angles made by a 9 ML stripe on top of the island. The island of interest (show by the red arrow in (a)) also branches out to join another bismuth island seen in the lower left hand corner of the image.

In Figure 6.3 (b) we show the island of interest with a higher magnification. However, in this case the bias voltage was changed to V_t = +0.2V (I_t = 500pA). The red arrow in both images shows the same 5 ML stripe. Black arrows in Figure 6.3 (b) show the typical Moiré pattern which is formed on

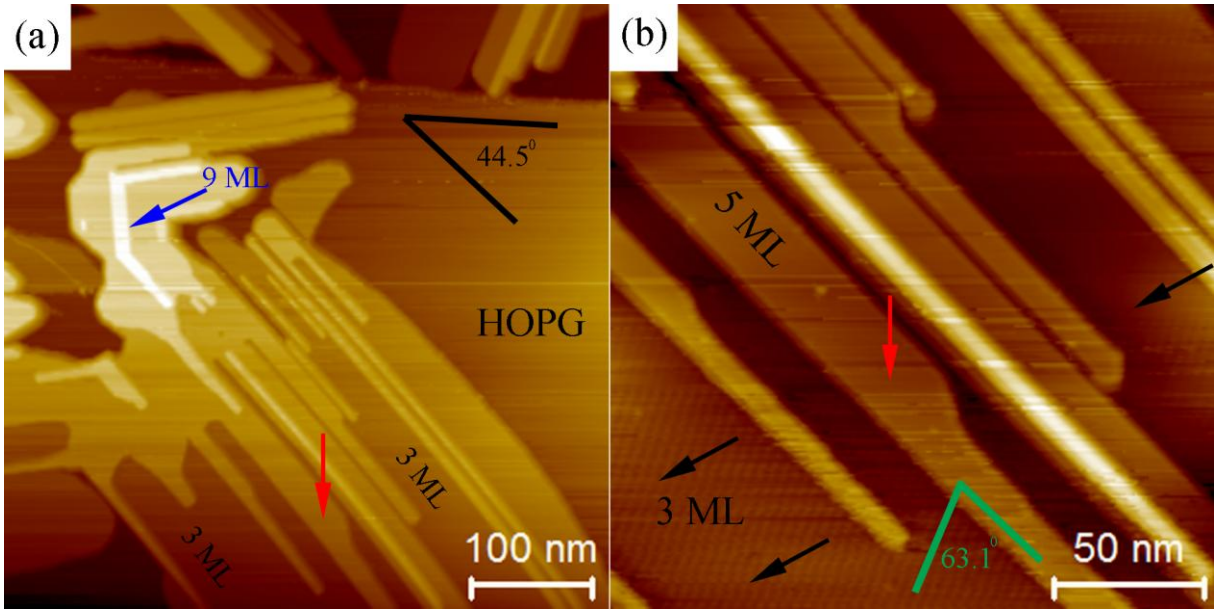

Figure 6.3: (a) STM image of an island formed near the step edge of HOPG (V_t = +1V, I_t = 500pA). The island shown by the red arrow is oriented at ~44.50 with the step edge. The blue arrows show abnormal angle formation in the 9 ML stripe. (b) A close up of the bismuth island shown in (a) (V_t = +0.2V, I_t = 500pA). Moiré pattern is visible (black arrows) on the 3 ML base which is oriented at ~63^0 to the main growth direction.

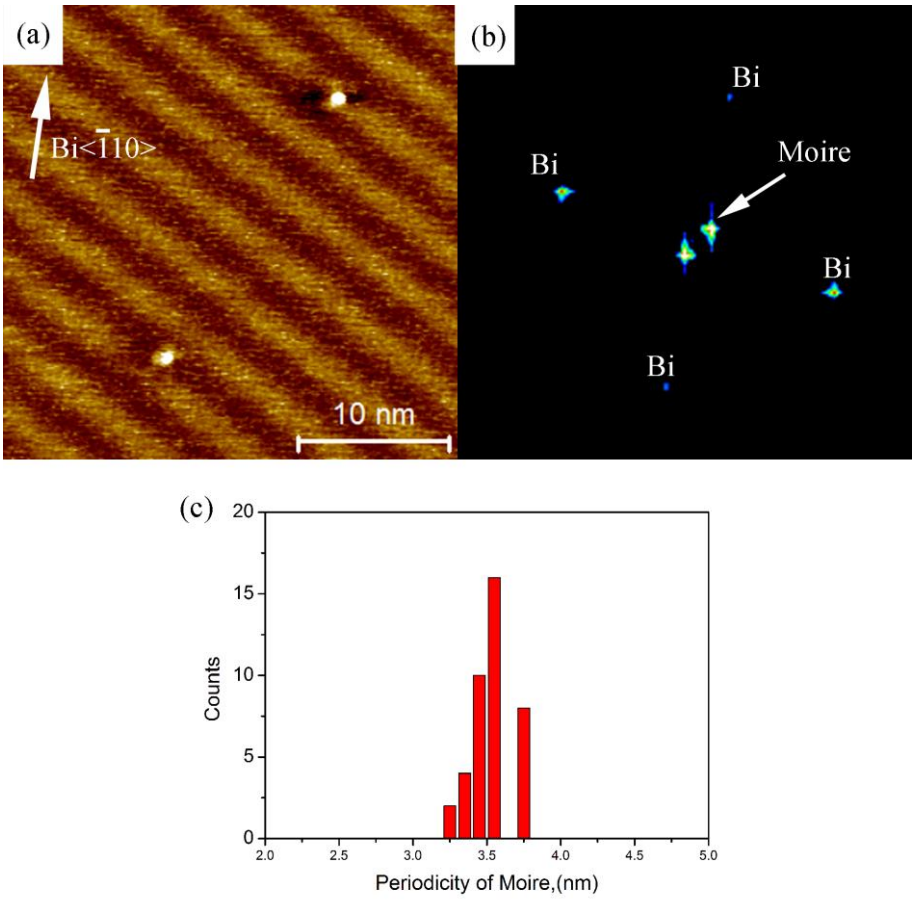

Figure 6.4: (a) Moiré pattern on a 3 ML base. Atomic rows are faintly visible in the background (V_t = +50mV, I_t = 1nA). The white arrow shows the main growth direction. (b) Fourier transform of the image shown in (a). Fourier spots corresponding to Moiré pattern are seen. (c) A plot showing the periodicity of Moiré pattern observed in our experiments

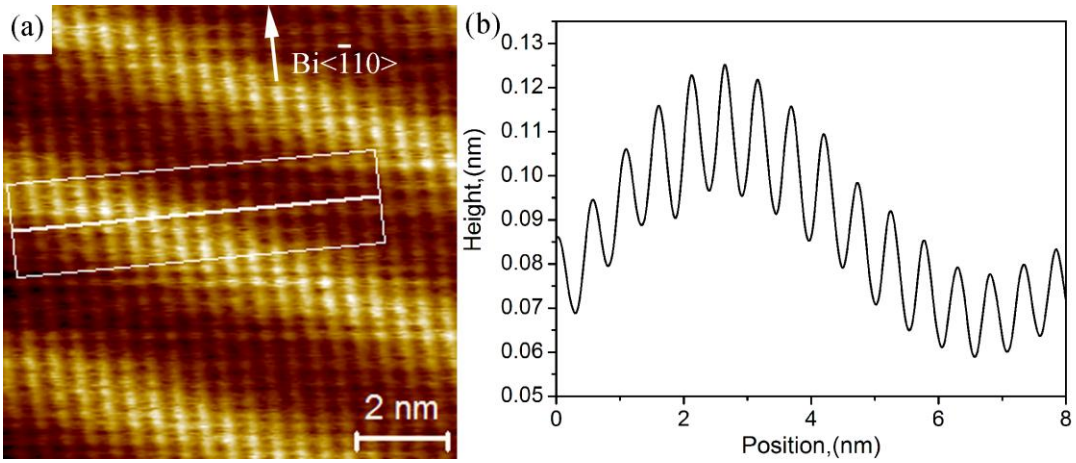

Figure 6.5: (a) Atomic resolution along with Moiré pattern on a 3 ML island (V_t = +50mV, I_t = 1nA) (b) Line profile corresponding to the white rectangle in (a).

the 3 ML base. The Moiré pattern is always oriented at ~60^0 to the main growth direction of the bismuth islands [43] and is typically observed in STM images at energies around Fermi level (~-100mV to +300mV).

In Figure 6.4 (a) we show another typical Moiré pattern on a separate bismuth island (V_t = +50mV, I_t = 1nA). Faint atomic resolution is visible in the background along with two defects. The main growth direction of the bismuth island is shown by a white arrow. In Figure 6.4 (b) we show a Fourier transform of (a) which shows six spots. The four spots on the periphery of the image correspond to bismuth lattice and two additional spots are seen in the middle of the image that corresponds to Moiré pattern. The angle between the Moiré pattern and Bi $< \bar{1}10 >$ direction can also be measured by inspecting the Moiré and bismuth lattice spots and it corresponds to ~60^0. The periodicity of the Moiré pattern formed in 3 ML islands in STM images was measured by Fourier transform and is shown in Figure 6.4 (c). The periodicity of the Moiré pattern shows a narrow distribution with a peak at ~3.6 nm.

In Figure 6.5 (a) we show an atomically resolved image of 3 ML island in which the Moiré pattern is seen very clearly. The image was recorded at V_t = +50mV and I_t = 1nA. The fast growth direction of the bismuth island is shown by the white arrow. The Moiré pattern is seen as three diagonal bright stripes in the image. It is interesting to see that the atoms in 3 ML island are resolved very clearly along with the Moiré pattern. A line profile drawn across the atomically resolved image is shown in Figure 6.5 (b). Individual bismuth atoms are seen as peaks in the line profile with a superimposed height modulation of the Moiré pattern.

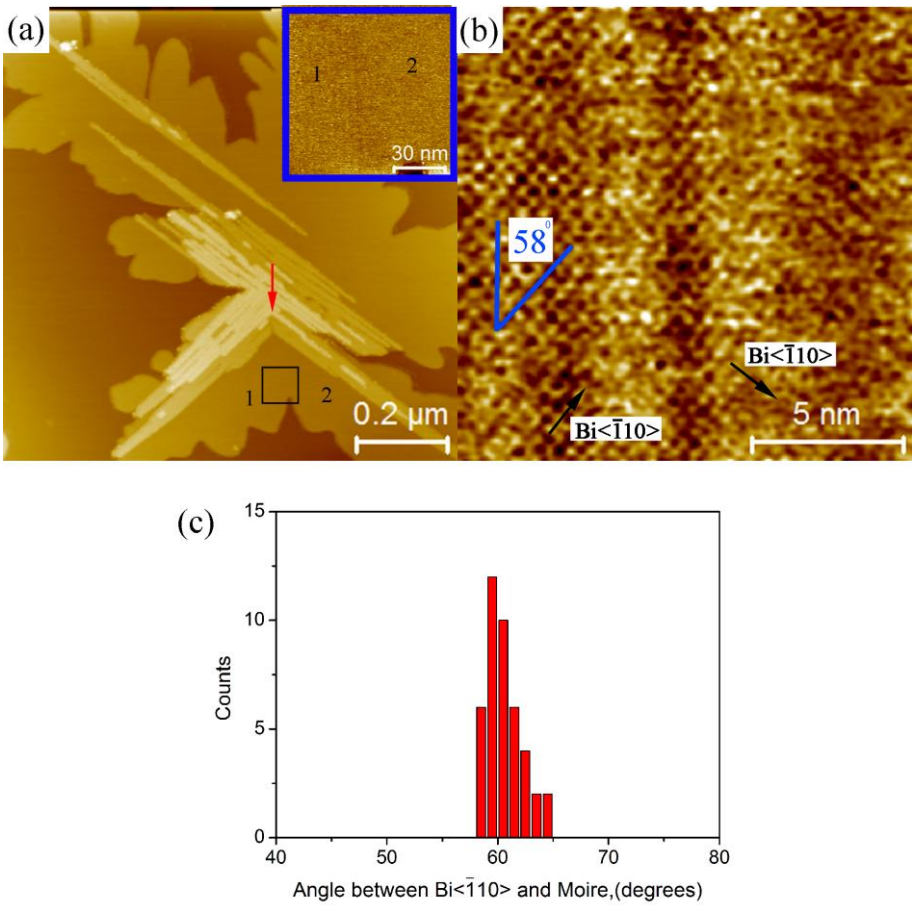

Figure 6.6: (a) STM image of a bismuth island in which one of the branches (labeled 1) grow out at 90^0 to the main growth direction (labeled 2) (V_t = -0.8V, I_t = 20pA). The blue inset shows a region shown by the black square(V_t = -0.3V, I_t = 20pA) (b) Closer inspection of the region shown by the black square in (a) (V_t = +0.2V, I_t = 200pA). The image show Moiré pattern on left hands side (island 1) and none on the right hand side (island 2). (c) A plot showing the angle between the Moiré pattern and Bi$< \bar{1}10 >$ direction.

The Moiré pattern divides the atomic rows into bright region and dark regions. The unit cell dimensions were investigated via Fourier transform of the atomic rows in the bright and dark region and it showed that the unit cell dimensions remained unchanged in the bright and dark regions. It is also interesting to see that the Moiré pattern is seen as a modulation in height in STM images that suggests that it could be associated with a morphological deformation on the surface of 3 ML island.

6.2.2 Influence of the orientation of the bismuth island

Moiré patterns are known to originate from misorientation of an overlayer with respect to the underlying substrate (see section 6.1.3). Therefore, we investigated the effect of the orientation of the bismuth island with respect to the underlying HOPG and the occurrence of Moiré pattern in our islands. An easy way to determine the orientation of a bismuth island is to observe the fast growth direction of that island with respect to the fast growth directions of the nearby islands, since most of the bismuth islands align themselves to the symmetry axes of graphite [13, 16].

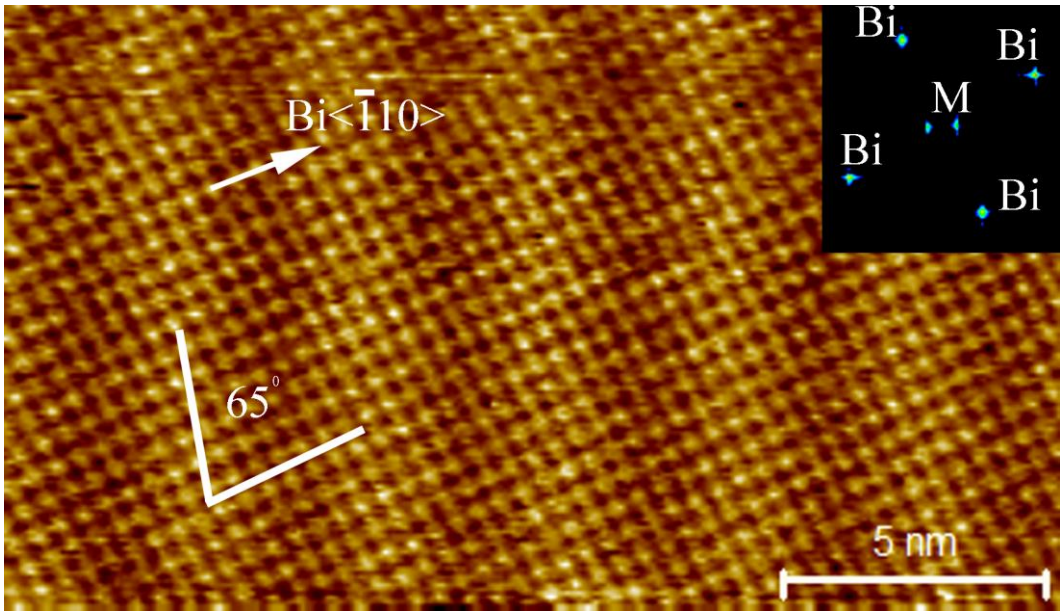

Figure 6.7: Moiré pattern on a 3 Ml bismuth island acquired at room temperature (V_t = +0.2V, I_t = 200pA). The inset shows the Fourier transform of the atomically resolved image.

In Figure 6.6 (a) we show an STM image recorded at 50 K on a bismuth island which has a typical Bi(110) island configuration with 3, 5 and 7 ML islands and stripes. Interestingly the stripes on are not parallel across the whole base and form a 90^0 angle (shown by red arrow). Such a situation indicates presence of two fast growth directions $< \bar{1}10 >$ in different regions of the base separated by a grain boundary. Another STM image (V_t = -0.3V, I_t = 10pA) taken in the black square region (shown in blue inset) show the presence of the Moiré pattern only on the base labelled number 1 and not on base labelled 2. Atomic resolution on the sample region in the black square in (a) is shown in Figure 6.6 (b). The Moiré pattern has a periodicity of ~3.4nm and is oriented at ~58^0 to the fast growth direction of base 1. The angle measured between the Moiré pattern and Bi $< \bar{1}10 >$ direction in other STM images is also predominantly around 60^0 (see Figure 6.6 (c)). This indicates that the Moiré pattern is associated with a change in orientation of the bismuth overlayer with respect to the substrate. However, the possibility of a charge density wave (CDW) also cannot be denied due to the interesting Fermi surface of bismuth. In section 3.5 we discussed that extremely small changes to the unit cell could lead to splitting of bands in the 3 ML band structure which could give rise to nesting vectors. However, nesting vectors and CDW are usually observed on bismuth films at very low temperatures [230, 40, 71]; thus we performed measurements at room temperature to determine if nesting vectors or CDW were responsible for the observed Moiré pattern.

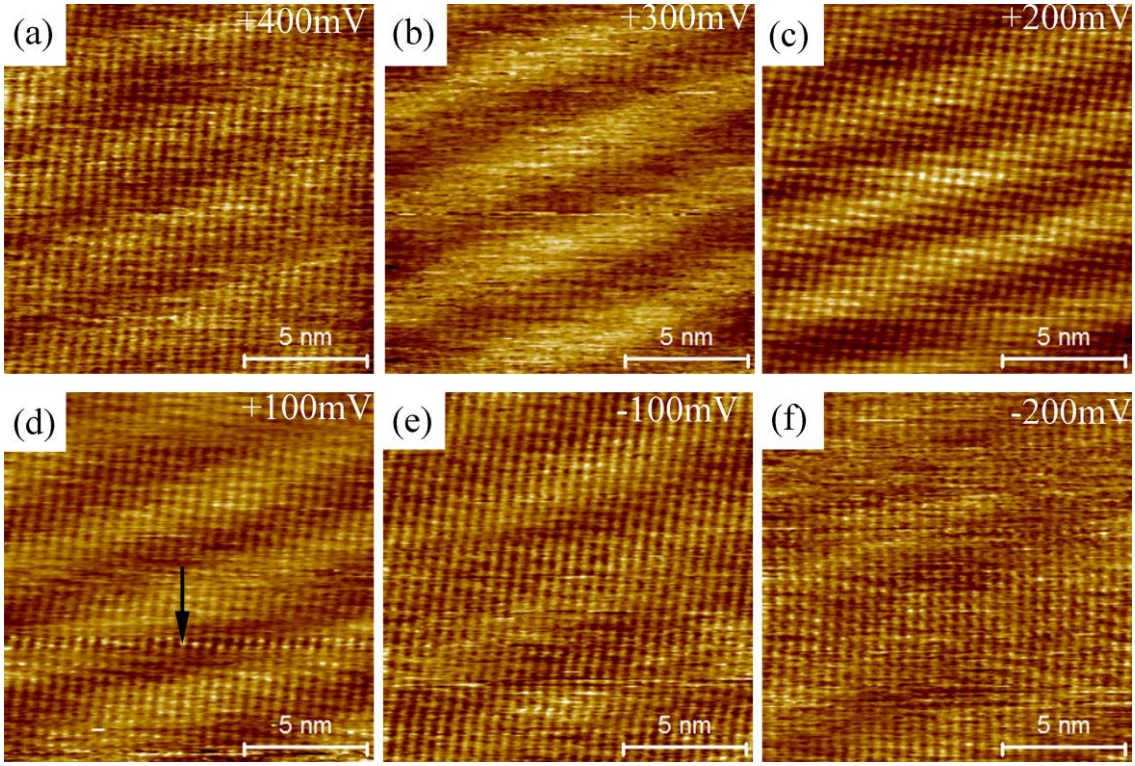

Figure 6.8: STM images taken at constant I_t = 200pA with (a) V_t = +400mV (b) V_t = +300mV (c) V_t = +200mV (d) V_t = +100mV (e) V_t = -100mV (f) V_t = -200mV. Sample temperature was 50 K.

In Figure 6.7 we show an atomically resolved STM image which was acquired at room temperature on a 3 ML island. The inset shows the Fourier transform of the STM image and the Moiré spots are visible clearly along with the lattice spots. The periodicity measured via Fourier transform is ~3.5 nm and the angle between Bi$< \bar{1}10 >$ and Moiré pattern is ~65^0. This image indicates that temperature has no influence on the Moiré pattern. It is therefore clear that the Moiré pattern is a result of misorientation between the overlayer and the substrate; and CDW or nesting does not contribute to the formation of Moiré pattern.

6.2.3 Bias dependence of Moiré pattern

To study the bias dependence of the Moiré pattern we conducted an experiment in which the tunneling current was kept constant (I_t = 200pA) and the bias voltage was changed in steps (+400mV to -200mV). STM images were recorded for each bias voltage step and are shown in Figure 6.8. The STM images shown in Figure 6.8 suffer from slight drift; therefore comparison of the exact position of the Moiré pattern in individual images is not possible. However, the images show the appearance and disappearance of the Moiré pattern as a function of bias voltage.

In Figure 6.8 (a) the Moiré pattern is seen faintly when V_t = +400mV. Atomic rows of bismuth atoms are also visible in the image. In Figure 6.8 (b) the bias voltage was changed to +300mV and in

this image the Moiré pattern is seen very prominently as a bright stripe diagonally across the image. However, atomic rows of atoms are not visible on the Moiré pattern. It appears as if the atomic rows of bismuth atoms hide behind the Moiré pattern. As the bias voltage is changed to +200mV in Figure 6.8 (c) the atomic rows and the Moiré pattern are both seen. In contrast to the image in (b) the rows of atoms are seen more clearly on the Moiré pattern. The tip is seen to interact with the 3 ML island and disturb few rows of scan in the middle part of the STM image. In Figure 6.8 (d), V_t = +100mV, the Moiré pattern is seen clearly. The atomic resolution on the Moiré pattern is also visible but is not as sharp as (c). Very interestingly, in a few lines of the scan in (d) the STM tip interacts with the island and in those lines the tip changes and the rows of atoms are seen very sharply. The sharpness of the image in those few lines shown by a black arrow in (d) is comparable to the atomic resolution achieved in (c). This indicates that the sharpness of the image or the Moiré pattern is affected by tip conditions. The Moiré pattern starts to become faint in Figure 6.8 (e) and (f) and disappears at higher negative bias voltages.

The images in Figure 6.8 indicate that the Moiré pattern shows some bias dependence and appears at energies close to the Fermi level. However, in the above experiment the tip-sample distance changes simultaneously with the change in bias voltage. It would be useful to keep the tip sample distance constant and then change the bias voltage and see if the Moiré pattern appears in a narrow band of energies around the Fermi level. Such kind of experiment is possible via STS and is discussed in next section.

6.2.4 CITS on Moiré pattern

In Figure 6.9 (a) we show an STM topograph of a region of a 3 ML island with a 5 ML stripe on top. CITS (±1V, 1.5nA) was performed in the region shown in (a) and the corresponding dI/dV maps of the region in (a) are shown in (b)-(h). Only selected bias voltages are shown to highlight important features. A Moiré pattern can be seen in the dI/dV maps in the bias voltage range between ~+200mV to -30mV (see red arrows in (d), (e) and (f)). The angle between the fast growth direction of the bismuth island and the Moiré pattern was measured as ~65^0. The Moiré pattern seen in CITS dI/dV maps are very similar to the ones observed in STM images e.g. they are observed at energies close to the Fermi level and they form similar angles between the Bi$< \bar{1}10 >$ direction and the Moiré pattern.

It is difficult to see any kind of dispersion in the Moiré pattern as a function of bias voltage in the dI/dV maps therefore a line profile was drawn on the Moiré pattern (see black line in Figure 6.9

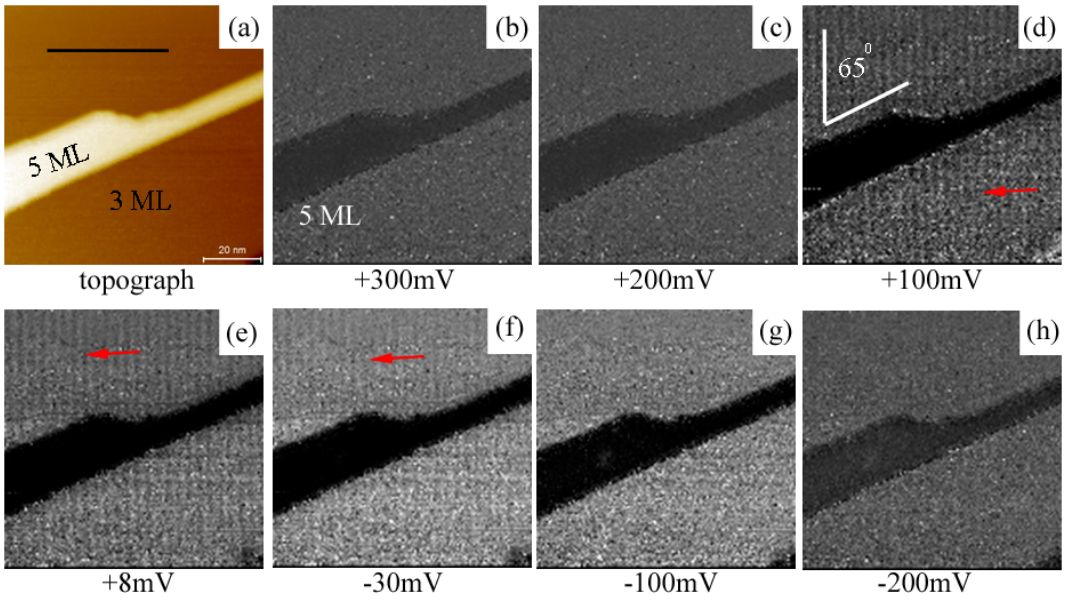

Figure 6.9: (a) STM image of a 3 ML island with a 5 ML stripe on top of it. (V_t = +1V, I_t = 100pA). (b)-(h) are CITS dI/dV maps showing the evolution of LDOS in the region. Selected bias voltages are shown to highlight important features. Moiré pattern is seen forming between +200mV to -30mV and is indicated by red arrows in (d), (e) and (f). The angle between the Moiré pattern and Bi$< \bar{1}10 >$ direction is shown in (d).

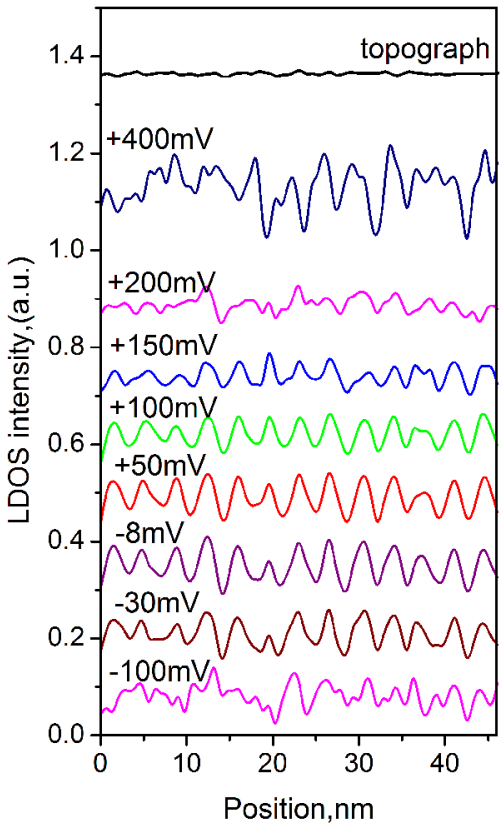

Figure 6.10: Line profiles corresponding to the black line shown in Figure 6.9 (a). The line profiles are drawn as a function of bias voltage. The first black line is recorded on STM image and the rest are dI/dV data.

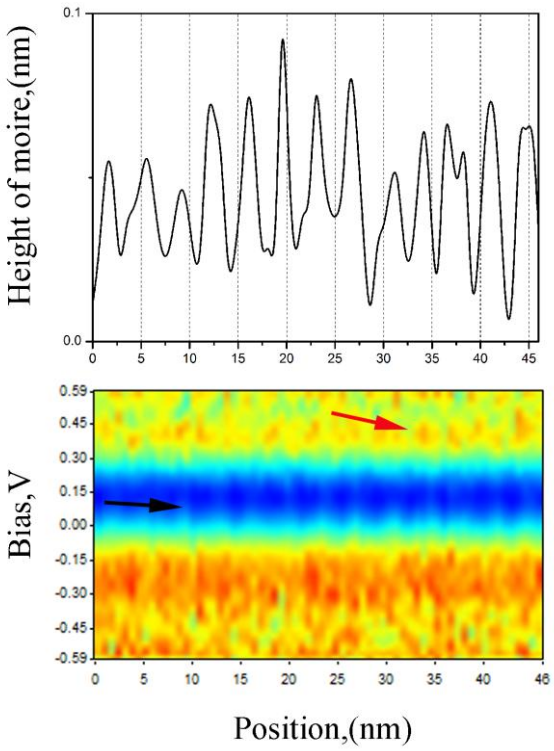

Figure 6.11: Line profile recorded at +100mV (taken from Figure 6.10) compared to its corresponding LDOS intensity plot. Black arrow shows modulation in the LDOS valley over Moiré pattern. The red arrow shows modulation in the LDOS peaks at ~+350mV.

(a)) as a function of bias voltage and is shown in Figure 6.10. The top black line in the image is topograph and the rest coloured lines are dI/dV data. The Moiré pattern is not visible between +400mV to +200mV. The peaks and troughs associated with Moiré pattern start to appear ~+150mV and are observed strongly between +100mV to -30mV. They disappear as the bias voltage approaches -100mV. The Moiré pattern doesn't show any kind of dispersion as a function of bias voltage i.e. the peaks do not shift or change their position as the bias voltage is changed. The periodicity as measured from the line profiles is ~3.5 nm (similar to STM images).

After establishing the non dispersive nature of the Moiré pattern we now turn to the LDOS associated with it. In Figure 6.11 (a) we show the +100mV line profile taken from Figure 6.10 and compare it to its LDOS intensity map shown in Figure 6.11 (b). The LDOS valley of the 3 ML island shows a distinct periodicity which appears as a modulation in shades of blue (see black arrow in Figure 6.11 (b)). This is an indication that the intensity of the LDOS minimum oscillates with the Moiré pattern. The LDOS peaks at ~+0.35 V also show a distinct modulation in intensity as shown by the red arrow in Figure 6.11 (b). Interestingly, the oscillation in the LDOS peaks at ~+0.35 V also has the periodicity of the Moiré pattern. If observed closely a faint periodicity is also visible in the LDOS peaks at higher negative energies.

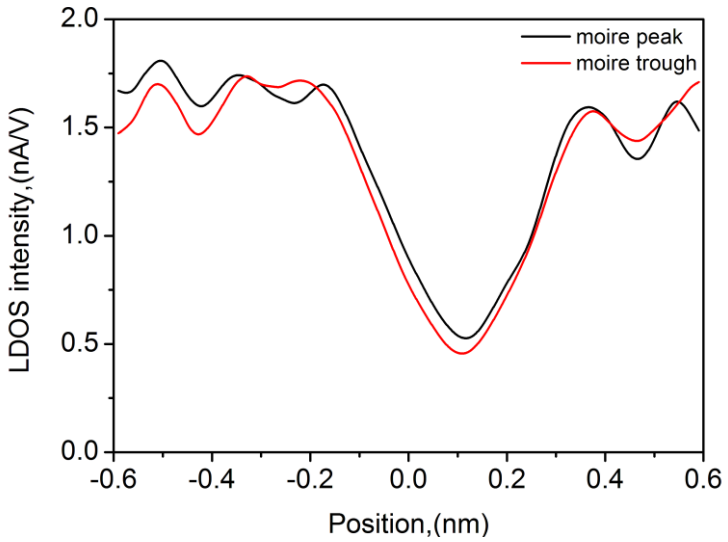

Figure 6.12: dI/dV(V) curves associated with Moiré peak (black) and trough (red).

In Figure 6.12 we show individual dI/dV curves extracted from a Moiré peak and Moiré trough. The black curve (Moiré peak) is slightly higher than the red (Moiré trough) at energies near the Fermi level, more specifically between ~+200mV to -100mV. This is the energy range in which the Moiré pattern is observed in the CITS dI/dV maps (and also similar to energy range observed in STM). The intensity of the LDOS peak at ~+350mV is also higher in the black (Moiré peak) curve as compared to the red curve, which results in the modulation of the LDOS peak in the LDOS intensity maps shown in Figure 6.11. There are also LDOS oscillations in peak at higher negative energies e.g. at -0.2V the red curve is higher in intensity than the black curve. To investigate the oscillations in the LDOS peaks in the LDOS intensity maps more closely, we performed CITS measurements in the bias voltage range ±0.35V (see next section).

6.2.5 Contrast inversion in CITS maps

In Figure 6.13 (a) we show an STM image (V_t = +0.35V, I_t = 1nA) of a 3 ML base with a 5 ML stripe on top of it. CITS was performed (±0.35V, 1.5nA) on the region shown in (a) and the corresponding maps are shown in (b)-(h). The Moiré pattern is visible clearly between +100mV to -100mV. Interestingly the Moiré pattern is visible very sharply in the negative bias voltages (i.e. -100mV) as compared to the ±1V dI/dV data in Figure 6.9. It must be noted that the tip sample distance is smaller in the ±0.35V CITS experiment as the set point voltage is V_t = +0.35V. This indicates that there is an effect of the tip sample distance in resolving the Moiré pattern. The CITS dataset recorded in ±0.35V is interesting because the STM topograph associated with it also exhibits the Moiré pattern. This gives an opportunity to compare the Moiré pattern observed in the STM images directly with the Moiré pattern in CITS dI/dV maps.

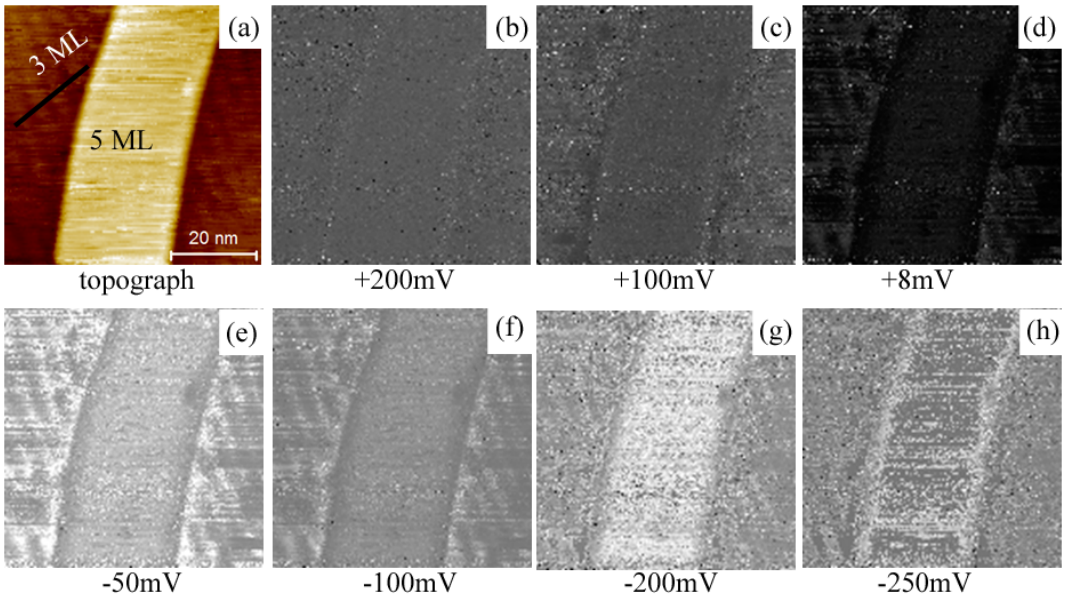

Figure 6.13: (a) STM image of a 3 ML base with a 5 ML stripe on top (V_t = +0.35V, I_t = 1.5 nA). (b) – (h) are CITS dI/dV maps. Moiré pattern is seen clearly between +100mV to -200mV.

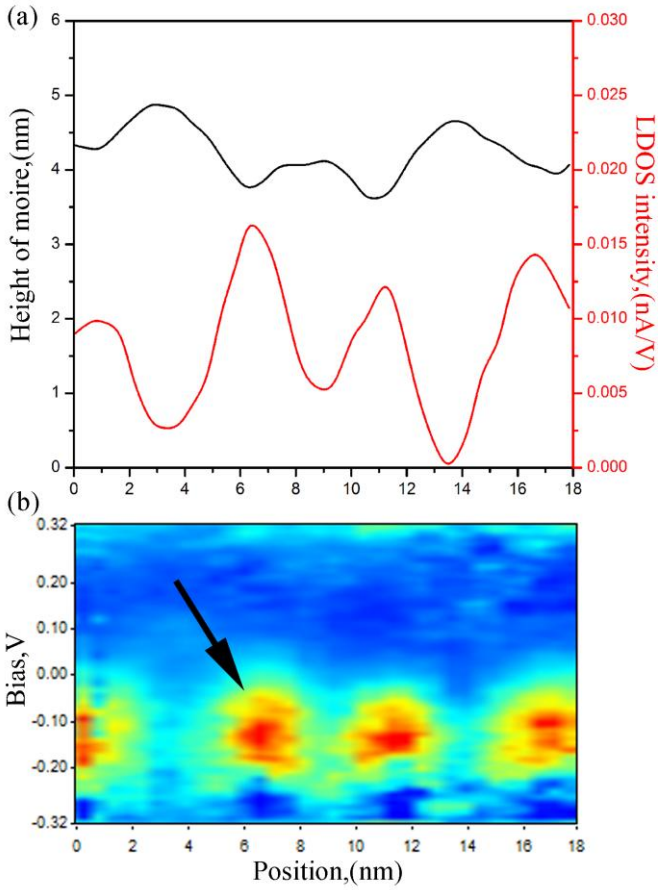

Figure 6.14: (a) Line profile from STM topograph in Figure 6.13 (a) compared to dI/dV(V) line profile at +100mV (red). (b) Corresponding LDOS intensity plot showing modulations in LDOS peaks at ~ -150mV.

A line profile was drawn on the 3 ML base in the STM topograph (black line in Figure 6.13 (a)) and on the +100mV dI/dV map. These line profiles are shown in Figure 6.14 (a) and are compared to the corresponding LDOS intensity plot shown in (b). Very surprisingly, the line profiles on the STM topograph and the dI/dV map do not coincide together. The peaks in the STM line profile correspond to troughs in the dI/dV data. This indicates that there is contrast inversion of the Moiré pattern in the CITS dI/dV maps with respect to the STM images. The periodicity of Moiré pattern measured by the line profile is ~4 nm. The deviation of the Moiré periodicity from its typical value of 3.5 nm is attributed to thermal drift during the CITS data acquisition. The effect of the drift can be clearly seen in the STM image shown in Figure 6.13 (a), where the edges of 5 ML stripe can be seen bending in shape of a parabola. The LDOS intensity plot in Figure 6.14 (b) shows very clear modulation in intensity of the LDOS peak at ~-150mV (see black arrow in Figure 6.14 (b)). The LDOS peak corresponds to a clear maximum in the dI/dV line profile in (a).

6.2.6 Energy range of Moiré pattern in CITS experiments

CITS was performed on the Moiré pattern for the voltage ranges ±1V, ±0.8V, ±0.5V, ±0.35V and ±0.2V. The tunneling current was kept constant at 1.5 nA in those experiments and the appearance and disappearance of the Moiré pattern was noted in the CITS dI/dV maps. In Figure 6.15 (a) we summarize the energy range in which the Moiré pattern was observed in all the CITS experiments. The black squares are energies where the Moiré pattern starts to appear in the dI/dV maps and the red circles depict the energy at which the Moiré pattern disappears. It is seen that the Moiré pattern in most of the cases is visible between ~+150mV to -50mV. There are two exceptions in which the Moiré pattern is visible at higher negative bias voltages till ~-200mV.

To understand the influence of the tip sample distance on the appearance and disappearance of Moiré pattern in CITS dI/dV maps, the energy range of the Moiré pattern was plotted against the stabilization bias voltage in Figure 6.15 (b). It can be seen that changing the polarity and the amplitude of the stabilization bias voltage has little effect on the energy of the Moiré pattern. For example when the stabilization bias voltage was set to V_t = +1V then the Moiré was visible between ~+150 to -50mV and when V_t = -1V then also the Moiré was visible between ~+150mV to -50mV.

An effect on the Moiré pattern is seen when the stabilization bias voltage is decreased below +0.5V. This results in a decrease in the tip sample distance and in these experiments the tip usually

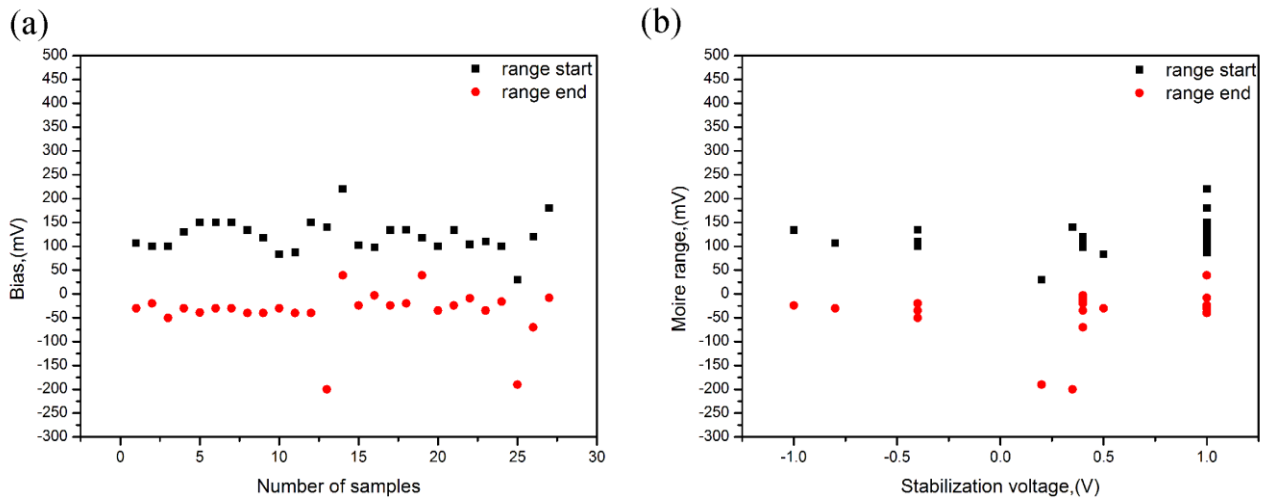

Figure 6.15: (a) Plot showing the distribution of occurrence of Moiré pattern on an energy scale. (b) Plot showing the dependence of Moiré pattern occurrence on stabilization voltage.

interacts a lot with the island. However measurements were possible in a few cases and in those cases the Moiré pattern was resolved even at higher negative bias voltages e.g. ~-200mV.

6.2.7 Moiré pattern in NCAFM

To ascertain the morphological or electronic origin of the Moiré pattern observed in bismuth films on HOPG we performed NCAFM experiments. We were unable to perform contact AFM experiments as the contact probe interacts strongly with the bismuth islands and in most cases destroys them. The NCAFM experiments were performed on two kinds of samples- (i) islands with small lateral extent (ii) islands with large lateral extent.

In Figure 6.16 (a) we show an NCAFM image of bismuth islands with small lateral extent. It can be seen that the islands are much smaller and the density of islands is higher. There is only one 5 ML stripe on top of each 3 ML base. The island that was deemed suitable to investigate the Moiré pattern is shown in the black circle in (a) and labelled 2. The island inside the circle forms an angle 54^0 with the fast growth direction of the adjoining main island labelled 1. The circled island is shown with higher magnification in Figure 6.16 (b). It can be seen that a Moiré pattern is visible only on the island labelled 2 and is absent on island labelled 1. The Moiré pattern forms an angle of ~55^0 with the Bi$< \bar{1}10 >$ direction of island 2. It is interesting to note that the periodicity of the observed Moiré pattern is ~8-9 nm which is almost triple than the observed periodicity in STM and CITS experiments.

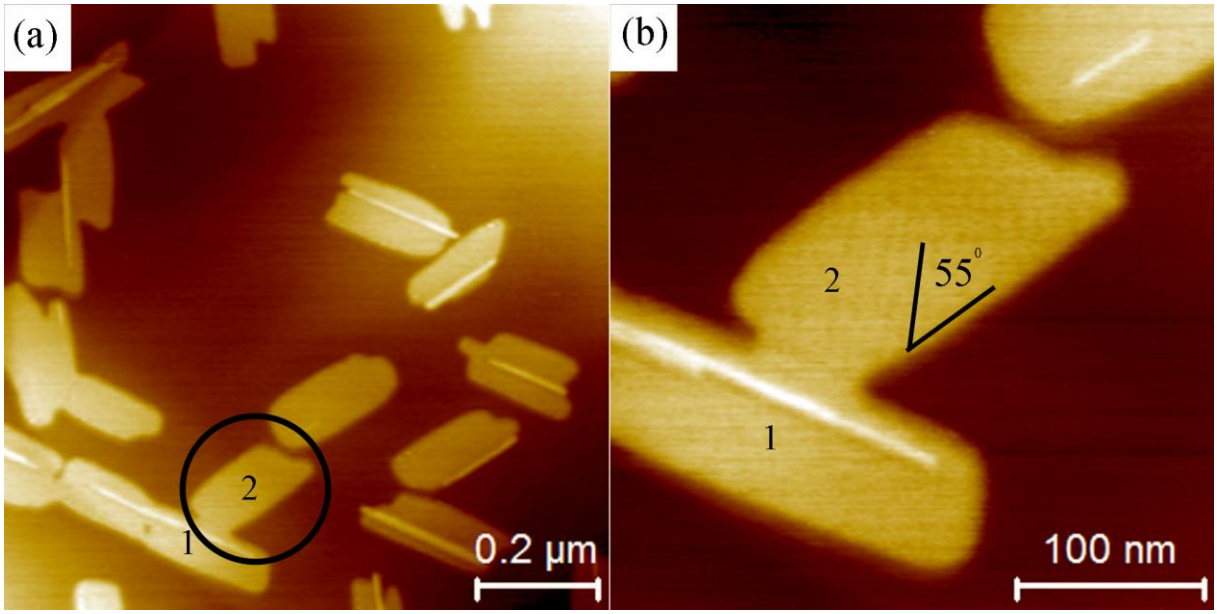

Figure 6.16: (a) NCAFM image of a region showing bismuth islands. Island labeled 2 is of interest because it forms 55^0 with the main island 1. (b) Close up of island 1 and 2 showing presence of Moiré pattern only on island 2.

In section 6.2.2 we established that the Moiré pattern is formed due to the misorientation between the bismuth island and the underlying HOPG substrate. However, in the NCAFM images of bismuth islands we observe something peculiar. The Moiré pattern on bismuth islands in the NCAFM images is present on random islands irrespective of the orientation of the island (see Figure 6.17). In Figure 6.17 (a) we show an NCAFM image which shows bismuth islands oriented at 60^0 with respect to each other. The sample region bounded by the black square and blue square were investigated at higher magnification and are shown in (b) and (c) respectively. In Figure 6.17 (b) we can see that there is only one island in the frame (shown by red arrow and labelled 1) which exhibits a faint Moiré pattern. The other two islands (shown by white arrows and labelled 2 and 3) do not show any Moiré pattern. This phenomenon is interesting because island 3 is parallel to 1 and thus should exhibit Moiré pattern as they both share the same orientation. In (c) the Moiré pattern on island 1 is seen clearly. Interestingly, island 1 and 4 exhibit Moiré pattern but island 3 which is also in the same orientation doesn't show any Moiré. The periodicity observed in these NCAFM images is also ~8-9 nm.

The observation of Moiré patterns in NCAFM images indicates that the Moiré pattern on bismuth islands is morphological in nature. However, the Moiré pattern observed in NCAFM images differs significantly from the STM and CITS measurements. The periodicity in NCAFM images is roughly three times that of the ones observed in STM. The Moiré pattern observed in NCAFM images also do not obey the misorientation principle and appear randomly on some islands. Interestingly, the Moiré pattern is also not observed in NCAFM images acquired on islands with large lateral

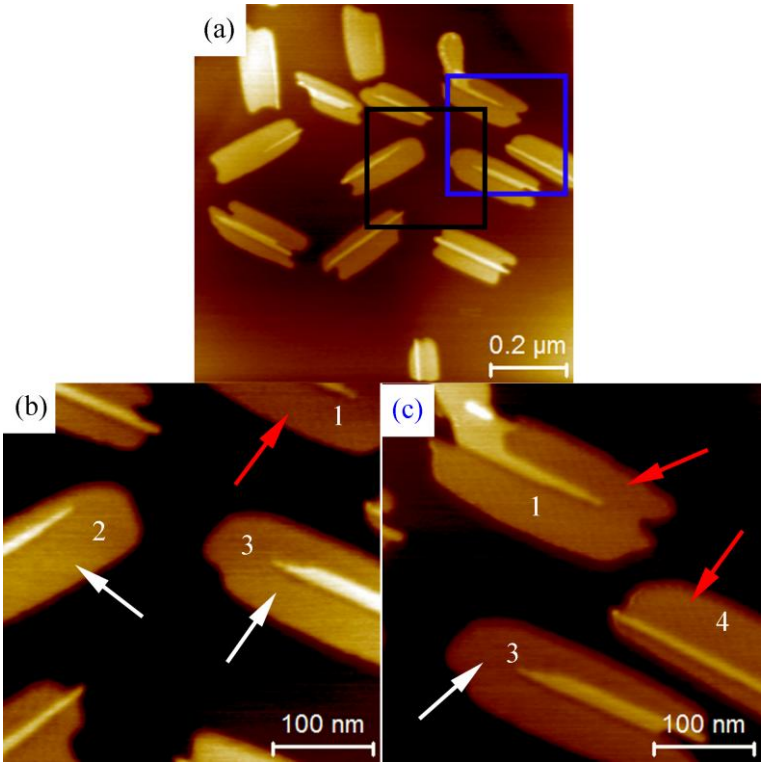

Figure 6.17: (a) NCAFM image of bismuth islands. The black and blue squares are shown in higher magnification in (b) and (c). (b) The islands 2 and 3 shown by white arrows show no Moiré pattern. Island 1 shown by red arrow shows faint Moiré. (c) The islands 3 and 4 shown by white arrows show no Moiré while the island 1 shown by red arrow shows Moiré pattern clearly.

extent. These observations suggest that the Moiré pattern observed via the NCAFM images have a different origin and have completely different set of characteristics which needs more investigation.

6.2.8 Preliminary calculations on Moiré pattern

Dr Pawel Kowalczyk has performed simulations to understand the origin and nature of the Moiré pattern in bismuth islands on HOPG substrate based on a simple superposition model of Bi on HOPG. The calculations took into account any changes in the unit cell which could result out of stress at the film-substrate interface (The simulation was performed for seven different combination of unit cells as seen in Figure 6.18). Results of the simulations are shown in Figure 6.18 in two parts. Figure 6.18 (a) shows the dependence of the angle between the Moiré pattern and Bi$< \bar{1}10 >$ direction. Figure 6.18 (b) shows the periodicity of the Moiré pattern vs the overlayer rotation in respect to underlying HOPG (where 0^0 indicate Bi$< \bar{1}10 >$ ||HOPG$< 110 >$) for a few different unit cell dimensions.

The data in the (a) reveals that Moiré pattern can be seen nearly for all rotation angles and this angle weakly depends on surface unit cell selection. In these simulations two kinds of symmetries

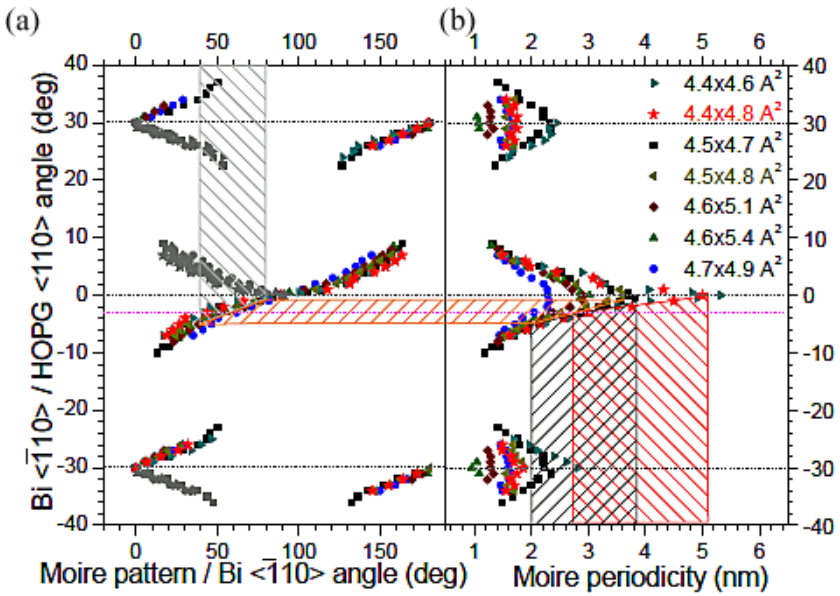

Figure 6.18: Preliminary slab calculations showing misorientation between HOPG and Bi. (See text for details).

were identified; first one related to the substrate three fold symmetry which results in the same pattern every 60^0, and the other one is related to the experimental difficulty of finding the Bi$< \bar{1}10 >$ and Bi$< 1\bar{1}0 >$ directions which leads to situation in which one cannot properly measure the angle between the Moiré pattern and fast growth direction $< \bar{1}10 >$.

For experimentally observed Moiré pattern angles (angle between Moiré pattern and Bi$< \bar{1}10 >$ direction) equalling ~50^0-70^0, it is observed that the overlayer is rotated by $\pm 5^0$ with respect to the HOPG. The corresponding Moiré periodicity in the calculations ranges between ~2-4 nm (close to experimental periodicity of 3.6 nm in STM and CITS experiments). The Moiré periodicity also shows strong dependence on the surface unit cell dimensions. Good agreement between the experimentally observed Moiré pattern and the calculations is achieved when the estimated surface unit cell equals 0.44 nm x 0.48 nm (red star symbol) which is close to the measured unit cell in our experiments (see section 3.2.2). For Moiré angle in range 40^0-70^0 (grey dashed in region in left plot), the over layer rotation is ~$\pm 3^0$ which corresponds to a periodicity in the range of 2.8-5.5 nm.

The calculation shown in Figure 6.18 satisfactorily explains the occurrence of Moiré pattern in STM and STS data but fails to explain the Moiré pattern observed in NCAFM experiments. The Moiré pattern in NCAFM experiments are observed on islands which do not follow the 'misorientation principle' for observing Moiré pattern on the overlayer. We speculate that the origin of Moiré observed in STM and NCAFM could be different. However, more experiments and calculations are needed to conclusively comprehend Moiré pattern observed via NCAFM.

6.3 Summary

Moiré patterns were observed on some of the 3 ML base of Bi(110) islands via STM imaging. The Moiré pattern appears in the STM images at energies close to the Fermi level. It shows a distinct periodicity of ~3.5 nm and is oriented at ~60^0 to the Bi$< \bar{1}10 >$ direction which is independent of bias voltage. There is a very pronounced effect of the misorientation of the bismuth island with respect to the underlying graphite which gives rise to Moiré pattern. The misorientation of the bismuth island can be interpreted by comparing it to neighbouring islands. Interestingly the Moiré pattern often appears with atomically resolved rows at low bias voltage scans which is quite similar to Figure 6.2 in section 6.1.3. The sharpness of the Moiré pattern in STM images is also affected by tip conditions.

The Moiré pattern doesn't depend on temperature and can be observed both at room temperature and 50 K. The orientation of the Moiré pattern with respect to the Bi$< \bar{1}10 >$ direction and the periodicity doesn't change with temperature. This observation indicates that the Moiré pattern is not caused due to any charge density wave because they are observed mostly at very low temperatures in bismuth thin films. We also note here that the expansion coefficient of bismuth [231] and graphite [232-234] are 10.8 x 10^{-6} and 14.7 x 10^{-6} respectively between 100 to 500K. Therefore the extent of changes in lattice parameters with respect to temperature is extremely small and consequently the lattice mismatch leading to Moiré pattern formation will not be affected by temperature.

To understand the bias dependence of Moiré pattern, CITS was performed on bismuth islands. The Moiré pattern is also observed in CITS dI/dV maps in which it appears in a bias voltage range between ~+200mV to -30mV. The periodicity and orientation of the Moiré pattern is similar to that observed in STM images. The peaks and troughs associated with the Moiré pattern do not shift as a function of bias voltage which was demonstrated by drawing line profiles across the dI/dV maps. An LDOS intensity plot associated with the line profile shows modulations in the LDOS valley which exhibits correlation with the Moiré pattern's peak and trough. Modulations in intensity of LDOS peaks was also recorded at +350mV and -150mV. In the CITS performed at voltage range ±0.35V the Moiré pattern appeared between +30mV and -200mV. Very clear modulations were observed in the LDOS peaks which were associated with the Moiré pattern. A contrast inversion was observed between the Moiré pattern in STM image and CITS dI/dV maps.

NCAFM measurements were carried out on two sets of samples (i) islands with small lateral extent and (ii) islands with large lateral extent. Interestingly, the Moiré pattern was observed in NCAFM images recorded only on the islands with small lateral extent. The Moiré pattern observed in NCAFM images differs completely from the ones observed via STM. The periodicity of the Moiré observed in NCAFM images is ~8-9 nm and it is observed on few islands with random orientation.

We also presented preliminary calculations performed by Dr Pawel Kowalczyk that satisfactorily predict the periodicity and the angle of the Moiré pattern observed in STM and CITS results. However, we are unable to find any match between the calculations and the Moiré pattern observed in the NCAFM results. We speculate that the Moiré pattern observed in NCAFM has a completely different origin than the ones observed in STM and more detailed experiments and calculations are required to understand the NCAFM results.

7. NaCl on HOPG

NaCl is an insulator but ultra thin films of NaCl have been reported to be conducting enough for STM measurements [222, 235-237]. The NaCl ultra thin films have been a topic of interest as they decouple the electronic density of states of molecules or nanoparticles deposited on top with that of the underlying substrate. In this chapter we describe the deposition of NaCl on HOPG and the formation of cross shaped islands on HOPG terraces. Large flat islands can be obtained when the local flux is low enough. The topography and morphology of the islands were extensively studied by non contact atomic force microscopy (NCAFM). We deposited bismuth on top of the pre-existing NaCl/HOPG islands to study and understand the electronic interaction of the bismuth film with the HOPG substrate. We also report results from STM and STS measurements on NaCl islands.

7.1 Literature review

Ultra-thin insulating films have been identified as potential substrates for investigations of atomic, molecular and nanoscale systems in STMs [222, 235-238]. These insulating layers are used to decouple the electronic structure of the system of interest from the substrate, which allows the local properties of the adsorbate to be probed [236, 237, 239-243]. NaCl films are of particular interest because atomically flat films can be produced. NaCl has been deposited with varying degree of success on Cu(311) [238], Cu(532) [244], Au(111) [236], Ag(100) [222], Ge(100) [245] and Al(111) [242] substrates.

The growth and morphology of NaCl islands have been studied by tapping mode atomic force

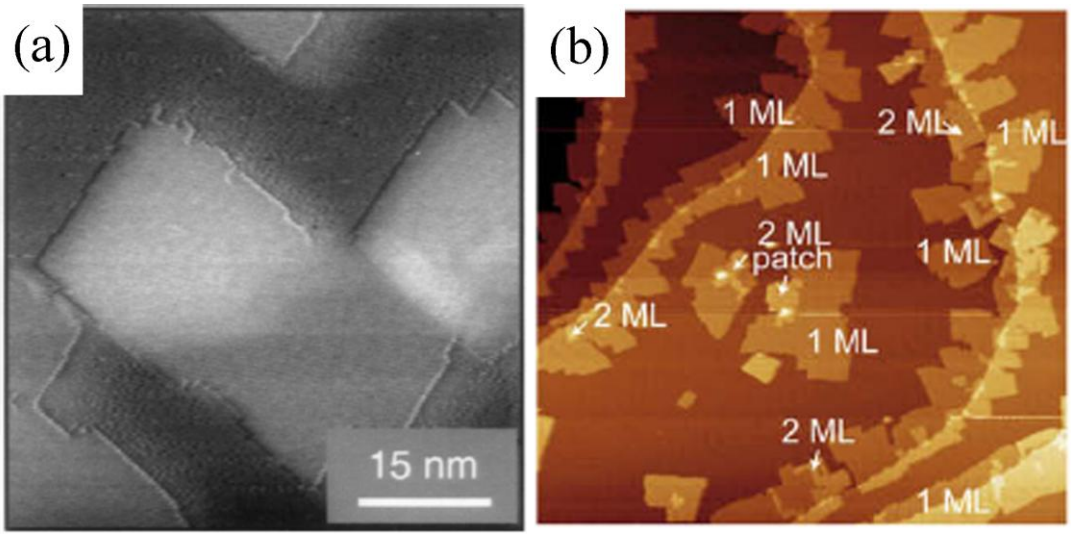

Figure 7.1: Tapping AFM images of monatomic NaCl islands grown on top of a continuous NaCl film which covers a step of the Cu(111) substrate. Image reproduced from [246] (b) STM images of the surface topography resulting from deposition of NaCl on Au(111) at 180 K. Steps act as nucleation sites for the growth of straight edged NaCl islands. Image reproduced from [239]

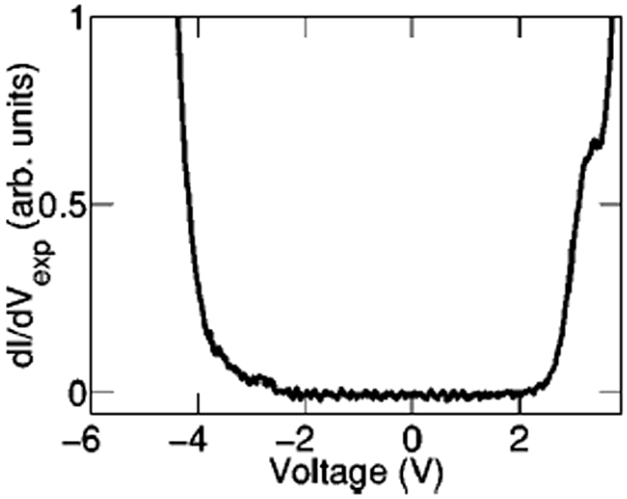

Figure 7.2: Experimental dI /dV spectrum for a monolayer NaCl on Cu(311). The tip-sample distance corresponds to a current set point of I_t =0.3 nA at V_t = 3.8 V. Image reproduced from [238]

microscopy, non contact AFM and STM. In Figure 7.1 (a) we show images of NaCl islands on Cu(111) acquired via tapping mode AFM [246]. NaCl on Cu(111) grows in 'carpet like' fashion i.e. it covers the Cu(111) step as a carpet. In Figure 7.1 (b) we show an image of NaCl islands on Au(111) which was acquired by STM [239]. The growth mode of NaCl on Au(111) is also 'carpet like'. This well-known carpet-like overgrowth of steps, kinks, and defects [247] is due to strong internal cohesion of the film, which avoids misfit dislocations in the NaCl layer. However, the growth of NaCl islands is not carpet like on all substrates. NaCl islands on Cu(311) exhibits a remarkably strong and localized binding between adlayer and substrate and show preferential nucleation on the $< 311 >$ step edges owing to minimized interface energy between NaCl overlayer and Cu template [235]. The polar nature of alkali halides such as NaCl plays an important role in the binding to the substrate. The deposition of NaCl on metal surfaces and its interaction with them in the form of Coulomb forces have long been established [235, 238].

7.1.1 STS on NaCl films

The insulating properties of an NaCl monolayer on Cu(311) were investigated via dI /dV spectroscopy by Olsson *et al* [238]. The dI/dV spectrum is shown in Figure 7.2. The poor conductivity of the monolayer is manifested by a very small tunneling current between -4 and +3V and exponential onsets of dI /dV at these voltages. The other characteristic feature in the spectra is the shoulder at about 3.2 V. This drastic reduction in the tunneling current suggests a depletion of the LDOS in the corresponding energy region, which can be attributed to the absence of propagating states in the overlayer in this energy region and the formation of a band gap.

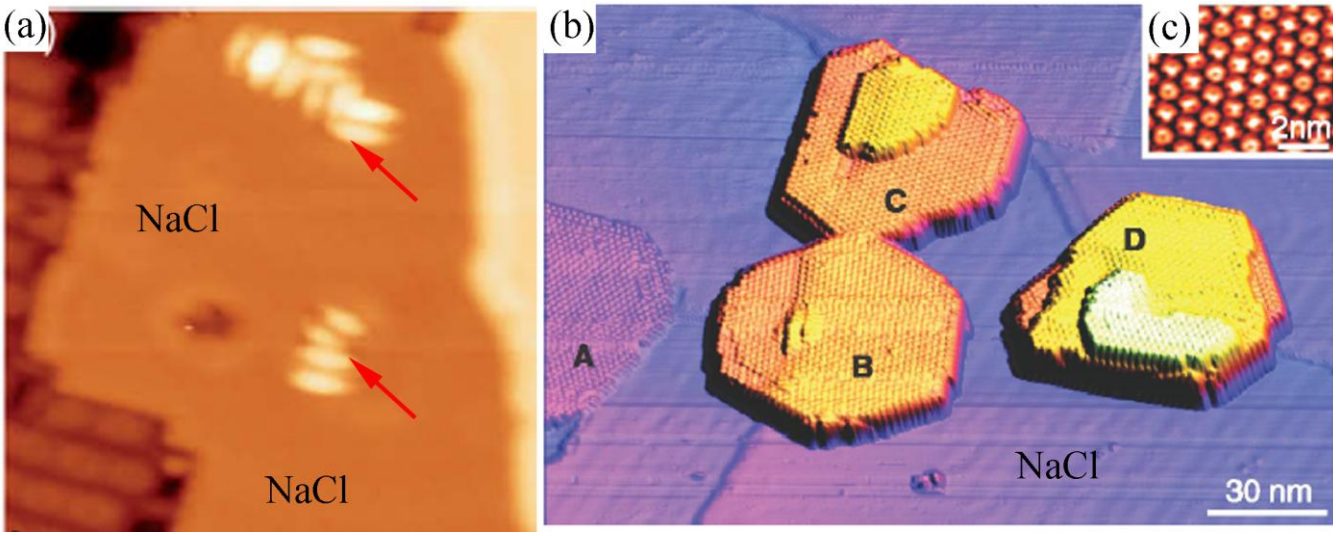

Figure 7.3: STM images showing molecular structures resulting from co-deposition of PTCDI and BDATB on a partially NaCl-covered Au(111) surface. Most of the imaged areas are 2 ML high NaCl islands apart from the left hand side showing the bimolecular layer on Au(111). Some molecules are found to adsorb on the NaCl islands – most likely at defects within the salt layer. Image reproduced from [239] (b) STM image of C_{60} nanocrystals formed on a NaCl ultrathin film grown on Au(111) (V_t = -3V, I_t = 0.02 nA). Island A is a C_{60} monolayer on Au(111); the small blue triangle below A is part of the bare Au surface. Hexagonal island B and truncated triangular islands C and D consist of up to two, three, and four C_{60} molecular layers, respectively, on NaCl. (c) Submolecular resolution on island B (V_t = -3V, I_t = 0.1 nA). Image reproduced from [240]

7.1.2 Deposition of molecules on NaCl islands

Both molecules [239, 248, 249] and nanoparticles [240, 250] have been successfully deposited on NaCl thin films. Ventura *et al* deposited 3, 4, 9, 10-perylenetetracarboxylic diimide (PTCDI) and 1, 4-bis-(2, 4-diamino-1, 3, 5,-triazine)-benzene (BDATB) on NaCl islands on Au(111) and demonstrated a good decoupling between the molecular electronic structure from the metals states by the NaCl layer (see red arrows in Figure 7.3 (a)).

Cavar *et al* were successful in depositing C_{60} molecules on NaCl islands on Au(111) (shown in Figure 7.3 (b)). Island A is a C_{60} monolayer on Au(111). The small blue triangle below A is part of the bare Au surface. Hexagonal island B and truncated triangular islands C and D consist of up to two, three, and four C_{60} molecular layers, respectively, on NaCl. The inset in (c) shows submolecular resolution on island B (V= -3 V, I = 0.1 nA). Using the highly localized current of electrons tunneling through a double barrier scanning tunneling microscope junction, luminescence was exhibited from a selected C_{60} molecule in the surface layer of fullerene nanocrystals grown on an ultrathin NaCl film on Au(111). In the observed fluorescence and phosphorescence spectra, pure electronic as well as vibronically induced transitions of an individual C_{60} molecule were identified, leading to unambiguous chemical recognition on the single-molecular scale.

In all the cases shown above, the NaCl film acts as a spacer layer to decouple the electronic structure of the deposited species with that of the underlying substrate [240, 251]. However the number of similar investigations on ultra thin NaCl films is quite limited and in large part this is because of the small lateral dimensions of the NaCl films which limit the area in which the species of interest can be captured and studied. The lateral dimension of the NaCl films is usually limited by the size of the atomically flat terraces available on the substrates. In principle substrates with larger flat terraces should lead to the larger lateral dimensions of the insulating films which would enhance the capture of molecules and clusters. Scanning tunneling spectroscopy (STS) studies on single molecules and clusters deposited on NaCl films have also met with limited success because of insufficient stability of the molecular systems [239].

In this chapter we present a strategy to obtain thin NaCl islands with large lateral extent on HOPG substrate. We show that these islands are transparent to tunneling current and allow STM and STS measurements.

7.2 Results

7.2.1 Morphology

In Figure 7.4 we show a typical NCAFM image of cross-shaped islands of a deposited low coverage NaCl sample grown on the terraces of HOPG. It can be seen that even after deposition of 2 ML of NaCl the actual coverage is much lower owing to desorption from the HOPG surface. The remaining material has self assembled to form cross-shaped islands. The cross shaped islands follow a branching pattern with two primary arms (which make the cross), secondary branches perpendicular to the primary ones, and finally smaller tertiary branches which form at right angles to the secondary arms. While defected structures exist with misplaced branches, the angle between the branches is overwhelmingly 90^0.

NCAFM images like Figure 7.4 reveal two types of structures - (i) rod like decorations of HOPG step edges (arrow 1 in Figure 7.4) (ii) and cross-shaped islands on the HOPG terraces (arrow 2 in Figure 7.4). The islands nucleate via molecule-molecule collisions on flat terraces and the rods by defect trapping (at step edges). Similar structures have been observed after deposition and diffusion of various clusters e.g. Sb_4 [252], Ag_{400} [253], $Sb_{4\text{-}2200}$ [254].

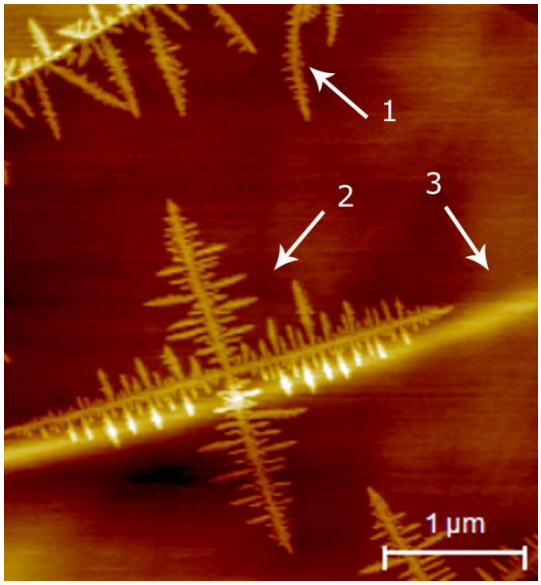

Figure 7.4: Non Contact AFM image of NaCl grown on HOPG (flux = 0.058 Å/sec and coverage = 2 ML). Arrows 1 and 2 indicate rods formed due to the decoration of HOPG step edges by NaCl and a cross-shaped island formed on a flat terrace respectively. Arrow 3 points to a fold in the underlying layer of HOPG which appears as a bright line in the NCAFM scan.

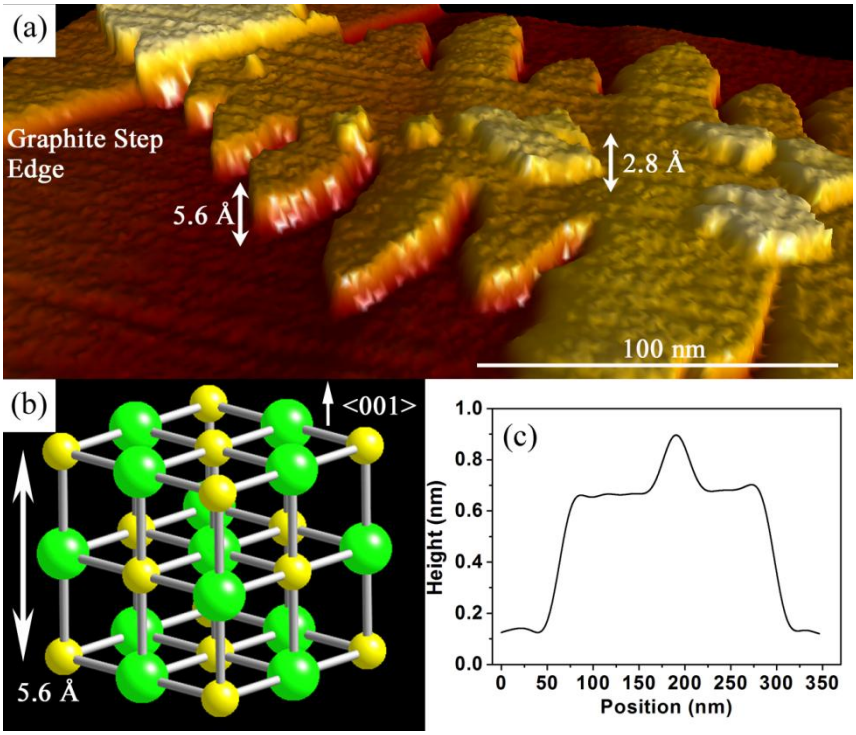

Figure 7.5: (a) 3D representation of a NCAFM image of one of the arms of a cross-shaped island. The height of the base of the island is determined to be 5.6 Å which corresponds to a height of 2 ML (b) NaCl lattice. Chlorine and sodium atoms are shown in green and yellow respectively. (c) Line profile of a NaCl island. An Additional 1 ML layer is formed from atoms that impinge directly on top of the 2ML high NaCl base.

A three dimensional representation of a branch of an NaCl island is shown in Figure 7.5 (a). All islands, at low and high coverage, exhibit bases of height 5.6 ± 0.1 Å which corresponds to a height of 2 ML of NaCl (see NaCl lattice in Figure 7.5 (b)). Islands formed at higher coverages usually exhibit an additional 1 ML on top of the base (see line profile in Figure 7.5 (c)). Interestingly carpet like growth of NaCl islands is also observed on HOPG where the island shown in Figure 7.5 (a) grows over a step edge in the top left corner of the image. Higher coverage islands will be discussed in section 7.2.4. We also observe that the islands grow laterally when the coverage is increased and that a fixed base height (2 ML) is maintained in all depositions. This behavior indicates that the activation energy barrier to upward mobility of NaCl molecules is large.

7.2.2 Growth of NaCl islands

The formation of the NaCl islands can be described within the framework of diffusion limited aggregation (DLA) [255, 256]. In this process NaCl molecules diffuse randomly across the substrate terraces before encountering a growing aggregate and then they attach permanently to its growth front (similar to bismuth nanostructures [16]). The structures observed in the present case are similar to that observed by Zhang and Lagally [256] where the underlying substrate's crystal structure forces formation of highly branched and cross-shaped structures.

The island shapes are a function of an intricate balance between growth kinetics and thermodynamics in which the former drives the system to form non-equilibrium dendritic structures (at high local fluxes), while the latter reduces the free energy of the system resulting in compact structures (at low local fluxes) [16]. It is important to clearly distinguish the local flux of molecules impinging laterally onto an island from the apparent flux deposited vertically onto a given area of the substrate. The local flux is affected by the presence of step edges, or nearby growing islands, since they act as sinks for diffusing material. Isolated islands growing on large terraces (with distant step edges) experience high local fluxes as the weakly bound NaCl molecules diffuse rapidly and there are no competing sinks.

The growth mechanism and the effect of differing local fluxes are illustrated in Figure 7.6 which shows the early stages of growth of an island which happens to have nucleated close to a step edge. The initial seed particle which nucleates on the HOPG surface is a cube (or a square if viewed from the top) as NaCl crystallizes into a face centered cubic unit cell. It is observed that two arms quickly grow out from the top corners of the seed (i.e. $< 110 >$ directions). However on the other side next to the step edge of graphite a (010) facet is formed.

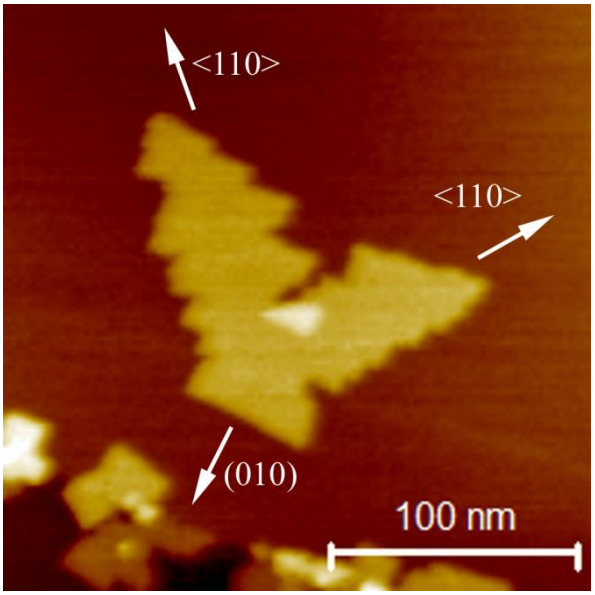

Figure 7.6: Early stages of growth of a NaCl island (see text).

Fast growth at the upper corners is a consequence of a high local flux: these corners of the square extend more into the diffusion field and catch more molecules resulting in rapid growth in the $< 110 >$ directions. The high local flux on the upper side of this island is because the island's upper side faces a large terrace. In contrast the lower side of the island grows slowly owing to low local flux because of the proximity to a step edge. This gives enough time for the molecules to arrange themselves in a more thermodynamically favorable configuration and hence a (010) facet is

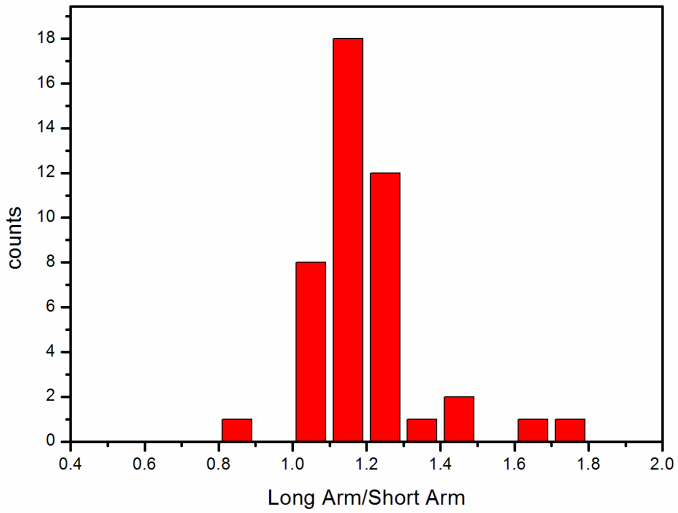

Figure 7.7: Ratio between the long arm versus short arm of the cross shaped NaCl islands

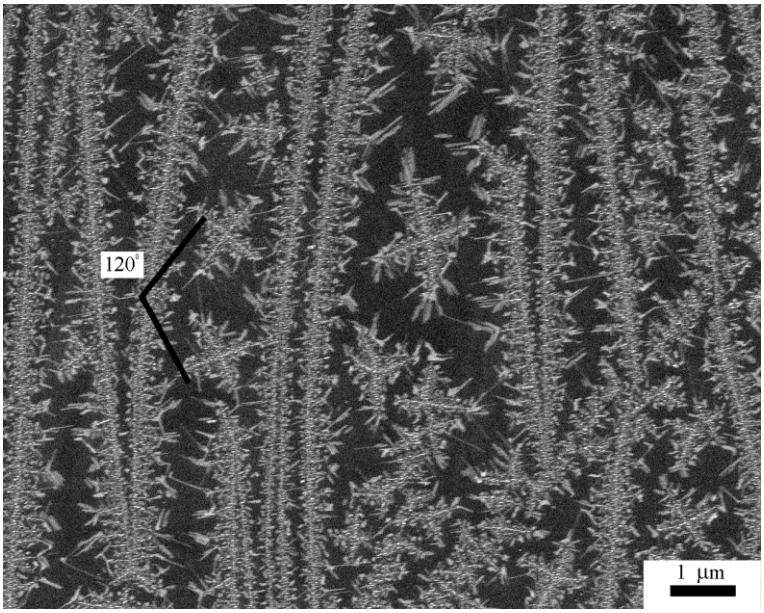

Figure 7.8: SEM image of bismuth deposited on NaCl islands. The NaCl islands are destroyed when taken out of vacuum but the bismuth remains and shows an outline of the NaCl islands.

observed [15].

7.2.3 Interaction with the substrate

Interestingly the lengths of the two primary arms that make the cross appear unequal in the NCAFM images. We measured the ratio of the length of the arms from the center of the cross and found that the ratio between the short vs long arm was mostly ~1:1.2 – 1:1.3 (see Figure 7.7). This observation suggests that that one arm grows faster than the other. This phenomenon would indicate some degree of interaction with the substrate which could result in a fast growth direction in one of the arms. Such kind of interaction can be studied by monitoring the growth of the crosses with respect to each other.

However, the size of the islands usually ranged between few hundred nanometers to few microns which makes the visualization on a large scale very difficult in a NCAFM scan. SEM is a better option in these cases but the NaCl islands were destroyed by the moisture in the air as soon as the islands were taken out of the vacuum chamber. This problem was overcome by evaporating bismuth on top of the pre-existing NaCl islands which assembled on and around the islands. The bismuth forms an outline of the NaCl islands. SEM was possible on such samples in which bismuth would indicate the shape and positions of the NaCl islands as shown in Figure 7.8. It can be seen that in most of the cross shaped islands, the lengths of the two primary arms that make the cross are unequal. SEM images demonstrate that the cross shaped islands are mostly aligned at 60^0 with

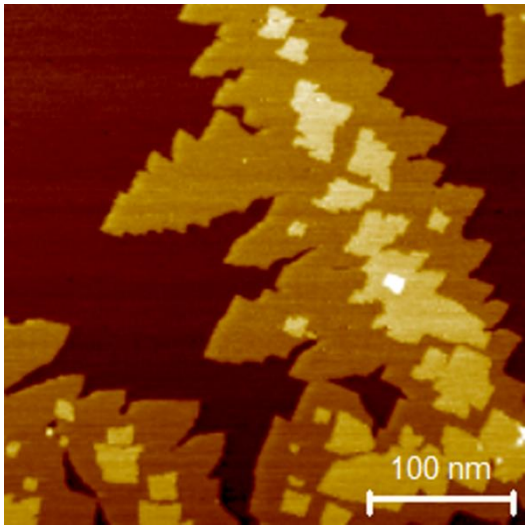

Figure 7.9: Direct impingement of material on top of island base at higher coverages (flux was 0.058 Å/sec, coverage 6 ML).The structures exhibit a higher density of 1 ML high islands on the top of the bases. These 1 ML structures are formed due to direct impingement of material onto pre-existing bases.

respect to each other (as shown by the angle in Figure 7.8), indicating an interaction with the underlying HOPG.

7.2.4 Direct impingement

A characteristic feature of higher coverage films is the presence of additional 1 ML islands of NaCl on top of the base (see Figure 7.9). The 1 ML islands are more prevalent near the center of the cross which forms the base and become less common as one approaches the tip of the island. If the additional 1 ML layer is the result of the aggregation of molecules that directly impinge on the base then the ratio of the areas of the additional layer and the base can be calculated straightforwardly. The probability of a molecule landing on the base is simply the fraction of the surface covered by the bases at that time. By integrating over time:

$$\frac{A_2}{A_1} = \frac{\theta}{1 - exp(-\theta)} - 1 \qquad \text{Equation 7.1}$$

where A_2 = the area of the 1ML on top of the base; A_1 = area of the base and θ = coverage [16]. We estimate A_2/A_1~0.5 and which correlates well with the experimental value θ = 0.85 in Figure 7.9. This suggests that the material on top of the islands aggregates after direct impingement. In the process of the formation of this two tier structure the base regions which were formed early in the growth process tend to capture more NaCl molecules leading to a gradient of the density of the 1ML islands from the center of the cross to the tip.

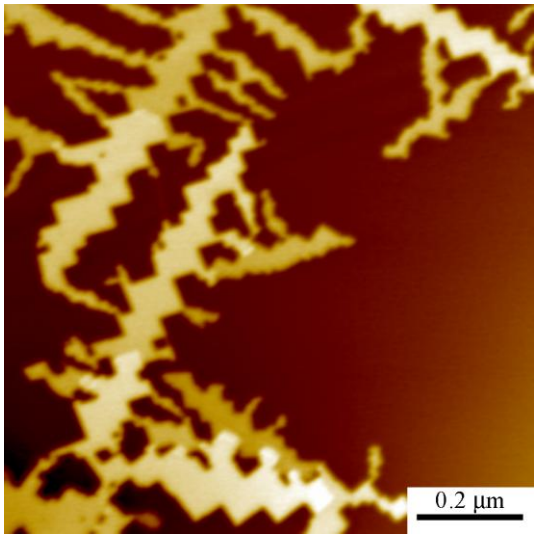

Figure 7.10: NCAFM image of annealed bismuth islands from low coverage (annealed at 200^{0}C for 30 minutes)

7.2.5 Annealing

The islands were annealed at 200^{0}C for 30 minutes to observe any change in their morphology and configuration. Annealing of the islands results in formation of compact and more defined shapes as seen in Figure 7.10. The base is taller (4ML) as compared to the non annealed structures. The islands also undergo a drastic change in their morphology. Now the islands have sharper corners owing to edge diffusion [16] which is heightened at higher temperatures and in absence of incoming molecules. The islands look more like square shaped islands and it is noticeable how the squares join each other at their corners, i.e. $< 011 >$ direction. Another interesting feature of the image is that the cross shape seems to have degraded into a single, longer island with remnants of what would have been secondary and tertiary branches. Because of annealing the molecules tend to diffuse to a more thermodynamically viable location and most of them preferred to align along the direction of main axis. We tried to perform STM measurements on the annealed islands but it resulted in very streaky, noisy images and after sometime destruction of the tip. Since the annealed islands were taller we decided to use low coverage island for bismuth deposition.

7.2.6 Bismuth on HOPG

We established in section 7.2.1 that our NaCl islands have a flat top surface which can be used to deposit molecules or nanoparticles. In this section we show preliminary results of deposition of bismuth on top of pre-existing low coverage NaCl islands on HOPG substrate. The Bi/NaCl/HOPG system was characterized by STM and STS.

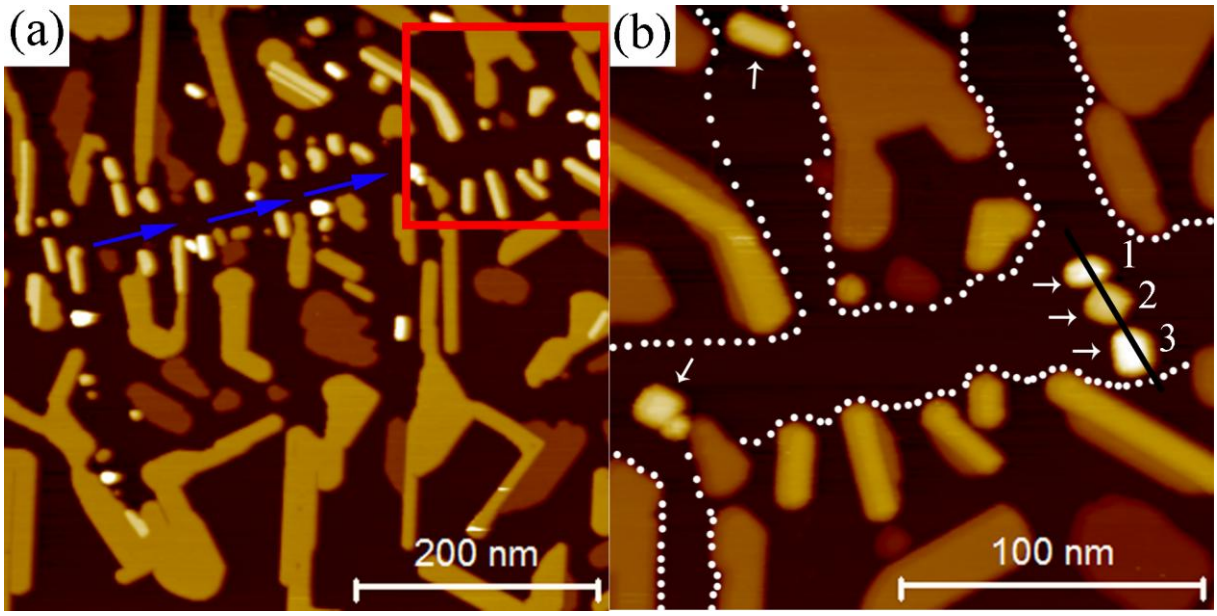

Figure 7.11: (a) STM image of deposited bismuth over preexisting NaCl islands. Only a NaCl outline is visible as a clear region in between the bismuth islands (shown by blue arrows) (V_t = +1V, I_t = 100pA). (b) High magnification of the region shown by the red square in (a). The clear region shows presence of few bismuth islands which are formed on top of the NaCl islands (shown by white arrows).

7.2.6.1 STM measurements

In Figure 7.11 (a) we show an STM image of bismuth islands deposited on top of pre-existing NaCl/HOPG islands. This image was recorded at V_t = +1V and I_t = 100pA. Very interestingly, only bismuth islands are seen in this image and the NaCl islands are not visible. As we stated earlier NaCl is an insulator and it has a band gap in the range of -4 to +3V [238]. Therefore at +1V we are scanning in the bias range where there are no density of states for the NaCl islands.

The bismuth islands in Figure 7.11 (a) are seen to form a straight clear region on HOPG which is shown by blue arrows. The bismuth islands form an outline around the invisible NaCl island indicating its presence. Our previous STM experiments with only NaCl/HOPG islands yielded extremely streaky and noisy images. We speculate that this was because of the interaction between the STM tip and the NaCl island resulting in the moving of the NaCl islands. However, after the deposition of the bismuth islands the NaCl islands appear to be anchored to their place as the Bi/NaCl/HOPG system did not pose any problems with STM imaging.

The region shown by the red square in Figure 7.11 (a) is shown in higher magnification in Figure 7.11 (b). The position of the NaCl island is shown by white dots. It can be seen from the image that the bismuth atoms treat the NaCl island as a defect and nucleate around it forming a clear outline of the NaCl island. Interestingly there are few islands which are also formed on top of the NaCl island

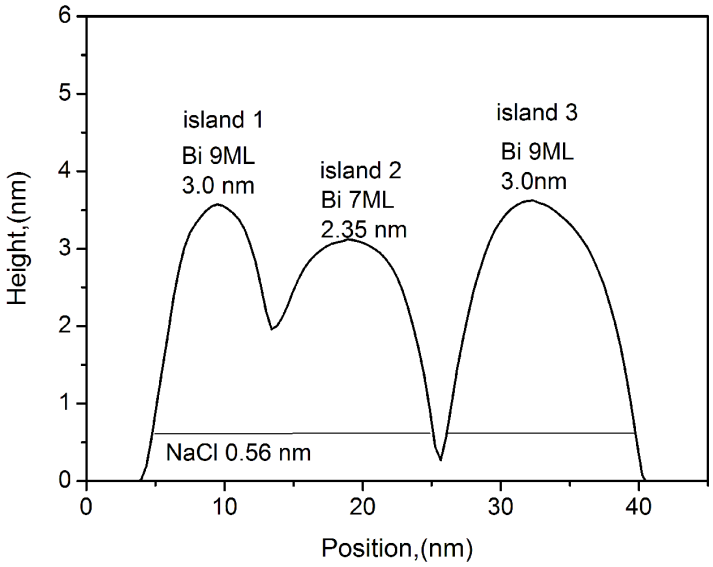

Figure 7.12: Line profile of island 1, 2 and 3 shown in Figure 7.11 (b).

(shown by white arrows in Figure 7.11 (b)), which indicates that few bismuth islands also nucleated on top of the NaCl islands. To verify this we drew line profile (black line across the bismuth islands labeled 1, 2 and 3 in Figure 7.11 (b) on the bismuth islands) and it is shown in Figure 7.12. The height analysis shows that the islands 1 and 3 are ~3.56 nm high which corresponds to 9 ML of bismuth (2.97 nm) + 2 ML of NaCl (0.56 nm). Island 2 is 7 ML of bismuth on top of a 2 ML NaCl base. The height of the individual islands confirmed that they were located on top of the 2 ML base of the invisible NaCl island. It is interesting to see that the position of the three islands was influenced by tip-sample interaction. The position of island 2 is not the same in Figure 7.11 (a) and (b); it seems to be pushed a bit inward to come in line with island 1 and 2 in (b).

Another interesting thing to note here is that the bismuth islands grow exactly in the same manner as on top of HOPG i.e. the standard paired layer configuration with 1 ML dead wetting layer is same on top of the NaCl islands.

7.2.6.2 STS measurements

Since the Bi/NaCl/HOPG system was stable enough for STM measurements we took the opportunity to perform STS measurements. Along with grid CITS measurements in ±1V bias voltage range, single point spectroscopy measurements were performed in ±4V bias voltage range. In single point spectroscopy, the STM tip is positioned on a sample spot and a single I(V) curve is measured. We measured 20 single I(V) curves from the clear region (NaCl island) on the STM image shown in Figure 7.11 (b). They were averaged and numerically differentiated to yield the final curve shown in Figure 7.13.

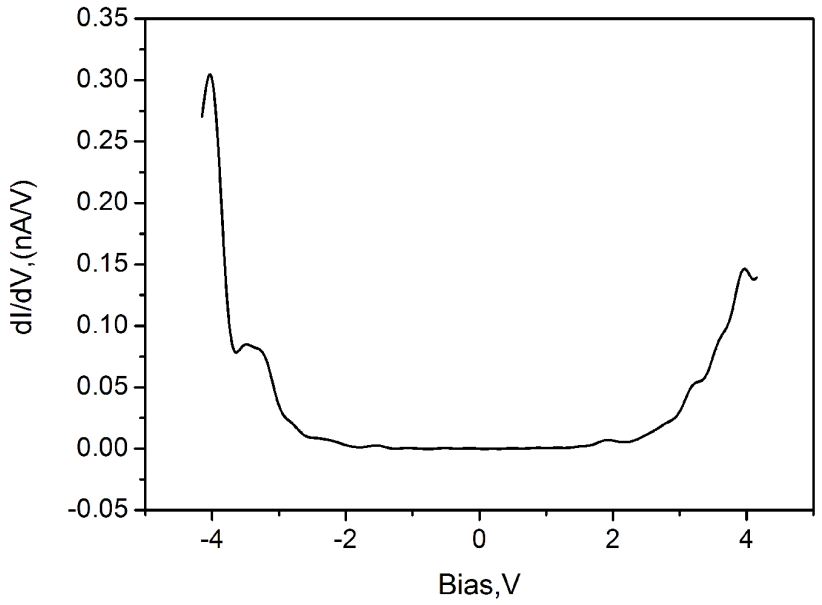

Figure 7.13: dI/dV(V) curve on NaCl island obtained by single point spectroscopy method. The dI/dV(V) curve is an average of 20 single measurements.

The dI/dV curve of NaCl is very flat within a few volts of zero bias which is expected because NaCl is an insulator. The positive side of the spectrum shows an onset at +2V and the negative side of the curve shows a steep onset between -3V and -4V. The exponential rise can be attributed to the field emission regime which is encountered at higher voltages where the tunneling probability of the electrons increase exponentially because of tunneling through the energies close to the vacuum level [13]. The spectrum is similar to that of NaCl islands on Cu(311) obtained by Olsson *et al* (shown in Figure 7.2) [238]. Faint shoulders are visible on the dI/dV(V) curve at -3.2V, -3V, -2.2V, -1.5 V, +2V, +3.2V and +3.8V whose origin is still unknown.

Grid CITS measurements were performed in ±1V bias voltage range on the sample region shown in Figure 7.11 (b). The corresponding CITS dI/dV map (V_t = +258mV) is shown in Figure 7.14. Lighter color in the dI/dV maps indicate high LDOS and vice versa. The dI/dV map shows the presence of HOPG, NaCl and various heights of bismuth islands. The area marked by NaCl (see green arrow) is slightly darker as compared to HOPG. The contrast observed between NaCl and HOPG in the CITS dI/dV map correlates well with the outline drawn by white dots in Figure 7.11 (b). This is direct evidence that the bismuth islands are formed around the NaCl islands and few bismuth islands are captured on top of the NaCl island.

There is a bismuth island in the lower right hand corner of the image which is not formed on top of an NaCl island (confirmed by height analysis of the island). The 5 ML island (on HOPG) is

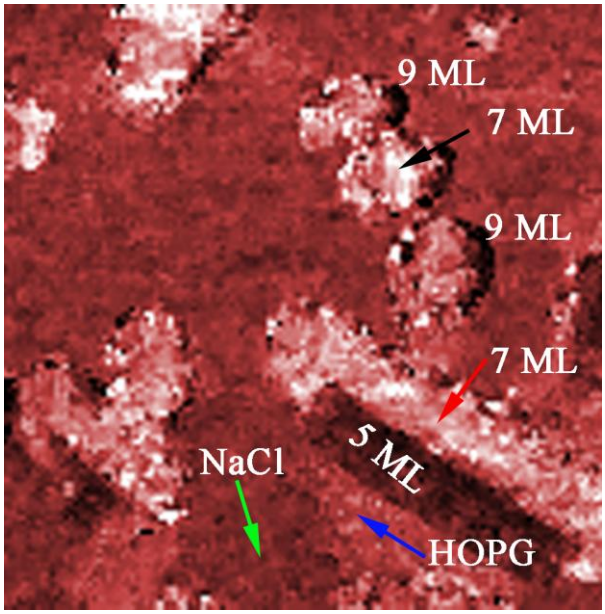

Figure 7.14: A CITS dI/dV map (V = +258mV) of the region shown in Figure 7.11 (b). The NaCl island (green arrow) appears darker as compared to HOPG (blue arrow). The 7 ML stripe formed on HOPG (red arrow) appears to have same contrast as the 7 ML island formed on NaCl island.

darker than the 7 ML stripe which is formed on top of it. Interestingly the 7 ML stripe (formed on 5 ML island and shown by red arrow) has the same contrast as compared to the 7 ML island that is formed on top of the NaCl island.

This is interesting because NaCl is an insulator and theoretically it should decouple the electronic states of bismuth from the underlying HOPG and we would hope that there is some difference in the LDOS of Bi/HOPG islands as compared to Bi/NaCl/HOPG e.g. charging of the islands. However we do not see any difference which shows that the NaCl islands in our experiments allow the passage of tunneling current and make CITS measurements possible.

In Figure 7.15 (a) we compare the dI/dV(V) curves recorded via CITS on bare HOPG and NaCl/HOPG. The LDOS minima of the NaCl curve (green) has shifted slightly towards the positive energies (~80meV) as compared to the bare HOPG curve (blue). The difference in contrast leading to darker NaCl island in the CITS dI/dV map (shown in Figure 7.14) is explained by comparing the relative difference in intensities between dI/dV(V) curves recorded in Figure 7.15 (a). At +258mV the NaCl/HOPG curve has comparatively less LDOS intensity as compared to HOPG and hence appears darker in the dI/dV map.

In Figure 7.15 (b) we compare dI/dV(V) recorded on bismuth island on top of NaCl/HOPG (black arrow in Figure 7.14) and bismuth island on HOPG (red arrow in Figure 7.14). The peaks in both the curves arise out of DOS in bismuth (see section 3.3). It is very interesting to see that both the curves

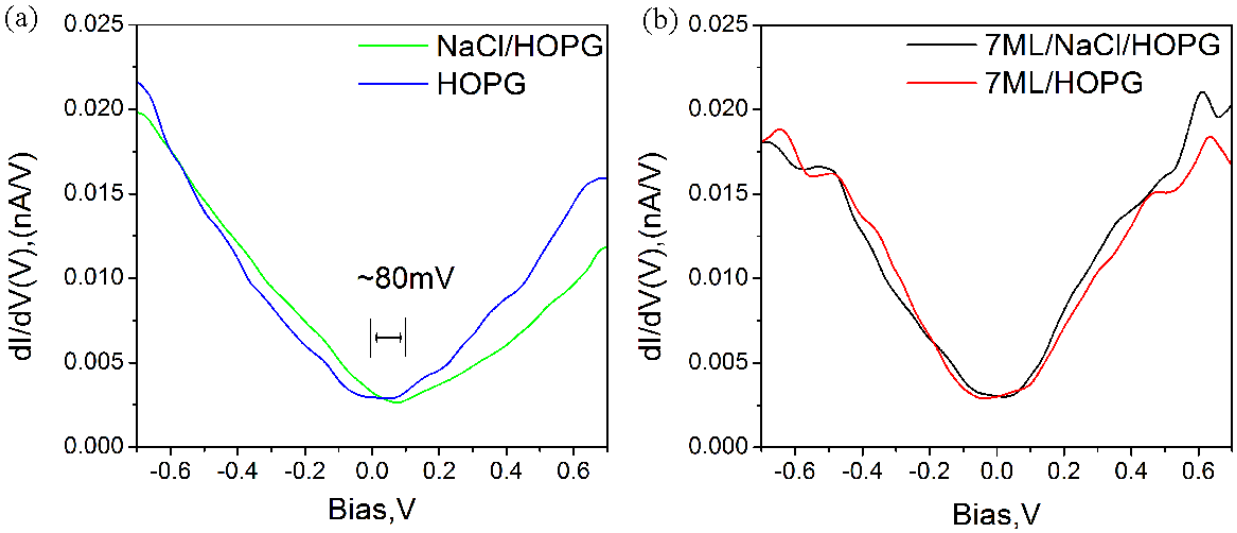

Figure 7.15: (a) Comparison of dI/dV(V) curves recorded on NaCl island on HOPG (green) and bare HOPG (blue). (b) Comparison of dI/dV(V) curves between 7 ML island on bare HOPG (red) and on top of NaCl island (black).

show similar LDOS peaks e.g. the LDOS peak at ~+0.65V, -0.4V, -0.5V and -0.66V are reproduced well in both the curves. The effects of decoupling via the NaCl spacer is not very evident as the LDOS minima in the Bi islands on NaCl/HOPG curve is also reproduced quite well in Bi/HOPG islands.

The similar LDOS of Bi/HOPG and Bi/NaCl/HOPG is extremely interesting as it indicates that the wetting layer underneath the bismuth islands plays an important role in limiting the interaction between the paired bismuth layers and the HOPG substrate. The exact mechanism of the decoupling of the bismuth film from the underlying HOPG by the wetting layer is mysterious.

7.3 Summary

We have developed a strategy to produce well-defined cross-shaped islands of NaCl with large lateral extent on HOPG. The cross shaped islands follow a branching pattern with two primary arms (which make the cross), secondary branches perpendicular to the primary ones, and finally smaller tertiary branches which form at right angles to the secondary arms. The islands are formed via DLA and the shape of the island can be controlled by experimental parameters e.g. apparent flux, coverage etc. The islands grow laterally when the coverage is increased and a fixed base height of 2 ML is maintained in all the depositions.

There is a significant effect of the atomic structure of the NaCl and the underlying substrate that results in a fast growth direction (long axis of the cross) and a 60^0 angle between the crosses on the same HOPG grain as seen from SEM images.

As the coverage of the NaCl islands is increased the islands grow laterally maintaining a 2 ML base height. An additional 1 ML NaCl island is observed in all high coverage experiments which is a result of direct impingement of material on top of the existing 2 ML base. Annealing of the NaCl islands resulted in compact and sharply defined square NaCl islands. The squares appear to join to each other at the diagonals ($< 110 >$ direction) in the annealed structures.

STM measurements on Bi/NaCl/HOPG were successful however the STM images at V_t = +1V showed only the bismuth islands. The NaCl islands were invisible because of absence of any DOS in the wide band gap between -4V and +3V. We were successful in observing bismuth islands on top of NaCl islands and also in measuring the height of the individual islands. The height analysis revealed the formation of 7 and 9 ML bismuth islands on top of a 2 ML NaCl base. The growth of bismuth nanostructures on NaCl islands is very interesting because the islands grew in the same manner as on bare HOPG e.g. there was no additional wetting layer and the typical Bi(110) island bilayer stacking with 1 ML dead wetting layer was maintained.

We performed single point spectroscopy measurements on the NaCl islands in ±4V range. The dI/dV curve of NaCl was very flat within a few volts of zero bias which is expected because NaCl is an insulator.

Grid CITS measurements were performed on the Bi/NaCl/HOPG islands. The dI/dV map obtained at +258mV clearly showed the presence of NaCl islands on HOPG substrate and the bismuth nanostructure formed around it. The dI/dV(V) curves extracted from 7 ML islands formed on bare HOPG and on top of NaCl islands was found to be very similar. This demonstrates that our NaCl islands are transparent to the flow of tunneling current and also allow CITS measurements. The similar LDOS of Bi/NaCl/HOPG and Bi/HOPG suggests that the wetting layer under the bismuth islands plays an important role in limiting the interaction between the bismuth islands and HOPG i.e. the same decoupling behavior is observed in bismuth islands on HOPG or on NaCl/HOPG. There have been no reports of CITS measurements (dI/dV(V) curves) on nanoparticle/molecules deposited on NaCl films.

8. Conclusion

The focus of this thesis was a detailed STM/STS study of ultra thin films of bismuth on HOPG. This work is a continuation from the previous work on the precise fabrication of Bi(110) islands and rods on HOPG substrate by Dr Shelley Scott [13-16] and Dr David McCarthy [43, 75] at University of Canterbury, NZ. In the previous research at University of Canterbury the physical characteristics of the bismuth films were studied extensively, and in the current research work we concentrated on the electronic structure of Bi(110) thin films. The work was also motivated by the recent discovery of exotic topological states in bismuth thin films and the lack of published STS studies on Bi(110) thin films.

The bismuth films on HOPG were grown and studied in an Omicron VT AFM XA system. The Omicron system is a UHV SPM that works at a base pressure of 10^{-10} mbar. The films were initially characterized via XPS. The XPS results revealed good quality and metallic nature of the film which facilitated STM studies. The XPS results also suggest absence of bonds between the HOPG and the bismuth film or a weakly physi-sorbed film [43]. The height measurements via STM showed that the islands grow in paired layers on top of a 3 ML base (3, 5, 7, 9… ML). Previous electron diffraction with height analysis shows that the films grow with the (110) plane parallel to the substrate. The surface unit cell of the Bi(110) film estimated via STM was 0.48 ± 0.03 nm x 0.46 ± 0.02 nm which is reasonably similar to the bulk surface unit cell.

Comparison of the experimental STS data with DFT calculations showed that the LDOS of a ‘n’ ML thick island matches well with the calculated DOS of a free standing ‘n-1’ ML thick bismuth slab. This implied the presence of a ‘dead’ 1 ML wetting layer which was present only underneath the bismuth islands. The free standing nature of the Bi(110) films on HOPG results in two symmetrical surfaces (top and bottom). The two surfaces interact and couples rendering all the electronic bands doubly degenerate in the 3, 5 and 7 ML thick films. The surface energy calculations performed by the team at University of Illinois, Urbana Champagne, USA, show bilayer damped oscillations which explain the stability of paired layers in Bi(110) islands.

We observed a bright feature on the perimeter of 3, 5 and 7 ML islands and stripes in the dI/dV maps and STM images at energies close to the Fermi level. We refer to these features as ‘bright beaches (BB)’. These BBs are observed at both room temperature and low temperatures. The BBs do not disperse as a function of bias voltage nor show additional modulations which suggest they are not Friedel oscillations or quantum confined state. We have also observed edge reconstruction of

the edges of a 7 ML stripe. The width of the BB on a 5 ML stripe on a 3 ML base is ~2-4 nm, and the width of the BB on a 5 ML island on HOPG is 4-5 nm. This suggests that there could be an effect of the boundary conditions on the widths of the bright beaches. The BBs are also observed in the dI/dV maps on grain boundaries and defects indicating that the BBs are associated with the termination of the chains of bismuth atoms. Similar bright features have been reported on edges of Bi(111) islands in the literature which were referred to as 'edge states'. The edge states observed on Bi(111) have also been predicted to be topologically protected. The widths of our BB and the energy range of the occurrence are very similar to the edge states in the literature. It would be interesting to perform calculations to understand the origin of these bright beaches on Bi(110) islands.

We have observed well defined periodicities in the widths of 3, 5 and 7 ML Bi(110) islands and stripes. The periodicities were analyzed via STM images which showed widths (measured in $< 112 >$* direction) with a periodicity of ~15 nm in 3 ML, ~6 nm in 5 ML and ~4 nm is 7 ML islands and stripes. The quantized widths are first indication that the growth of the bismuth islands is governed by quantum size effects (QSE) in which the island width (w) follows the rule $w = n\lambda_F/2$. We therefore estimated the experimental Fermi wavelength of 3, 5 and 7 ML islands to be λ_F^{2ML} = 30 nm, λ_F^{4ML} = 12 nm and λ_F^{6ML} = 8nm. The mechanism behind the formation of quantized widths was investigated by means of the band structure and the corresponding Fermi surfaces. The Fermi surfaces of the 2 and 4 ML bismuth slabs showed an electron pocket in $\bar{\Gamma}$-$\bar{X}_1$ direction. This pocket has a k_F in the $\bar{\Gamma}$-$\bar{X}_2$ ($< 112 >$*) direction and with E_F shifts equal to 35 meV and 120 meV for the 2 and 4 ML films respectively the experimental Fermi wavelength matched the calculated Fermi wavelength. In the case of 6 ML the Fermi surface consisted of an electron pocket and hole pocket and the required Fermi wavelength could be generated by both of them by E_F shifts of 90 meV and 145 meV. However, since the QSE in 2 and 4 ML islands was associated with the electron pocket, we believe that the electron pocket is responsible for the observation of QSE in 6 ML islands.

In some of the 3 ML islands we observed a distinct and periodic Moiré pattern via STM images and CITS dI/dV maps at energies close to the Fermi level. It shows a periodicity of ~3.5 nm and is oriented at ~60^0 to the Bi$< \bar{1}10 >$ direction. The periodicity was independent of the bias voltage. We show that the misorientation of the bismuth island with respect to the underlying HOPG gives rise to the Moiré pattern in STM images and CITS dI/dV maps. The Moiré pattern is observed at both room and low temperatures. LDOS intensity maps associated with the Moiré pattern show peaks in the LDOS valley which correlate with the Moiré pattern. A modulation in intensity of LDOS peaks with respect to the Moiré pattern was also recorded at +350mV and -150mV. We also observe a

contrast inversion of the Moiré pattern in the STM images and corresponding dI/dV maps. Dr Pawel Kowalczyk performed calculations which were based on the principle of misorientation between the bismuth islands and the underlying HOPG substrate and was able to predict the periodicity and the angle of the Moiré pattern observed in STM and CITS results. Very strangely, we also observed Moiré pattern in NCAFM images of bismuth islands. The Moiré pattern observed in the NCAFM images had a periodicity of ~8-9 nm. We speculate that the Moiré pattern observed in NCAFM has a completely different origin than the ones observed in STM and certainly more detailed experiments and calculations would be interesting to understand the NCAFM results.

NaCl was deposited on HOPG substrate that resulted in formation of cross shaped islands. The cross shaped NaCl islands were characterized primarily by NCAFM. STM measurements were extremely difficult because of the insulating nature of the NaCl film and the STM tip displaced the NaCl island while scanning. The islands were formed by diffusion limited aggregation and the shape of the island could be controlled by experimental parameters e.g. apparent flux, coverage etc. The islands grew laterally when the coverage was increased, a fixed base height of 2ML being maintained by the NaCl islands in all the depositions. An additional 1 ML NaCl island is observed in all high coverage experiments which is a result of direct impingement of material on top of the existing 2 ML base. An effect of the underlying substrate was seen in the islands as they were oriented at 60^0 to each other.

We were successful in observing bismuth islands on top of NaCl islands and also in measuring the height of the individual islands. The growth of bismuth nanostructures on NaCl islands is very interesting because the islands grew in the same manner as on bare HOPG i.e. there was no additional wetting layer and the typical Bi(110) island bilayer stacking with 1 ML dead wetting layer was maintained. In the CITS measurements the dI/dV(V) curves extracted from 7 ML islands formed on bare HOPG and on top of NaCl islands was found to be very similar. The similar LDOS of Bi/NaCl/HOPG and Bi/HOPG suggested that the wetting layer under the bismuth islands plays an important role in limiting the interaction between the bismuth islands and HOPG i.e. the same decoupling behavior is observed in bismuth islands on HOPG or on NaCl/HOPG.

Many opportunities clearly exist to extend the current research work on Bi(110)/HOPG system. We have initiated collaborations with Prof. Mineo Saito, Kanazawa University, Japan for calculations on a free standing Bi(110) slab with finite width. These calculations would help us to understand the density of the states at the edges of Bi(110) islands and stripes. The difficulty in such calculations are

that the exact model of the Bi(110) edge is currently unknown. We also propose to incorporate appropriate boundary conditions in the calculations to understand its implications on the widths of the bright beaches.

To understand the Moire pattern in NCFAM images we suggest detailed and systematic NCAFM experiments on 3 ML Bi(110) islands. The experiments should chiefly focus on bismuth islands with small lateral extents. It would also be intersting to perform contact AFM on these bismuth islands at low temperatures (50 K) when their stability is better (compared to room temperature).

The most appealing follow up of our research work is to verify the topological properties of the Bi(110) islands, if any. It has been indicated in literature that Bi(110) system is topologically trivial in nature, however with our discovery of quantized widths we speculate that a combination of the thickness of the island and the quantized widths could give rise to interesting properties in the system.

9. References

[1] Shoenberg D 1939 The magnetic properties of bismuth. III. Further measurements on the de Haas-Van Alphen effect *Proceedings of the Royal Society of London. Series A. Mathematical and Physical Sciences* **170** 341

[2] Behnia K, Balicas L and Kopelevich Y 2007 Signatures of electron fractionalization in ultraquantum bismuth *Science* **317** 1729

[3] Pippard A and Chambers R 2002 The Mean Free Path of Conduction Electrons in Bismuth *Proceedings of the Physical Society. Section A* **65** 955

[4] Edelman V S 1976 Electrons in Bismuth *Advances in Physics* **25** 555

[5] Zhang Z, Sun X, Dresselhaus M, Ying J Y and Heremans J 2000 Electronic transport properties of single-crystal bismuth nanowire arrays *Physical Review B* **61** 4850

[6] Weitzel B and Micklitz H 1991 Superconductivity in granular systems built from well-defined rhombohedral Bi-clusters: Evidence for Bi-surface superconductivity *Physical Review Letters* **66** 385

[7] Yang F, Liu K, Hong K, Reich D, Searson P and Chien C 1999 Large magnetoresistance of electrodeposited single-crystal bismuth thin films *Science* **284** 1335

[8] Cho S, Kim Y, Olafsen L, Vurgaftman I, Freeman A, Wong G, Meyer J, Hoffman C and Ketterson J 2002 Large magnetoresistance in post-annealed polycrystalline and epitaxial Bi thin films *Journal of magnetism and magnetic materials* **239** 201

[9] Hicks L, Harman T, Sun X and Dresselhaus M 1996 Experimental study of the effect of quantum-well structures on the thermoelectric figure of merit *Physical Review B* **53** 10493

[10] Cho S, Kim Y, Freeman A, Wong G, Ketterson J, Olafsen L, Vurgaftman I, Meyer J and Hoffman C 2001 Large magnetoresistance in postannealed Bi thin films *Applied Physics Letters* **79** 3651

[11] Wang H, Jing J, Mallik R, Chu H and Henriksen P 1993 Crystallographic structure and defects in epitaxial bismuth films grown on mica *Journal of crystal growth* **130** 571

[12] Partin D, Heremans J, Morelli D, Thrush C, Olk C and Perry T 1988 Growth and characterization of epitaxial bismuth films *Physical Review B* **38** 3818

[13] Scott S, Kral M and Brown S 2005 A crystallographic orientation transition and early stage growth characteristics of thin Bi films on HOPG *Surface Science* **587** 175

[14] Scott S A, Kral M V and Brown S A 2005 Growth of oriented Bi nanorods at graphite step-edges *Physical Review B* **72** 205423

[15] Scott S A, Kral M V and Brown S A 2006 Growth of nanorods and mesoscale stars prior to an orientation transition in thin Bi films on graphite *Applied Surface Science* **252** 5563

[16] Scott S A, Kral M V and Brown S A 2006 Bi on graphite: Morphology and growth characteristics of star-shaped dendrites *Physical Review B* **73** 205424

[17] Abu-Samak M 2008 Quantum size effects in Bi films grown on GaAs (110) *Journal of Applied Physics* **104** 123714

[18] Payer T, Rajkovic I, Ligges M, von der Linde D, Hoegen M H V and Heringdorf F J M Z 2008 Ultrathin epitaxially grown bismuth (111) membranes *Applied Physics Letters* **93** 093102

[19] Robins J 1988 Thin film nucleation and growth kinetics *Applied Surface Science* **33** 379

[20] Koma A, Sunouchi K and Miyajima T 1985 Fabrication of ultrathin heterostructures with van der Waals epitaxy *Journal of Vacuum Science & Technology B: Microelectronics and Nanometer Structures* **3** 724

[21] Tavger B and Demikhovskiĭ V Y 1969 Quantum size effects in semiconducting and semimetallic films *Physics-Uspekhi* **11** 644

[22] De Renzi V, Betti M G and Mariani C 1993 Quantum size effects and temperature dependence of low-energy electronic excitations in thin Bi crystals *Physical Review B* **48** 4767

[23] Ogrin Y F, Lutskii V and Elinson M 1966 Observation of quantum size effects in thin bismuth films *Soviet Journal of Experimental and Theoretical Physics Letters* **3** 71

[24] Lutskii V, Korneev D and Elinson M 1966 Observation Of Quantum size effects in bismuth thin films by the method of tunnel spectroscopy *Soviet Physics Jetp-Ussr* **22** I966
[25] Hoffman C, Meyer J, Bartoli F, Di Venere A, Yi X, Hou C, Wang H, Ketterson J and Wong G 1993 Semimetal-to-semiconductor transition in bismuth thin films *Physical Review B* **48** 11431
[26] Heremans J, Thrush C M, Lin Y M, Cronin S, Zhang Z, Dresselhaus M and Mansfield J 2000 Bismuth nanowire arrays: Synthesis and galvanomagnetic properties *Physical Review B* **61** 2921
[27] Rogacheva E, Grigorov S, Nashchekina O, Lyubchenko S and Dresselhaus M 2003 Quantum-size effects in n-type bismuth thin films *Applied Physics Letters* **82** 2628
[28] Xu J, Wang E, Ting C and Su W 1993 Tight-binding theory of the electronic structures for rhombohedral semimetals *Physical Review B* **48** 17271
[29] Liu Y and Allen R E 1995 Electronic-Structure of the Semimetals Bi and Sb *Physical Review B* **52** 1566
[30] Hofmann P 2006 The surfaces of bismuth: Structural and electronic properties *Progress in Surface Science* **81** 191
[31] Koroteev Y M, Bihlmayer G, Chulkov E V and Bluegel S 2008 First-principles investigation of structural and electronic properties of ultrathin Bi films *Physical Review B* **77** 045428
[32] Patthey F, Schneider W D and Micklitz H 1994 Photoemission study of the Bi(111) surface *Physical Review B* **49** 11293
[33] Hengsberger M, Segovia P, Garnier M, Purdie D and Baer Y 2000 Photoemission study of the carrier bands in Bi(111) *The European Physical Journal B-Condensed Matter and Complex Systems* **17** 603
[34] Ast C R and Höchst H 2001 Fermi surface of Bi(111) measured by photoemission spectroscopy *Physical Review Letters* **87** 177602
[35] Ast C R and Höchst H 2002 Two-dimensional band structure and self-energy of Bi(111) near the Γ point *Physical Review B* **66** 125103
[36] Agergaard S, Sondergaard C, Li H, Nielsen M B, Hoffmann S V, Li Z and Hofmann P 2001 The effect of reduced dimensionality on a semimetal: the electronic structure of the Bi(110) surface *New Journal of Physics* **3** 151
[37] Jona F 1967 Low-energy electron diffraction study of surfaces of antimony and bismuth *Surface Science* **8** 57
[38] Sun J, Mikkelsen A, Jensen M F, Koroteev Y M, Bihlmayer G, Chulkov E V, Adams D L, Hofmann P and Pohl K 2006 Structural determination of the Bi(110) semimetal surface by LEED analysis and ab initio calculations *Physical Review B* **74** 245406
[39] Koroteev Y M, Bihlmayer G, Gayone J E, Chulkov E V, Blugel S, Echenique P M and Hofmann P 2004 Strong spin-orbit splitting on Bi surfaces *Physical Review Letters* **93** 046403
[40] Pascual J I, Bihlmayer G, Koroteev Y M, Rust H P, Ceballos G, Hansmann M, Horn K, Chulkov E V, Blugel S, Echenique P M and Hofmann P 2004 Role of spin in quasiparticle interference *Physical Review Letters* **93** 196802
[41] Wada M, Murakami S, Freimuth F and Bihlmayer G 2011 Localized edge states in two-dimensional topological insulators: Ultrathin Bi films *Physical Review B* **83** 121310
[42] Cucka P and Barrett C 1962 The crystal structure of Bi and of solid solutions of Pb, Sn, Sb and Te in Bi *Acta Crystallographica* **15** 865
[43] Kowalczyk P, Mahapatra O, McCarthy D, Kozlowski W, Klusek Z and Brown S 2011 STM and XPS investigations of bismuth islands on HOPG *Surface Science* **605** 659
[44] Nagao T, Sadowski J T, Saito M, Yaginuma S, Fujikawa Y, Kogure T, Ohno T, Hasegawa Y, Hasegawa S and Sakurai T 2004 Nanofilm allotrope and phase transformation of ultrathin Bi film on Si(111)-7 x 7 *Physical Review Letters* **93** 105501

[45] Sadowski J, Nagao T, Yaginuma S, Fujikawa Y, Sakurai T, Oreshkin A, Saito M and Ohno T 2006 Stability of the quasicubic phase in the initial stage of the growth of bismuth films on Si (111)-7× 7 *Journal of Applied Physics* **99** 014904
[46] Yaginuma S, Nagao T, Sadowski J, Saito M, Nagaoka K, Fujikawa Y, Sakurai T and Nakayama T 2007 Origin of flat morphology and high crystallinity of ultrathin bismuth films *Surface Science* **601** 3593
[47] Sharma H, Fournée V, Shimoda M, Ross A, Lograsso T, Gille P and Tsai A 2008 Growth of Bi thin films on quasicrystal surfaces *Physical Review B* **78** 155416
[48] Winkler R, Papadakis S, De Poortere E and Shayegan M 2000 Anomalous magneto-oscillations in two-dimensional systems *Physical Review Letters* **84** 713
[49] Thomas L H 1926 The motion of the spinning electron *Nature* **117** 514
[50] Fu L and Kane C L 2007 Topological insulators with inversion symmetry *Physical Review B* **76** 045302
[51] Zhang T, Cheng P, Chen X, Jia J F, Ma X, He K, Wang L, Zhang H, Dai X and Fang Z 2009 Experimental demonstration of topological surface states protected by time-reversal symmetry *Physical Review Letters* **103** 266803
[52] Fu L, Kane C L and Mele E J 2007 Topological insulators in three dimensions *Physical Review Letters* **98** 106803
[53] Hirahara T, Nagao T, Matsuda I, Bihlmayer G, Chulkov E, Koroteev Y M, Echenique P, Saito M and Hasegawa S 2006 Role of spin-orbit coupling and hybridization effects in the electronic structure of ultrathin Bi films *Physical Review Letters* **97** 146803
[54] Veuillen J Y, Mallet P, Magaud L and Pons S 2003 Electron confinement effects on Ni-based nanostructures *Journal of Physics-Condensed Matter* **15** S2547
[55] Bihlmayer G, Koroteev Y M, Echenique P, Chulkov E and Blügel S 2006 The Rashba-effect at metallic surfaces *Surface Science* **600** 3888
[56] Bychkov Y A and Rashba E 1984 Properties of a 2D electron gas with lifted spectral degeneracy *JETP lett* **39** 78
[57] Petersen L and Hedegård P 2000 A simple tight-binding model of spin–orbit splitting of *sp*-derived surface states *Surface Science* **459** 49
[58] Bihlmayer G, Koroteev Y M, Chulkov E V and Blugel S 2010 Surface and edge states in ultrathin Bi-Sb films *New Journal of Physics* **12** 065006
[59] Hasan M Z and Kane C L 2010 Colloquium: topological insulators *Reviews of Modern Physics* **82** 3045
[60] Moore J E 2010 The birth of topological insulators *Nature* **464** 194
[61] Hirahara T, Nagao T, Matsuda I, Bihlmayer G, Chulkov E, Koroteev Y M and Hasegawa S 2007 Quantum well states in ultrathin Bi films: Angle-resolved photoemission spectroscopy and first-principles calculations study *Physical Review B* **75** 035422
[62] Hofmann P, Gayone J E, Bihlmayer G, Koroteev Y M and Chulkov E V 2005 Electronic structure and fermi surface of Bi(100) *Physical Review B* **71** 195413
[63] Takayama A, Sato T, Souma S, Oguchi T and Takahashi T 2012 Tunable Spin Polarization in Bismuth Ultrathin Film on Si (111) *Nano letters* **12** 1776
[64] Kotaka H, Ishii F, Saito M, Nagao T and Yaginuma S 2012 Edge States of Bi Nanoribbons on Bi Substrates: First-Principles Density Functional Study *Japanese Journal of Applied Physics* **51** 025201
[65] Hirahara T, Miyamoto K, Matsuda I, Kadono T, Kimura A, Nagao T, Bihlmayer G, Chulkov E, Qiao S and Shimada K 2007 Direct observation of spin splitting in bismuth surface states *Physical Review B* **76** 153305
[66] Golin S 1968 Band structure of bismuth: pseudopotential approach *Physical Review* **166** 643
[67] Chu H and Ji Y 1990 de Haas–van Alphen effect in two-dimensional thin films of pure bismuth *Physical Review B* **41** 920

[68] Gonze X, Michenaud J P and Vigneron J P 1990 First-principles study of As, Sb, and Bi electronic properties *Physical Review B* **41** 11827
[69] Ziman J M 1979 *Principles of the Theory of Solids*: Cambridge University Press
[70] Cohen M H 1961 Energy Bands in the Bismuth Structure. I. A Nonellipsoidal Model for Electrons in Bi *Physical Review* **121** 387
[71] Stróżecka A, Eiguren A and Pascual J I 2011 Quasiparticle Interference around a Magnetic Impurity on a Surface with Strong Spin-Orbit Coupling *Physical Review Letters* **107** 186805
[72] Cottin M C, Bobisch C A, Schaffert J, Jnawali G, Sonntag A, Bihlmayer G and Moller R 2011 Anisotropic scattering of surface state electrons at a point defect on Bi(111) *Applied Physics Letters* **98** 022108
[73] Alpichshev Z, Analytis J, Chu J H, Fisher I R, Chen Y, Shen Z X, Fang A and Kapitulnik A 2010 STM Imaging of Electronic Waves on the Surface of Bi_2Te_3: Topologically Protected Surface States and Hexagonal Warping Effects *Physical Review Letters* **104** 16401
[74] Hirahara T, Miyamoto K, Matsuda I, Kadono T, Kimura A, Nagao T, Bihlmayer G, Chulkov E V, Qiao S, Shimada K, Namatame H, Taniguchi M and Hasegawa S 2007 Direct observation of spin splitting in bismuth surface states *Physical Review B* **76** 153305
[75] McCarthy D N, Robertson D, Kowalczyk P J and Brown S A 2010 The effects of annealing and growth temperature on the morphologies of Bi nanostructures on HOPG *Surface Science* **604** 1273
[76] Scott S A 2005 Self-Assembly of Sb and Bi Nanostructures on Graphite. In: *Physics and Astronomy,* (Christchurch: University of Canterbury)
[77] McCarthy D N 2008 Nucleation and equilibration via surface diffusion : an experimental study In: *Physics and Astronomy,* (Christchurch: University of Canterbury)
[78] Yang F, Miao L, Wang Z, Yao M Y, Zhu F, Song Y, Wang M X, Xu J P, Fedorov A V and Sun Z 2012 Spatial and Energy Distribution of Topological Edge States in Single Bi(111) Bilayer *Physical Review Letters* **109** 16801
[79] Kowalczyk P, Belic D, Mahapatra O, Brown S, Kadantsev E, Woo T, Ingham B and Kozlowski W 2012 Anisotropic oxidation of bismuth nanostructures: Evidence for a thin film allotrope of bismuth *Applied Physics Letters* **100** 151904
[80] Wood E A 1964 Vocabulary of surface crystallography *Journal of Applied Physics* **35** 1306
[81] Weissler G and Carlson R W 1979 *Vacuum physics and technology* vol 14: Academic Press
[82] Redhead P, Hobson J and Kornelsen E 1993 *The Physical Basis of Ultrahigh Vacuum* American Institute of Physics
[83] Omicron 2008 VT AFM XA User's guide
[84] Metois J, Heyraud J and Takeda Y 1978 Experimental conditions to obtain clean graphite surfaces *Thin Solid Films* **51** 105
[85] Inc S I 1997 *Sycon Instruments Users Manual*
[86] Becker T, Hövel H, Tschudy M and Reihl B 1998 Applications with a new low-temperature UHV STM at 5 K *Applied Physics A: Materials Science & Processing* **66** 27
[87] Binnig G, Rohrer H, Gerber C and Weibel E 1982 Surface studies by scanning tunneling microscopy *Physical Review Letters* **49** 57
[88] Giaever I 1960 Energy gap in superconductors measured by electron tunneling *Physical Review Letters* **5** 147
[89] Fisher J and Giaever I 1961 Tunneling through thin insulating layers *Journal of Applied Physics* **32** 172
[90] Chen C J 1993 *Introduction to scanning tunneling microscopy* vol 4: Oxford University Press, USA
[91] Feenstra R, Ramachandran V and Chen H 2001 Recent developments in scanning tunneling spectroscopy of semiconductor surfaces *Applied Physics A: Materials Science & Processing* **72** 193

[92] Güntherodt H J, Wiesendanger R and Anselmetti D 1994 *Scanning tunneling microscopy I: general principles and applications to clean and adsorbate-covered surfaces*: Springer-Verlag
[93] Hamers R 1989 Atomic-resolution surface spectroscopy with the scanning tunneling microscope *Annual Review of Physical Chemistry* **40** 531
[94] Ukraintsev V A 1996 Data evaluation technique for electron-tunneling spectroscopy *Physical Review B* **53** 11176
[95] Ermakov A and Garfunkel E 1994 A novel AFM/STM/SEM system *Review of scientific instruments* **65** 2853
[96] Nagahara L, Thundat T and Lindsay S 1989 Preparation and characterization of STM tips for electrochemical studies *Review of scientific instruments* **60** 3128
[97] Ekvall I, Wahlström E, Claesson D, Olin H and Olsson E 1999 Preparation and characterization of electrochemically etched W tips for STM *Measurement Science and Technology* **10** 11
[98] Yu Z, Wang C M, Du Y, Thevuthasan S and Lyubinetsky I 2008 Reproducible tip fabrication and cleaning for UHV STM *Ultramicroscopy* **108** 873
[99] Yurov V Y and Klimov A 1994 Scanning tunneling microscope calibration and reconstruction of real image: Drift and slope elimination *Review of scientific instruments* **65** 1551
[100] Selloni A, Carnevali P, Tosatti E and Chen C 1985 Voltage-dependent scanning-tunneling microscopy of a crystal surface: Graphite *Physical Review B* **31** 2602
[101] Bonnell D A 1993 *Scanning tunneling microscopy and spectroscopy: Theory, techniques, and applications*: VCH
[102] Mäder R 2010 *Scanning tunneling microscopy and spectroscopy of aluminum based quasicrystals and approximants*: Logos Verlag Berlin GmbH
[103] Feenstra R M 2009 A prospective: Quantitative scanning tunneling spectroscopy of semiconductor surfaces *Surface Science* **603** 2841
[104] Binnig G, Quate C F and Gerber C 1986 Atomic force microscope *Physical Review Letters* **56** 930
[105] Meyer E 1992 Atomic force microscopy *Progress in Surface Science* **41** 3
[106] Blanchard C R 1996 Atomic force microscopy *The chemical educator* **1** 1
[107] Martin Y, Williams C and Wickramasinghe H K 1987 Atomic force microscope–force mapping and profiling on a sub 100-Å scale *Journal of Applied Physics* **61** 4723
[108] Baer Y and Myers H 1977 An XPS study of the valence bands in solid and liquid bismuth *Solid State Communications* **21** 833
[109] Hamm U, Kramer D, Zhai R and Kolb D 1998 On the valence state of bismuth adsorbed on a Pt (111) electrode: an electrochemistry, LEED and XPS study *Electrochimica acta* **43** 2969
[110] Akturk O U and Tomak M 2010 Bismuth doping of graphene *Applied Physics Letters* **96** 081914
[111] Morgan W E, Stec W J and Van Wazer J R 1973 Inner-orbital binding-energy shifts of antimony and bismuth compounds *Inorganic Chemistry* **12** 953
[112] Dharmadhikari V S, Sainkar S, Badrinarayan S and Goswami A 1982 Characterisation of thin films of bismuth oxide by X-ray photoelectron spectroscopy *Journal of Electron Spectroscopy and Related Phenomena* **25** 181
[113] Hayazaki S, Matsui T, Zhang H, Chen W, Wee A and Yuhara J 2008 Formation of bismuth nanodot in (4× 4) vanadium oxide nanomesh on Pd (111) *Surface Science* **602** 2025
[114] Moulder J F, Chastain J and King R C 1995 *Handbook of X-ray photoelectron spectroscopy: a reference book of standard spectra for identification and interpretation of XPS data*: Physical Electronics Eden Prairie, MN
[115] Wagner C, Briggs D and Seah M 1983 Practical surface analysis by auger and X-ray photoelectron spectroscopy *by D. Briggs and MP Seah, John Wiley & Sons Ltd*
[116] Yeh J 1993 *Atomic calculation of photoionization cross-sections and asymmetry parameters*: Gordon & Breach Science

[117] Jeffrey C A, Zheng S H, Bohannan E, Harrington D A and Morin S 2006 X-ray characterization of as-deposited, epitaxial films of Bi (012) on Au (111) *Surface Science* **600** 95
[118] Zhang H L, Chen W, Wang X S, Yuhara J and Wee A T S 2009 Growth of well-aligned Bi nanowire on Ag (111) *Applied Surface Science* **256** 460
[119] Kowalczyk P 2009 Investigation of STM tip influence on the recorded position of the Shockley surface state on Au (111) *Surface Science* **603** 747
[120] Fischer Ø, Kugler M, Maggio-Aprile I, Berthod C and Renner C 2007 Scanning tunneling spectroscopy of high-temperature superconductors *Reviews of Modern Physics* **79** 353
[121] Weisman A D, Dougherty E R, Mizes H A and Miller R 1992 Nonlinear digital filtering of scanning-probe-microscopy images by morphological pseudoconvolutions *Journal of Applied Physics* **71** 1565
[122] Arenhold K, Surnev S, Coenen P, Bonzel H and Wynblatt P 1998 Scanning tunneling microscopy of equilibrium crystal shape of Pb particles: test of universality *Surface Science* **417** L160
[123] Niimi Y, Matsui T, Kambara H, Tagami K, Tsukada M and Fukuyama H 2005 Scanning tunneling microscopy and spectroscopy studies of graphite edges *Applied Surface Science* **241** 43
[124] Rohrer G S and Bonnell D A 1991 Probing the surface chemistry of polycrystalline ZnO with scanning tunneling microscopy and tunneling spectroscopy *Journal of Vacuum Science & Technology B: Microelectronics and Nanometer Structures* **9** 783
[125] Odom T W, Huang J L, Kim P, Ouyang M and Lieber C M 1998 Scanning tunneling microscopy and spectroscopy studies of single wall carbon nanotubes *Journal of Materials Research* **13** 2380
[126] Kowalczyk P, Mahapatra O, Brown S, Bian G, Wang X X and Chiang T 2012 Electronic Size Effects in Three-Dimensional Nanostructures *Nano letters* **13** 43
[127] Yin F, Akola J, Koskinen P, Manninen M and Palmer R E 2009 Bright Beaches of Nanoscale Potassium Islands on Graphite in STM Imaging *Physical Review Letters* **102** 106102
[128] Binnig G, Rohrer H, Gerber C and Weibel E 1983 7× 7 reconstruction on Si (111) resolved in real space *Physical Review Letters* **50** 120
[129] He T, Pan F, Xi Z, Zhang X, Zhang H, Wang Z, Zhao M, Yan S and Xia Y 2010 First-Principles Study of Titania Nanoribbons: Formation, Energetics, and Electronic Properties *The Journal of Physical Chemistry C* **114** 9234
[130] Park C H and Louie S G 2008 Energy gaps and stark effect in boron nitride nanoribbons *Nano letters* **8** 2200
[131] Sun L, Li Y, Li Z, Li Q, Zhou Z, Chen Z, Yang J and Hou J 2008 Electronic structures of SiC nanoribbons *The Journal of chemical physics* **129** 174114
[132] Nakada K, Fujita M, Dresselhaus G and Dresselhaus M S 1996 Edge state in graphene ribbons: Nanometer size effect and edge shape dependence *Physical Review B* **54** 17954
[133] Fujita M, Wakabayashi K, Nakada K and Kusakabe K 1996 Peculiar localized state at zigzag graphite edge *Journal of the Physical Society of Japan* **65** 1920
[134] Son Y W, Cohen M L and Louie S G 2006 Half-metallic graphene nanoribbons *Nature* **444** 347
[135] Kan E, Li Z, Yang J and Hou J 2008 Half-metallicity in edge-modified zigzag graphene nanoribbons *Journal of the American Chemical Society* **130** 4224
[136] Zhu L, Zhang T and Wang J Electronic Structure of Bi Nanoribbon: Greatly Influenced by Edge Chirality and Edge Reconstruction *The Journal of Physical Chemistry C* **114** 19289
[137] Hasegawa Y and Avouris P 1993 Direct Observation of Standing-Wave Formation at Surface Steps Using Scanning Tunneling Spectroscopy *Physical Review Letters* **71** 1071
[138] Crommie M F, Lutz C P and Eigler D M 1993 Confinement of electrons to quantum corrals on a metal surface *Science* **262** 218
[139] Heller E, Crommie M, Lutz C and Eigler D 1994 Scattering and absorption of surface electron waves in quantum corrals *Nature* **369** 464

[140] Crommie M, Lutz C, Eigler D and Heller E 1995 Quantum corrals *Physica D: Nonlinear Phenomena* **83** 98
[141] Crommie M F, Lutz C, Eigler D and Heller E 1995 Waves on a metal surface and quantum corrals *Surface Review and Letters* **2** 127
[142] Friedel J 1958 Metallic alloys *Il Nuovo Cimento (1955-1965)* **7** 287
[143] Crommie M, Lutz C and Eigler D 1993 Imaging standing waves in a two-dimensional electron gas *Nature* **363** 524
[144] Pivetta M, Silly F, Patthey F, Pelz J P and Schneider W D 2003 Reading the ripples of confined surface-state electrons: Profiles of constant integrated local density of states *Physical Review B* **67** 193402
[145] Pons S, Mallet P and Veuillen J Y 2001 Electron confinement in nickel and copper nanostructures on Cu (111) *Physical Review B* **64** 193408
[146] Kliewer J, Berndt R and Crampin S 2001 Scanning tunnelling spectroscopy of electron resonators *New Journal of Physics* **3** 22
[147] Memmel N 1998 Monitoring and modifying properties of metal surfaces by electronic surface states *Surface Science Reports* **32** 91
[148] Crommie M, Lutz C and Eigler D 1993 Confinement of electrons to quantum corrals on a metal surface *Science* **262** 218
[149] Braun K F and Rieder K H 2002 Engineering electronic lifetimes in artificial atomic structures *Physical Review Letters* **88** 96801
[150] Pons S, Mallet P, Magaud L and Veuillen J Y 2002 Spontaneous evolution of the Ni/Cu (111) interface at 300 K *Surface Science* **511** 449
[151] Avouris P and Lyo I W 1994 Observation of quantum-size effects at room temperature on metal surfaces with STM *Science* **264** 942
[152] Smoluchowski R 1941 Anisotropy of the electronic work function of metals *Physical Review* **60** 661
[153] Berthold W, Höfer U, Feulner P, Chulkov E, Silkin V and Echenique P 2002 Momentum-resolved lifetimes of image-potential states on Cu(100) *Physical Review Letters* **88** 56805
[154] Bartels L, Hla S W, Kuhnle A, Meyer G, Rieder K H and Manson J R 2003 STM observations of a one-dimensional electronic edge state at steps on Cu(111) *Physical Review B* **67** 205416
[155] Bernevig B A, Hughes T L and Zhang S C 2006 Quantum spin Hall effect and topological phase transition in HgTe quantum wells *Science* **314** 1757
[156] Hsieh D, Xia Y, Wray L, Qian D, Pal A, Dil J, Osterwalder J, Meier F, Bihlmayer G and Kane C 2009 Observation of unconventional quantum spin textures in topological insulators *Science* **323** 919
[157] Kane C L and Mele E J 2005 Z_2 Topological Order and the Quantum Spin Hall Effect *Physical Review Letters* **95** 146802
[158] Moore J and Balents L 2007 Topological invariants of time-reversal-invariant band structures *Physical Review B* **75** 121306
[159] Murakami S 2007 Phase transition between the quantum spin Hall and insulator phases in 3D: emergence of a topological gapless phase *New Journal of Physics* **9** 356
[160] Qi X L, Hughes T L and Zhang S C 2008 Topological field theory of time-reversal invariant insulators *Physical Review B Condensed Matter And Materials Physics* **78** 195424
[161] Roy R 2009 Topological phases and the quantum spin Hall effect in three dimensions *Physical Review B* **79** 195322
[162] Seo J, Roushan P, Beidenkopf H, Hor Y S, Cava R J and Yazdani A 2010 Transmission of topological surface states through surface barriers *Nature* **466** 343
[163] Stone M 1981 *Quantum Hall Effect*: World Scientific Publishing Company Incorporated
[164] Roushan P, Seo J, Parker C V, Hor Y, Hsieh D, Qian D, Richardella A, Hasan M Z, Cava R and Yazdani A 2009 Topological surface states protected from backscattering by chiral spin texture *Nature* **460** 1106

[165] Alpichshev Z, Analytis J, Chu J H, Fisher I and Kapitulnik A 2011 STM imaging of a bound state along a step on the surface of the topological insulator Bi_2Te_3 *Physical Review B* **84** 041104
[166] Kowalczyk P, Belić D, Mahapatra O and Brown S 2012 Grain boundaries between bismuth nanocrystals *Acta Materialia* **60** 674
[167] Knight W, Clemenger K, de Heer W A, Saunders W A, Chou M and Cohen M L 1984 Electronic shell structure and abundances of sodium clusters *Physical Review Letters* **52** 2141
[168] Zhang Z, Niu Q and Shih C K 1998 "Electronic Growth" of Metallic Overlayers on Semiconductor Substrates *Physical Review Letters* **80** 5381
[169] Miller T, Chou M and Chiang T C 2009 Phase relations associated with one-dimensional shell effects in thin metal films *Physical Review Letters* **102** 236803
[170] Bian G, Miller T and Chiang T C 2009 Electronic structure and surface-mediated metastability of Bi films on Si(111)-7x7 studied by angle-resolved photoemission spectroscopy *Physical Review B* **80** 245407
[171] Tringides M C, Jałochowski M and Bauer E 2007 Quantum size effects in metallic nanostructures *Physics Today* **60** 50
[172] Chiang T C 2000 Photoemission studies of quantum well states in thin films *Surface Science Reports* **39** 181
[173] Liu Y, Paggel J, Upton M, Miller T and Chiang T C 2008 Quantized electronic structure and growth of Pb films on highly oriented pyrolytic graphite *Physical Review B* **78** 235437
[174] Wei C and Chou M 2002 Theory of quantum size effects in thin Pb (111) films *Physical Review B* **66** 233408
[175] Feng R, Conrad E H, Tringides M, Kim C and Miceli P F 2004 Wetting-layer transformation for Pb nanocrystals grown on Si(111) *Applied Physics Letters* **85** 3866
[176] Otero R, de Parga A L V and Miranda R 2002 Observation of preferred heights in Pb nanoislands: A quantum size effect *Physical Review B* **66** 115401
[177] Liu K, Chien C L and Searson P 1998 Finite-size effects in bismuth nanowires *Physical Review B* **58** 14681
[178] Yao W T, Yu S H and Wu Q S 2007 From Mesostructured Wurtzite ZnS-Nanowire/Amine Nanocomposites to ZnS Nanowires Exhibiting Quantum Size Effects: A Mild-Solution Chemistry Approach *Advanced Functional Materials* **17** 623
[179] Chiang T C 2004 Superconductivity in thin films *Science* **306** 1900
[180] Stormer H, Schlesinger Z, Chang A, Tsui D, Gossard A and Wiegmann W 1983 Energy structure and quantized Hall effect of two-dimensional holes *Physical Review Letters* **51** 126
[181] Garcia N, Kao Y and Strongin M 1972 Galvanomagnetic studies of bismuth films in the quantum-size-effect region *Physical Review B* **5** 2029
[182] Chiang T C 2010 One-Dimensional Shell Effects in Thin Metal Films *Bulletin of the American Physical Society* **55** 2
[183] Evans D, Alonso M, Cimino R and Horn K 1993 Observation of quantum size effects in photoemission from Ag islands on GaAs (110) *Physical Review Letters* **70** 3483
[184] Jia Y, Wu B, Weitering H H and Zhang Z 2006 Quantum size effects in Pb films from first principles: The role of the substrate *Physical Review B* **74** 035433
[185] Mans A, Dil J, Ettema A and Weitering H 2002 Quantum electronic stability and spectroscopy of ultrathin Pb films on Si (111) 7× 7 *Physical Review B* **66** 195410
[186] Huang L, Jay Chey S and Weaver J 1998 Metastable structures and critical thicknesses: Ag on Si (111)-7× 7 *Surface Science* **416** L1101
[187] Lu S, Yang M, Su W, Jiang C, Hsu T, Chang C and Tsong T T 2007 Strength modulation of quantum-well states in Pb islands with periodic distortions on Si (111) *Physical Review B* **75** 113402
[188] Hupalo M and Tringides M 2002 Correlation between height selection and electronic structure of the uniform height Pb/Si (111) islands *Physical Review B* **65** 115406

[189] Chan T L, Wang C Z, Hupalo M, Tringides M and Ho K M 2006 Quantum size effect on the diffusion barriers and growth morphology of Pb/Si (111) *Physical Review Letters* **96** 226102
[190] Crottini A, Cvetko D, Floreano L, Gotter R, Morgante A and Tommasini F 1997 Step height oscillations during layer-by-layer growth of Pb on Ge (001) *Physical Review Letters* **79** 1527
[191] Czoschke P, Hong H, Basile L and Chiang T C 2004 Quantum beating patterns observed in the energetics of Pb film nanostructures *Physical Review Letters* **93** 36103
[192] Blunt M O, Martin C, Ahola-Tuomi M, Pauliac-Vaujour E, Sharp P, Nativo P, Brust M and Moriarty P 2007 Coerced mechanical coarsening of nanoparticle assemblies *Nature Nanotechnology* **2** 167
[193] Gierz I, Riedl C, Starke U, Ast C R and Kern K 2008 Atomic hole doping of graphene *Nano letters* **8** 4603
[194] Bian G and Chiang T C 2012 unpublished
[195] Bian G, Miller T and Chiang T C 2009 Electronic structure and surface-mediated metastability of Bi films on Si (111)-7× 7 studied by angle-resolved photoemission spectroscopy *Physical Review B* **80** 245407
[196] Meadows D, Johnson W and Allen J 1970 Generation of surface contours by moiré patterns *Applied Optics* **9** 942
[197] Oster G, Wasserman M and Zwerling C 1964 Theoretical interpretation of moiré patterns *JOSA* **54** 169
[198] Houzay F, Guille C, Moison J, Henoc P and Barthe F 1987 First stages of the MBE growth of InAs on (001) GaAs *Journal of crystal growth* **81** 67
[199] Jasinski J, Dumpala S, Sumanasekera G, Sunkara M and Ouseph P 2011 Observation and interpretation of adjacent Moire patterns of different shapes in bilayer graphene *Applied Physics Letters* **99** 073104
[200] Ritter M, Ranke W and Weiss W 1998 Growth and structure of ultrathin FeO films on Pt (111) studied by STM and LEED *Physical Review B* **57** 7240
[201] Sellam F, Schmitz-Hübsch T, Toerker M, Mannsfeld S, Proehl H, Fritz T, Leo K, Simpson C and Müllen K 2001 LEED and STM investigations of organic–organic heterostructures grown by molecular beam epitaxy *Surface Science* **478** 113
[202] Rong Z Y and Kuiper P 1993 Electronic effects in scanning tunneling microscopy: Moiré pattern on a graphite surface *Physical Review B* **48** 17427
[203] Albrecht T, Mizes H, Nogami J, Park S and Quate C 1988 Observation of tilt boundaries in graphite by scanning tunneling microscopy and associated multiple tip effects *Applied Physics Letters* **52** 362
[204] Kobayashi K 1996 Moiré pattern in scanning tunneling microscopy: Mechanism in observation of subsurface nanostructures *Physical Review B* **53** 11091
[205] Kobayashi K 1994 Moiré pattern in scanning tunneling microscopy of monolayer graphite *Physical Review B* **50** 4749
[206] Nysten B, Roux J C, Flandrois S, Daulan C and Saadaoui H 1993 AFM and STM studies of the carbonization and graphitization of polyimide films *Physical Review B* **48** 12527
[207] Patrin J, Li Y, Chander M and Weaver J 1992 Sb and Bi on GaAs (110): Substrate-stabilized overlayer structures studied with scanning tunneling microscopy *Physical Review B* **46** 10221
[208] Müller U, Carnal D, Siegenthaler H, Schmidt E, Lorenz W, Obretenov W, Schmidt U, Staikov G and Budevski E 1992 Superstructures of Pb monolayers electrochemically deposited on Ag (111) *Physical Review B* **46** 12899
[209] Itoh H, Ichinose T, Oshima C, Ichinokawa T and Aizawa T 1991 Scanning tunneling microscopy of monolayer graphite epitaxially grown on a TiC (111) surface *Surface Science* **254** L437
[210] Land T, Michely T, Behm R, Hemminger J and Comsa G 1992 Direct observation of surface reactions by scanning tunneling microscopy: ethylene→ ethylidyne→ carbon particles→ graphite on Pt (111) *The Journal of chemical physics* **97** 6774

[211] Parkinson B, Ohuchi F, Ueno K and Koma A 1991 Periodic lattice distortions as a result of lattice mismatch in epitaxial films of two-dimensional materials *Applied Physics Letters* **58** 472
[212] Mori T, Saiki K and Koma A 1992 Atom intensity variation in the scanning tunneling microscope image of mixed crystals of transition metal dichalcogenides *Japanese Journal of Applied Physics Part2 Letters* **31** 1370
[213] Mori T, Abe H, Saiki K and Koma A 1993 Characterization of epitaxial films of layered materials using Moiré images of scanning tunneling microscope *Japanese Journal of Applied Physics* **32** 2945
[214] Feenstra R, Woodall J and Pettit G 1993 Observation of bulk defects by scanning tunneling microscopy and spectroscopy: Arsenic antisite defects in GaAs *Physical Review Letters* **71** 1176
[215] Johnson M, Albrektsen O, Feenstra R and Salemink H 1993 Direct imaging of dopants in GaAs with cross-sectional scanning tunneling microscopy *Applied Physics Letters* **63** 2923
[216] Zheng J, Liu X, Newman N, Weber E, Ogletree D and Salmeron M 1994 Scanning tunneling microscopy studies of Si donors (Si_{Ga}) in GaAs *Physical Review Letters* **72** 1490
[217] Kuwabara M, Clarke D R and Smith D 1990 Anomalous superperiodicity in scanning tunneling microscope images of graphite *Applied Physics Letters* **56** 2396
[218] Xhie J, Sattler K, Ge M and Venkateswaran N 1993 Giant and supergiant lattices on graphite *Physical Review B* **47** 15835
[219] Cee V J, Patrick D L and Beebe T P 1995 Unusual aspects of superperiodic features on highly oriented pyrolytic graphite *Surface Science* **329** 141
[220] Hupalo M, Yeh V, Chan T, Wang C, Ho K and Tringides M 2005 Interface relaxation and electronic corrugation in the Pb⁄ Si (111)-Pb-α-√ 3×√ 3 *Physical Review B* **71** 193408
[221] Giordano L, Pacchioni G, Goniakowski J, Nilius N, Rienks E D L and Freund H J 2007 Interplay between structural, magnetic, and electronic properties in a FeO⁄ Pt (111) ultrathin film *Physical Review B* **76** 075416
[222] Pivetta M, Patthey F, Stengel M, Baldereschi A and Schneider W D 2005 Local work function Moiré pattern on ultrathin ionic films: NaCl on Ag (100) *Physical Review B* **72** 115404
[223] Rienks E D L, Nilius N, Rust H P and Freund H J 2005 Surface potential of a polar oxide film: FeO on Pt (111) *Physical Review B* **71** 241404
[224] Repp J, Meyer G and Rieder K H 2004 Snell's law for surface electrons: refraction of an electron gas imaged in real space *Physical Review Letters* **92** 36803
[225] Nilius N, Rienks E D L, Rust H P and Freund H J 2005 Self-organization of gold atoms on a polar FeO (111) surface *Physical Review Letters* **95** 66101
[226] Pan Y, Gao M, Huang L, Liu F and Gao H J 2009 Directed self-assembly of monodispersed platinum nanoclusters on graphene Moiré template *Applied Physics Letters* **95** 093106
[227] Liao Q, Zhang H, Wu K, Li H, Bao S and He P 2011 Nucleation and growth of monodispersed cobalt nanoclusters on graphene moiré on Ru (0001) *Nanotechnology* **22** 125303
[228] Sicot M, Bouvron S, Zander O, Rudiger U, Dedkov Y S and Fonin M 2010 Nucleation and growth of nickel nanoclusters on graphene Moiré on Rh (111) *Applied Physics Letters* **96** 093115
[229] Chen C H, Kepler K D, Gewirth A A, Ocko B and Wang J 1993 Electrodeposited bismuth monolayers on gold (111) electrodes: comparison of surface x-ray scattering, scanning tunneling microscopy, and atomic force microscopy lattice structures *The Journal of Physical Chemistry* **97** 7290
[230] Ast C R and Höchst H 2003 Indication of charge-density-wave formation in Bi (111) *Physical Review Letters* **90** 16403
[231] Cave E and Holroyd L 1960 Thermal expansion coefficients of bismuth *Journal of Applied Physics* **31** 1357
[232] Morgan W 1972 Thermal expansion coefficients of graphite crystals *Carbon* **10** 73

[233] Nelson J and Riley D 2002 The thermal expansion of graphite from 15° c. to 800° c.: part I. Experimental *Proceedings of the Physical Society* **57** 477
[234] Bailey A and Yates B 1970 Anisotropic thermal expansion of pyrolytic graphite at low temperatures *Journal of Applied Physics* **41** 5088
[235] Repp J, Folsch S, Meyer G and Rieder K H 2001 Ionic films on vicinal metal surfaces: Enhanced binding due to charge modulation *Physical Review Letters* **86** 252
[236] Sun X N, Felicissimo M P, Rudolf P and Silly F 2008 NaCl multi-layer islands grown on Au(111)-(22 x √ 3) probed by scanning tunneling microscopy *Nanotechnology* **19** 495307
[237] Sun X N and Silly F 2010 NaCl islands decorated with 2D or 3D 3,4,9,10-perylene-tetracarboxylic-dianhydride nanostructures *Applied Surface Science* **256** 2228
[238] Olsson F E, Persson M, Repp J and Meyer G 2005 Scanning tunneling microscopy and spectroscopy of NaCl overlayers on the stepped Cu(311) surface: Experimental and theoretical study *Physical Review B* **71** 075419
[239] Canas-Ventura M E, Xiao W, Ruffieux P, Rieger R, Mullen K, Brune H and Fasel R 2009 Stabilization of bimolecular islands on ultrathin NaCl films by a vicinal substrate *Surface Science* **603** 2294
[240] Cavar E, Blum M C, Pivetta M, Patthey F, Chergui M and Schneider W D 2005 Fluorescence and phosphorescence from individual C-60 molecules excited by local electron tunneling *Physical Review Letters* **95** 196102
[241] Freysoldt C, Rinke P and Scheffler M 2009 Controlling Polarization at Insulating Surfaces: Quasiparticle Calculations for Molecules Adsorbed on Insulator Films *Physical Review Letters* **103** 056803
[242] Hebenstreit W, Redinger J, Horozova Z, Schmid M, Podloucky R and Varga P 1999 Atomic resolution by STM on ultra-thin films of alkali halides: experiment and local density calculations *Surface Science* **424** L321
[243] Olsson F E, Paavilainen S, Persson M, Repp J and Meyer G 2007 Multiple charge states of Ag atoms on ultrathin NaCl films *Physical Review Letters* **98** 176803
[244] Folsch S, Riemann A, Repp J, Meyer G and Rieder K H 2002 From atomic kinks to mesoscopic surface patterns: Ionic layers on vicinal metal surfaces *Physical Review B* **66** 161409
[245] Glocker K, Sokolowski M, Soukopp A and Umbach E 1996 Initial growth of insulating overlayers of NaCl on Ge(100) observed by scanning tunneling microscopy with atomic resolution *Physical Review B* **54** 7705
[246] Bennewitz R, Barwich V, Bammerlin M, Loppacher C, Guggisberg R, Baratoff A, Meyer E and Guntherodt H J 1999 Ultrathin films of NaCl on Cu(111): a LEED and dynamic force microscopy study *Surface Science* **438** 289
[247] Schwennicke C, Schimmelpfennig J and Pfnür H 1993 Morphology of thin NaCl films grown epitaxially on Ge (100) *Surface Science* **293** 57
[248] Ramoino L, Von Arx M, Schintke S, Baratoff A, Guntherodt H J and Jung T 2006 Layer-selective epitaxial self-assembly of porphyrins on ultrathin insulators *Chemical physics letters* **417** 22
[249] Scarfato A, Chang S H, Kuck S, Brede J, Hoffmann G and Wiesendanger R 2008 Scanning tunneling microscope study of iron (II) phthalocyanine growth on metals and insulating surfaces *Surface Science* **602** 677
[250] Repp J, Meyer G, Olsson F E and Persson M 2004 Controlling the charge state of individual gold adatoms *Science* **305** 493
[251] Ćavar E, Blüm M C, Pivetta M, Patthey F, Chergui M and Schneider W D 2005 Fluorescence and Phosphorescence from Individual C_{60} Molecules Excited by Local Electron Tunneling *Physical Review Letters* **95** 196102
[252] Scott S and Brown S 2006 Three-dimensional growth characteristics of antimony aggregates on graphite *The European Physical Journal D-Atomic, Molecular, Optical and Plasma Physics* **39** 433

[253] Carroll S, Seeger K and Palmer R 1998 Trapping of size-selected Ag clusters at surface steps *Applied Physics Letters* **72** 305
[254] Bréchignac C, Cahuzac P, Carlier M d F, A. Masson F, Mory C, Colliex C and Yoon B 1998 Size effects in nucleation and growth processes from preformed soft-landed clusters *Physical Review B* **57** 2084
[255] Witten T A and Sander L M 1981 DIFFUSION-LIMITED AGGREGATION, A KINETIC CRITICAL PHENOMENON *Physical Review Letters* **47** 1400
[256] Zhang Z Y and Lagally M G 1997 Atomistic processes in the early stages of thin-film growth *Science* **276** 377

10. Publications from this thesis

(i) Kowalczyk P, **Mahapatra O**, Brown S, Bian G, Wang X X and Chiang T 2012 Electronic Size Effects in Three-Dimensional Nanostructures *Nano letters*

(ii) Kowalczyk P, Belic D, **Mahapatra O**, Brown S, Kadantsev E, Woo T, Ingham B and Kozlowski W 2012 Anisotropic oxidation of bismuth nanostructures: Evidence for a thin film allotrope of bismuth *Applied Physics Letters* **100** 151904

(iii) Kowalczyk P, Belić D, **Mahapatra O** and Brown S 2012 Grain boundaries between bismuth nanocrystals *Acta Materialia* **60** 674

(iv) Kowalczyk P J, **Mahapatra O**, McCarthy D N, Kozlowski W, Klusek Z and Brown S A 2011 STM and XPS investigations of bismuth islands on HOPG *Surface Science* **605** 659

(v) Kowalczyk P J, **Mahapatra O**, Brown S A, Bian G, Chiang T C 2012 Origin of the Moiré pattern in thin Bi films deposited on HOPG (unpublished)

(vi) **Mahapatra O**, Kowalczyk P J, Brown S A 2012 Edge States in Bi(110) thin films on HOPG (unpublished)

(vii) **Mahapatra O**, Kowalczyk P J, Brown S A 2012 Growth and electronic properties of NaCl on HOPG (unpublished)

11. Appendix 1

Table of unit cell measurements

Measurement Number	Measured value in $< 112 >$* direction (nm)	Measured value in $< \bar{1}10 >$ direction (nm)
1	0.48	0.46
2	0.48	0.457
3	0.47	0.45
4	0.476	0.46
5	0.47	0.46
6	0.484	0.467
7	0.483	0.467
8	0.483	0.47
9	0.477	0.459
10	0.477	0.46
11	0.51	0.44
12	0.507	0.44
13	0.489	0.468
14	0.51	0.457
15	0.51	0.45
16	0.482	0.46
17	0.484	0.457
18	0.51	0.46
19	0.48	0.46
20	0.46	0.45
21	0.467	0.45
22	0.486	0.458
23	0.48	0.449
24	0.474	0.46
25	0.48	0.46
26	0.51	0.453
27	0.476	0.46
28	0.475	0.453

29	0.483	0.456
30	0.48	0.46

From the table above it can be seen that the measured value of the unit cell in $< 112 >$* direction is ~0.48 ± 0.03 nm and the measured value in $< \bar{1}10 >$ direction is ~0.46 ± 0.02 nm.

12. Appendix 2

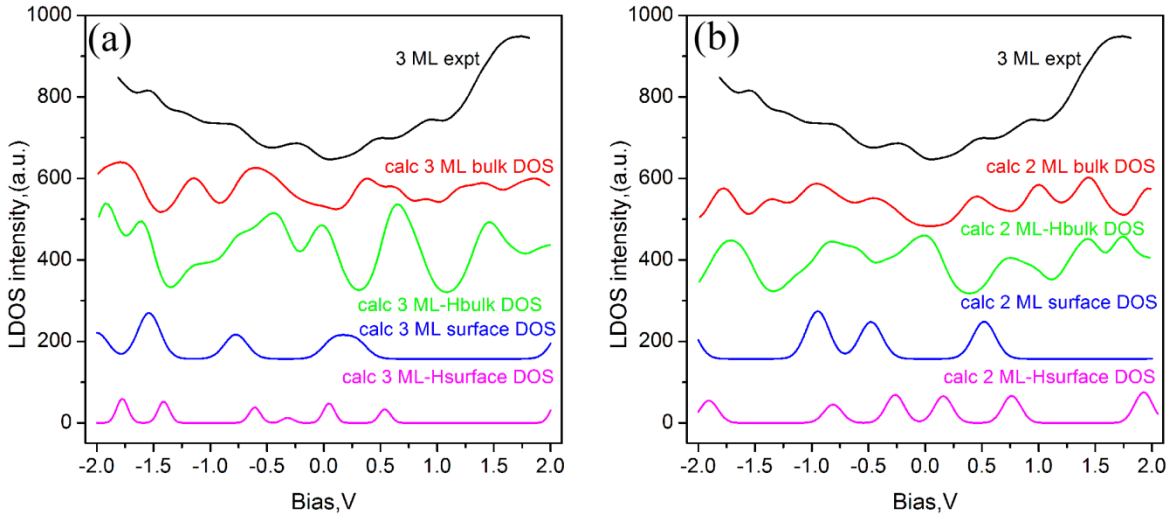

Figure 1: (a) Comparison of 3 ML experimental dI/dV(V) curve with various calculated 3 ML data (b) Comparison of 3 ML experimental dI/dV(V) curve with various calculated 2ML data. The best match is obtained between 3 ML experimental dI/dV(V) curve with calculated 2 ML bulk DOS curve.

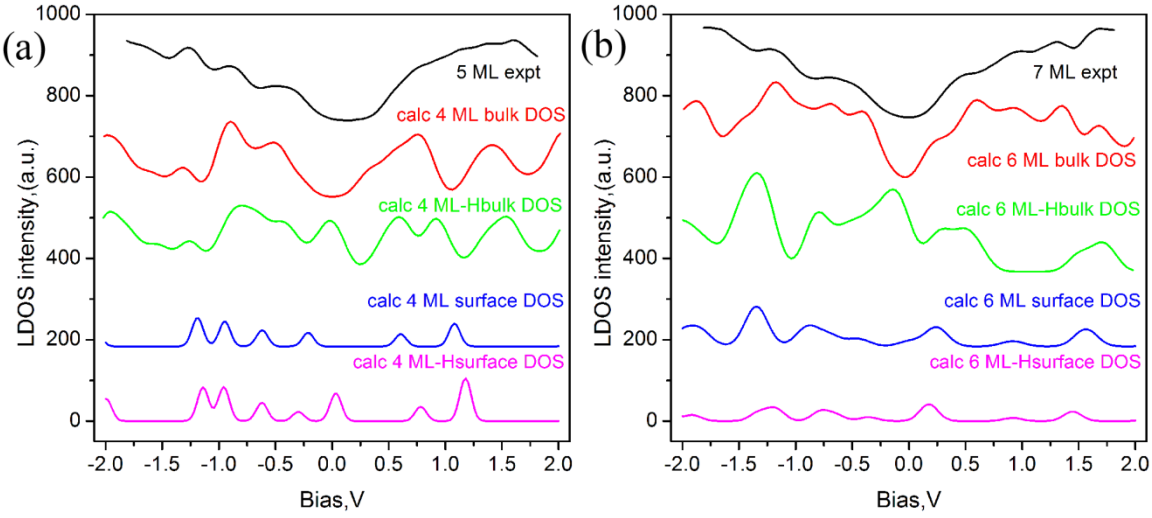

Figure 2: (a) Comparison of 5 ML experimental dI/dV(V) curve with various calculated 4 ML data. Best match is attained between 5 ML experimental dI/dV(V) curve with calculated 4 ML bulk DOS. (b) Comparison of 7 ML experimental dI/dV(V) curve with various calculated 6 ML data. The best match is obtained between 7 ML experimental dI/dV(V) curve with calculated 6 ML bulk DOS curve.

13. Appendix 3

Fourier transform filter

Frequency filtering is based on the Fourier Transform. The operator usually takes an image and a filter function in the Fourier domain. This image is then multiplied with the filter function in a pixel-by-pixel fashion:

$$A(k,l) = B(k,l)C(k,l)$$

where $B(k,l)$ is the input image in the Fourier domain, $C(k,l)$is the filter function and $G(k,l)$ is the filtered image. To obtain the resulting image in the spatial domain, $A(k,l)$ has to be re-transformed using the inverse Fourier Transform. Since the multiplication in the Fourier space is identical to convolution in the spatial domain, all frequency filters can in theory be implemented as a spatial filter. However, in practice, the Fourier domain filter function can only be approximated by the filtering kernel in spatial domain. The form of the filter function determines the effects of the operator.

There are basically three different kinds of filters: low pass, high pass and band pass filters. A low-pass filter attenuates high frequencies and retains low frequencies unchanged. The result in the spatial domain is equivalent to that of smoothing filter; as the blocked high frequencies correspond to sharp intensity changes, i.e. to the fine-scale details and noise in the spatial domain image. A high pass filter, on the other hand, yields edge enhancement or edge detection in the spatial domain, because edges contain many high frequencies. Areas of rather constant gray level consist of mainly low frequencies and are therefore suppressed. A band pass attenuates very low and very high frequencies, but retains a middle range band of frequencies. Band pass filtering can be used to enhance edges (suppressing low frequencies) while reducing the noise at the same time (attenuating high frequencies).

14. List of Figures

15. Acknowledgements

I always looked forward to write this last section of my thesis but now when I am here I am out of words. One of the joys of completion is to look over the past and remember all the feelings you went through – excitement, enthusiasm, joy, sadness, pain, suffering, self doubt, self realization, conviction and belief. Amongst all these overwhelming feelings what I remember most are my colleagues, friends and my family who have helped and supported me along this long but fulfilling road. This research work is the result of collaboration of some fabulous minds that I have met in past three years. Before any formal thanksgiving I would like to say few informal words to my supervisor Prof. Simon Brown and my co-supervisor Dr. Pawel Kowalczyk.

Simon,

You are an amazing boss, a good friend and above all a great human being. Thanks for believing in me, for pushing me beyond my limits and enhancing my abilities. Your active guidance and support made this research work possible.

Pawel,

I express my heartfelt gratitude to you. You introduced me to Scanning Tunneling Microscopy and Spectroscopy and guided me at every stage of my PhD. I have learnt the meaning of sincerity and dedication from you. You are the best teacher that I have ever had!

This research work is partially composed of theoretical calculations. I am very grateful to our collaborators who were actively involved with us to support and validate our experimental results:

(i) G.Bian, X.Wang and Prof Tai.C.Chiang, University of Illinois, Urbana Champagne, USA

(ii) E.S.Kadantsev, Prof T.K.Woo, University of Ottawa, Canada

(iii) B.Ingham, Industrial Research Limited, New Zealand

(iv) W.Kozlowski and Z.Klusek, University of Lodz, Poland

The TEM investigations by Dr. Domagoj Belic were invaluable in the oxidation experiments.

We at Department of Physics and Astronomy are extremely lucky to have an excellent team of workshop technicians. I specially thank Mr. Bob Flygenring at Cryogenics who made all my liquid helium experiments possible. Thank you Mr. Graeme MacDonald, Mr. Wayne Smith, Mr. Stephen, Hemmingson, Mr. Robert Thirkettle, Mr. Graeme Kershaw, Mr. Orlon Petterson and Mr. Tim Delany for all your help and support.

I would like to acknowledge the funding provided by The MacDiarmid Institute for Advanced Materials and Nanotechnology, and by the University of Canterbury.

I thank the postdoctoral fellows in our group: Dr Haifeng Ma, Dr. Shawn Fostner and Dr. Nadia Grillet for their suggestion and stimulating conversations. I would also like to thank Dr. Abdul Sattar, Dr. David MacKenzie, Mr. Jack Grigg and Mr. Amol Nande for lively discussions and wonderful company.

I wish I could describe how grateful I am to my love Akshita. She stood by me every time and took care of me. You are the most wonderful girl in the world and I am the luckiest person to have you in my life.

I love and respect my parents Dr. R.B.Mahapatra and Dr. Manju Sharma Mahapatra who have loved and supported me all my life. You have taken pains so that I could be comfortable. You have given me a treasure of blessings which have made me what I am today. I'll always take care of you and make you proud.

My best friend and my sister, Ms Deepti Mahapatra. You are my strength and my pride. Thank you for being by my side and lead me through right ways in life.

Love to my siblings- Nishtha, Vartika, Varchas, Poonam and Rikku.